Design optimisation of Reluctance Synchronous Machines: A Motor and Generator Study

by

Eduan Howard

Dissertation approved for the degree of Doctorate of Philosophy in Engineering in the Faculty of Engineering at Stellenbosch University

Department of Electrical Engineering,
Stellenbosch University,
Private Bag X1, Matieland 7602, South Africa.

Promoter: Prof. M.J. Kamper

December 2017

Declaration

By submitting this dissertation electronically, I declare that the entirety of the work contained therein is my own, original work, that I am the sole author thereof (save to the extent explicitly otherwise stated), that reproduction and publication thereof by Stellenbosch University will not infringe any third party rights and that I have not previously in its entirety or in part submitted it for obtaining any qualification.

Signature: E. Howard

Date: December 2017

Abstract

Design optimisation of Reluctance Synchronous Machines: A Motor and Generator Study

E. Howard

Department of Electrical Engineering,
Stellenbosch University,
Private Bag X1, Matieland 7602, South Africa.

Dissertation: PhdEng (Elec)

August 2017

This study focuses on the design and optimisation of the recently popular synchronous reluctance machine. The increase of this machine's popularity is because of its inherent high efficiency, with industry pushing for an ever higher efficiency machine drive package.

The study proposes design techniques that can be implemented in the design process to minimise or remove the inherent weaknesses. Machines designed by implementing the study techniques are manufactured and tested, with proposed design techniques validated through testing.

Finally, the developed machine model is implemented in a design study in the high power range for wind generator application. It was found, assuming mechanical feasibility, that the type of machine can be implemented in the very high power range, with competitive efficiency and power factor values achieved.

In order to even further improve machine performance and thus its competitiveness, an assisted reluctance synchronous machine model is proposed and optimised by implementing a retrofit rotor design and pre-designed machine stator. Results of this proposed machine indicate highly competitive machine performance, comparable with currently implemented machines in the field, thus warranting further investigation.

Uittreksel

Ontwerp optimalisering van Reluktansie Sinchroonmasjiene: 'n Motor en Generator Studie

E. Howard

Departement Elecktrise Ingenieurswese,
Universiteit van Stellenbosch,
Privaatsak X1, Matieland 7602, Suid Afrika.

Proefskrif: PhdEng (Elec)

Augustus 2017

Hierdie studie fokus op die ontwerp en optimeering van die onlangs gewilde reluktansie sinchroonmasjien. Die toename in die gewildheid van hierdie masjien is as gevolg van sy inherente hoë doeltreffendheid, met die industrie wat streef na steeds hoër doeltreffendheidstelsel.

Die studie stel ontwerptegnieke voor wat in die ontwerpproses geïmplementeer kan word om die inherente swakhede van die masjien te verminder of te verwyder. Masjiene ontwerp deur die implementering van die studietegnieke word vervaardig en getoets, met voorgestelde ontwerpstegnieke wat deur toetse bevestig word.

Ten slotte word die ontwikkelde masjienmodel geïmplementeer in 'n ontwerpstudie in die hoë drywingreeks vir windgeneratoraanwending. Daar is gevind, met die aanvaarding van meganiese haalbaarheid, dat die tipe masjien in die baie hoë drywingreeks geïmplementeer kan word, met mededingende doeltreffendheid en arbeidsfaktorwaardes behaal.

Ten einde die prestasie van die masjien te verbeter, en dus ook sy mededingendheid, word 'n hulp reluktansie sinchroonmasjien voorgestel en geoptimaliseer deur die implementering van 'n vervangde rotor ontwerp op n vooraf ontwerpte masjien stator. Die resultate van hierdie voorgestelde masjien dui op 'n hoogs mededingende masjienprestasie, vergelykbaar met die huidige geïmplementeerde masjiene in die veld, wat sodoende verdere ondersoek regverdig.

Acknowledgements

I would like to express my sincere gratitude to the following people and organisations:

- **ABB** - For the financial support during the study, that includes travel arrangements and tours of factories in Stockholm, Sweden and Helsinki Finland.
- **Prof M.J Kamper** - For the theoretical advice, guidance and financial support during the study.
- To all the colleagues in the electrical machines laboratory that contributed directly and indirectly to the study, that lightened the days load though comedy laughter and support. A specific thank you to :
  - **Christiaan Willem Vorster (a.k.a Pof)** - Without the assistance, support, motivation and knowledge I learned from Pof, this study would have never culminated to what it is today. Your vision and work ethic is hard to find, I wish you only success for the future.
  - **Johannes Hendrik Jacob Potgieter** - A better role model I could not have asked for. Thank you to everything you thought me.
  - **Wikus Theo Villet** - Thank you for your technical assistance, patience and friendship during our encounters.
  - **Albert Sorgdrager** - A new friend and colleague, assisting with brainstorming sessions late into the night. Thank you for all your assistance and support.
  - **Jon-Pierre du Plooy** - For your technical assistance during testing procedures and brainstorming.
- **Nicole René Howard** - To my wife, thank you for your rock solid support through the years, in the good times and bad, in the late nights and long weekend. Without you, this would have not been possible. You are my heart's keeper, I love you.
- **My Parents** - Thank you for believing in me. This would not have been possible without your support.

Contents

List of Figures

List of Tables

Nomenclature

Constants

$\pi =$	3.141 592 654
$g =$	9.81 m/s^2

Abbreviations

A_n	- Asymmetric Simulation Number n
ALA	- Axially Laminated
ALPSO	- Augemented Lagragian Particle Swarm Optimizer
ARSM	- Assisted Reluctance Synchronous Machine
B_{EL}	- Guide Line for Point S_{H2} and S_{L2}
Bi-Axial	- An combination between IPM and ARSM
B_{LL}	- Guide Line for Point S_{L1}
B_{TL}	- Guide Line for Point S_{H1}
C	- Copper
CRSM	- Compensated Reluctance Synchronous Machine
CONMIN	- Constrained Function Minimization
DFIG	- Doubly-Fed Induction Generator
FDCH	- Finite Difference Steps Size
FE	- Finite Element Package
FILTERSD	- A generalization of Robinson's optimiser, globalised by using a filter and trust region
FI-IPM	- Field Intensified Interior Permanent Magnet Machine
H_n	- Study n Results from Howard
IE1	- Standard Efficiency
IE2	- High Efficiency
IE3	- Premium Efficiency
IE4	- Super Premium Efficiency
IE5	- Ultra Efficiency
IEC	- International Electrotechnical Committee
IM	- Induction Machine

IPM	- Interior Permanent Magnet Machine
KSOPT	- Kreisselmeier Steinhauser Optimizer
LSPMSM	- Line Start Permanent Magnet Synchronous Machine
M_n	- Study n Results from Moghaddam
MMFD	- Modified Method of Feasible Directions
P_1	- Point 1
P_{11}	- Point 1 Spline Departure Angle Point
P_{12}	- Point 2 Spline Arrival Angle Point
P_{1S}	- Symmetric Point 1 Around Local Axis Y_{L1}
P_{1H}	- Point 1 High Spline Departure Point
P_{1L}	- Point 1 Low Spline Departure Point
P_2	- Point 2
P_{22}	- Point 2 Spline Departure Angle Point
P_{23}	- Point 3 Spline Arrival Angle Point
P_3	- Point 3
P_{33}	- Point 3 Spline Departure Angle Point
P_{34}	- Point 4 Spline Arrival Angle Point
P_4	- Point 4
P_{44}	- Point 4 Spline Departure Angle Point
P_{45}	- Point 5 Spline Arrival Angle Point
P_5	- Point 5
P_{5S}	- Symmetric Point 5 Around Local Axis Y_{L2}
PA_n	- Study n Results from Palmieri
P_{FIT1}	- Polynomial Curve Fit 1
P_{FIT2}	- Polynomial Curve Fit 2
PM	- Permanent Magnet
PMSG	- Permanent Magnet Synchronous Generator
PMSM	- Permanent Magnet Synchronous Motor
RO	- Rotor
RSM	- Reluctance Synchronous Machine
S_n	- Symmetric Simulation Number n
SCIM	- Squirrel-Cage Induction Motor
SDPEN	- Sequential Penalty Derivative free Method for Nonlinear Constrained Optimisation
ST	- Stator
SLP	- Sequential Linear Programming
SLSQP	- Sequential Least Squares Programming
SOLVOPT	- Solver for Local Optimization Problems
SQP	- Sequential Quadratic Programming
SynRm	- Synchronous Reluctance Machine

SRM	- Switched Reluctance Machine
S_{H1}	- Spline Departure Angle Point High 1
S_{H2}	- Spline Departure Angle Point High 2
S_{L1}	- Spline Departure Angle Point Low 1
S_{L2}	- Spline Departure Angle Point Low 2
T	- Tooth
TLA	- Transversely Laminated
VSD	- Variable Speed Drive
Y	- Yoke
Y_G	- Global Y-Axis
Y_{L1}	- Local Y-Axis 1
Y_{L2}	- Local Y-Axis 2
X_G	- Global X-Axis
X_{L1}	- Local X-Axis 1
X_{L2}	- Local X-Axis 2

Variables

A	Area	$[\mathrm{m}^2]$
B	Magnetic Flux Density	$[\mathrm{WB/m}^2]$
B_{mt}	Maximum Tooth Magnetic Flux Density	$[\mathrm{WB/m}^2]$
B_{my}	Maximum Yoke Magnetic Flux Density	$[\mathrm{WB/m}^2]$
B_r	Barrier Number	[ ]
C_{MASS}	Copper Active Mass	[kg : tn]
D_B	Bearing Radius	[m]
E_a	Phase Voltage	[V]
E_d	D-Axis Speed Voltage	[V]
E_{de}	D-Axis End Winding Leakage Speed Voltage	[V]
E_{FF}	Efficiency	[%]
E_q	Q-Axis Speed Voltage	[V]
E_{qe}	Q-Axis End Winding Leakage Speed Voltage	[V]
F	Force	[N]
F_A	Field Winding Slot Area	$[\mathrm{m}^2]$
f_e	Frequency	[Hz]
F_{FF}	Field Winding Fill Factor	[ ]
h	Air gap length	[ ]
I_{abc}	ABC Phase Current Matrix	[A]

I_d	D-Axis Phase Current Excluding Core Loss	[A]
I_{d1}	D-Axis Phase Current Including Core Loss	[A]
I_{dq0}	DQ-Axis Phase Current Matrix	[A]
I_F	Field Current	[A]
I_q	Q-Axis Phase Current Excluding Core Loss	[A]
I_{q1}	Q-Axis Phase Current Including Core Loss	[A]
I_s	Phase Current	[A]
J	Current Density	[A/mm^2]
J_F	Field Current Density	[A/mm^2]
J_S	Stator Current Density	[A/mm^2]
L_A	Megawatt Generator End Winding Arc Length	[m]
l_c	Stack Coil Length	[m]
L_{Coil}	Total Coil Length	[m]
L_d	D-Axis Inductance	[H]
L_e	Leakage Inductance	[H]
l_{end}	End Winding Length	[m]
L_H	Megawatt Generator End Winding Height	[m]
L_S	Stack Length	[m]
L_q	Q-Axis Inductance	[H]
m	Mass	[kg]
M_a	Active Mass	[kg : tn]
M_W	Machine Winding Layout	[ ]
N_{INV}	Inverter Efficiency	[%]
N_{ST}	Number of Turns in Series per phase per Pole	[ ]
N_t	Number of Turns Per Stator Slot	[ ]
P_{1SP}	Point 1 Barrier Width	[m]
P_{5SP}	Point 5 Barrier Width	[m]
p	Pole Pairs	[ ]
P	Number of Poles	[ ]
P_B	Bearing Power Loss	[W]
P_C	Core Loss Power	[W]
P_F	Power Factor	[ ]
P_{Field}	Field Power	[W]
P_{In}	Power In	[W]
P_{Out}	Power Out	[W]
P_R	Stator Coil Resistance Power Loss	[W]
P_R^R	Rotor Coil Resistance Power Loss	[W]
P_T	Total Power Loss	[W]
$P_{W\&V}$	Windage and Friction Power Loss	[W]
R_C	Core Loss Resistance	[ω]

R_{FIX}	Fixed Point 1 and 5 Radius	[m]
R_{GAP}	Air Gap Radius	[m]
RO_{MASS}	Rotor Active Mass	[kg : tn]
RO_I	Inside Rotor Radius	[m]
RO_O	Outside Rotor Radius	[m]
R_{Slot}	Stator Slot Center Radius	[m]
R_{SSO}	Stator Slot Outer Radius	[m]
R_{SSI}	Stator Slot Inner Radius	[m]
S	Complex Power	[VAR]
S_{ARSG}	Complex Power Inverter Rating for the ARSG	[MVAR]
S_{1P}	Complex Power	[VAR]
S_{2P}	Complex Power	[VAR]
SF	Safety Factor	[ ]
S_P	Stator Slots Per Pole	[ ]
S_{RSG}	Complex Power Inverter Rating for the RSG	[MVAR]
ST_I	Inside Stator Radius	[m]
ST_O	Outside Stator Radius	[m]
T	Instant Torque	[Nm]
T_A	Average Torque	[Nm]
T_{MASS}	Stator Tooth Mass	[Kg]
T_{MAX}	Max Torque in Array	[Nm]
T_{MIN}	Min Torque in Array	[Nm]
T_R	Torque Ripple	[%]
V_{DC}	DC Voltage	[V]
V_d	D-Axis Voltage	[V]
V_q	Q-Axis Voltage	[V]
V_s	Phase Voltage	[V]
Y_{MASS}	Stator Yoke Mass	[Kg]
Z_F	Field Winding Turns	[ ]

Greek Variables

α_R	Point 1 Radial Displacement	[Rad]
α_L	Point 5 Radial Displacement	[Rad]
β_R	Point 2 Radial Displacement	[Rad]
β_L	Point 4 Radial Displacement	[Rad]
δ	Load Angle	[°]
λ_d	D-Axis Flux Linkage	[Wb − t]
λ_{df}	D-Axis Field Winding Flux Linkage	[Wb − t]

λ_{de}	D-Axis Leakage Flux Linkage	[Wb – t]
λ_l	Leakage Flux Linkage	[Wb – t]
λ_m	Air Gap Flux Linkage	[Wb – t]
λ_s	Flux Linkage Sum	[Wb – t]
λ_q	Q-Axis Flux Linkage	[Wb – t]
λ_{qe}	Q-Axis Leakage Flux Linkage	[Wb – t]
ω_m	Mechanical Speed	[rad/s]
ω_e	Electrical Speed	[rad/s]
ω_s	Synchronous Speed	[rad/s]
ρ	Resistivity	[Ωm]
κ	Megawatt Generator End Winding Arc Length	[rad]
τ_p	Pole Pitch	[Rad]
θ	Current Angle	[◦]
χ	P_{1H} and P_{1L} Radial Displacement	[rad]

Chapter 1

Introduction

1.1 Current Energy Standards & Industry Trends

The introduction highlights some aspects of the current electrical machine market and how current efficiency classes are defined. Furthermore, current machine technologies are described to provide background of the study. This study focuses on the field of synchronous machines, and more specifically, reluctance synchronous machines. The introduction provides a brief background on the field, along with the study motivation, its challenges and a full scope definition of the study.

1.1.1 Efficiency & Current Trends

In an ever increasing energy demanding world, the method of energy production and consumption has come into the spotlight. The impact of this focus has vast implications on the current electrical machines industry, with the industry striving

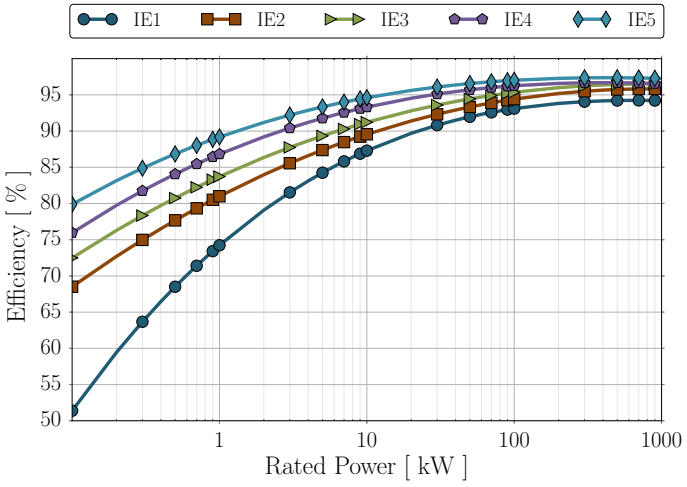

Figure 1.1: IEC 60034-30 nominal efficiency class limits and main national minimum energy-efficiency performance standard schemes world wide [1].

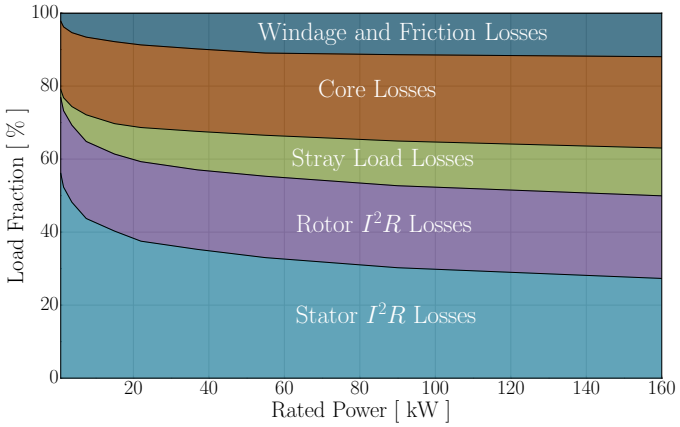

Figure 1.2: IEC 60034-30 nominal efficiency classes limits and main national minimum energy-efficiency performance standard schemes world wide [2].

for a more cost effective, efficient and environmentally friendly solution to their energy conversion needs.

As a result of this increasing pressure, a new international standard, International Electrotechnical Committee Standard (IEC Standard) 60034-30, was formed in 2008 to help harmonize global machine efficiency standards [3]. In the latest version of these efficiency standards, four efficiency classes for electrical machine are proposed, with a fifth in the final stages of evaluation. These efficiency classes consist of, standard efficiency (IE1), high efficiency (IE2), premium efficiency (IE3) and super premium efficiency (IE4). They are illustrated in Figure 1.1, with an additional ultra efficiency (IE5) standard envisioned for the future addition to the efficiency classes.

Considering the large variety of available machine topologies and types, currently the vast majority of the market is dominated by squirrel-cage induction motors (SCIM's) [4–6]. The main reason for the implementation of this type of machine is its operating simplicity, its ability to operate with a variable speed drive (VSD) with simple open loop control, its ability to operate under direct grid connection and its very robust and simple rotor. The main drawback of this type of machine is its additional losses that occur on the rotor, due to the rotor cage resistance. This factor limits the efficiency and the IEC class rating of the machine, with large machine manufacturers only recently able to achieve an IE4 standard SCIM [7]. This class however is believed to be the upper limit of efficiency for this specific technology [2].

In order to develop machines that reach even higher IEC classes, research in permanent magnet synchronous machines with line-start capabilities (LSPMSM) and with VSD operation such as reluctance synchronous machines (RSM) and switched reluctance machines (SRM) has intensified [2, 8].

The fundamental losses of any electrical machines can be divided into five main sections as illustrated in Figure 1.2: [1] windage and friction losses, [2] core/iron losses, [3] stray load losses, [4] rotor winding or cage resistance losses and [5] stator winding resistance losses. By simply removing the rotor losses present in SCIM's, higher efficiency can be obtained with synchronous machine technologies.

Type	2D Geometry	3D Picture
Squirel-Cage Induction Machine (SCIM)	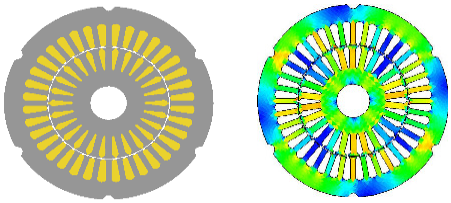 Stator & Rotor Geometry	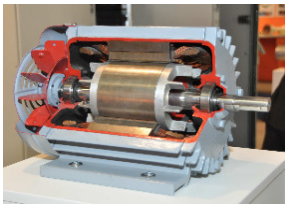 Stator & Rotor
Permanent-Magnet Synchronous Machine (PMSM)	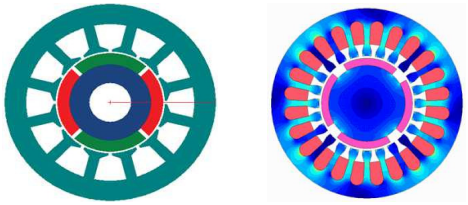 Stator & Rotor Geometry	 Stator & Rotor
Line-Start PM Synchronous Machine (LSPMSM)	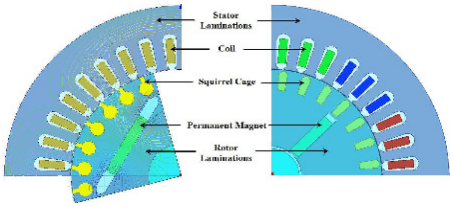 Stator & Rotor Geometry	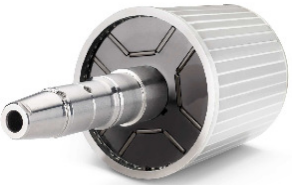 Rotor
Reluctance Synchronous Machine (RSM)	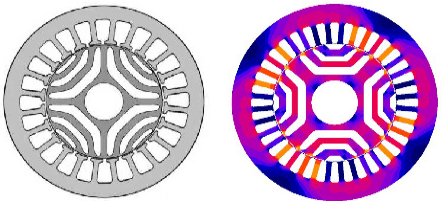 Stator & Rotor Geometry	 Stator & Rotor
Switch Reluctance Machine (SRM)	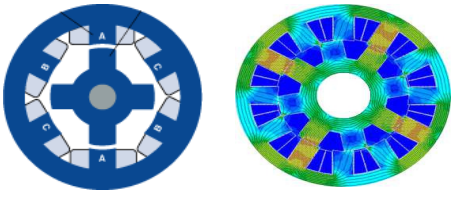 Stator & Rotor Geometry	 Stator & Rotor

Figure 1.3: Examples of commercial induction and synchronous machine models.

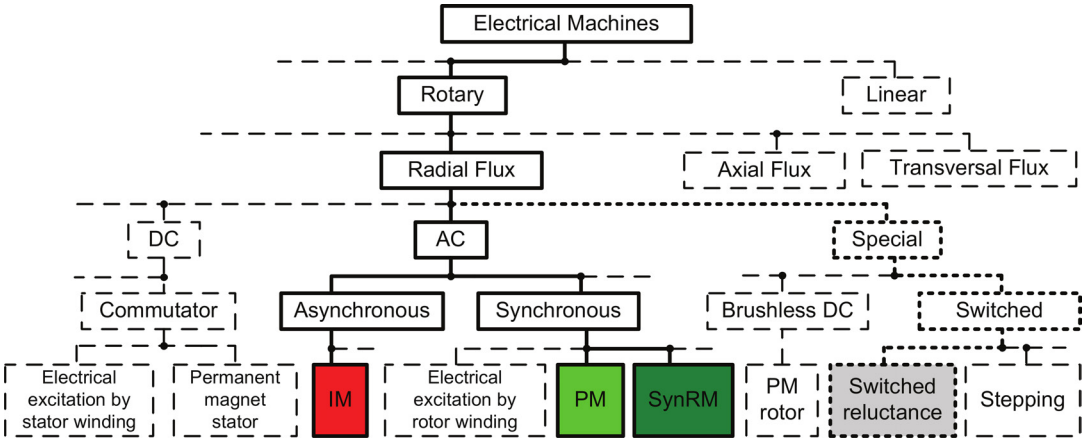

Figure 1.4: Electrical machine family [9] (RSM a.k.a SynRm).

Current popular synchronous machine technologies that are implemented as alternatives to SCIMs are presented in Figure 1.3 with the electrical machine family tree illustrated in Figure 1.4. These synchronous machine technologies consist of:

1. the Permanent-Magnet Synchronous Machine (PMSM) operating with a VSD
2. the Line-Start Permanent Magnet Synchronous Machine (LSPMSG) operating as SCIM during start-up and PMSM after machine synchronisation.
3. the Reluctance Synchronous Machine (RSM or SynRm) operating with a VSD and
4. the Switched Reluctance Machine (SRM) operating with a VSD

It is well known in the machine design industry and literature that by adding permanent magnet (PM) material, higher efficiencies and an increase in power density can be achieved. There are however several drawbacks associated with the implementation of this material, with the main drawbacks associated with the high fluctuating prices of the material and its restricted market supply. Additional disadvantages can include an increase of machine design complexity due to the permanent rotor magnetic field that can affect rotor manufacture, machining and assembly.

Although certain synchronous machine technologies were discredited in previous years due to its insufficient performance, this area is now being revisited. This is due to the increase in modern design techniques that implement finite element modelling and the advances in VSDs. The two most popular machines in this field are the RSM and the SRM, with the research of these two machines having drastically increased in the past decade [10–13]. The main reasons for this renewed interest in these two machines are their extremely simple rotors, that implement no PM material, and the achievable increase in efficiency compared to the conventional SCIM, that places it in the IE4/IE5 efficiency class [2, 8].

In this study, RMSs are extensively investigated, with the study focusing on strengthening the inherent weaker and strong aspects of this machine topology with a variation of design techniques. Additionally, the study also implements the design

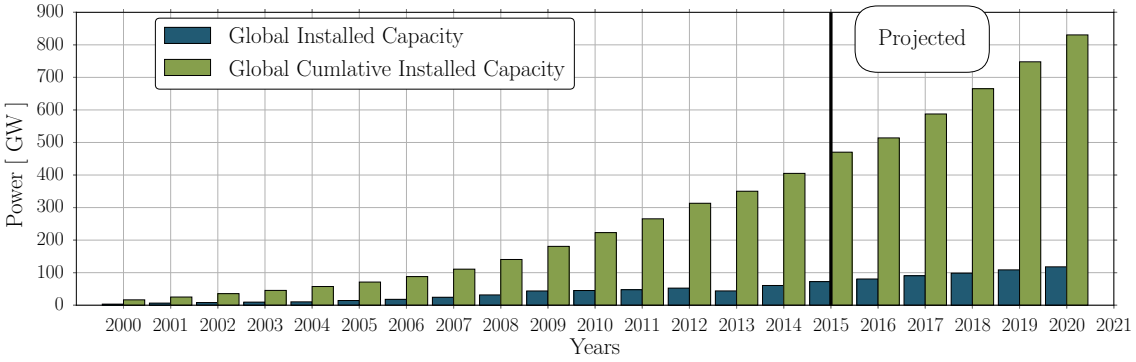

Figure 1.5: New and cumulative installed total wind energy capacity [14].

techniques to investigate the feasibility of implementing RSMs for wind energy in the megawatt power level. In the next section, current wind energy trends are discussed and motivation is provided for the selection of the specific sector in the field for investigation. The SRM falls outside the scope of this study.

1.2 Wind Energy Developments

Among the rapidly growing renewable energy industries is the wind energy sector as presented in Figure 1.5 [14,15]. From this chart, presented by the global wind energy council, it is clear that wind energy is one of the largest growing renewable energy sectors in the world. The acceleration in installed capacity is evident in the past 10 years with the forecast installation for the next 4 years indicating a continuation of this trend.

One of the key areas of research in wind energy is the generator of the wind turbine, with research focusing on the improvement of the reliability and efficiency of the generator along with the reduction of manufacturing cost. Traditionally, small scaled wind turbines commonly implemented DC machine, SMs and SCIM's. This compared to the doubly-fed induction generators (DFIG) that currently dominate the medium to large power range, with PMSGs implemented in the very large power ranges. An additional focus point of the study is to investigate the feasibility of implementing RSGs in this very large power range that is currently dominated by PMSGs. The next section focuses on describing current market trends in wind turbines, with the focus on increasing overall system reliability.

1.2.1 System Reliability & Market Trends

During the past decade, drastic increases have been made in the maximum wind turbine average hub height and turbine rotor diameter, seen in Figure 1.6. In conjunction with this turbine size growth is the generator power level, with average rated power increasing from around 2 MW in 2000 to a newly announced 7 MW scheduled for installation in 2018. The main motivation for this drastic growth is the desire to increase the capacity factor of a wind turbine. The capacity factor is defined as the ratio of the actual energy captured over a period of time compared

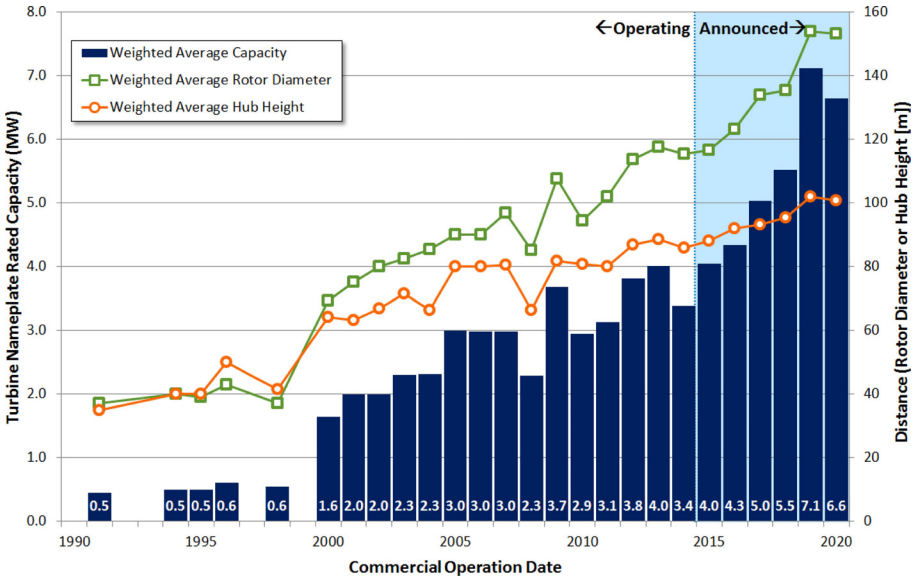

Note: The values for the expected turbine capacities, rotor diameters, and hub heights from 2015 to 2020 are determined from projects that have announced turbine supply agreements. The turbine characteristic weighted average values were calculated by considering each of the project's contribution of annual capacity additions.

Figure 1.6: Global turbine capacities, rotor diameters, and hub heights over time [16].

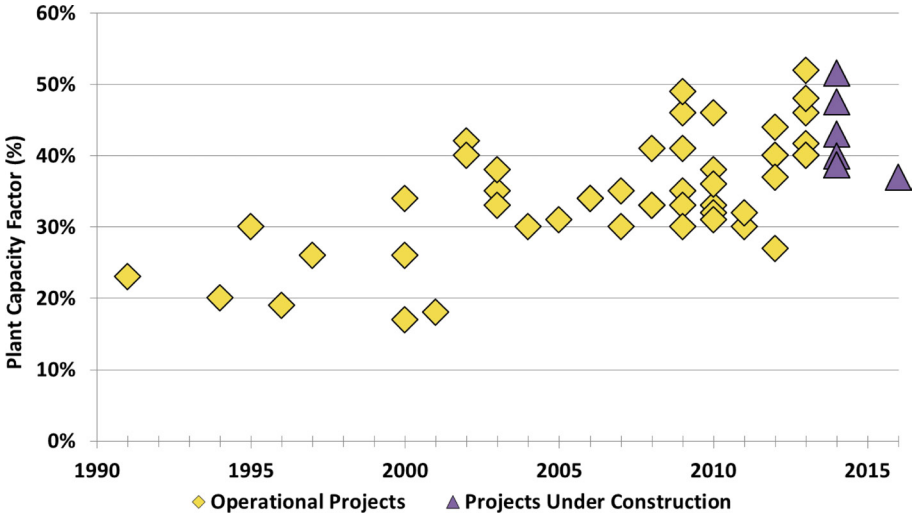

Note: Plant capacity factors are shown for the year each project reached completion. Multi-phase projects were combined to show a single capacity factor and are reported at the latest year when turbines were added at the project site. Figure includes commercial-scale projects; test and demonstration-scale projects are excluded.

Figure 1.7: Reported capacity factors for global offshore wind plants over time [17].

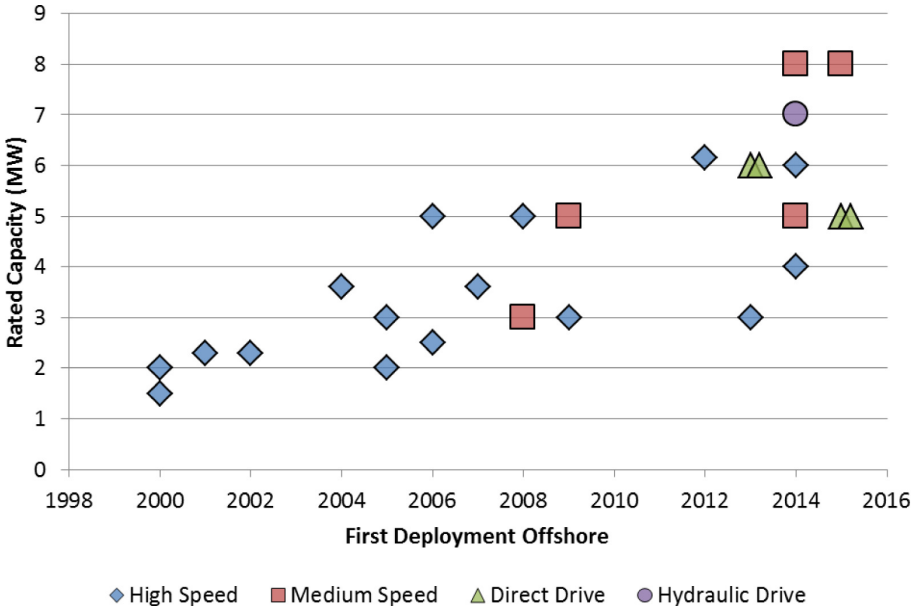

Note: Deployments after 2013 based upon wind turbine manufacturers' announced schedules.

Figure 1.8: Offshore wind turbine prototypes by drivetrain configuration and year of first offshore deployment [17].

to the theoretical maximum available nameplate energy capture over the same time period. The trend between the increase of turbine size and the increase in capacity factor as a result can clearly be seen in Figures 1.6 and 1.7.

Due to the limitations that onshore wind turbine sites have with respect to logistics among others, the growth in turbine size has mainly been in the offshore sector. Additionally, in an effort to increase reliability, efficiency and reduce the overall drivetrain size of the generator, a new sector of wind generators are increasingly being investigated in the medium speed range, with the trend in newly installed generators presented in Figure 1.8. This sector is defined as wind generators operating at a generator shaft speed of between $\pm$ 100 and 500 rpm, as seen from available products from large energy sector companies like ABB, General Electric and The Switch. Figure 1.9 illustrates an example of a typical medium speed drive train that is being developed by Advanced Magnet Lab and NREL for the U.S Department of Energy [18].

The advantage of this medium speed range is the reduction in required gear box stages that increase efficiency, reliability and reduce the overall drive train package weight. Due to these facts, this sector has lately been favoured for offshore wind energy, where reliability, low maintenance and lower drive train mass have proven to be a great advantage in difficult maintenance conditions that are present in offshore wind farms.

Currently a large section of the medium speed range sector consist of PMSGs. The advantages of these machines are an extremely high torque density, a favourable power factor and very high efficiency rating. Due to the current increasing instability of the rare earth magnet market, an increasing interest in research for alternative medium speed generator technologies that do not implement rare earth material

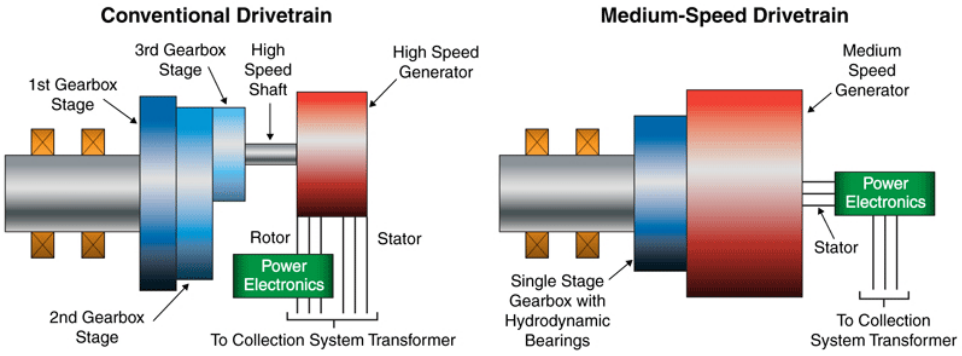

Figure 1.9: Comparative example of current drive train and medium speed drive train with permanent magnet synchronous generator [18].

has emerged. The investigation into alternative technologies for the medium speed range is where the second part of this study focuses on. More specifically, the study investigates the feasibility of implementing RSMs in the medium speed range as possible alternative to the PMSGs.

1.3 Overview of this Study

In this section, the challenges and objectives of the study is laid out. A description of the scope of the study indicates what factors the study includes, the factors that are excluded and the assumptions made. Finally an overview of the thesis is be laid out by chapter to illustrated the step wise procedure the study incorporated.

1.3.1 Challenges

In order to effectively design a competitive RSM in the megawatt power range to compete with existing machine topologies, the machine needs some or other form of optimisation. The initial challenge for the study is to develop a machine topology and design technique to study RSMs and its characteristics. By gaining knowledge of these specific factors, the specific topology can be manipulated to positively effect the desired machine parameters to produce a more competitive machine.

The two main drawbacks that current designers of RSMs face are relatively large torque harmonics and a poor power factor. The objectives of the study are to partially or entirely mitigate these two drawbacks by implementing the knowledge gained by studying the results of a varying number of design techniques.

The cumulative knowledge gained from these studies, validated by prototype manufacture, is implemented in the final RSM study in the megawatt power range. Further work is conducted on the megawatt design by implementing a type of hybrid RSM, with the intention to produce a machine competitive with current implemented machine generators.

1.3.2 Objectives

The objectives of the study consists of:

1. The development of a modelling tool that can be connected to a finite element package to simulate RSM topologies. Additionally, the toolbox also consists of the development of a new, alternative flux barrier topology.

2. The implementation of the developed modeling tool to study torque harmonics in RSMs, an inherent weakness of this specific machine. The objective is to study torque harmonic reduction techniques that implement asymmetric flux barriers and rotor skew design optimisation.

3. The implementation of the developed modeling tool to study power factor in RSMs, an inherent weakness of this specific machine. The objective of the study is to investigate the power factor limitations by implementing a pareto front optimisation technique to compare competitive average torque and the inherent weaker power factor of RSMs.

4. The implementation of the developed modeling tool to study medium speed RSMs, by designing and testing a machine in the medium speed range. The objective is to study the operation of a RSM in motor and generator mode in the medium speed range.

5. The implementation of the developed tool to investigate RSMs in the 5 MW power range. The objective is to determine whether RSMs can be implemented as generators in large scale wind turbines.

6. The implementation of the developed tool to investigate an assisted RSM, that implements flux assistance on the rotor, in the 5 MW power range. The objective is to determine whether an assisted RSM can be implemented as a generator in large scale wind turbines. The definition of the assisted RSM is be discussed in Chapter 2.

1.3.3 Scope

The scope of the defined objectives are as follows:

1. The scope of the initial study investigates the proposed symmetric, asymmetric topologies by only comparing average torque and torque ripple values for optimised machines. This study incorporates two existing machine stators for the rotor retrofit optimisation study. The first consists of an induction machine stator in a 90L machine frame size and the second, a previously optimised RSM stator in a 132L frame size. A further investigation on the effect of rotor skew on the proposed topology is conducted with the focus on the effect on torque ripple, average torque and power factor.

   Furthermore, even though the script includes power factor and efficiency calculations, no attempt is made to include these parameters in the machine design

optimisation. Power factor is however be included in the rotor skew evaluation on the proposed topology.

2. The scope of the second study includes the optimisation of a rotor and stator implementing knowledge gained from the first study. This machine is optimised to fit into existing machine frame sizes. The attention of this study focuses not only on average torque and torque ripple as in the previous study, but attention is given to machine power factor values. With the latter in mind, an average torque, power factor relation pareto front is constructed in order to select a suitable machine from this front.

   Once again, as in the first study, even though efficiency values are calculated for the machine during optimisation, efficiency is not be included in the design process and is only evaluated at the end before manufacture to ensure acceptable levels.

3. The scope of the final study includes the design of a medium speed RSM and assisted RSM in the 5 MW power range implementing knowledge gained from the first two studies. Given the complexity of this design process, this machine design only includes electromechanical optimisation for a close to "perfect" motor topology, with mechanical stress and deformation not taken into consideration. This study focuses not only on average torque and torque ripple, but power factor, efficiency and machine mass will be included.

1.4 Layout of this Thesis

In order to achieve the objectives of the study and fall within the studies scope, the study is divided into four chapters. Each chapter focuses on the objectives set out above:

- **Chapter 2:** The main objective of this chapter is to investigate the history and theoretical models of reluctance synchronous machines in order to estimate performance parameters. This chapter forms the base of the study on which all optimisation models and strategies are based. Topics in the chapter include a brief history of the machine, design methodologies, theoretical estimation of performance parameters and how it is implemented to investigate the machine in each respective study.

- **Chapter 3:** This chapter consists of two sections, firstly in order to investigate the proposed machine, a highly variable and adaptable physical rotor model is created with symmetric and asymmetric rotor profile capabilities. The second section consists of the implementation of this developed model in an optimisation study, focused on torque ripple, in order to investigate its effectiveness of the developed model. This investigation focuses directly on one of the inherent weaknesses of reluctance synchronous machines, namely torque ripple and how this disadvantage can be mitigated with the proposed

rotor model. This chapter effectively describes the study objectives two and three.

- **Chapter 4** This chapter consists of three sections, firstly a stator profile is developed in order to study reluctance synchronous machine models in its entirety. Secondly, a brief study is conducted to determine the optimum optimiser algorithm to be implemented from the available optimisers in the implemented package. Thirdly, the main objective of the chapter, that discusses the studies objective four, is to investigate and optimise another inherent weakness of reluctance synchronous machines namely power factor. This study aims to not only achieve optimum power factor parameters for the respective machines studied, but also investigates possible relationships between average torque and power factor, and possible prediction methods that can be implemented to predict machine performance before optimization.

- **Chapter 5 :** This chapter focuses on studying reluctance synchronous machines in the 5 MW power range, with both rotor and stator profiles developed in the previous two studies. Additionally, in order to further improve the machine's performance and improve its competitiveness, an assisted reluctance synchronous machine, which implements the DC-link inverter current is presented. This chapter effectively describes the study objective five and six.

- **Chapter 6 :** This chapter consists of recommendations and conclusions for the respective studies completed and results obtained.

1.5 Publications and Engineering Scientific Contributions

The following publications summarize the work presented in this study by chapter.

1.5.1 Paper Publications

- **The following paper publication summarises the work discussed in Chapter 3.**

  – E. Howard, M. J. Kamper and S. Gerber, "Flux barrier and skew design optimisation of reluctance synchronous machines", Electrical Machines (**ICEM**), 2014 International Conference on, Berlin, Germany, 2014, pp. 1186-1192. doi: 10.1109 ICELMACH.2014.6960332

- **The following paper publication summarises the work discussed in Chapter 4.**

  – E. Howard and M. J. Kamper, "Weighted factor multi-objective design optimisation of a reluctance synchronous machine", 2015 IEEE International Electric Machines & Drives Conference (**IEMDC**), Coeur d'Alene, USA, ID, 2015, pp. 1781-1789. doi: 10.1109 IEMDC.2015.7409305

- **The following paper publication summarises the work discussed in Chapter 5.**

– E. Howard and M. J. Kamper, "Reluctance Synchronous Wind Generator Design Optimisation in the Megawatt, Medium Speed Range", 2017 IEEE Energy Conversion Congress & Exposition (**ECCE**), Cincinnati, Ohio, [Attending Conference from 1 - 5 October]

1.5.2 Journal Publications

- **The following journal publication is an upgrade of the publication presented at the 2014 ICEM conference.**

– E. Howard, M. J. Kamper and S. Gerber, "Asymmetric Flux Barrier and Skew Design Optimization of Reluctance Synchronous Machines", in **IEEE Transactions on Industry Applications**, vol. 51, no. 5, pp. 3751-3760, Sept.-Oct. 2015. doi: 10.1109 TIA.2015.2429649

- **The following journal publication is an upgrade of the publication presented at the 2015 IEMDC conference.**

– E. Howard; M. Kamper, "Weighted Factor Multi-Objective Design Optimisation of a Reluctance Synchronous Machine", in **IEEE Transactions on Industry Applications** , vol.PP, no.99, pp.1-1. doi: 10.1109 TIA.2016.2532287

Chapter 2

RSM Principles & Model

2.1 Introduction

The reluctance torque concept was discovered very early in the development of electrical machines and can be traced back to before the 1900s [19]. Reluctance is a concept that describes a materials ability to provide resistance to magnetic flux caused by a magnetic field, with the flux flowing in the path with the lowest magnetic reluctance. The reluctance torque concept is presented in Figure 2.1 with two objects in Figure 2.1a, object A and B, providing isotropic reluctance and anisotropic reluctance. As defined in literature, the path of least reluctance is defined as the D-axis and highest reluctance the Q-axis, as annotated to the rotor reference frame in Figures 2.1a and 2.1c. As presented, when the anisotropic reluctance bar is placed in a magnetic flux field, the magnetic flux chooses the path of least reluctance i.e. through the magnetic bar, as with Figure 2.1b. The offset in alignment between the D-axis and the magnetic field causes a force F that tries to align the bar with the flux field direction, this force in turn produces a torque around the bar's central axis.

Torque production in RSMs utilise this reluctance force concept, together with a rotating magneto motive force, created by a conventional IM stator winding. The field Ψ, rotating at synchronous speed ω_s, illustrated in Figure 2.1, is produced by a sinusoidally distributed winding in a slotted stator, with the field linking to the

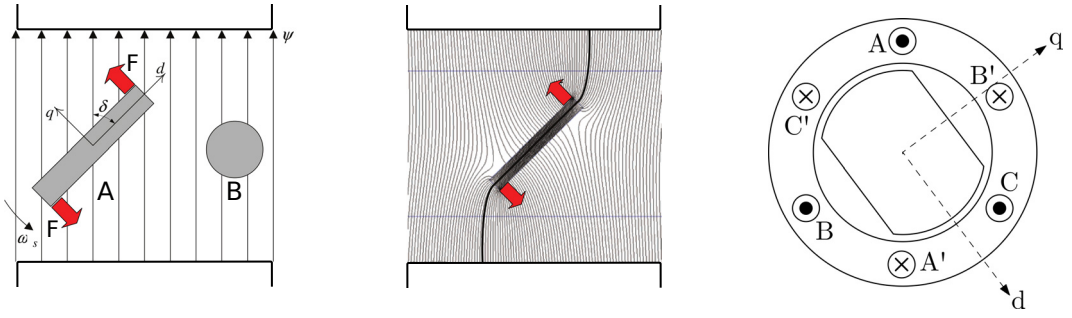

(a) **(b)** **(c)**

Figure 2.1: An object with anisotropic geometry **A** and isotropic geometry **B** in a magnetic field with DQ rotor reference frame [20–22].

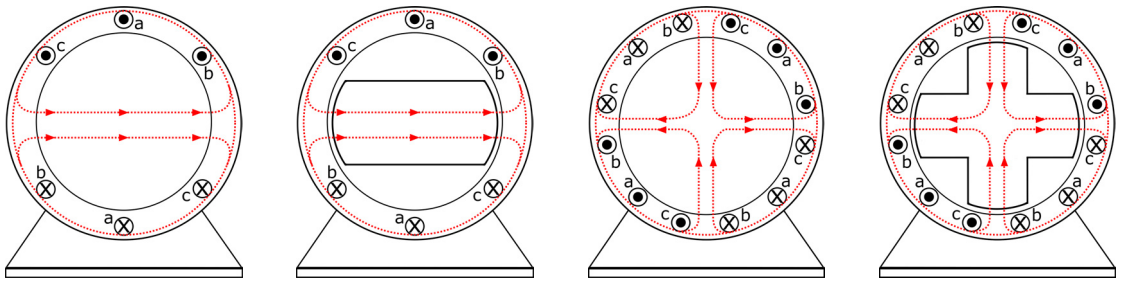

Figure 2.2: Flux path of a two pole and four pole three phase machine.

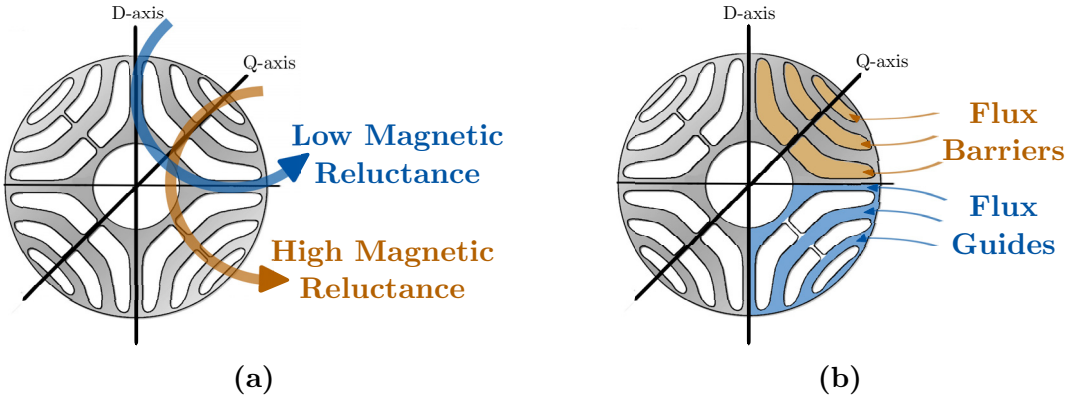

Figure 2.3: Illustration of four-pole, transversely laminated designed rotor lamination by Vagati [23–26].

rotor through a small air-gap. In this situation, the angle δ in Figure 2.1a represents the load angle, with the increase and decrease in this angle representing the increase and decrease in produced torque.

A representation of a two and four-pole stator and flux field is presented in Figures 2.2a and 2.2c, with the anisotropic rotors illustrating the rotor profile required for torque production presented in Figures 2.2b and 2.2d. Since there is no magnetic field production on the rotor, the stator currents are responsible for both the torque production and the magnetisation that can be controlled by controlling the stator winding current angle.

An example of a modern day, four-pole RSM is illustrated in Figure 2.3, with the high and low reluctance paths indicated. Additionally shown in Figure 2.3b is the description of a modern day RSM rotor, with flux barriers implemented to increase the q-axis reluctance and motor anisotropy in order to improve the performance characteristics of the machine. This feature of the rotor forms a critical part in the design of a RSM, with the shaping and number of barriers critical in the design process. The next section describes a short history of RSMs, the development in the shaping of the flux barriers and how the modern day optimisation is implemented to design competitive machines.

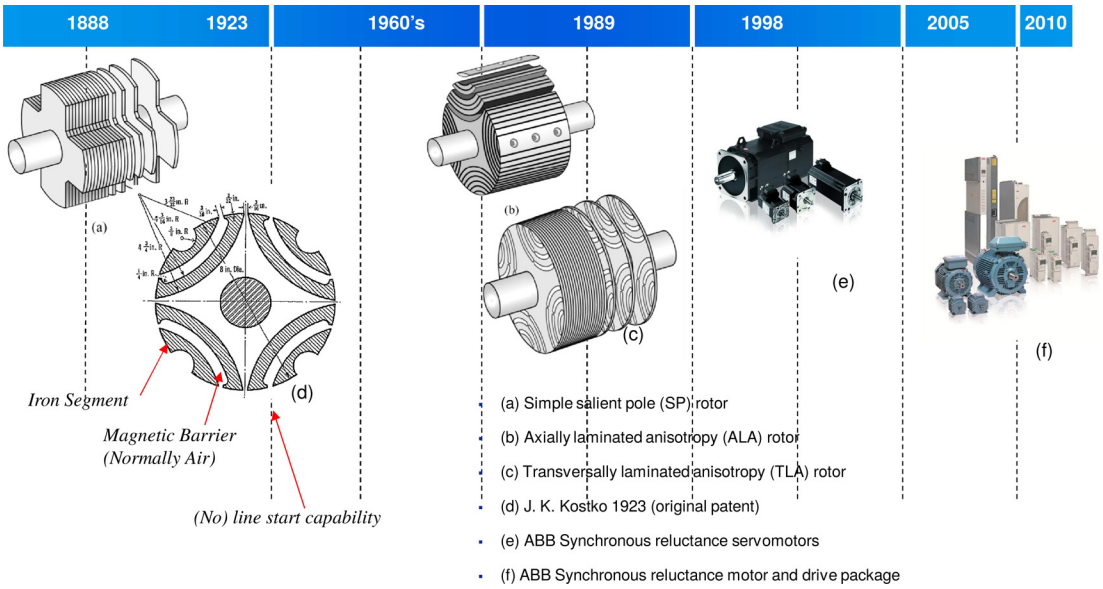

Figure 2.4: Synchronous reluctance technology history and key technology steps [27].

2.2 History

A brief guide on RSM history is illustrated in Figure 2.4. A key step in the development of modern day RSMs was published by Kostko in 1923 [19] and is illustrated at **(d)** in the figure. In this published paper, Kostko moved away from previous salient pole structures, illustrated in 1888, to a more rounded rotor lamination, with lamination cutouts acting as flux barriers to provide rotor anisotropy.

Further development in power electronics during the period between Kostko to the 1990's saw the development of inverter and control systems. These systems made it possible to remove the squirrel cage in the rotor. Designers could achieve even higher rotor anisotropy and larger torque densities that ever before. From the 1990's, research focus on the design of RSM drastically increased, with the two main machine topologies consisting of axially laminated (ALA) and transversely laminated (TLA) rotors as illustrated by **(b)** and **(c)** in Figure 2.4 respectively.

Even though ALA rotors proved to inherently have a high anisotropic rotor, they normally suffer from excessive rotor core losses and a large increase in production complexity compared to TLA rotors. Current trends in research moved towards TLA rotors because of its simplistic and more standard manufacturing process.

Considering the TLA rotors, it became clear that optimisation of the flux barrier shape in conjunction with the stator has become mandatory in order to produce a competitive RSM with low torque harmonics and a favourable torque density. Two main solution techniques to solve this optimisation problem was presented by Vagati in [26] and Kamper in [11, 28].

The first implemented generalised lumped-parameter modeling of the rotor magnetic circuit, which implements a pure Magneto Motive Force sinusoidal shape. This theoretical approach was applied in [24], where a low torque ripple objective was obtained and validated. One of the designed lamination topologies of Vagati is

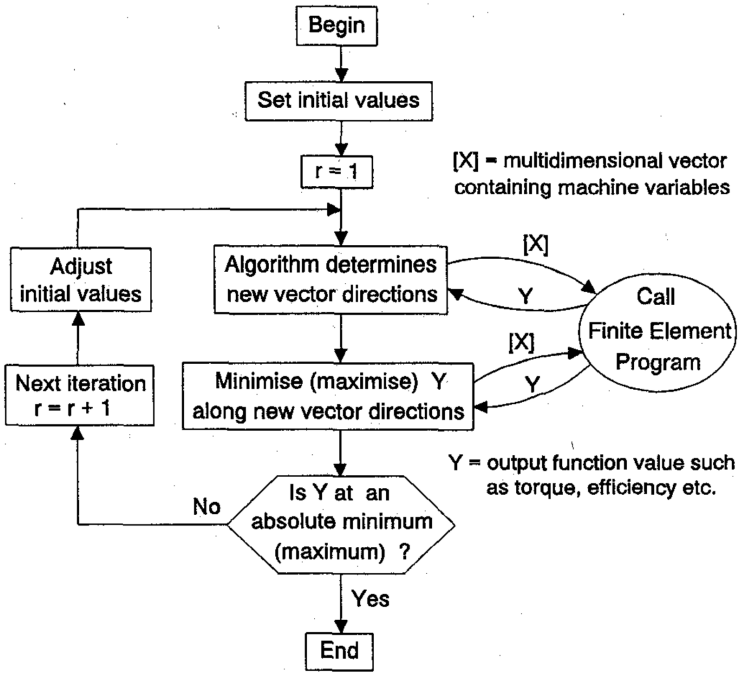

Figure 2.5: Optimisation using the finite element solution directly [11].

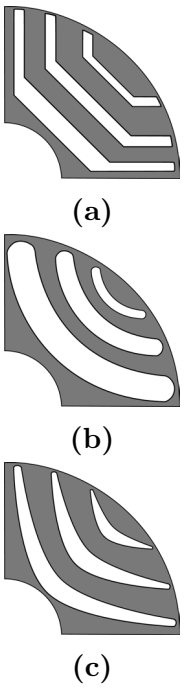

Figure 2.6: Rotor flux barrier profiles of four-pole RSMs in literature.

illustrated in Figure 2.3.

The second technique described by Kamper implements numeric design optimisation on a basic rotor flux barrier structure. This structure consists of a number of variables (barrier tip angle, barrier width, etc.) which are optimised by implementing an optimisation algorithm and finite element package (FE) to evaluate each variable change per function call. The advantage of this approach is that it takes complex phenomena like cross saturation and torque harmonics into account. This approach is limited to the initial barrier shape chosen by the designer, with limitations also including extensive optimisation time. Presented in Figure 2.5 is the implemented flow diagram that Kamper implemented in [11] for the first time.

For this specific study, the technique presented by Kamper is implemented for the design optimisation of the RSM. By choosing this technique, the study then led to an investigation into existing rotor topologies implementing this optimisation technique. This investigation revealed three base topologies structures, with slight variations in literature, illustrated in Figure 2.6. The shapes are simplistic in their design, this is specifically intended by the designer in order to keep the flux barrier defining variables to a minimum, which would in turn keep the optimisation time of the profile to a minimum.

The first of these shapes implemented straight lines to form the flux barriers, with studies implementing this shape conducted in [29–34]. This shape has proven to be quite simple and adaptable, with very large number of barriers and high pole

numbers easily reachable. The second topology, **(b)**, implements circles to form the flux barriers. This topology is one of the widest implemented with studies implementing the topology in [28, 33, 35–37], to name but a few. The great disadvantage this topology holds is its lack of implementing the available rotor area as the machine pole number increases. This poses a major problem in the intended medium speed as a high pole number RSM is required for the study.

The final topology in the figure, **(c)**, is a second order polynomial, or parabola. This topology has been implemented in studies [38–44] and proved to have the advantage above the circle topology in the higher pole number range. The reason for this was, as in **(a)**, that the topology is able to utilise more effectively the available rotor pole area during higher than four-pole machine optimisation.

The main problem with these topologies is that the optimisation algorithm is limited in its solution by the predetermined shape that the designer selects. In an effort to provide more variability for the optimisation algorithms, designers started to combine these base topologies to form new ones, with examples of these combination topologies illustrated in studies by [45–48].

This study implements a combined topology, as implemented by the latter authors. It also implement an asymmetric pole structure to give the optimisation algorithm even more variability in the available pole area. This proposed topology is intended to relate more closely to the validated results from Vagati, with the addition of asymmetry on the rotor pole.

The implemented flux barrier topology has an extensively variable flux barrier, with a high number of optimisation variables. The selection of this type of topology is motivated by the desire of the designer to study the optimum flux barrier shape produced by the optimiser under varying objective conditions.

The next section discusses the literature developments in the RSM field to try and increase performance specifications. This increase was achieved by designing hybrid RSM motors that implement permanent magnet materiel and/or a field winding on the rotor.

2.3 Variations on RSM Topologies

In an effort to increase the performance characteristics of a RSM, authors started experimenting with alternative rotor topologies that implement permanent magnet (PM) material and more recently by implementing a field winding to replace the PM material. The aim of these studies were to improve rotor saliency, power factor characteristics and improve the machine performance in the constant power speed range.

Illustrated in Figure 2.7 and 2.8, are six RSM rotor topologies implementing PM and field windings respectively to improve machine characteristics. These six topologies consist of:

1. **RSM** - The traditional reluctance synchronous machine rotor.
2. **C-RSM** - A compensated reluctance synchronous machine rotor that implements a field winding, with compensating flux in the q-axis. The intention of

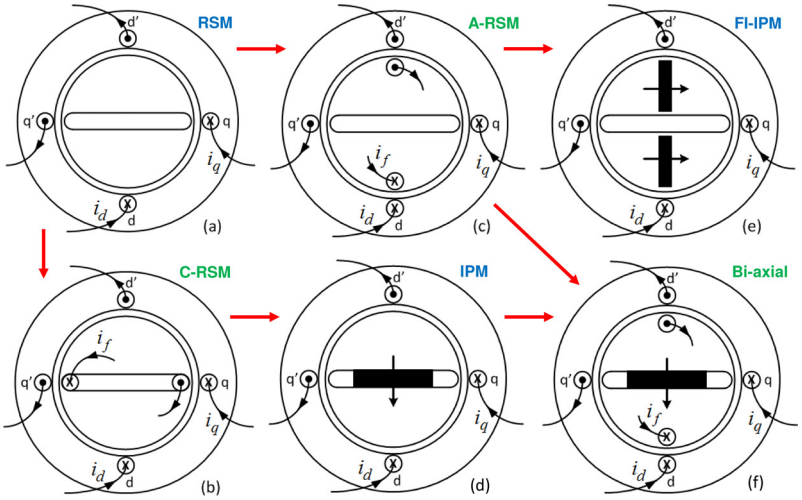

Figure 2.7: Two pole reluctance synchronous machine topologies that implement PM material and rotor winding for machine performance improvement [49].

the rotor winding is to increase the rotor anisotropy by producing opposing q-axis flux to the generated stator field flux. The first available literature of this machine was presented by Kamper in 2012 [49] with the rotor illustrated in Figure 2.8.

3. **A-RSM** - An assisted reluctance synchronous machine rotor that implements a field winding, with the assisting flux in the d-axis. The intention of the rotor winding is to increase the rotor anisotropy by producing assisting d-axis flux to the generated stator field flux. Extremely sparse literature exists of this machine, with the only similar available research conducted on a brush-less electrically excited SM [50] and a rewound C-RSM [49].

4. **IPM** - An interior permanent magnet machine, with widely available late literature implementing this topology [57–61]. The intention of the added rotor PM material is to increase the rotor anisotropy by producing opposing q-axis flux to the generated stator field flux. The motivation for the popular implementation of this motor is due to the already available flux barrier areas that can simply be modified to accommodate PM material as illustrated in Figure 2.8.

5. **FI-IPM** - A field intensified interior permanent magnet machine rotor that has, in recent literature, become a popular alternative to the IPM [55, 56, 62–67]. The intention of the added rotor PM material is to increase the rotor anisotropy by producing assisting d-axis flux to the generated stator field flux. Examples of possible topologies under the FI-IPM field is illustrated in Figure 2.8.

6. **Bi-Axial** - A combination between an IPM and an A-RSM rotor. This example was first presented by Boldea in [54, 68–71] and is illustrated in Figure 2.8.

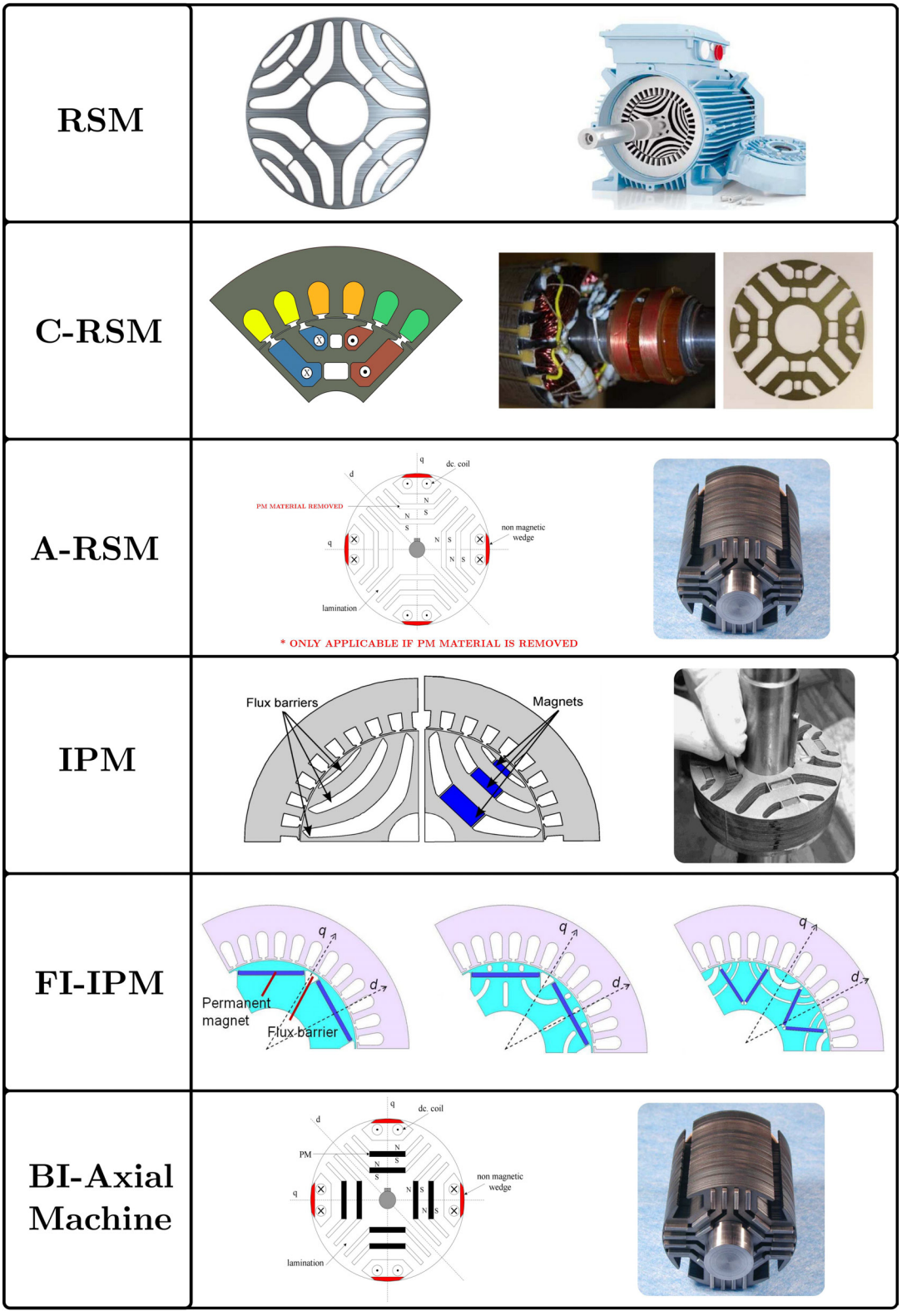

Figure 2.8: Possible RSM and hybrid-RSM topology examples as presented in Figure 2.7 [49–56].

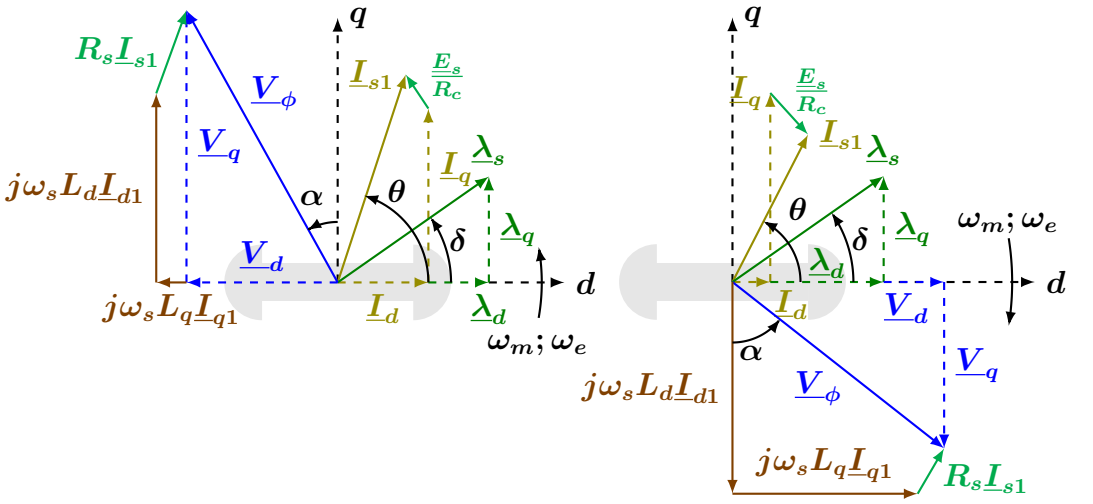

(a): Motor operation including P_C. **(b):** Generator operation including P_C.

Figure 2.9: Reluctance synchronous machine phasor diagram.

For this specific study, focus is placed on developing an improved optimisation technique to develop a traditional RSM. Additionally, the study also implements this improved technique to study and develop an A-RSM, with the very limited available literature on this specific topology indicating an void in the field that needs to be addressed.

2.4 Modelling & Performance Estimation

In order to analyse a RSM, a space phasor diagram fix to the rotor reference frame is implemented, with this diagram in motor and generator operation presented in Figure 2.9. The torque for the machine can be calculated by

$$T = k\underline{\lambda}_s \times \underline{I}_{s1} \tag{2.4.1}$$

or

$$T = k\lambda_s I_{s1} sin(\delta) \tag{2.4.2}$$

with the flux linkage λ_s consisting of the sum of the air-gap flux linkage λ_m and the leakage flux linkage phasor λ_l, with k a constant. As previously described in Figure 2.1, δ is the torque angle, which is zero when the current phasor $\underline{I}_{s1}$ is either on the d or q axis of the rotor.

Rewriting the torque equation into the DQ axis reference for a machine with p pole-pairs, the torque equation is represented by

$$T = \frac{3}{2}p(\lambda_d I_q - \lambda_q I_d). \tag{2.4.3}$$

The d and q-axis inductances can then be defined by

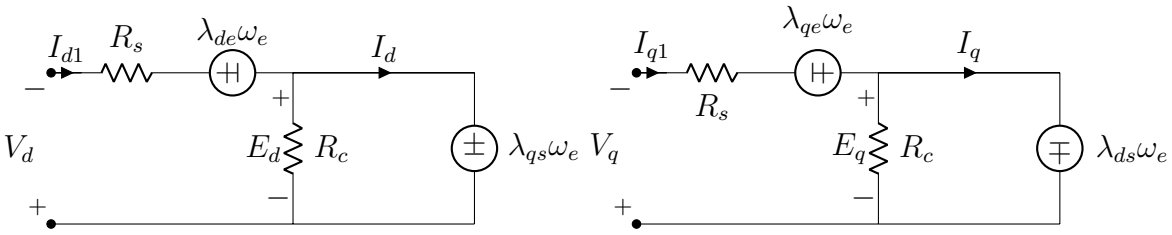

(a): Equivalent d-axis circuit. **(b):** Equivalent q-axis circuit.

Figure 2.10: Steady-state d- and q-axis equivalent circuit diagram.

$$L_d = \lambda_d / I_d \qquad (2.4.4) \text{ and} \qquad L_q = \lambda_q / I_q \qquad (2.4.5)$$

The equivalent circuit diagram in the DQ reference frame is illustrated in Figure 2.10. The equivalent circuit parameters are calculated for the RSM by implementing the Park transform matrix

$$K = \frac{2}{3}\begin{bmatrix} cos\theta & cos(\theta - 120°) & cos(\theta + 120°) \\ -sin\theta & -sin(\theta - 120°) & -sin(\theta + 120°) \\ \frac{1}{2} & \frac{1}{2} & \frac{1}{2} \end{bmatrix}. \qquad (2.4.6)$$

From the rotor supplied ABC stator current and induced flux linkage, the DQ equivalent current and flux linkage is calculated by

$$\left[I_{dq0}(n)\right] = K\left[I_{abc}(n)\right] \qquad (2.4.7) \text{ and} \qquad \left[\lambda_{dq0}(n)\right] = K\left[\lambda_{abc}(n)\right]. \qquad (2.4.8)$$

From these calculated values, it is possible to calculate the speed voltages of the circuit diagram with equations

$$E_d = -\lambda_q \omega_e \qquad (2.4.9) \text{ and} \qquad E_q = \lambda_d \omega_e \qquad (2.4.10)$$

with λ_d and λ_q the calculated flux linkages from Equation 2.5.2. The electrical rotational speed ω_e, in radians/s, is calculated from the mechanical rotational speed ω_m with

$$\omega_e = \frac{\omega_m}{0.5P} \qquad (2.4.11)$$

with P the number of machine poles.

The phase resistance R_s is calculated from the machine model stator slot dimensions as presented in Figure 2.11. The resistance estimation consists of equations

$$\tau_p = \frac{2\pi}{P} \qquad (2.4.12) \qquad R_{Slot} = 0.5(R_{SSO} - R_{SSI}) + R_{SSI} \qquad (2.4.13)$$

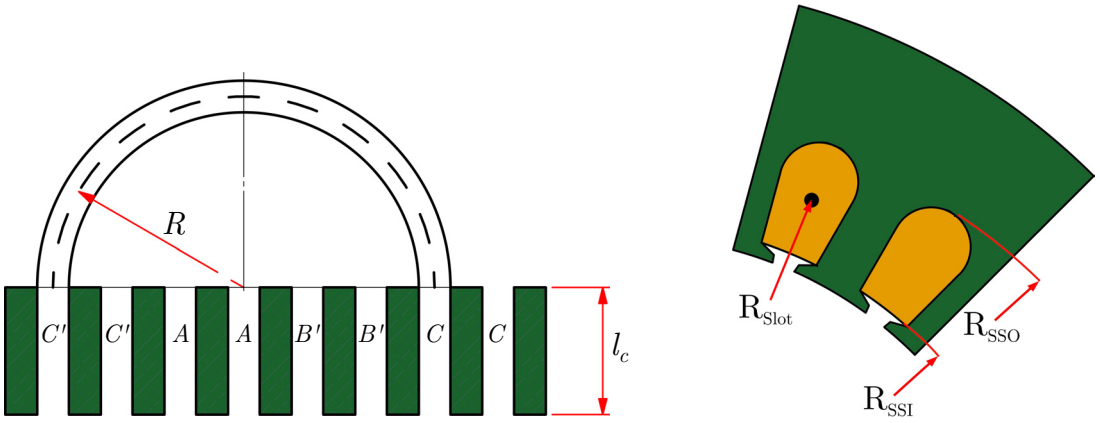

(a): End winding length circular approximation. **(b):** Centre slot radius.

Figure 2.11: Phase resistance estimation with end winding.

$$l_{end} = \pi R_{Slot} sin(0.5\tau_p) = \pi R \quad (2.4.14) \qquad L_{Coil} = (l_{end} + L_S) S_p P N_t \quad (2.4.15)$$

$$A_{Coil} = \frac{S_A F_f}{N_t} \quad (2.4.16) \text{ and } \quad R_c = \frac{\rho L_{Coil}}{A_{Coil}}, \quad (2.4.17)$$

with τ_p equal to the pole pitch, R_{Slot} is the radius to the centre of a stator slot, l_{end} the length of a single end winding. The total length of the winding L_{Coil} is then calculated with S_p, the stator slots per pole per phase and N_t, the number of turns per stator slot.

In order to compensate for the temperature rise in the stator windings, the copper resistivity ρ at $20°C$ is scaled to $65°C$ with equation

$$\rho_{65} = \rho_{20} + T_c(65 - 20)\rho_{20} \quad (2.4.18)$$

with

$$T_c = 0.0039 \quad (2.4.19) \text{ and } \quad \rho_{20} = 1.68 * 10^{-8} \Omega m \quad (2.4.20)$$

The end winding leakage flux linkage speed voltages E_{de} and E_{qe} are calculated by equations

$$E_{de} = -\lambda_{de}\omega_e = -L_e I_{d1}\omega_e \quad (2.4.21) \text{ and } \quad E_{qe} = \lambda_{qe}\omega_e = L_e I_{q1}\omega_e. \quad (2.4.22)$$

The end winding leakage inductance L_e for a three phase machine, single layer end windings is calculated by

$$L_e = 2.5 d_i (\frac{W k_d}{P})^2 k_{e(0.5P)} * 10^{-5} \quad (2.4.23)$$

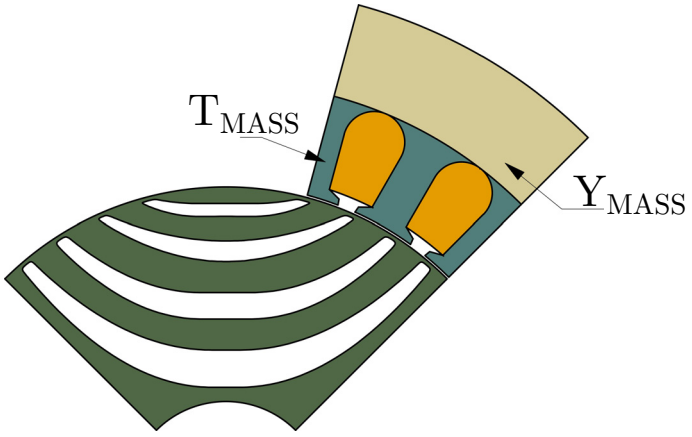

Figure 2.12: Core loss calculation model, with T_{MASS} the total mass of the stator teeth and Y_{MASS} the total mass of the yoke.

Material	y	x	c
M-400 Steel	2.11035	1.28805	0.0110176

Table 2.1: Core loss equation variables & results (calculated values for optimised machine to be discussed)

with d_i the inside stator diameter as presented by Kamper in [72]. The variables k_d is calculated by

$$k_d = \frac{sin(\pi/6)}{S_P sin(\pi/(6S_P))} \tag{2.4.24}$$

and $k_{e(0.5P)}$ is read from

$$k_{e(2)} = 0.595; k_{e(3)} = 0.64; k_{e(4)} = 0.785 \tag{2.4.25}$$

with $0.5P$ equal to the number of pole pairs of the machine investigated.

In order to calculate the core loss resistance R_C, the core losses must estimated. This is done by implementing the core loss equation

$$P_C = cf_1^x(B_{mt}^y T_{MASS} + B_{my}^y Y_{MASS}) \tag{2.4.26}$$

presented in [72] that only considers the fundamental flux core losses in the stator. Variables c, x and y represent constant variables determined from the selected lamination material core loss data sheet. For the selected lamination material M400-A50, the constants implemented are presented in Table 2.1. The electrical frequency is represented by f, with the total stator tooth and yoke mass illustrated in Figure 2.12. The maximum flux densities of the respective areas are determined directly from the finite element package, with B_{mt} the maximum flux density in the stator tooth and B_{my} the maximum flux density in the stator yoke.

With the core losses estimated, the core loss resistance R_C is calculated with equations

$$E_a = \sqrt{\frac{E_d^2 + E_q^2}{2}} \qquad (2.4.27) \text{ and} \qquad R_C = \frac{3E_a^2}{P_C} \qquad (2.4.28)$$

Finally, after all the circuit component values are calculated, the circuit DQ voltage and current can be calculated. The DQ currents are both calculated with equations

$$I_{d1} = I_d + E_d/R_c \qquad (2.4.29) \text{ and} \qquad I_{q1} = I_q + E_q/R_c \qquad (2.4.30)$$

where the values for I_d and I_q represent the given FEM package simulation values and I_{d1} and I_{q1} the actual value that will be seen at the machine terminals that include core loss. The peak terminal current is calculated by

$$I_s = \sqrt{I_{d1}^2 + I_{q1}^2}. \qquad (2.4.31)$$

The DQ voltage is then calculated, as motor, by equations

$$V_d = E_d + E_{de} + I_{d1}R_s \qquad (2.4.32) \text{ and} \qquad V_q = E_q + E_{qe} + I_{q1}R_s, \qquad (2.4.33)$$

with the peak phase voltage calculated with

$$V_s = \sqrt{V_d^2 + V_q^2}. \qquad (2.4.34)$$

2.5 Script Based Post Processing & Performance Estimation

The performance parameter calculation consisted of a script based post-processing of the FE simulation run for each of the optimisation function calls. This script implements the simulation mesh data and result file in its calculations.

Each FE simulation is conducted consisting of N number of static rotor angle steps. The number of steps and step angle is dependant on the specific optimisation objective and stator topology implemented in the optimisation. The FE simulation consists of a time step method, solving consecutive static magnetic field models.

The 2D FE software package implemented in the simulation is SEMFEM, developed in-house by Gerber in [73]. The advantage of implementing this package is its large adaptability with respect to machine model generation as a result of its script based interface. Additionally, the package also implements first order mesh elements that greatly decrease simulation time with negligible reduction in model simulation accuracy.

The result file produced after each FE simulation consists of the torque, flux linkage for each phase and the phase current for each phase, printed for each static simulation step conducted. By implementing this data, average torque (T_A), torque ripple (T_R) and all the equivalent circuit parameters can be estimated.

Additionally, the mesh data generated by the FE simulation consists of the flux density and material mass that can be extracted at specific points in the mesh and for specific materials. This is then in turn implemented to estimate the machine core losses and the machine mass during the design process.

By implementing these simulation step values, the total DQ flux linkage and current for the complete FE simulation is calculated by implementing equations

$$\left[I_{dq0}\right] = \frac{1}{N}\left[\sum_{n=0}^{N} I_{dq0}(n)\right] \qquad (2.5.1) \text{ and } \qquad \left[\lambda_{dq0}\right] = \frac{1}{N}\left[\sum_{n=0}^{N} \lambda_{dq0}(n)\right]. \qquad (2.5.2)$$

The torque for each static simulation is calculated in Semfem by implementing Coulomb's Method. This method is used to calculate forces and torques in a moving body by implementing the virtual work principle. A comparison between this method and the popularly implemented Maxwell stress tensor method is available in [74]. The torque calculated with this method for each static step is presented by

$$T = \frac{l}{\mu_0}\sum_{e=1}^{N_{eag}}\int_{\Omega_e}\left[-B^T G^{-1}\frac{\partial G}{\partial \varphi}B + \tfrac{1}{2}B^2\left|G\right|^{-1}\frac{\partial|G|}{\partial\varphi}\right]d\Omega \qquad (2.5.3)$$

where the finite element band element number is represented by N_{eag}, G represents the Jacobian matrix and B the magnetic flux density.

The average torque of the FE simulation is calculated by reading in each calculated static step torque value and implementing equation

$$T_A = \frac{\sum_{n=0}^{N} T(n)}{N} \qquad (2.5.4)$$

with N the total number of simulation steps and n representing the specific static step. Alternatively the torque of the machine for each step can also have been calculated by the well known RSM torque equation

$$T = \frac{3}{2}\frac{P}{2}(L_d - L_q)I_d I_q \qquad (2.5.5)$$

that implements the equivalent circuit parameters in the Figure 2.9. Where P is the number of machine poles, L_d and L_q the DQ equivalent inductance's with I_d and I_q the DQ equivalent currents.

Torque ripple is calculated by implementing both the calculated T_A value and equations

$$T_R = \left(\frac{T(MAX) - T(MIN)}{T_A}\right)100\%. \qquad (2.5.6)$$

This equation calculates the peak to peak torque value percentage, with an accurate representation of the torque periodicity required and a large number of simulation steps N to avoid aliasing.

The main performance parameters of the machine, depending on application, consists of T_A, T_R, machine power output (P_{Out}), Efficiency (E_{FF}), Power Factor (hP_F) and machine active mass (M_a). Machine E_{FF} is estimated by implementing equation

$$E_{FF} = \frac{P_{Out}}{P_{In}} * 100\%. \tag{2.5.7}$$

For both motor and generator modes of operation. Equation 2.5.7 and be rewritten as

$$E_{FF}^{M} = \frac{P_{Out}}{P_{In}} = \frac{\omega_m T_A}{\omega_m T_A + P_T} \quad (2.5.8) \text{ and} \qquad E_{FF}^{G} = \frac{P_{Out}}{P_{In}} = \frac{\omega_m T_A - P_T}{\omega_m T_A} \tag{2.5.9}$$

where E_{FF}^{M} and E_{FF}^{G} are motor and generator mode efficiency respectively. The total loss of the machine is represented by P_T and calculated by equation

$$P_T = P_B + P_{W\&V} + P_R + P_C. \tag{2.5.10}$$

The total losses in Equation 2.5.10 consist of the summation of bearing losses (P_B), windage and friction losses ($P_{W\&V}$), coil resistance losses (P_R) and core losses as calculated by Equation 2.4.26. The former parameters can be calculated by equations

$$P_{W\&V} = 2k_p RO_o(l_c + 0.6\tau_p)v_r^2 \quad (2.5.11)\ , \qquad P_B = 0.5\kappa\mu F D_B \tag{2.5.12}$$

and

$$F = mg = 2M_R g. \tag{2.5.13}$$

with k_p the experimental factor equal to 15 Ws^2/m^4 for small/medium machines and 8 Ws^2/m^4 for large machines [75]. The rotor outer radius is represented by RO_O and the rotor surface speed by v_r. The inner bearing diameter dimension is represented by D_B, with the frictional coefficient κ equal to 0.015 and F the vertical gravitational bearing force, calculated from the rotor mass extracted from the FE program. The angular frequency of the shaft is represented by μ.

The power factor estimation equation, as popularly implemented in RSM power factor estimation [72, 76], consists of

$$P_F = cos(tan^{-1}(\frac{\sigma/\nu + \nu}{\sigma - 1})) \tag{2.5.14}$$

with the variables σ and ν calculated by Equations 2.5.15 and 2.5.18 implementing the calculated machine DQ equivalent current and inductance.

$$\sigma = \frac{L_d}{L_q} \quad (2.5.15) \qquad L_d = \frac{\lambda_d}{I_d} \quad (2.5.16)$$

$$L_q = \frac{\lambda_q}{I_q} \quad (2.5.17) \qquad \nu = \frac{I_q}{I_d} \quad (2.5.18)$$

Finally, the active mass of the machine M_a is calculated by

$$M_a = RO_{MASS} + T_{MASS} + Y_{MASS} + C_{MASS} \tag{2.5.19}$$

with RO_{MASS} representing the total rotor mass, C_{MASS} the total copper mass including the end windings, T_{MASS} the total stator tooth mass and Y_{MASS} the total stator yoke mass.

Chapter 3

Flux Barrier Design & Torque Ripple Study

In this chapter, the first and second research objectives laid out are discussed. The first objective consists of the development of an alternative flux barrier model creation technique, that can be implemented in conjunction with optimisation to study reluctance synchronous machines. The second objective that will be addressed, by implementing the developed rotor model, is the reduction of machine torque harmonics.

3.1 Proposed Flux Barrier Topology

In this section, a newly suggested rotor topology will be introduced. This new topology is a combination of current literature topology structures combined to increase the model's degree of freedom.

As has been identified in the literature, RSMs suffer from high torque ripple and this forms a critical part in the design of the machine [79–89]. In order to mitigate this inherent high torque ripple, an asymmetric pole structure is proposed

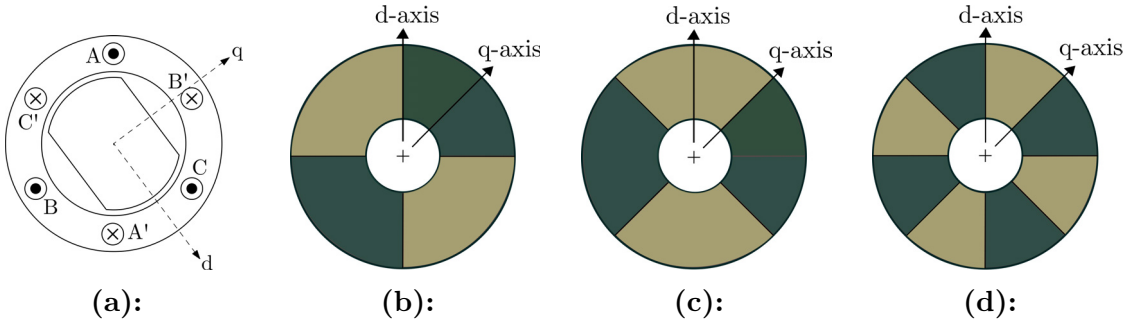

Figure 3.1: Structures illustrating the different pole topologies [77, 78] : **(a)** Two pole cross-section of the RSM and space phasor diagram fixed in the rotor reference ; **(b)** Four pole asymmetric rotor structure about the d-axis with symmetric q-axis ; **(c)** Four pole asymmetric rotor structure about the q-axis with symmetric d-axis ; **(d)** Four pole asymmetric rotor structure about the q and d-axis.

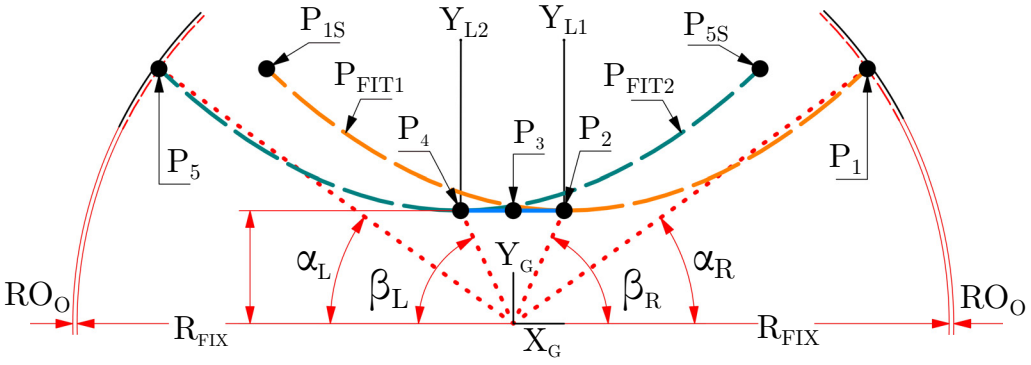

Figure 3.2: Flux barrier creation variables with subscript **G**, the global axis and **L**, the two local axes. Y_G represents the q-axis asymmetric line illustrated in Figure 3.1 [77, 78].

as illustrated in Figure 3.1. In this figure, three asymmetric rotor structures are illustrated, with (b) and (c) the current conventional asymmetric structure implemented for torque ripple reduction [47, 48, 90, 91]. These two conventional structures implement two asymmetric poles in order to reduce the torque harmonics, with the asymmetric line either the d or q-axis.

The proposed topology, (d) in Figure 3.1, implements an asymmetric structure over one pole, with the d and q-axis implemented as the asymmetric lines. The advantage of implementing this asymmetric structure is twofold with one possible disadvantage:

- Firstly, the model only requires one pole during FE simulation thus, the FE simulation time is greatly reduced compared to the required two poles of the alternative asymmetric structure.
- Secondly, by only simulating one pole, a great reduction in model variables is achievable which in turn will greatly reduce the optimisation time of the model.
- The disadvantage of this proposed topology is a possible reduction in machine performance depending on mode of operation and rotor rotation direction. In this study, machines under unidirectional operation are assumed, including conveyor drives, generators, pumps and fans among others.

The new proposed topology is illustrated in Figure 3.2. The topology consisted of two curve fitted, second order polynomials. The first curve consisting of points P_1, P_2 and a symmetric P_{1S} point around Y_{L1} for Parabola Fitting 1 or P_{FIT1}. The second curve consists of points P_5, P_4 and a symmetric P_{5S} point around Y_{L2} for Parabola Fitting 2 or P_{FIT2}. These two fitted curve vertex points P_2 and P_4 are connected by a horizontal line through P_3 to complete the flux barrier mid line.

Points P_1 and P_5's coordinates consisted of a constant pre-set radius and an angle α as indicated in Figure 3.2. Point P_3 specifies the vertex point y-coordinate of the 2 fitted polynomials with the angle β specifying the lateral displacement, or angle to x-coordinate, from point P_3 to vertex points P_2 and P_4 respectively. Once

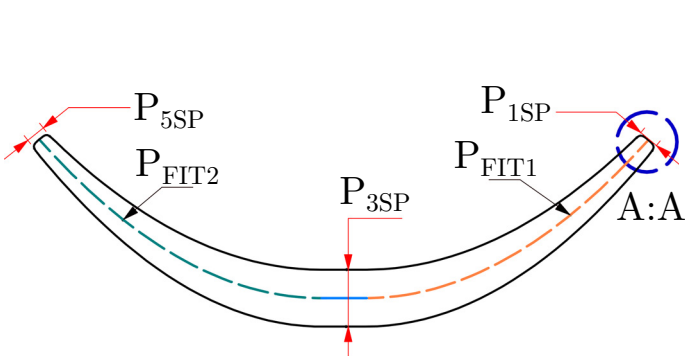

(a): Complete barrier rotor profile [77, 78].

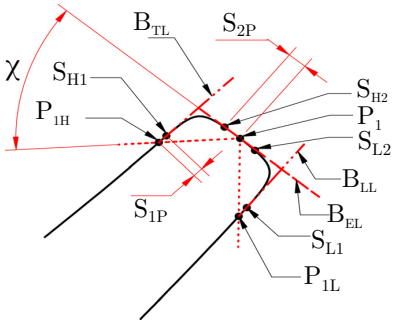

(b): Bezier Cubic Spline fitting of section **A:A** [77, 78].

Figure 3.3: Barrier thickness variables and Bezier cubic spline fitting on barrier tips.

Figure 3.4: Five examples of the possible flux barrier tip shapes, with a multitude of in-between variations that could be achieved with the variables in Figure 3.3b [77, 78].

the mid line of the barrier is created, the line is given a "thickness" at points P_1, P_3 and P_5 as illustrated in Figure 3.3a to complete the flux barrier.

Additionally, each barrier tip is fitted with a bezier spline (an illustration of fitting process available in Appendix B.2). This additional fitting is added in order to reduce the sharp force concentrating area at the barrier tip and to give the model even more degrees of freedom. Examples of the large variability that the optimiser has in the shaping of the flux barrier tip is shown in Figure 3.4. This additional variability of the barrier tips also gives the optimiser even more freedom in one of the critical areas with respect to torque ripple [90].

The upper part of the fitted spline consisted of two departure points P_{1H} and P_1, and two points specifying the departure angles from P_{1H} and P_1, points S_{H1} and S_{H2}. Likewise, the lower part of the barrier consisted of the same structure with the departure points P_{1L} and P_1 and departure angle points S_{L1} and S_{L2}. Additionally, these splines are not only variable by the departure angle variation, but is also manipulated by the variation of the departure points P_{1H} and P_{1L} along the fitted polynomial top and bottom path by angle χ as illustrated in Figure 3.3b.

A detailed representation of a symmetric half of a rotor structure can be found in Figures 3.5 to 3.8, with the variables shown in Table 3.1. Here, an example of how the barrier fitting is produced is presented, with the main variables shown. Table 3.1 shows a summation of the variables required for one flux barrier for the symmetric and the asymmetric case. The number of variables required for the symmetric case is 8 and for the asymmetric case 11. A direct comparison between a symmetric

Table 3.1: Symmetric, A-Symmetric barrier variables for one flux barrier$^{\forall}$.

Barrier Variables				
Points	**Symmetric**		**A-Symmetric**	
Polar	R	θ	R	θ
$P_{1(n)}$	R_{FIX}	$*\ \alpha_{(n)}$	R_{FIX}	$*\ \alpha_{(B+n)}$
$P_{2(n)}$	$R_{(n)}$	$*\ \beta_{(n)}$	$R_{(n)}$	$*\ \beta_{(B+n)}$
$P_{3(n)}$	$*\ R_{(n)}$	$\pi/2$	$*\ R_{(n)}$	$\pi/2$
$P_{4(n)}$	$R_{(n)}$	$\beta_{(n)}$	$R_{(n)}$	$*\ \beta_{(B+n)}$
$P_{5(n)}$	R_{FIX}	$\alpha_{(n)}$	R_{FIX}	$*\ \alpha_{(B+n)}$
$P_{1sp(n)}$	R_{FIX}	$*\ P_{1SP(n)}$	R_{FIX}	$*\ P_{1SP(n)}$
$P_{5sp(n)}$	R_{FIX}	$P_{1SP(n)}$	R_{FIX}	$*\ P_{5SP(n)}$
Cartesian	x	y	x	y
$P_{3sp(n)}$	0	$*\ P_{3SP(n)}$	0	$*\ P_{3SP(n)}$
Spline Tip Variables				
Polar	R	θ	R	θ
P_{1H}	NA	$*\ \chi_{(n)}$	NA	$*\ \chi_{(n)}$
P_{1L}	NA	$\chi_{(n)}$	NA	$\chi_{(n)}$
Percentage	$*\ B^*_L$		$*\ B^*_L$	
S_{H1}	$*\ S_2P_{(n)}$		$*\ S_2P_{(n)}$	
S_{H2}	$*\ S_1P_{(n)}$		$*\ S_2P_{(n)}$	

$*$ - indicating the applicable variables manipulated by the optimisation algorithm ; **n** - Indicating the specific flux barrier number ; **B** - Indicating the number of flux barriers in model ; * - Indicating the percentage movement on the barrier limit lines ($\boldsymbol{B_{TL}}$,$\boldsymbol{B_{LL}}$,$\boldsymbol{B_{TL}}$) for the departure angel points in Figure 3.5.

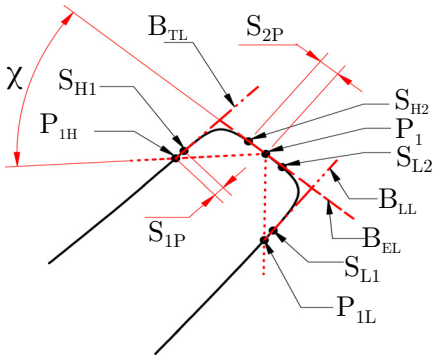

Figure 3.5: Bezier Cubic Spline fitting of section **A:A** [77, 78].

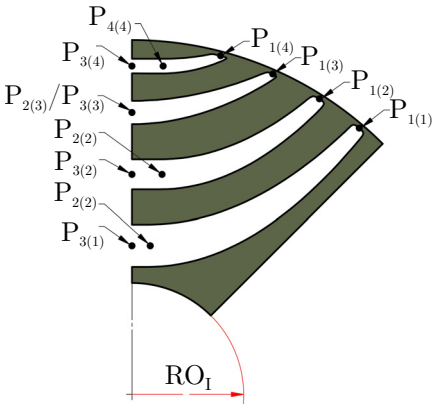

Figure 3.6: Main symmetric barrier mid points (Point Description P_{X-Y} : X - Description of barrier number Y - Description of point number).

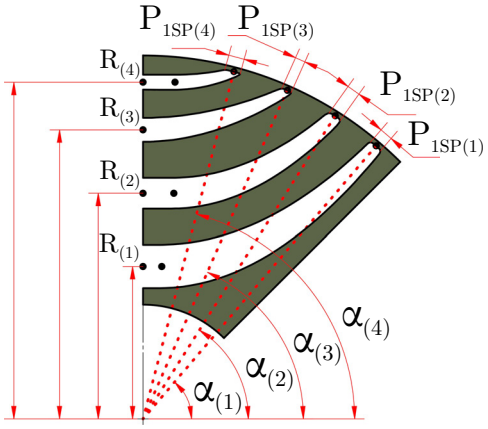

Figure 3.7: Set 1 variables describing barrier construction of the symmetric case (subscript R).

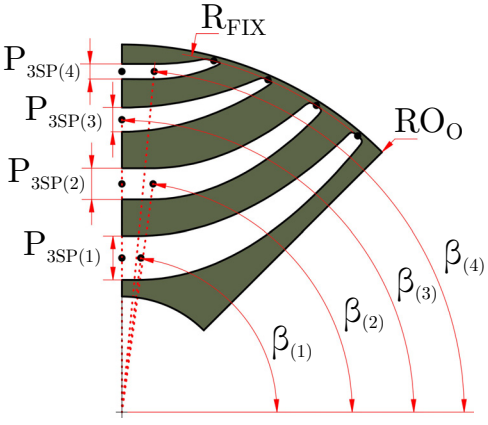

Figure 3.8: Set 2 variables describing barrier construction of the symmetric case (subscript R).

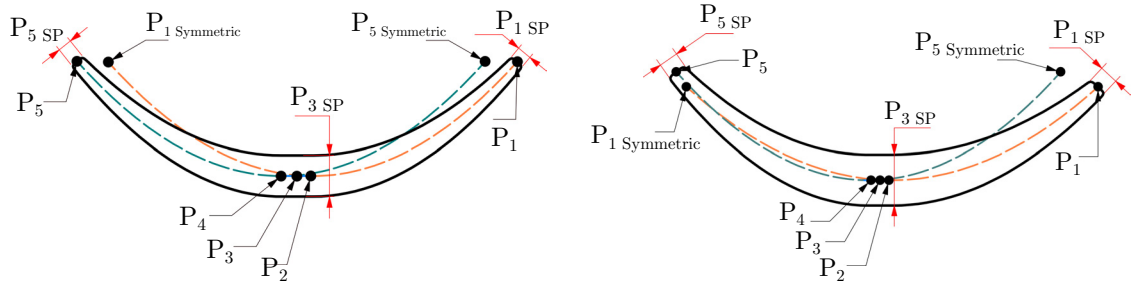

(a): Symmetric flux barrier mid line spacing variables.

(b): Asymmetric flux barrier mid line spacing variables.

Figure 3.9: Illustration of a symmetric and asymmetric flux barrier.

Table 3.2: Stator Specifications of the 24 and 36 Slot machines [77, 78].

Stator Rated Machine Specifications							
Stator	V $[V]$	I $[A]$	f_e $[Hz]$	ST_I $[m]$	ST_O $[m]$	N_{ST}	J $[A/mm^2]$
24 Slot	400	3.5	50	0.08	0.13	132	±6.4
36 Slot	150	42	50	0.1051	0.2032	36	±6.4

V - Line Voltage ; I - Field Current ; f_e - Frequency ; ST_I - Inner Stator Radius ; ST_O - Outer Stator Radius ; N_{ST} - Series Turns per phase per pole; J - Current Density

and an asymmetric flux barrier can be found in Figure 3.9, with the barrier width and the respective centre lines shown.

3.2 Machine Optimisation

For the model, an existing 1.5 kW IM stator is implemented to investigate the new suggested topology. Additionally, after this initial model investigation, the optimisation strategy of the rotor is applied to an existing 36 slot 9.5 kW optimised RSM stator to compare performance across two machine power ranges and stator topologies.

An illustration of the suggested topology along with the existing 24 slot IM stator and 36 slot RSM stator is illustrated in Figure 3.10. As can be seen in the figure, the central support web commonly implemented by [24, 35, 92, 93], for rotor rigidity has been omitted. This omission is done in an attempt to increase the performance of the machine by increasing its rotor anisotropy as done by [33, 40, 83, 90, 94–96]. The question of mechanical integrity as a result of this omission will be addressed later in this chapter. The IM and RSM stator specifications are shown in Table 3.2, with the current density of both stators taken as 6.4A/mm^2.

For the machine optimisation, a commercial optimisation software package VisualDoc [97] is implemented. The flow diagram of the optimisation procedure is illustrated in Figure 3.11. The optimisation package is connected to the FE package by a python script, with the purpose of the script to

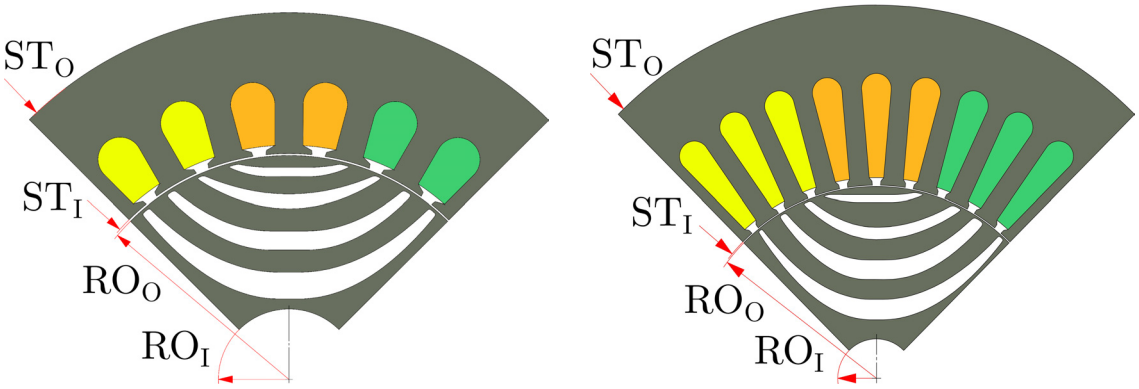

(a): four-pole, 24 Slot RSM with IM-stator and RO_O=39.7mm, RO_I=12.5mm and a stack length of 0.122 m with air gap length $0.3mm$ [77, 78].

(b): four-pole, 36 Slot existing RSM stator with RO_O=52,2mm, RO_I=21,5mm and a stack length of 0.1334 m with air gap length $0.35mm$ [77, 78].

Figure 3.10: Machine stators implemented in the retrofit design optimisation.

1. read in the updated machine variables produced by the optimisation package
2. reconstruct the machine from the updated variables
3. set up the FE package with the updated machine and run the simulation
4. post processing of simulation results and write results back to the optimisation package

with this process repeated for each optimiser function call.

The selection of the specific optimiser for the study is discussed in the next section.

3.2.1 Optimiser Selection

In order to study the objectives in this chapter, two independent optimisation steps are proposed. The initial step is the maximisation of T_A, with the rotor model adapted and optimised to study the effects on the converged results. The second step is a T_R minimisation. Once again, this optimisation is repeated by varying the rotor model and initial start variables in order to study the converged results of the optimiser.

Because of the relatively large number of optimisation variables, gradient based optimisation algorithms are considered for the optimisation. The selection of this family of optimisers is motivated by the well known fact that most non-gradient based optimisers are computationally very expensive. This selection is even further motivated by the fact that a large set of optimised topologies is required to compare and evaluate the proposed topology effectively, where a long optimisation time per topology would not be viable.

The gradient based algorithms that the VisualDoc suit offers consists of

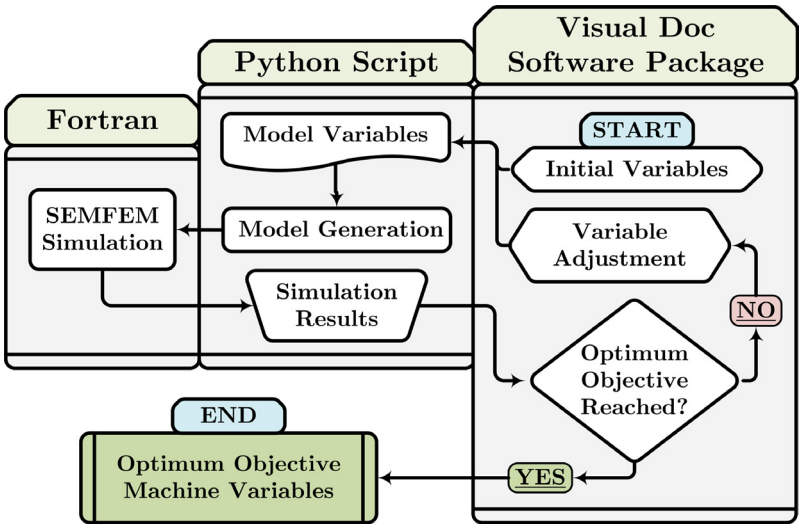

Figure 3.11: Optimisation flow diagram implementing a Python script to link the optimisation package VisualDoc with the FE Simulation package SEMFEM [77, 78].

1. **MMFD** - Modified Method of Feasible Directions is an extension of the constrained function minimisation method (CONMIN). CONMIN solves the nonlinear programming problem by moving from one feasible point to an improved one by choosing at each iteration a feasible direction and step size that improves the objective function. MMFD utilizes the direction-finding subproblem from the Method of Feasible Directions to find a search direction [97].

2. **SLP** - Sequential linear programming consists of linearising the objective and constraints in a region around a nominal operating point by a Taylor series expansion. The linear approximate problem is then solved by the modified method of feasible directions.

3. **SQP** - Sequential Quadratic Programming is very similar to SLP, where the problem is solved by implementing a Taylor series expansion. The solution problem is found by solving a series of quadratic approximate objective functions by implementing the modified method of feasible directions.

MMFD is the most widely used algorith in VisualDoc, shown to be successfully implemented in previous electrical machine optimisation studies [76, 98, 99]. Because of the successes achieved with MMFD in the previous studies, the optimiser is selected to form part of the initial step in the optimisation study, namely he maximisation of $T_A(X)$. This selection is also motived by the fact that MMFD is well know to be among the most robust gradient based algorithms available, capable of solving a very large array of problems effectively [97].

For the second step of the optimisation strategy, the minimisation of $T_R(X)$, SLP is selected for the optimisation algorithm. Taking into account the high complexity of torque harmonics that the optimiser must deal with during the minimisation of objective function $T_R(X)$, an optimiser was needed that is not susceptible to possible rounding errors that may occur by implementing high order methods like SQP and

MMFD [100]. A similar evaluation was found to be true for the structural optimisation study by Yang [101]. In this study, higher order optimisers were compared and found ineffective due to the complexity of the optimisation problem encountered.

3.2.2 Variable Scaling & Strategy

In the formulation of large complex optimisation problems, great care should be taken in the scaling of the respective model variables. Improper scaling of the variables may cause some variables to be insensitive to optimiser variation causing the optimiser to struggle to find a converge point. This problem is as a result of objective function contour distortion due to the poorly scaled variables. The proposed "good practice" rule presented by [102] is followed in order to mitigate this potential problem. Applying this rule, the variables of the model is scaled to vary between 0 and 1. These variables include all the flux barrier variables, current angle and stator variables.

With this variable scaling applied to the model variables, the variable inequality constraints consists of

$$0 \leqslant G_j(X_m) \leqslant 1 \quad ; \quad j = 1, 2, ..., n \tag{3.2.1}$$

with G_j the specific variable j in the matrix X_m. The complete variable sets for the symmetric flux barrier consists of

$$X_m = \begin{bmatrix} \alpha \\ \beta \\ R \\ P_{1sp} \\ P_{3sp} \\ \chi \\ S_1P \\ S_2P \\ \theta \end{bmatrix} = \begin{bmatrix} \alpha_{(1)} & . & . & \alpha_{(B)} \\ \beta_{(1)} & . & . & \beta_{(B)} \\ R_{(1)} & . & . & R_{(B)} \\ P_{1sp(1)} & . & . & P_{1sp(B)} \\ P_{3sp(1)} & . & . & P_{3sp(B)} \\ \chi_{(1)} & . & . & \chi_{(B)} \\ S_1P_{(1)} & . & . & S_1P_{(B)} \\ S_2P_{(1)} & . & . & S_2P_{(B)} \\ \theta & & & \end{bmatrix} \tag{3.2.2}$$

with the variables described in Table 3.1. The asymmetric variables consists of the same variables as the symmetric case, with the addition of the asymmetric variables illustrated by

$$X_m = \begin{bmatrix} \alpha \\ \beta \\ R \\ P_{1sp} \\ P_{3sp} \\ P_{(5sp)} \\ \chi \\ S_1P \\ S_2P \\ \theta \end{bmatrix} = \begin{bmatrix} \alpha_{(1)} & . & . & \alpha_{(B)} & \alpha_{(B+1)} & . & . & \alpha_{(B+B)} \\ \beta_{(1)} & . & . & \beta_{(B)} & \beta_{(B+1)} & . & . & \beta_{(B+B)} \\ R_{(1)} & . & . & R_{(B)} & & & & \\ P_{1sp(1)} & . & . & P_{1sp(B)} & & & & \\ P_{3sp(1)} & . & . & P_{3sp(B)} & & & & \\ & & & & P_{5sp(1)} & . & . & P_{3sp(B)} \\ \chi_{(1)} & . & . & \chi_{(B)} & & & & \\ S_1P_{(1)} & . & . & S_1P_{(B)} & & & & \\ S_2P_{(1)} & . & . & S_2P_{(B)} & & & & \\ \theta & & & & & & & \end{bmatrix}. \tag{3.2.3}$$

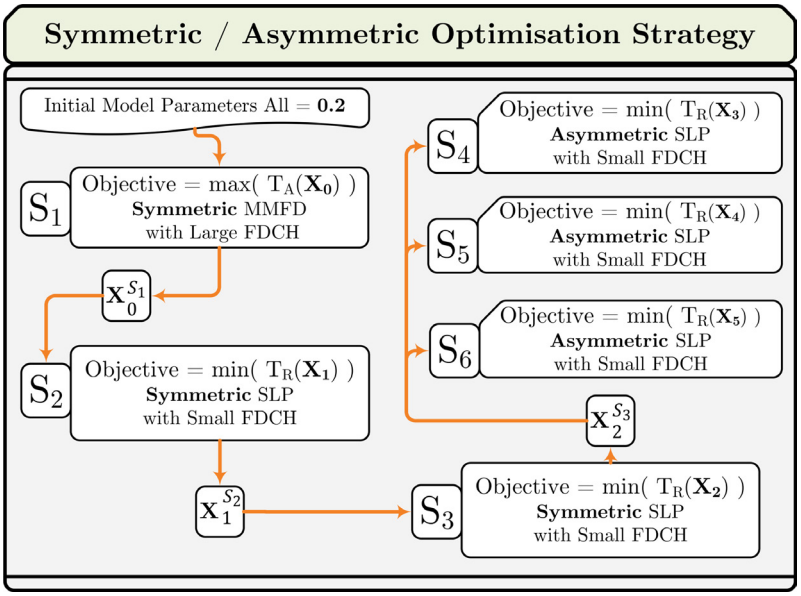

MMFD : Modified Method of Feasible Direction. **SLP** : Sequential Linear Programming. **FDCH** : Relative finite difference step size.

Figure 3.12: Optimisation strategies implemented and variable flow diagram, with the superscript S the symmetric-asymmetric procedure [77].

3.3 Symmetric Asymmetric Optimisation Study

In order to compare the symmetric and asymmetric topology proposed, the optimisation strategy illustrated in Figure 3.12 is implemented and only applied to the rotor in the 24 slot stator machine. The strategy consisted of 6 independent optimisations, with each successive optimisation from step $\boldsymbol{S_2}$ to $\boldsymbol{S_6}$ implementing the formers converged optimisation variables as initial variables, with the first optimisation step $\boldsymbol{S_1}$ implementing a initial 0.2 value for all variables. This strategy consists of two main sections, the first a symmetric optimisation study and the second, an asymmetric variation optimisation study. The variables implemented per optimisation study is shown in Table 3.3, with each of the variable sets defined by X_n.

3.3.1 Symmetric Optimisation Study

The first section is a symmetric flux barrier optimisation from step $\boldsymbol{S_1}$ to $\boldsymbol{S_3}$. This optimisation was done in order to create a base line for asymmetric flux barrier comparison. The optimisation strategy consisted of three objective functions with :

$\Rightarrow$ Step $\boldsymbol{S_1}$

$$\begin{aligned} \text{The maximisation of :} \quad & T_A(X_0) \\ \text{Subject to :} \quad & 0 \leqslant G_j(X_0) \leqslant 1 \quad ; \quad j = 1, 2, ..., n \end{aligned}$$

Table 3.3: Symmetric asymmetric optimisation strategy variables.

Optimisation Variables*						
	SAS Optimisation					
Variables	X_0	X_1	X_2	X_3	X_4	X_5
α	$\surd_S$	$\surd_S$	$\surd_S$	$\surd$	$\surd$	$\surd$
β	$\surd_S$		$\surd_S$		$\surd$	$\surd$
R	$\surd$		$\surd$		$\surd$	$\surd$
P_{1sp}	$\surd$		$\surd$		$\surd$	$\surd$
P_{3sp}	$\surd$		$\surd$		$\surd$	$\surd$
P_{5sp}					$\surd$	$\surd$
χ	$\surd_S$		$\surd_S$		$\surd$	$\surd$
S_1P	$\surd_S$		$\surd_S$		$\surd_S$	$\surd_S$
S_2P	$\surd_S$		$\surd_S$		$\surd_S$	$\surd_S$
θ	$\surd$			$\surd$		$\surd$

$\surd_R$ - Asymmetric flux barrier variables ; $\surd$ - Symmetric flux barrier valuables.

with the variables consisting of :

$$X_0 = \begin{bmatrix} \alpha \\ \beta \\ R \\ P_{1sp} \\ P_{3sp} \\ \chi \\ S_1P \\ S_2P \\ \theta \end{bmatrix} = \begin{bmatrix} \alpha_{(1)} & . & . & \alpha_{(4)} \\ \beta_{(1)} & . & . & \beta_{(4)} \\ R_{(1)} & . & . & R_{(4)} \\ P_{1sp(1)} & . & . & P_{1sp(4)} \\ P_{3sp(1)} & . & . & P_{3sp(4)} \\ \chi_{(1)} & . & . & \chi_{(4)} \\ S_1P_{(1)} & . & . & S_1P_{(4)} \\ S_2P_{(1)} & . & . & S_2P_{(4)} \\ \theta & & & \end{bmatrix} \tag{3.3.1}$$

$\Rightarrow$ Step $\boldsymbol{S_2}$,

$$\begin{aligned} \text{The minimisation of :} \quad & T_R(X_1) \\ \text{Subject to :} \quad & 0 \leqslant G_j(X_1) \leqslant 1 \quad ; \quad j = 1, 2, ..., n \end{aligned}$$

with only the barrier tip variables implemented with

$$X_1 = \begin{bmatrix} \alpha \end{bmatrix} = \begin{bmatrix} \alpha_{(1)} & . & . & \alpha_{(4)} \end{bmatrix}. \tag{3.3.2}$$

The optimisation implemented the converged variables X_0^{S1} of $\boldsymbol{S_1}$ as initial variables with finite difference steps size (FDCH) set relatively small. This was done in order to force the optimisation algorithm to search a minimum $T_R(X_1)$ point in the local maximised $T_A(X_0)$ location.

$\Rightarrow$ Step $\boldsymbol{S_3}$,

$$\begin{aligned} \text{The minimisation of :} \quad & T_R(X_2) \\ \text{Subject to :} \quad & 0 \leqslant G_j(X_2) \leqslant 1 \quad ; \quad j = 1, 2, ..., n \end{aligned}$$

with all the symmetric barrier variables allowed to vary excluding the current angle. The optimisation implemented the converged variables X_1^{S2} of $\boldsymbol{S_2}$, with initial variables with FDCH set relatively small. This was done in order to even further try and reduce T_R with an entire flux barrier variable set, that consists of

$$X_2 = \begin{bmatrix} \alpha \\ \beta \\ R \\ P_{1sp} \\ P_{3sp} \\ P_{5sp} \\ \chi \\ S_1P \\ S_2P \end{bmatrix} = \begin{bmatrix} \alpha_{(1)} & . & . & \alpha_{(4)} \\ \beta_{(1)} & . & . & \beta_{(4)} \\ R_{(1)} & . & . & R_{(4)} \\ P_{1sp(1)} & . & . & P_{1sp(4)} \\ P_{3sp(1)} & . & . & P_{3sp(4)} \\ P_{5sp(1)} & . & . & P_{5sp(4)} \\ \chi_{(1)} & . & . & \chi_{(4)} \\ S_1P_{(1)} & . & . & S_1P_{(4)} \\ S_2P_{(1)} & . & . & S_2P_{(4)} \end{bmatrix} \tag{3.3.3}$$

The converged objective in step $\boldsymbol{S_3}$ is now implemented in the comparison study as the base line, symmetric optimised rotor.

3.3.2 Asymmetric Variation Study

The second section is an asymmetric variation implementing the converged objective variables X_2^{S3} of step $\boldsymbol{S_3}$ as initial start variables in steps $\boldsymbol{S_4}$ to $\boldsymbol{S_6}$. The purpose of this strategy is to indicate whether there are any performance improvements to the symmetric machine by varying the flux barriers asymmetrically with three different asymmetric variable sets.

The optimisation strategy consisted of three independent objective functions with :

$\Rightarrow$ Step $\boldsymbol{S_4}$,

$$\begin{aligned} \text{The minimisation of :} \quad & T_R(X_3) \\ \text{Subject to :} \quad & 0 \leqslant G_j(X_3) \leqslant 1 \quad ; \quad j = 1, 2, ..., n \end{aligned}$$

by implementing small FDCH with only the left side variables and current angle implemented, with variable set

$$X_3 = \begin{bmatrix} \alpha \\ \theta \end{bmatrix} = \begin{bmatrix} \alpha_{(5)} & . & . & \alpha_{(8)} \\ \theta & & & \end{bmatrix}. \tag{3.3.4}$$

$\Rightarrow$ Step $\boldsymbol{S_5}$,

$$\begin{aligned} \text{The minimisation of :} \quad & T_R(X_4) \\ \text{Subject to :} \quad & 0 \leqslant G_j(X_4) \leqslant 1 \quad ; \quad j = 1, 2, ..., n \end{aligned}$$

by implementing small FDCH with the complete asymmetric variable set allowed to vary, excluding the current angle, with

$$X_4 = \begin{bmatrix} \alpha \\ \beta \\ R \\ P_{1sp} \\ P_{3sp} \\ P_{5sp} \\ \chi \\ S_1P \\ S_2P \end{bmatrix} = \begin{bmatrix} \alpha_{(1)} & . & . & . & . & . & . & \alpha_{(8)} \\ \beta_{(1)} & . & . & . & . & . & . & \beta_{(8)} \\ R_{(1)} & . & . & R_{(4)} & & & & \\ P_{1sp(1)} & . & . & P_{1sp(4)} & & & & \\ P_{3sp(1)} & . & . & P_{3sp(4)} & & & & \\ & & & & P_{5sp(1)} & . & . & P_{3sp(4)} \\ \chi_{(1)} & . & . & \chi_{(4)} & & & & \\ S_1P_{(1)} & . & . & S_1P_{(4)} & & & & \\ S_2P_{(1)} & . & . & S_2P_{(4)} & & & & \end{bmatrix}. \tag{3.3.5}$$

$\Rightarrow$ Step $\boldsymbol{S_6}$

$$\begin{aligned} \text{The minimisation of :} \quad & T_R(X_5) \\ \text{Subject to :} \quad & 0 \leqslant G_j(X_5) \leqslant 1 \quad ; \quad j = 1, 2, ..., n \end{aligned}$$

by implementing small FDCH with the complete asymmetric variable set allowed to vary, including the current angle, with

$$X_5 = \begin{bmatrix} \alpha \\ \beta \\ R \\ P_{1sp} \\ P_{3sp} \\ P_{5sp} \\ \chi \\ S_1P \\ S_2P \\ \theta \end{bmatrix} = \begin{bmatrix} \alpha_{(1)} & . & . & . & . & . & . & \alpha_{(8)} \\ \beta_{(1)} & . & . & . & . & . & . & \beta_{(8)} \\ R_{(1)} & . & . & R_{(4)} & & & & \\ P_{1sp(1)} & . & . & P_{1sp(4)} & & & & \\ P_{3sp(1)} & . & . & P_{3sp(4)} & & & & \\ & & & & P_{5sp(1)} & . & . & P_{3sp(4)} \\ \chi_{(1)} & . & . & \chi_{(4)} & & & & \\ S_1P_{(1)} & . & . & S_1P_{(4)} & & & & \\ S_2P_{(1)} & . & . & S_2P_{(4)} & & & & \\ \theta & & & & & & & \end{bmatrix}. \tag{3.3.6}$$

3.3.3 Result Analysis

The results of this optimisation strategy is shown in Figure 3.13 and tabulated in Table 3.4. Presented in the table and figure is the optimisation results of the symmetric optimisation strategy and the three asymmetric variations done in steps $\boldsymbol{S_3}$ to $\boldsymbol{S_6}$, with the symmetric case results taken as unity for the per unit calculations. Inspecting the results, it is clear that by varying the flux barrier asymmetrically there

Table 3.4: Symmetric-asymmetric optimisation strategy results of the 24-slot machines [77, 78].

Symmetric-Asymmetric Optimisation Strategy Results							
	Stator		$\boldsymbol{\theta}$	$\boldsymbol{T_A}$		$\boldsymbol{T_R}$	
Step*	**Slots**	**Objective Function**	[°]	[Nm]	[pu]	[%]	[pu]
S_3	24	$\boldsymbol{T_R(X_2)}$ - (Max $\boldsymbol{T_A}$)	57	**11.88**	1.00	11.35	1.00
	24	$\boldsymbol{T_R(X_2)}$ - (Min $\boldsymbol{T_R}$)	57	11.88	1.00	**11.35**	1.00
S_4	24	$\boldsymbol{T_R(X_3)}$ - (Max $\boldsymbol{T_A}$)	57	**11.84**	1.00	7.85	0.69
	24	$\boldsymbol{T_R(X_3)}$ - (Min $\boldsymbol{T_R}$)	52	11.62	0.97	**7.19**	0.63
S_5	24	$\boldsymbol{T_R(X_4)}$ - (Max $\boldsymbol{T_A}$)	57	**11.86**	1.00	8.40	0.74
	24	$\boldsymbol{T_R(X_4)}$ - (Min $\boldsymbol{T_R}$)	51	11.54	0.98	**6.91**	0.61
S_6	24	$\boldsymbol{T_R(X_5)}$ - (Max $\boldsymbol{T_A}$)	57	**11.85**	1.00	8.10	0.71
	24	$\boldsymbol{T_R(X_5)}$ - (Min $\boldsymbol{T_R}$)	48	11.21	0.94	**6.15**	0.54

* - Simulation Step in Figure 3.12 ; θ - Current Angle ; T_A - Average Torque ; T_R - Torque Ripple

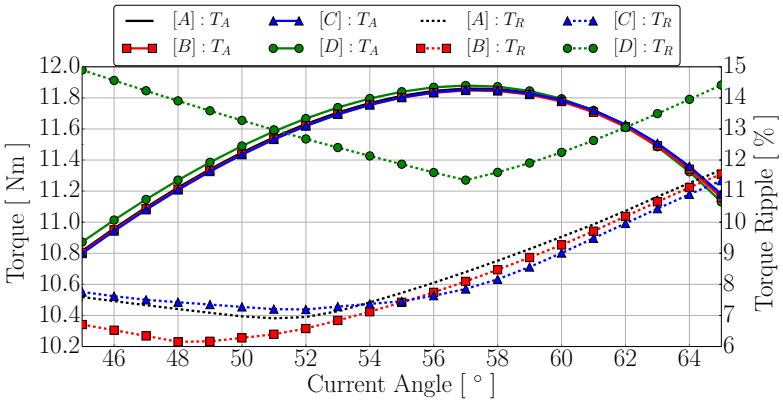

[***A***] - $\boldsymbol{T_R(X_5)}$ Asymmetric maximization with final step $\boldsymbol{S_6}$ minimization.

[***B***] - $\boldsymbol{T_R(X_3)}$ Asymmetric maximization with final step $\boldsymbol{S_4}$ minimization.

[***C***] - $\boldsymbol{T_R(X_4)}$ Asymmetric maximization with final step $\boldsymbol{S_5}$ minimization.

[***D***] - $\boldsymbol{T_R(X_2)}$ Full symmetric optimization step $\boldsymbol{S_3}$.

Figure 3.13: Symmetric-asymmetric optimisation objective T_R and torque results versus current angle of the 24 - slot machine [77, 78].

Table 3.5: Full asymmetric optimisation variables.

Optimisation Variables			
	FAS Optimisation		
Variables	X_6	X_7	X_8
α	$\surd$	$\surd$	$\surd$
β	$\surd$		$\surd$
R	$\surd$		$\surd$
P_{1sp}	$\surd$		$\surd$
P_{3sp}	$\surd$		$\surd$
P_{5sp}	$\surd$		$\surd$
χ	$\surd$		$\surd$
S_1P			
S_2P			
θ	$\surd$		

[1] * $\surd_R$ - S_1/Right Side ; $\surd_L$ - S_2/Left Side ; $\surd$ - Right & Left Sides

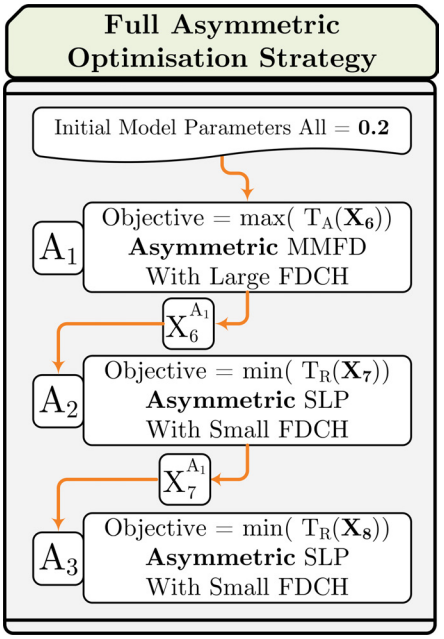

MMFD : Modified Method of Feasible Direction. **SLP** : Sequential Linear Programming. **FDCH** : Relative finite difference step size.

Figure 3.14: Optimisation strategies implemented and variable flow diagram, with superscript A the full-asymmetric procedure [77, 78].

is no significant drop in the rated T_A value. There is however a drastic reduction in T_R, with the reduction in T_R ranging from 26% to 31% below the symmetric case results. Additionally, it is noted that the asymmetric flux barrier tip variables in variable set X_3, in optimisation step S_4, had the largest effect on optimisation objective T_R. This shown in Table 3.4, with a reduction in T_R of 27%, with the subsequent optimisation steps S_5 and S_6 only reducing T_R by a further 2 and 9% respectively.

This asymmetric variation then illustrates that it is possible to reduce T_R without affecting T_A of the machine. An additional problem investigated is that by applying this asymmetric variation to the symmetric case, the coherent maximum T_A, minimum T_R current angle position no longer exists, this seen from Figure 3.13. A possible mitigation process that implements a complete asymmetric variable set will be implemented in the next section.

3.4 Full Asymmetric Optimisation

In this section, the shift from coherent maximum T_A, T_R current angle point found in the symmetric/asymmetric variation will be investigated by a simplified, complete asymmetric optimisation strategy. The simplified optimisation strategy is shown in Figure 3.14, with the optimisation variables presented in Table 3.5. This simplified

strategy will be applied to the 24-slot and the 36-slot machine stators to compare the asymmetric results over two power ranges.

Once again the strategy implements a step wise optimisation procedure as in the previous study, with the successive optimisation step implementing the formers converged variables as initial variables. It should be noted that in the study in Section 3.3, it was found that the optimiser continuously maximised variables S_1P and S_2P to its maximum constrained point, as can be seen in Figure 3.16. These two variables where thus omitted from the optimisation variables with a constant maximum value. With this reduced set of variables, the variable constraints remained as in Equation 3.2.1.

This simplified full asymmetric optimisation strategy once again implemented a step wise procedure, with the successive optimisation steps, A_2 and A_3 implementing the formers converged variables as initial variables. The strategy steps consist of:

$\Rightarrow$ Step $\boldsymbol{A_1}$,

$$\begin{aligned} \text{The maximisation of :} \quad & T_A(X_6) \\ \text{Subject to :} \quad & 0 \leqslant G_j(X_6) \leqslant 1 \quad ; \quad j = 1, 2, ..., n \end{aligned}$$

by implementing large FDCH with the complete set of variables allowed to vary asymmetrically, with the variables consisting of

$$X_6 = \begin{bmatrix} \alpha \\ \beta \\ R \\ P_{1sp} \\ P_{3sp} \\ P_{5sp} \\ \chi \\ \theta \end{bmatrix} = \begin{bmatrix} \alpha_{(1)} & . & . & . & . & . & . & \alpha_{(8)} \\ \beta_{(1)} & . & . & . & . & . & . & \beta_{(8)} \\ R_{(1)} & . & . & R_{(4)} & & & & \\ P_{1sp(1)} & . & . & P_{1sp(4)} & & & & \\ P_{3sp(1)} & . & . & P_{3sp(4)} & & & & \\ & & & & P_{5sp(1)} & . & . & P_{3sp(4)} \\ \chi_{(1)} & . & . & \chi_{(4)} & & & & \\ \theta & & & & & & & \end{bmatrix}. \tag{3.4.1}$$

$\Rightarrow$ Step $\boldsymbol{A_2}$,

$$\begin{aligned} \text{The minimisation of:} \quad & T_R(X_7) \\ \text{Subject to :} \quad & 0 \leqslant G_j(X_7) \leqslant 1 \quad ; \quad j = 1, 2, ..., n \end{aligned}$$

by implementing small FDCH with only the barrier tip variables allowed to vary asymmetrically, with the variables consisting of :

$$X_7 = \begin{bmatrix} \alpha \end{bmatrix} = \begin{bmatrix} \alpha_{(1)} & . & . & . & . & . & . & \alpha_{(8)} \end{bmatrix} \tag{3.4.2}$$

$\Rightarrow$ Step $\boldsymbol{A_3}$,

$$\begin{aligned} \text{The minimisation of :} \quad & T_R(X_8) \\ \text{Subject to :} \quad & 0 \leqslant G_j(X_8) \leqslant 1 \quad ; \quad j = 1, 2, ..., n \end{aligned}$$

Table 3.6: Full asymmetric optimisation strategy versus full-symmetric optimisation strategy results of the 24-slot and 36-slot machines [77, 78].

Sim*	Stator Slots	Objective Function	θ [°]	T_A [Nm]	T_A [pu]	T_R [%]	T_R [pu]
Full Symmetric Optimisation Strategy Results							
S_3	24	$\boldsymbol{T_R(X_2)}$ - (Max $\boldsymbol{T_A}$)	57	**11.88**	1.00	11.35	1.00
	24	$\boldsymbol{T_R(X_2)}$ - (Min $\boldsymbol{T_R}$)	57	11.88	1.00	**11.35**	1.00
S_3	36	$\boldsymbol{T_R(X_2)}$ - (Max $\boldsymbol{T_A}$)	66	**75.23**	1.00	8.49	1.00
	36	$\boldsymbol{T_R(X_2)}$ - (Min $\boldsymbol{T_R}$)	66	75.23	1.00	**8.49**	1.00
Full Asymmetric Optimisation Strategy Results							
A_1	24	$\boldsymbol{T_R(X_6)}$ - (Max $\boldsymbol{T_A}$)	52.2	**11.93**	1.00	51.54	4.54
	24	$\boldsymbol{T_R(X_6)}$ - (Min $\boldsymbol{T_R}$)	52.2	11.93	1.00	**51.54**	4.54
A_3	24	$\boldsymbol{T_R(X_8)}$ - (Max $\boldsymbol{T_A}$)	52.5	**11.83**	1.00	5.72	0.50
	24	$\boldsymbol{T_R(X_8)}$ - (Min $\boldsymbol{T_R}$)	52.5	11.83	1.00	**5.72**	0.50
A_1	36	$\boldsymbol{T_R(X_6)}$ - (Max $\boldsymbol{T_A}$)	64	**78.53**	1.04	52.79	6.22
	36	$\boldsymbol{T_R(X_6)}$ - (Min $\boldsymbol{T_R}$)	64	78.53	1.04	**52.79**	6.22
A_3	36	$\boldsymbol{T_R(X_8)}$ - (Max $\boldsymbol{T_A}$)	64	**77.06**	1.02	3.90	0.46
	36	$\boldsymbol{T_R(X_8)}$ - (Min $\boldsymbol{T_R}$)	64	77.06	1.02	**3.90**	0.46

* - Simulation Step in Figure 3.12 and 3.14 ; θ - Current Angle ; T_A - Average Torque ; T_R - Torque Ripple

by implementing small FDCH with the complete set of variables allowed to vary asymmetrically excluding the current angle, with the variables consisting of

$$X_8 = \begin{bmatrix} \alpha \\ \beta \\ R \\ P_{1sp} \\ P_{3sp} \\ P_{5sp} \\ \chi \end{bmatrix} = \begin{bmatrix} \alpha_{(1)} & \cdots & \cdots & \cdots & \alpha_{(8)} \\ \beta_{(1)} & \cdots & \cdots & \cdots & \beta_{(8)} \\ R_{(1)} & \cdots & R_{(4)} & & \\ P_{1sp(1)} & \cdots & P_{1sp(4)} & & \\ P_{3sp(1)} & \cdots & P_{3sp(4)} & & \\ & & & P_{5sp(1)} \cdots & P_{3sp(4)} \\ \chi_{(1)} & \cdots & \chi_{(4)} & & \end{bmatrix}. \tag{3.4.3}$$

3.4.1 Result Analysis

Presented in Table 3.6 and Figure 3.15 are the results of the simplified asymmetric optimisation compared to the full symmetric optimisation of Section 3.3, step $\boldsymbol{S_3}$. The symmetric results of $\boldsymbol{S_3}$ are implemented as unity for the per unit calculation.

As can be seen from the figure, there is no significant reduction in T_A between the symmetric optimisation of step $\boldsymbol{S_3}$ and the full asymmetric optimisation results of step $\boldsymbol{A_3}$ for the 24 slot stator machine. There is however a significant reduction in T_R

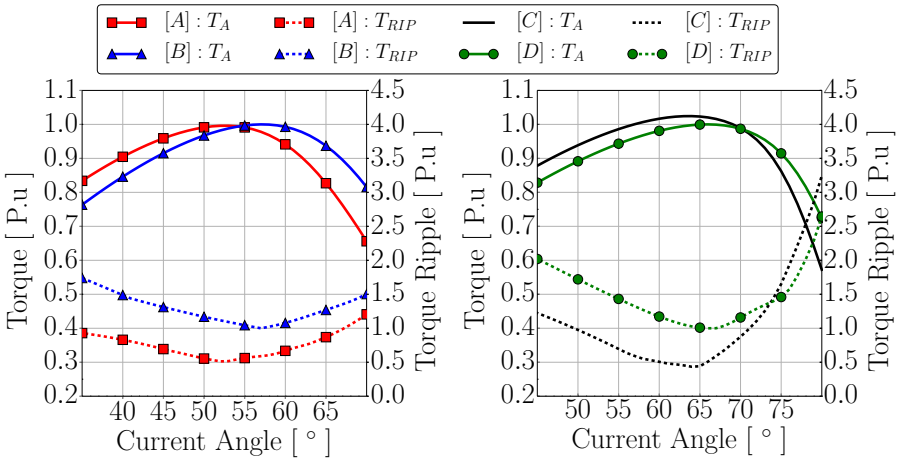

[$\boldsymbol{A}$] - $\boldsymbol{T_R(X_8)}$ A-Symmetric maximization with final step $\boldsymbol{A_3}$ minimization on the 24 slot stator machine.

[$\boldsymbol{B}$] - $\boldsymbol{T_R(X_2)}$ Symmetric maximization with final step $\boldsymbol{S_3}$ minimization on the 24 stator slot Machine.

[$\boldsymbol{C}$] - $\boldsymbol{T_R(X_8)}$ A-Symmetric maximization with final step $\boldsymbol{A_3}$ minimization on the 36 stator slot machine.

[$\boldsymbol{D}$] - $\boldsymbol{T_R(X_2)}$ Symmetric maximization with final step $\boldsymbol{S_3}$ minimization on the 36 stator slot machine.

Figure 3.15: Full asymmetric and symmetric optimisation strategy result plot against current angel change [77, 78].

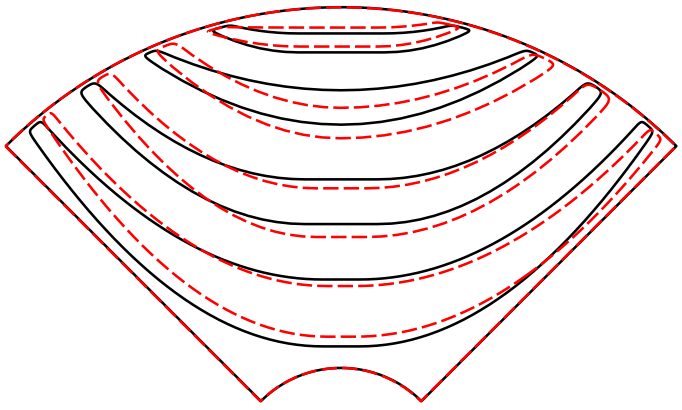

Figure 3.16: Optimisation result lamination of the full symmetric (solid lines) optimisation S3 and full asymmetric (dashed lines) optimisation A3 of the 36 slot stator illustrating the symmetric versus asymmetric pole-structure [77, 78].

at rated conditions, with a reduction of 50% in T_R from the symmetric optimisation step $\boldsymbol{S_3}$ to the full asymmetric step $\boldsymbol{A_3}$ results.

Also illustrated in Table 3.6 and Figure 3.15 is the results of these two strategies applied to the 36 slot stator machine. As can be seen from the figure, not only is there not reduction in T_A, but there is a 2% increase in the full asymmetric optimisation compared to the symmetric optimisation. There was also a significant reduction in T_R as noted for the 24 slot stator, with a reduction of 54% from the symmetric optimisation step $\boldsymbol{S_3}$ to the full asymmetric step $\boldsymbol{A_3}$.

An illustration of three of the optimised rotor topologies is presented in Figure

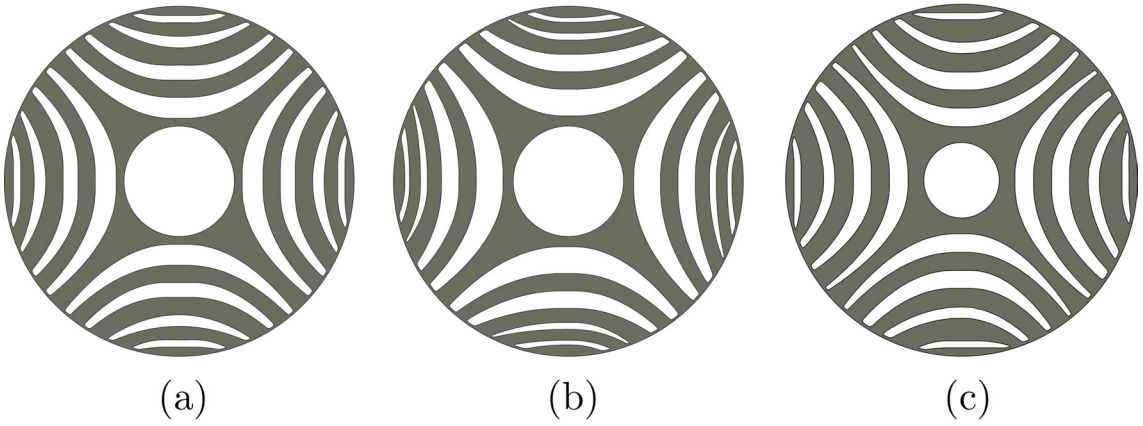

Figure 3.17: Laminations of optimisation objective results by objective functions: (a) - Optimisation step S_6 with objective function $T_R(X_5)$ implementing the 24-slot stator machine, (b) - Optimisation step A_3 with objective function $T_R(X_8)$ implementing the 24-slot stator machine, (c) - Optimisation step A_3 with objective function $T_R(X_8)$ implementing the 36-slot stator machine [77, 78].

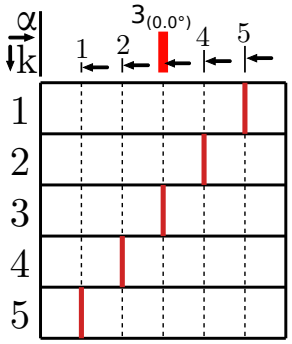

Figure 3.18: Illustration of the skew model implemented, with the skewed machine represented by 5 skew stepped machines.

3.17, with the laminations consisting of steps $\boldsymbol{S_6}$ and $\boldsymbol{A_3}$ for the 24 slot stator and step $\boldsymbol{A_3}$ for the 36 slot stator. A further comparison of the symmetric versus asymmetric optimisation results from step $\boldsymbol{S_3}$ and $\boldsymbol{A_3}$ for the 36 slot stator is presented in Figure 3.16.

Finally another key observation made from the optimisation study, is that the optimum barrier tip was found to be flattened as in Figure 3.4a. The variable set for the next optimisation studies was thus reduced by setting the barrier tip to a fixed flattened state. In the next section, the effect of the symmetric and asymmetric rotor on rotor skew with respect to torque ripple is studied.

3.5 Rotor Skew Study

In this section, the symmetric and asymmetric rotor topologies optimised for the 24 and 36 stator slot machines will be implemented in a rotor skew study. The rotor skew effects on the asymmetric rotor topology compared to the symmetric rotor

topology, with respect to T_R, is investigated.

The modelling of a skewed machine rotor can be simplified to a stepped rotor as shown in Figure 3.18, with the rotor skew modelled as 5 stepped machines, as presented in [92]. The 5 machines, represented by k in the figure, are each simulated by stepping the rotor an angle equivalent to one or two fifths of the total skew angle either side of the central un-skewed machine at $\alpha = 3$.

The torque for each simulation step of the five machines is calculated by implementing equation

$$T(s) = \frac{\sum_{k=1}^{5} T_k(s)}{5} \qquad (3.5.1) \qquad s = 1, 2, .., s_{steps} \qquad (3.5.2)$$

with the T_R then in turn calculated from this 5 machine averaged torque per step calculation with Equation 2.5.6, and the T_A by Equation 2.5.4. Likewise, flux linkage is calculated by averaging each simulation step of the five machines with

$$\lambda(s) = \frac{\sum_{k=1}^{5} \lambda_k(s)}{5} \qquad (3.5.3) \qquad s = 1, 2, .., s_{steps}. \qquad (3.5.4)$$

24 Slot Stator Machine Study

To study the effect of the asymmetric and symmetric topology on T_R, a skew and current angle T_R contour plot is constructed. The results of the full symmetric and full asymmetric optimised rotors of the 24 slot stator is presented in Figures 3.21, 3.19 and 3.23 respectively. An analysis table and, a T_A and T_R versus current angle plot is constructed from each of the contour maps, that consists of:

- Table 3.7 and Figure 3.20 that analyse the optimisation results of S3 in Figure 3.19 for the full symmetric rotor. With skew angles 0°, 10.6° and 15° selected for the table analysis and current angles 53° and 57° selected for the figure plot.
- Table 3.8 and Figure 3.22 that analyse the optimisation results of S6 in Figure 3.21. With skew angles 0°, 9.2° and 15° selected for the table analysis and current angles 55° and 57° selected for the figure plot.
- Table 3.9 and Figure 3.24 that analyse the optimisation results of A3 in Figure 3.23 for the full asymmetric rotor. With skew angles 0°, 7.6° and 15° selected for the table analysis and current angles 52° and 57° selected for the figure plot.

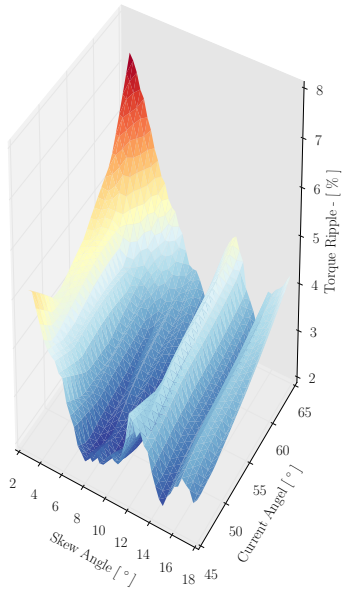

Figure 3.19: T_R versus skew and current angle contour plot of objective function $T_R(X_2)$ for the 24-slot machine.

Table 3.7: Skew angle results of objective function $T_R(X_2)$ of the 24 slot stator [77, 78].

Stator Slots	Skew Angle	θ [°]	T_A [Nm]	T_A [P.u]	T_R [%]	T_R [P.u]
24	0.0° - (Max T_A)	57	11.88	1.00	11.35	1.00
24	0.0° - (Min T_R)	57	11.88	1.00	11.35	1.00
24	10.6° - (Max T_A)	53	11.50	0.97	2.14	0.19
24	10.6° - (Min T_R)	53	11.47	0.97	2.1	0.19
24	15.0° - (Max T_A)	50	11.19	0.94	2.6	0.23
24	15.0° - (Min T_R)	45	11.0	0.93	2.28	0.20

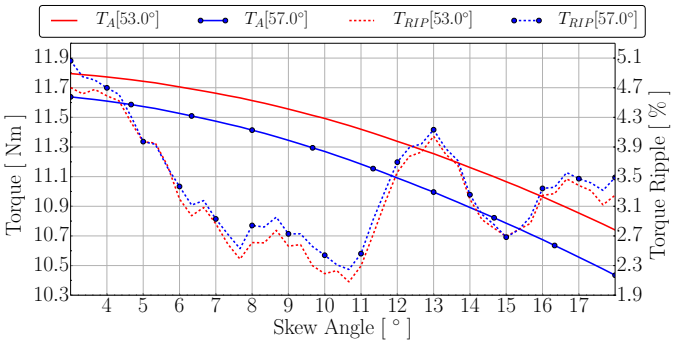

Figure 3.20: T_A and T_R versus skew angle of objective function $T_R(X_2)$ for the 24 slot stator.

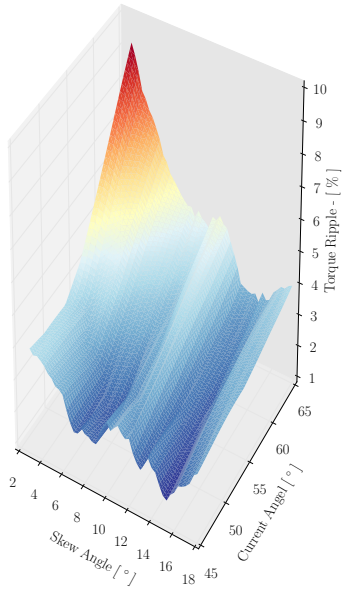

Figure 3.21: T_R versus skew and current angle contour plot of objective function $T_R(X_5)$ for the 24-slot machine.

Table 3.8: Skew angle results of objective function $T_R(X_5)$ of the 24 slot stator [77, 78].

Stator Slots	Skew Angle	θ [°]	T_A [Nm]	T_A [P.u]	T_R [%]	T_R [P.u]
24	0.0° - (Max T_A)	57	11.85	1.00	8.10	1.32
24	0.0° - (Min T_R)	48	11.21	0.95	6.15	1.00
24	9.2° - (Max T_A)	56	11.59	0.98	2.90	0.47
24	9.2° - (Min T_R)	49	11.18	0.94	2.01	0.33
24	15.0° - (Max T_A)	55	11.20	0.95	2.12	0.35
24	15.0° - (Min T_R)	45	10.50	0.89	1.72	0.28

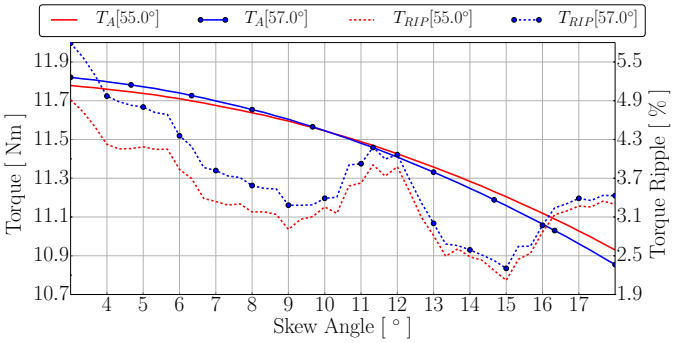

Figure 3.22: T_A and T_R versus skew angle of objective function $T_R(X_5)$ for the 24 slot stator.

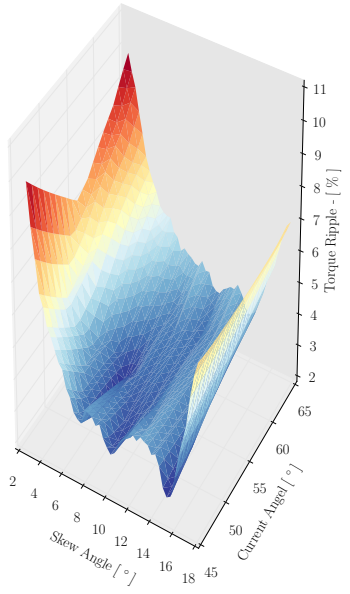

Figure 3.23: T_R versus skew and current angle contour plot of objective function $T_R(X_8)$ for the 24-slot machine.

Table 3.9: Skew angle results of objective function $T_R(X_8)$ of he 24 slot stator [77, 78].

Stator Slots	Skew Angle	θ [°]	T_A [Nm]	T_A [$P.u$]	T_R [%]	T_R [$P.u$]
24	0.0° - (Max T_A)	53	11.83	1.00	5.72	1.00
24	0.0° - (Min T_R)	53	11.83	1.00	5.72	1.00
24	7.6° - (Max T_A)	56	11.66	0.99	3.28	0.57
24	7.6° - (Min T_R)	54	11.62	0.99	2.84	0.50
24	15.0° - (Max T_A)	49	11.18	0.95	2.58	0.45
24	15.0° - (Min T_R)	45	10.99	0.93	2.27	0.40

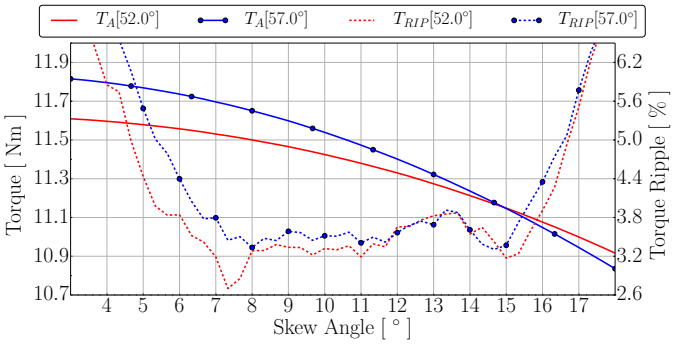

Figure 3.24: T_A and T_R versus skew angle of objective function $T_R(X_8)$ for the 24 slot stator.

For the validation of the optimisation and skew analysis, the rotor presented in Figure 3.17a, with skew results in Figures 3.21 and 3.22, is selected for manufacture. In a further analysis of the chosen machine, the three angles selected in Table 3.8 are plotted against current angle change in Figure 3.25. Additionally, the P_F for each skew angle is also taken into consideration, with the P_F plotted against current angle change for the three selected skew angles illustrated in Figure 3.26.

As can be seen in Figure 3.25, there is no significant difference in the low T_R value achieved between the 9.2° and 15° skew angle. There is however a significant difference in the peak T_A value, with a reduction of 2% for the 9.2° and a 5% reduction for the 15° skew angle.

Although P_F was not taken into consideration during the optimisation process, the effect of the two skew angles on power factor is also taken into consideration. Noting that the current angle position of the peak T_A decreases as the skew angle increases, the power factor is evaluated at this respective peak T_A current angle point. The result of this is shown in Figure 3.26, with a reduction on 1% present in P_F for the 9.2° skew angle and a reduction of 3% for the 15° skew angle. Taking the observations made in Figures 3.25 and 3.26 into account, the 9.2° skew angle is selected for the optimum skew angle for this specific rotor. This angle is thus implemented in the manufacturing process for the rotor skew angle, with the manufacturing and testing of the rotor conducted in the following section.

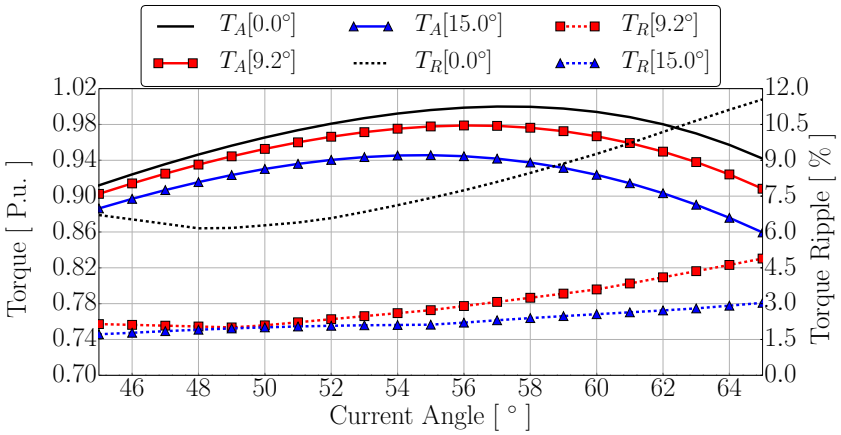

Figure 3.25: Optimisation objective function $T_R(X_5)$ T_A, T_R versus current angle for selected skew angles 0.0°, 9.2° and 15.0° for the 24-slot machine [77, 78].

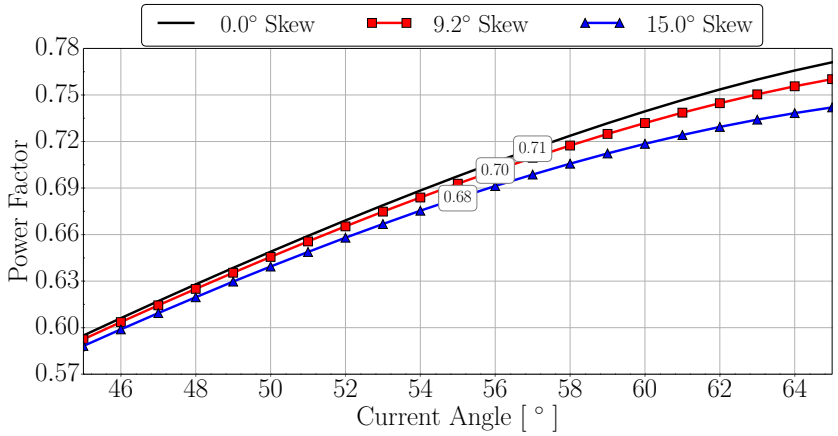

Figure 3.26: Optimisation objective function $T_R(X_5)$ P_F versus current angle for selected skew angles 0.0°, 9.2° and 15.0° for the 24-slot machine.

3.5.1 36 Slot Stator Machine Study

The similar study conducted on the 36 slot stator machine's symmetric and asymmetric rotors are illustrated in Figures 3.27 and 3.28. These two T_R machine mappings are also analysed by a table and figure, that consists of

- Table 3.10 and Figure 3.29 that analyse the results in Figure 3.27 with the full symmetric rotor. With skew angles 0°, 4.0°, 8.0° and 10° selected for the table analysis and current angles 62°, 63° and 64° selected for the figure plot.

- Table 3.11 and Figure 3.30 that analyse the results in Figure 3.28 for the full asymmetric rotor. With skew angles 0°, 3.0°, 8.0° and 10° selected for the table analysis and current angles 62°, 63° and 64° selected for the figure plot.

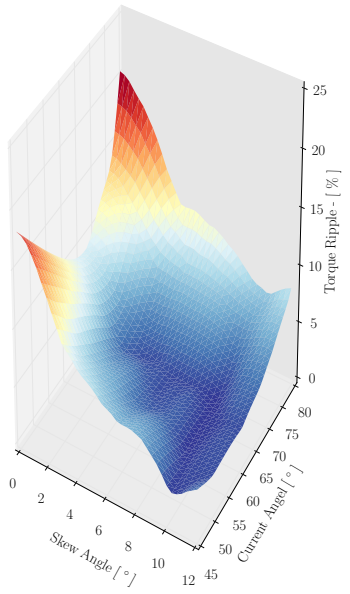

Figure 3.27: T_R versus skew and current angle contour plot of objective function $T_R(X_2)$ for the 36-slot machine.

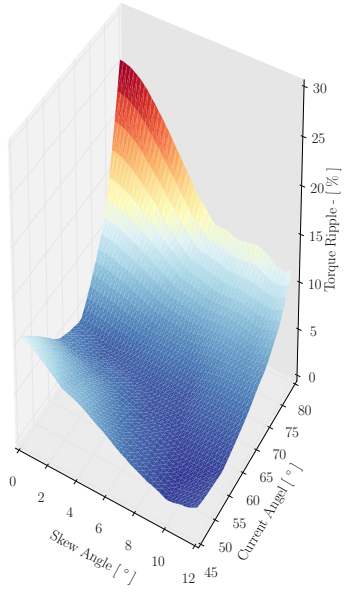

Figure 3.28: T_R versus skew and current angle contour plot of objective function $T_R(X_8)$ for the 36-slot machine.

Table 3.10: Skew angle results of objective function $T_R(X_2)$ for the 36 slot stator [77, 78].

Stator Slots	Skew Angle	θ [°]	T_A [Nm]	T_A [P.u]	T_R [%]	T_R [P.u]
36	0.0° - (Max T_A)	66	75.23	1.00	8.97	1.00
36	0.0° - (Min T_R)	66	75.23	1.00	8.97	1.00
36	4.0° - (Max T_A)	66	74.98	1.00	3.83	0.43
36	4.0° - (Min T_R)	66	74.66	1.00	2.87	0.32
36	8.0° - (Max T_A)	65	74.22	0.99	3.15	0.35
36	8.0° - (Min T_R)	53	74.19	0.99	2.87	0.32
36	10.0° - (Max T_A)	64	73.66	0.98	2.66	0.30
36	10.0° - (Min T_R)	63	73.58	0.98	2.53	0.28

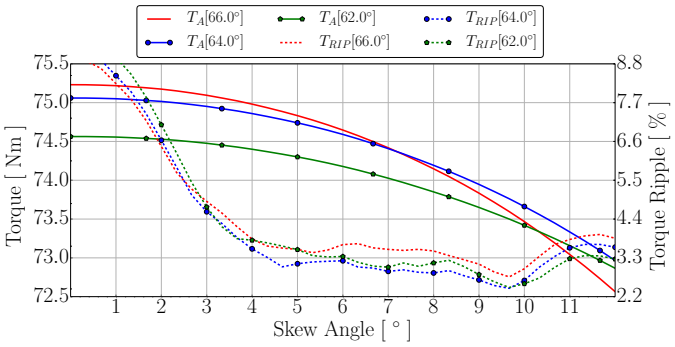

Figure 3.29: T_A and T_R versus skew angle of objective function $T_R(X_2)$ for the 36 slot stator.

Table 3.11: Skew angle results of objective function $T_R(X_8)$ for the 36 slot stator [77, 78].

Skew Angle Mapping						
Stator Slots	Skew Angle	θ [°]	T_A [Nm]	T_A [$P.u$]	T_R [%]	T_R [$P.u$]
36	0.0° - (Max T_A)	64	77.06	1.00	3.90	1.00
36	0.0° - (Min T_R)	64	77.06	1.00	3.90	1.00
36	3.0° - (Max T_A)	63	76.92	1.00	3.19	0.82
36	3.0° - (Min T_R)	63	76.92	1.00	3.19	0.82
36	8.0° - (Max T_A)	63	76.05	0.98	3.12	0.80
36	8.0° - (Min T_R)	56	74.23	0.96	2.68	0.69
36	10.0° - (Max T_A)	62	75.49	0.97	3.56	0.91
36	10.0° - (Min T_R)	49	69.24	0.90	1.83	0.47

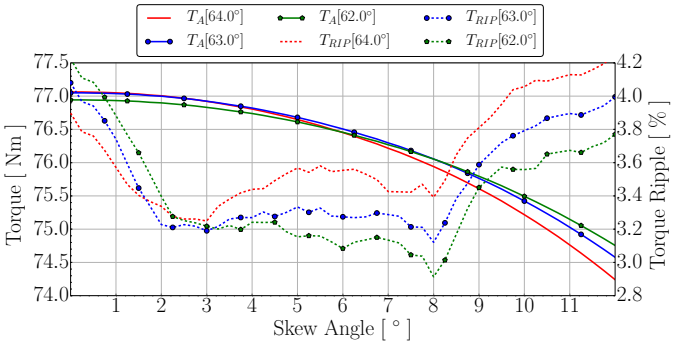

Figure 3.30: T_A and T_R versus skew angle of objective function $T_R(X_8)$ for the 36 slot stator.

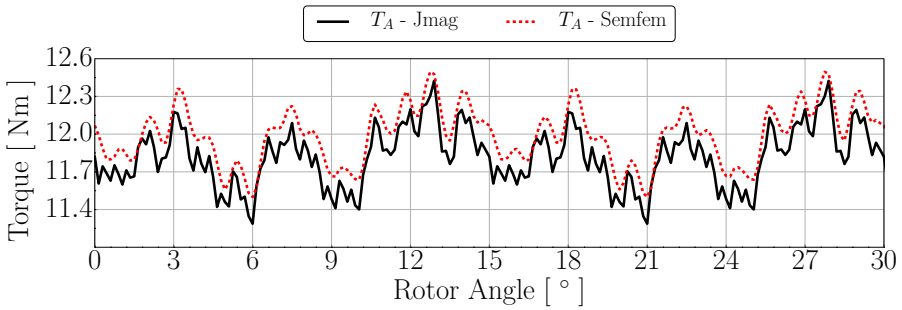

Figure 3.31: Objective function $F1_2(X_4)$ four-pole, 24 slot RSM torque comparison between the two FE packages JMag and SemFem over a two slot pitch angle.

3.5.2 Result Analysis

In an analysis of the T_R mappings conducted on the full symmetric and asymmetric rotors for both the 24 and 36 slot stator, it became evident that the optimum skew angle for all the machines studied did not consist of the conventional one stator slot pitch angle. Moreover, on average, a very effective T_R reduction can be achieved by implementing a one half stator slot skew angle. The selection of this angle provides a large reduction in T_R without drastically effecting the P_F and T_A, this compared to the drastic effects that the one stator lot pitch skew has on these parameters.

Furthermore, it is determined that the optimum skew angle for the machine to be manufactured consists of a 9.2° skew angle. This angle proved to show improved performance parameters compared to the one stator slot pitch skew angle of 15° and is thus selected as the optimum skew angle. The manufacturing of this rotor will be discussed in the next section.

3.6 Rotor Manufacture & Testing

In this section, the selected rotor from optimisation objective $T_R(X_5)$ will be implemented in the optimisation verification study (Tables 3.4 and 3.8 and Figures 3.17a and 3.21). In order to verify the results obtained in the optimisation strategy, the simulation was repeated in an alternative commercial FE package JMag. Presented in Figure 3.31 is the comparison plot of the simulation runs between the two FE packages over a two slot pitch angle, 30° in the case of the 24 slot stator. Taking into consideration that SemFem implements first order mesh elements in its simulation process, compared to JMag's second order elements, the respective simulation Torque waves agree well. With this closely correlating torque wave, the simulation results of the optimisation strategy is proven to be accurate, and validates the optimisation strategy results obtained.

3.6.1 Structural Analysis

In order to ensure acceptable mechanical rigidity under rated conditions before lamination manufacturing, the lamination was simulated by implementing two independent structural FE packages. The first package implemented is available in

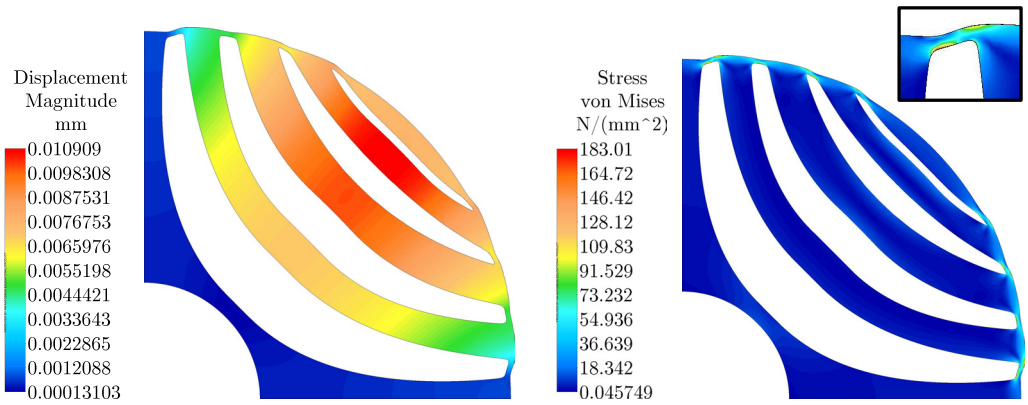

Figure 3.32: Illustration of stress and deformation analysis conducted on the selected rotor lamination to ensure mechanical rigidity under rated conditions [77, 78].

JMag. This structural package is implemented due to its ability to implement electromagnetic forces at rated conditions, along with the applicable centrifugal forces present.

The second package is Algor, a dedicated multi-physics simulation package that forms part of the Autodesk suit. This package does not have the ability to implement electromagnetic forces, and was thus implemented to only simulate centrifugal forces for comparison. The analysis consisted of simulating the lamination at four times the rated speed, or 6000 r/min, with the lamination temperature at 20 and 150° respectively.

Shown in Table 3.12 and Figure 3.32 are the results of this mechanical simulation study. The comparative centrifugal results of JMag and Algor agree well, with the centrifugal forces the dominating force contributing to the stress and deformation. The safety factor for the lamination is calculated by

$$SF = \frac{peak(\sigma_{Mises})}{\sigma_{yield}} \tag{3.6.1}$$

with σ_{Mises} representing the peak von Mises stress in the simulation, with the yield strength σ_{yield} taken from the material properties of M400 electrical steel as $300MPa$. From the table, the calculated safety factor for the lamination simulated at the most extreme condition is well within the acceptable limit. This result proves the mechanical integrity of the lamination at full load conditions for rate machine speed from 1500 r/min to 6000 r/min.

After the proven mechanical integrity of the rotor lamination, the skewed rotor lamination stack is manufactured, with the manufactured rotor illustrated in Figure 3.33. The rotor lamination is presented in Figure 3.33a and the rotor assembly presented in Figures 3.33b and 3.33c.

3.6.2 Test Setup

The test setup for the retrofit rotor RSM is illustrated in Figure 3.34a. The setup consists of two back to back inverters feeding the IM and RSM respectively, with the

Table 3.12: Stress and deformation analysis and comparison between structural analysis done in JMag and Algor Multiphysics on the selected 4 pole RSM rotor [77, 78].

Stress & Deformation Analysis								
			JMag			*Algor*		
Speed	**Temp**♣	**E-M**♠	**Mises** ℜ	SF	**Def** *	**Mises** ℜ	**SF**	**Def** *
[$P.u$]	[C°]		[MPa]		[μm]	[MPa]		[μm]
4	20	NA	172	1.74	10.5	183	1.64	10.9
4	20	√	207	1.45	12.4	NA	NA	NA
4	150	NA	172	1.74	69.4	183	1.64	69.6
4	150	√	207	1.45	71.3	NA	NA	NA

♣ - Lamination Temperature ; ♠ - Electromagnetic Forces ; ℜ - Von Mises Peak Stress ; * - Maximum Point Deformation ; Yield strength of M400-steel taken as $300MPa$

(a): Rotor Lamination. **(b):** Rotor Assembly. **(c):** Final rotor.

Figure 3.33: Illustration of the selected lamination and rotor assembly of the retrofit rotor design testing [77, 78].

inverter's switching frequency in turn being supplied by two previously developed rapid prototyping systems. The test bench implemented is illustrated in Figure 3.34b. The bench consists of a back to back connected RSM and IM, with a torque sensor and large inertia flywheel separating them. The purpose of the flywheel is to filter out the torque harmonics of the IM, so a more accurate RSM torque harmonic can be measured by the sensor. The test was conducted at full load, with the shaft speed at a constant 1000r/min.

The measured test results versus the simulated values are shown in Figure 3.35. As can be seen from the figures, the measured and simulated values agree well, with the average torque, current angle map plotted in Figure 3.35a. The torque harmonics comparison is presented in Figure 3.35b, with a slightly larger measured 24^{th} harmonic and the power factor comparison in Figure 3.35d.

The machine efficiency is presented in Figure 3.35c, with measured and estimated values deviating by less than 1 % at the peak efficiency current angle point. As with the efficiency, estimated power factor results also agree well with measured values, as seen in Figure 3.35d.

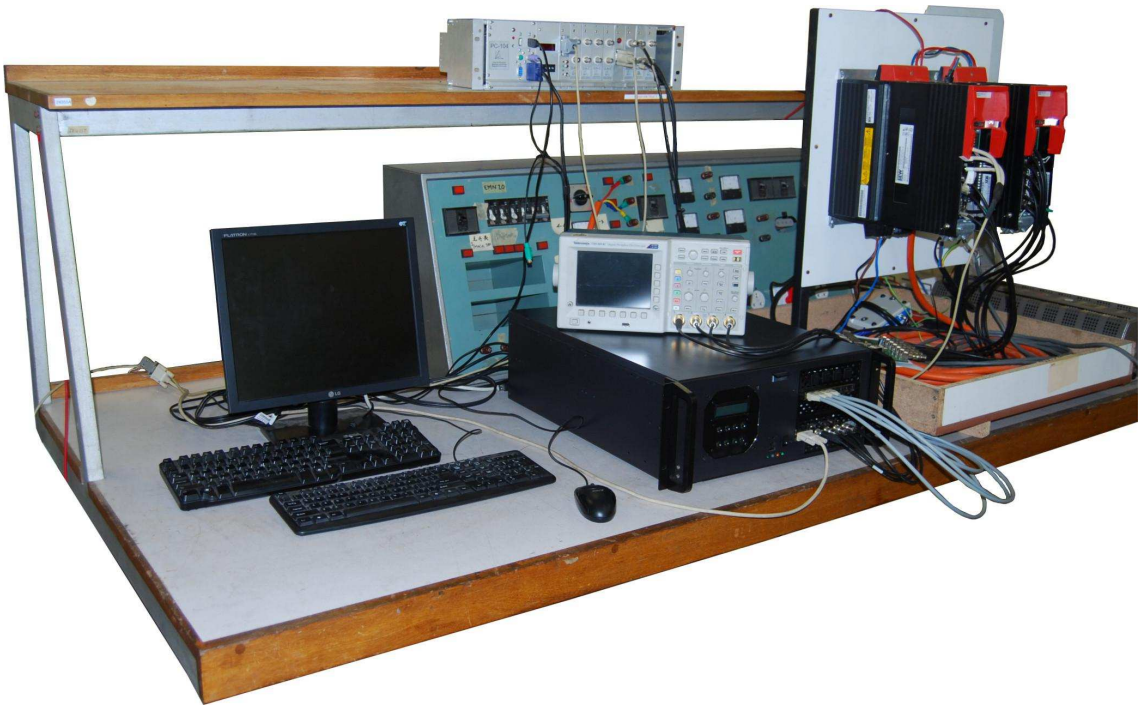

(a): Test station setup that includes two rapid prototyping machines sending switching frequencies to the back to back inverters that feed the RSM and IM.

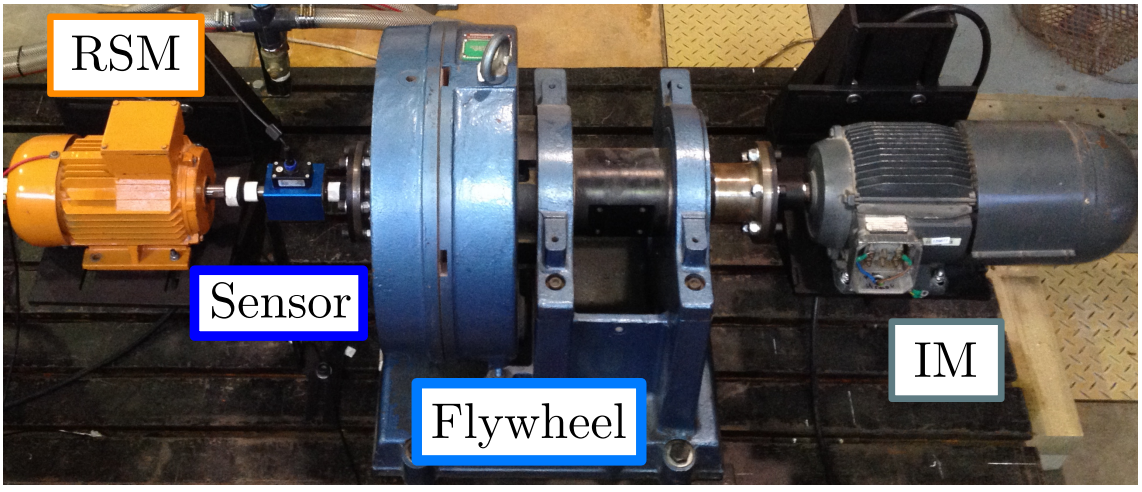

(b): Test bench setup that includes a back to back RSM and IM, separated by a torque sensor and large inertia flywheel [77, 78].

Figure 3.34: Test station and bench step of the retrofit RSM rotor design test.

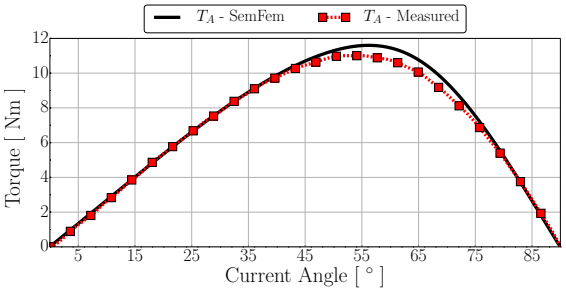

(a): Simulated versus measured average torque, current angle map.

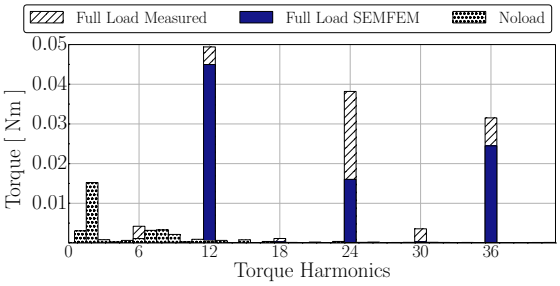

(b): Simulated versus measured torque harmonics.

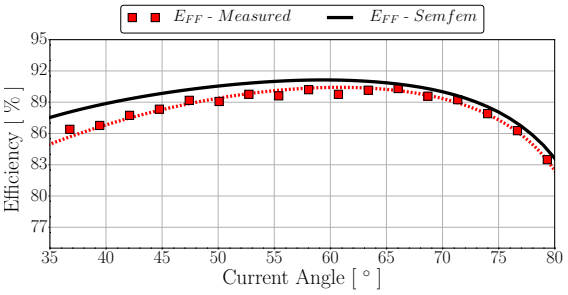

(c): Simulated versus measured efficiency, current angle map.

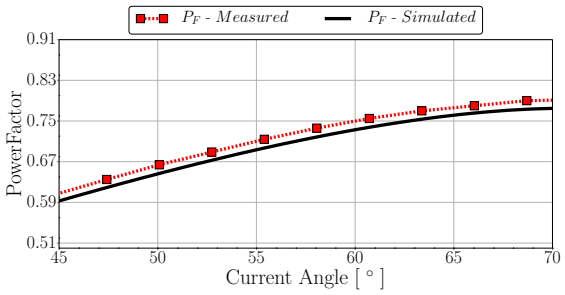

(d): Simulated versus measured power factore, current angle map.

Figure 3.35: Measured versus simulated parameters of the retrofit design study during motor operation.

3.7 Conclusion

In this chapter, an alternative asymmetric flux barrier creation technique was proposed in combination with design optimisation to study average torque and torque ripple. It was shown that a torque ripple of 5.7% and 3.9% is achievable by implementing a relatively high number of variables of between 29 and 37 for a 24-slot and 36-slot machine stators, respectively, without implementing rotor skew. Moreover, when comparing the full asymmetric to the symmetric topologies, no drop in T_A was shown, with an average torque ripple reduction of 50% for the 24-slot and 36-slot machines, respectively. This large reduction in torque ripple with the proposed asymmetric topology is confirmed by a similar study conducted by [30]. Additionally, the study also revealed the optimum flux barrier tip shape as illustrated in Figure 3.16.

It is further shown that by implementing rotor skew, a torque ripple of below 3.0% was achievable for both 24-slot and 36-slot machines. This is achieved for the 24 and 36 slot machines with rotor skew angles of between 60 to 70% and 30 to 80% respectively. The rotor skew analysis illustrates that the optimum rotor skew angle not only heavily depends on the specific stator configuration, but also on the rotor topology. The comparison between simulated and measured results for average torque and torque ripple harmonic correlates closely, with a slight increase in measured torque harmonics.

Chapter 4

Complete RSM Design Study

In this chapter, the third and forth research objective will be discussed, namely the study of the inherent weak power factor performance of RSMs and a RSM operating in the medium speed range. To study this inherent weakness, the relationship between the well known competitive torque density and less competitive power factor of reluctance synchronous machines is investigated by implementing a weighted factor optimisation strategy.

4.1 Optimisation Strategy

The optimisation strategy studies the relationship between power factor and average torque. This relationship is determined by implementing a weighted-sum (or scalarization) method that solves a multi-objective optimisation problem by combining the respective objectives into a single objective [103]. An illustration of the combined objective function pareto curve is presented in Figure 4.1. With the intended objectives, illustrated in the figure, consisting of average torque $T_A = f_1(x)$, power factor $P_F = f_2(x)$ and the combined single objective by

$$y = \gamma_1 f_1(x) + \gamma_2 f_2(x). \tag{4.1.1}$$

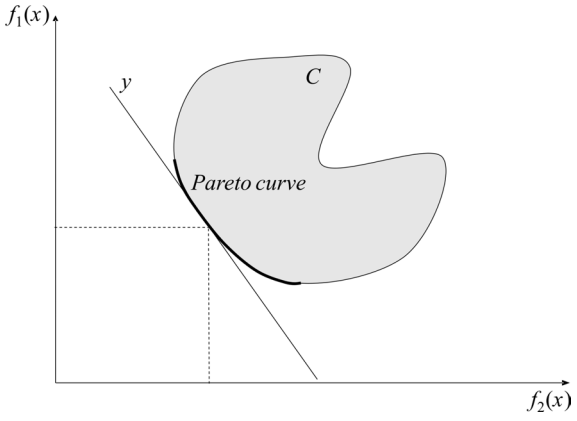

Figure 4.1: Weighted-sum combined single objective function [104, 105].

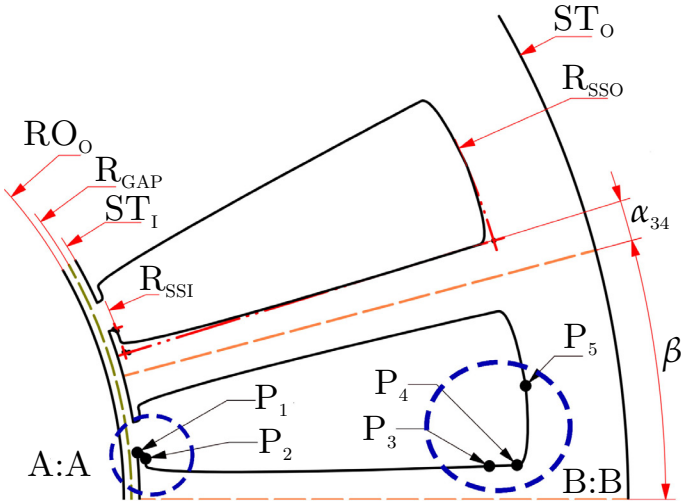

Figure 4.2: The main stator slot creation points, with β the available slot area, defined by dividing 2π by the number of stator slots [104, 105].

The objective function is determined by shifting the respective weighted factors from T_A to P_F, with the weighted factors represented by γ_1 and γ_2 respectively, with

$$\gamma_2 = 1 - \gamma_1 \tag{4.1.2}$$

and with

$$0 \leqslant \gamma_1 \leqslant 1 \tag{4.1.3}$$

and

$$0 \leqslant \gamma_2 \leqslant 1. \tag{4.1.4}$$

To effectively study this relationship in RSMs, the optimisation study will be conducted on a large range of pole number and flux barrier number combination machines. The next section will describe the stator slot design, along with the optimiser selection and optimisation strategy.

4.2 Proposed Stator Slot Design

In this section, the creation technique for the stator slots to be implemented in the optimisation procedure will be presented. Illustrated in Figure 4.2 are the main points implemented in the construction of the stator, with the main dimensions consisting of an outside stator radius R_{SO}, an air gap radius R_{GAP}, a slot inside radius R_{SSI} and a slot outside radius R_{SSO}.

The machine stator is divided into the number of sections equal to the number of stator slots, with the angle β equal to :

$$\beta = \frac{2\pi}{N_{SLOTS}} \tag{4.2.1}$$

as indicated in Figure 4.2. After the complete barrier construction, this equal section slot is then duplicated to complete the slot numbers per pole required for one machine pole simulation.

Table 4.1: Symmetric, A-Symmetric barrier variables for one flux barrier$^{\forall}$ [104, 105].

Stator Main Points		
Polar	R	θ
P_1	$R_{P_1} = {}^*R_{GAP}+0.5h$	θ_{P_1}
P_2	$R_{P_2} = {}^*R_{SSI}$	θ_{P_2}
P_3	${}^*R_{P_3}$	$\theta_{P_3} = {}^*\alpha_{34}$
P_4	${}^*R_{P_4}$	θ_{P_3}
P_5	$R_{P_5}={}^*R_{SSO}$	0.5β
Spline Angle Points$^{\spadesuit}$		
P_{11}	R_{P_2}	θ_{P_1}
P_{12}	R_{P_2}	θ_{P_1}
P_{22}	R_{P_2}	${}^*\theta_{\%22}$
P_{23}	${}^*R_{\%23}$	θ_{P_3}
P_{44}	R_{P_5}	θ_{P_3}
P_{45}	R_{P_5}	θ_{P_3}

$^{\spadesuit}$ - $\boldsymbol{R_{\%}}$ and $\boldsymbol{\theta_{\%}}$ is the percentage spacing of the points on the existing red dashed line ; $\boldsymbol{h}$ - air gap length ; * - Stator design optimisation variables.

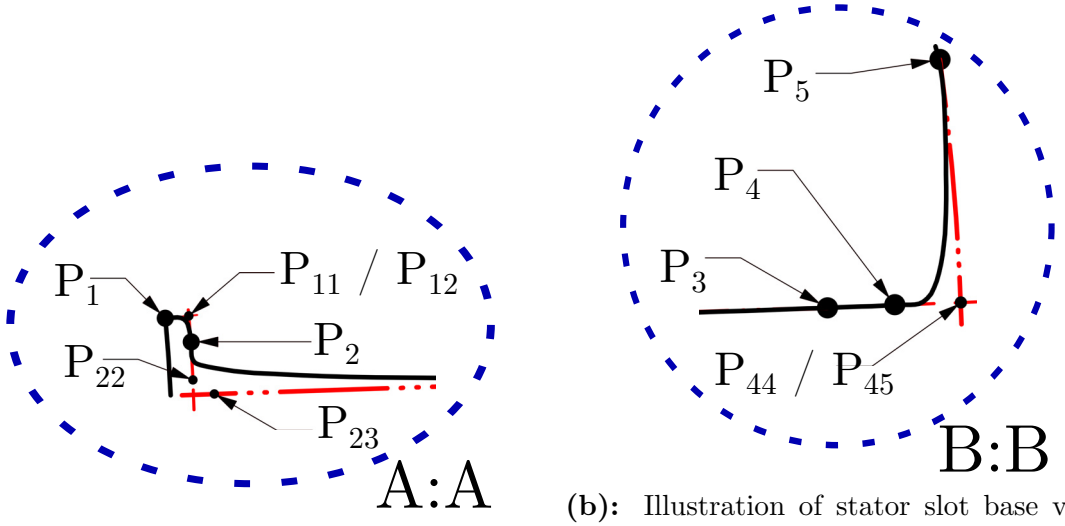

(a): Illustration of stator slot tip variables.

(b): Illustration of stator slot base variables.

Figure 4.3: Stator design variables of area AA and BB presented in Figure 4.2 [104, 105].

The slot is constructed by 5 main points P_1 to P_5, with the cubic spline implemented in the barrier tip construction once again implemented in the construction of the stator slot (description in Appendix B.2 and illustrate in Figure B.1). Figures 4.3a and 4.3b illustrate sections AA and BB in Figure 4.2, with the stator slot design variables shown in Table 4.1.

The slot entrance is described by departure points P_1 and P_2, with the departure angle points from P_1 and P_2 indicated as P_{11} and P_{12}. These two points are set at a fixed position as indicated in the figure to ensure a rounded slot entrance in order to support the completed winding entrance closing stopper.

Additionally, the second fitting from point P_2 to P_3, is described by the departure angles P_{22} and P_{23}. By varying these points, the optimiser has the ability to vary the tooth width as clearly visible in Figure 4.2 and 4.3a , where the constant tooth width line is represented by the red dashed line.

To complete the stator slot, a straight line is drawn between points P_3 and P_4, with a spline fitting from P_4 to P_5. The spline departure points are described by points P_{44} and P_{45} to finish the slot base. These spline points gave the optimisers the ability to vary the slot base shape, with either a rounded or flattened shape possible. As shown in Figure 4.2, the departure angle points were strictly allowed to vary on the red dashed lines, i.e. the basic square slot defined by R_{SSI}, R_{SSO} and α_{34}. This complete slot half section is then mirrored around point P_5 to complete one stator slot. The complete set of optimisation variables for the stator slot are described by

$$X_S = \begin{bmatrix} R_{GAP} & R_{SSI} & R_{P_3} & R_{P_4} & R_{SSO} & \alpha_{34} & R_{\%23} & \theta_{\%22} \end{bmatrix}^T \tag{4.2.2}$$

with the complete set of optimisation variables per barrier number B then represented by

$$X_B = \begin{bmatrix} \alpha_{LR} \\ \beta_{LR} \\ R \\ P_{1sp} \\ P_{3sp} \\ P_{5sp} \\ \theta \\ R_{GAP} \\ R_{SSI} \\ R_{P_3} \\ R_{P_4} \\ R_{SSO} \\ \alpha_{34} \\ R_{\%23} \\ \theta_{\%22} \end{bmatrix} = \begin{bmatrix} \alpha_{(1)} & \cdots & \cdots & \cdots & \cdots & \alpha_{(2*B)} \\ \beta_{(1)} & \cdots & \cdots & \cdots & \cdots & \beta_{(2*B)} \\ R_{(1)} & \cdots & R_{(B)} & & & \\ P_{1sp(1)} & \cdots & P_{1sp(B)} & & & \\ P_{3sp(1)} & \cdots & P_{3sp(B)} & & & \\ & & & P_{5sp(1)} & \cdots & P_{5sp(B)} \\ \theta & & & & & \\ R_{GAP} & & & & & \\ R_{SSI} & & & & & \\ R_{P_3} & & & & & \\ R_{P_4} & & & & & \\ R_{SSO} & & & & & \\ \alpha_{34} & & & & & \\ R_{\%23} & & & & & \\ \theta_{\%22} & & & & & \end{bmatrix}. \tag{4.2.3}$$

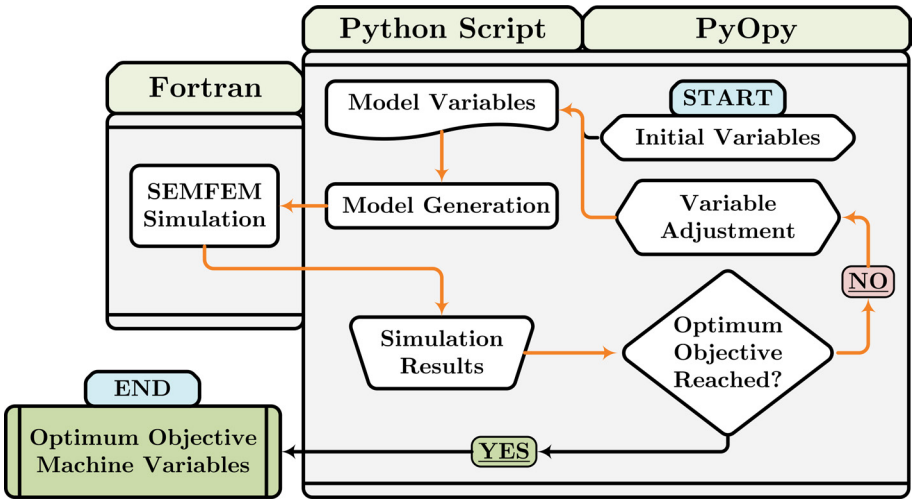

Figure 4.4: Optimisation flow diagram implementing PyOpt as optimisation package [104, 105].

4.3 Optimiser Study

The optimisation suite selected for the optimisation study is PyOpt [106], an open-source *Python* script based optimisation package. This change in optimisation package suite from the previously implemented VisualDoc package is motivated by:

1. PyOpt's *Python* script based interface, which can easily be incorporated into the existing *Python* script developed in Chapter 3.

2. The open-source benefits PyOpt adds to the optimisation procedure due to the lack of optimisation suit licence requirements. This fact greatly accelerates the optimisation study by allowing the author to run simultaneous optimisation studies on numerous work stations.

3. Due to the script based interface of PyOpt, elaborate optimisation strategies can be automated, which in turn allows the author to increase optimisation throughput and accelerate complicated optimisation procedures due to the lack of a human interaction requirement.

The updated optimisation flow diagram is show in Figure 4.4. This flow diagram closely resembles the previously implemented optimisation flow diagram in Figure 3.11, with the exception of the optimisation package suit that has been replaced by PyOpt.

One drawback of the optimisation suit change is that the optimisation algorithms implemented in Chapter 3 are no longer available.

Optimiser Selection

In order to select the new algorithms for the optimisation strategy, five gradient based algorithm available in PyOpt are selected for evaluation, with the addition of

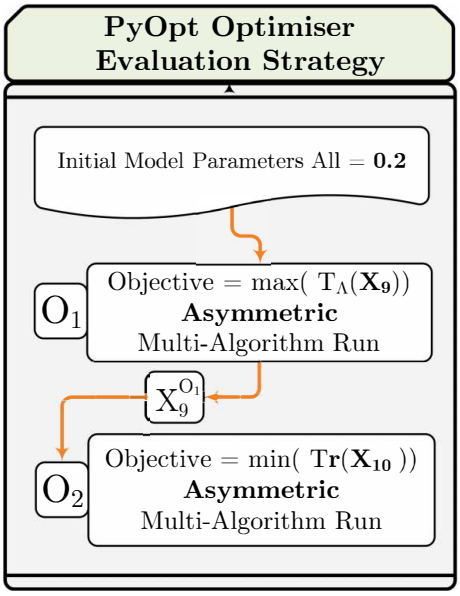

Figure 4.5: Optimisation strategy to evaluate the available optimisers in PyOpt [104, 105].

one non-gradient based algorithm for comparison. The algorithms selected consist of the following:

1. **SLSQP** - Sequential least squares programming algorithm that implements the Han-Powell quasi-Newton method with the solver implementing a slight modification of Lawson and Hanson's NNLS nonlinear least-squares solver [106].

2. **CONMIN** - Method of feasible directions optimiser that solves a nonlinear programming problem by moving from one feasible point to an improved one by choosing an improved feasible direction at each iteration [106].

3. **SOLVOPT** - This optimiser imlements a penalisation method to handle constraints and implements a modified version of Shor's r-algorithm with space dilation to find a local minimum [106].

4. **KSOPT** - This optimiser reformulates the constrained problem into an unconstrained one using a composite Kreisselmeier-Steinhauser objective function. The optimiser implements the Davidon-Fletcher-Powell (DFP) algorithm to solve the optimisation problem [106].

5. **FILTERSD** - This algorithm implements a generalization of Robinson's method. The code makes use of a Ritz values approach Linear Constraint Problem solver [106].

6. **SDPEN** - This optimiser is a derivative-free algorithm that implements a sequence of approximate minimisations of a merit function, where constraint violation is progressively, and increasingly penalised. A combination of penalty

Table 4.2: PyOpt optimiser study machine model [104, 105].

	$\boldsymbol{p}$	$\boldsymbol{S_p}$	$\boldsymbol{B_r}$	$\boldsymbol{RO_I}$ [mm]	$\boldsymbol{ST_O}$ [mm]	$\boldsymbol{L_S}$ [mm]	$\boldsymbol{h}$ [mm]	$\boldsymbol{J}$ [A/mm^2]
Model	4	6	4	12.5	65	122	0.5	6.4

$\boldsymbol{p}$ - Number of Poles ; $\boldsymbol{S_P}$ - Stator Slots per Pole ; $\boldsymbol{B_r}$ - Number of Flux Barriers ; $\boldsymbol{RI_I}$ - Rotor Inside Diameter ; $\boldsymbol{ST_O}$ - Stator Outside Diameter ; $\boldsymbol{L_S}$ - Stack Length ; $\boldsymbol{h}$ - Air Gap Hight ; $\boldsymbol{J}$ - Current Density

Table 4.3: Full asymmetric optimisation variables [104, 105].

Optimisation Variables															
	α	β	R	P_{1sp}	P_{3sp}	P_{5sp}	θ	R_{GAP}	R_{SSI}	R_{P_3}	R_{P_4}	R_{SSO}	α_{34}	$R_{\%23}$	$\theta_{\%22}$
X_9	√	√	√	√	√	√	√	√	√	√	√	√	√	√	√
X_{10}	√														

parameter updating and different sampling strategies is implemented in a line search based method to converge to a stationary optimum point [106].

The same optimisation strategy proven to be effective in Section 3.4 is once again implemented in the complete machine optimisation strategy. In order to effectively implement this strategy, two new algorithms need to be selected for the respective optimisation steps in the strategy, i.e. the maximisation of T_A and the subsequent minimisation of T_R.

In order to select the optimiser for each respective step, the algorithm evaluation consisted of the optimisation of each step by implementing various the optimisers for comparison. The first step of the optimisation study consists of

$$\begin{aligned} \text{The maximisation of :} \quad & T_A(X_9) \\ \text{Subject to :} \quad & 0 \leqslant G_j(X_9) \leqslant 1 \quad ; \quad j = 1, 2, ..., n \end{aligned}$$

with variables

$$X_9 = \big[\alpha_{(1-8)} \quad \beta_{(1-8)} \quad R_{(1-4)} \quad P_{1sp(1-4)} \quad P_{3sp(1-4)} \quad P_{5sp(1-4)} \quad \theta \quad . \quad . \quad . \quad . \quad R_{GAP} \quad R_{SSI} \quad R_{P_3} \quad R_{P_4} \quad R_{SSO} \quad \alpha_{34} \quad R_{\%23} \quad \theta_{\%22}\big]^T \tag{4.3.1}$$

and with all optimisers implementing identical start values. The second optimisation step is

$$\begin{aligned} \text{The minimisation of :} \quad & T_R(X_{10}) \\ \text{Subject to :} \quad & 0 \leqslant G_j(X_{10}) \leqslant 1 \quad ; \quad j = 1, 2, ..., n \end{aligned}$$

with the minimisation variables

$$X_{10} = \big[\alpha\big] = \big[\alpha_{(1)} \quad . \quad . \quad . \quad . \quad . \quad . \quad \alpha_{(8)}\big] \tag{4.3.2}$$

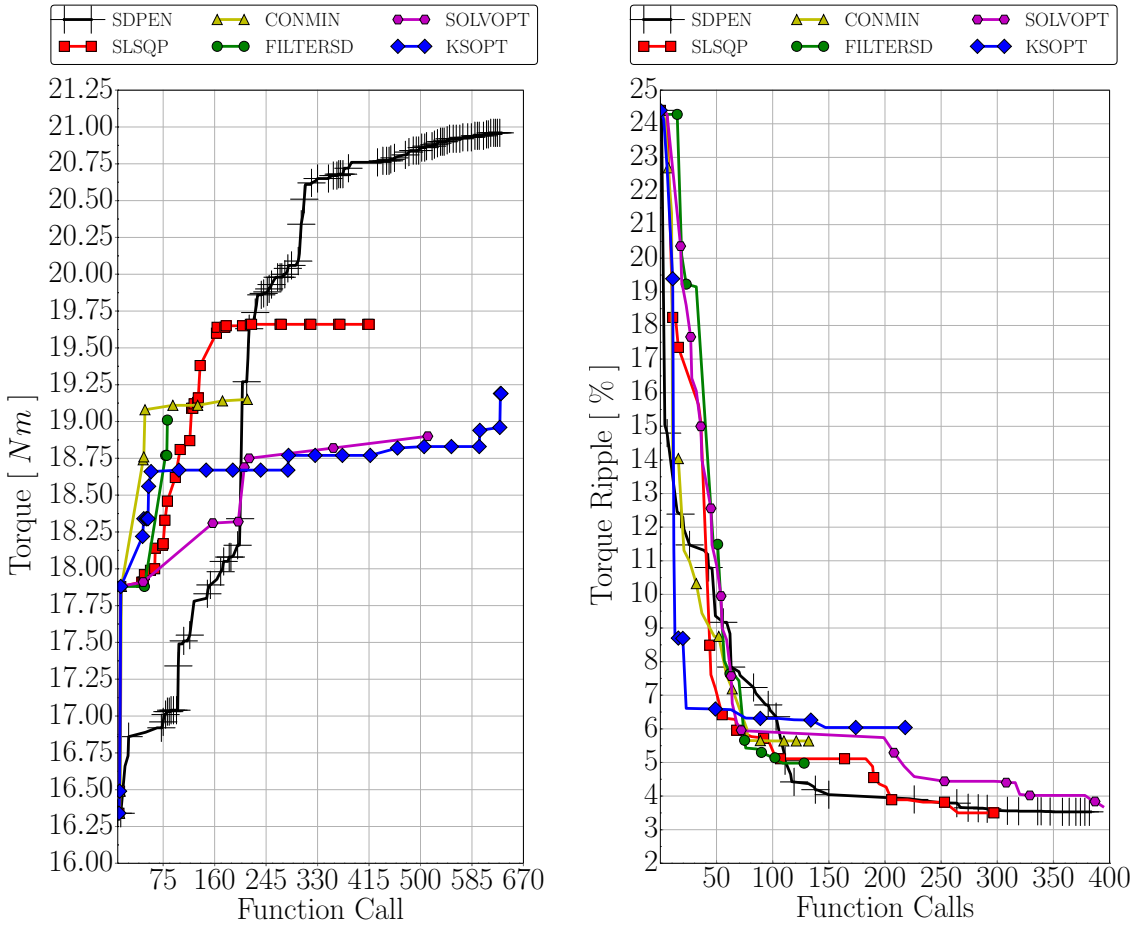

(a): Optimisation study to compare possible available algorithms for objective function $T_A(X)$.

(b): Optimisation study to compare possible available algorithms for objective function $T_R(X)$.

Figure 4.6: Optimisation with available algorithms considered consisting of SLSQP, CONMIN, SOLVOPT, KSOPT, FILTERSD and SDPEN [104–106].

and with all the optimisers implementing the best converged variable values of the former step as initial values. The variables implemented for the two studies are shown in Table 4.3, with the optimisation study flow diagram shown in Figure 4.5.

The model parameters implemented in the study is listed in Table 4.4. The main model volume dimensions were determined from existing machine frame sizes, with a 90 and 132 frame size taken as the machine models. For the optimiser study and selection, the frame size 90 dimensions are implemented.

The variables constraints implemented in the study are identical to the constraints implemented in Section 3.4,

$$0 \leqslant G_j(X_m) \leqslant 1 \quad ; \quad j = 1, 2, ..., n \tag{4.3.3}$$

with an identical barrier variable set implemented with omission of variable χ. This variable was found to be constantly maximised by the optimiser in the previous

Table 4.4: Specifications and some rated data of the RSMs studied.

Frame Size	P	S_p	B_r	RO_I $[mm]$	ST_O $[mm]$	L_S $[mm]$	h $[mm]$	n $[r/min]$
90	4	6	$1 \Rightarrow 6$	12.5	65	122	0.3	1500
132	4	9	$1 \Rightarrow 5$	41.0	105	110	0.35	1500
132	6	6	$1 \Rightarrow 6$	41.0	105	110	0.35	1000
132	8	6	$1 \Rightarrow 6$	41.0	105	110	0.35	450

$\boldsymbol{P}$ - Number of poles ; $\boldsymbol{S_P}$ - Stator slots per pole ; $\boldsymbol{B_r}$ - Number of flux barriers ; $\boldsymbol{RO_I}$ - Rotor inside radius ; $\boldsymbol{ST_O}$ - Stator outside radius ; $\boldsymbol{L_S}$ - Stack length ; $\boldsymbol{h}$ - Air gap length ; $\boldsymbol{J}$ - Current density = 6.4 $\boldsymbol{A/mm^2}$

study.

The results of this initial optimization study, with all six algorithms starting with identical initial variables is presented in Figure 4.6. With the interpretation of the convergence results, two important factors need to be defined:

1. It should be noted that for each gradient based algorithm, a relative gradient step size is chosen to produce the most accurate convergence point. This gradient step size for each algorithm is determined from iterative identical optimisations implementing the specific optimiser with a variation in step size.

2. The author is aware of the possibility that these specific gradient base algorithms could be "fine-tuned" to achieve a more accurate optimum point for a specific optimisation problem set. This "fine-tune" process will however prove extremely time expensive when considering the large spectrum and variation of optimisation problems that needs solving. Taking this fact into account, the algorithm selection criteria is based on robustness, optimum solution point repeatability and a low function call number.

From Figure 4.6a, the SDPEN algorithm clearly outperforms the gradient based algorithms, with a much higher optimum objective reached in roughly 600 function calls. This algorithm is thus selected for step one in the optimisation strategy.

The results of the second algorithm study is illustrated in Figure 4.6b. This figure illustrates a more competitive performance of the algorithms, explained by the large reduction of optimisation variables compared to the previous study. From these results, two algorithms, SLSQP and SDPEN show clear performance advantages above the rest, with an optimum convergence point achieved in the least amount of function calls.

After a comparison of these two algorithms, SLSQP is selected for the second minimisation step in the optimisation strategy. This as a result of the low or no variation in T_A achieved during T_R minimisation, compared to the much larger variation of T_A with the implementation of SDPEN. A possible explanation for this is as a result of the type of optimiser, with the gradient based optimiser having the ability to search very accurately in the local maximised T_A area. SDPEN on the

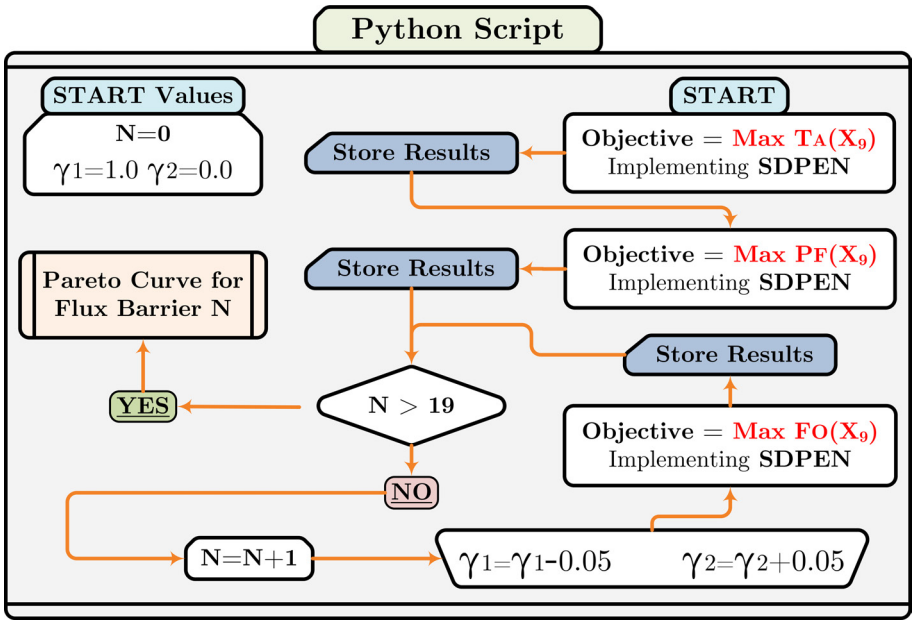

Figure 4.7: Pareto curve optimisation flow diagram [104, 105].

other hand implements a slightly less sensitive sequence of approximate minimisations. This algorithm is however implemented as a backup optimiser on certain optimisation strategies where a large number of variables are encountered.

4.3.1 Machine Optimisation Study

After optimiser selection, the multi-objective optimisation study is conducted. The study implemented a combination of flux barrier number and pole number combinations, with the summarised machine models implemented presented in Table 5.15. During the optimisation process, the machine volume was constrained, with the dimensions of this volumes obtained from standard machine frame size dimensions.

The optimisation flow diagram implemented, that includes the weighted optimisation method illustrated in Figure 4.1 and Equation 4.1.1, is shown in Figure 4.7. In order to effectively implement Equation 4.1.1, each objective had to be scaled to a per unit value, with the updated equation:

$$F_O(\gamma_1, \gamma_2, X_{9-B}) = \gamma_1\left(\frac{T_A(X_{9-B})}{T_A(X_{9-B})_{max}}\right) + \gamma_2\left(\frac{P_F(X_{9-B})}{P_F(X_{9-B})_{max}}\right), \tag{4.3.4}$$

where $T_A(X_{9-B})_{max}$ and $P_F(X_{9-B})_{max}$ are determined, respectively, by maximising the objective functions

$$F_O(1, 0, X_{9-B}) = (1)T_A(X_{9-B}) + (0)P_F(X_{9-B}) \tag{4.3.5}$$

and

$$F_O(0, 1, X_{9-B}) = (0)T_A(X_{9-B}) + (1)P_F(X_{9-B}), \tag{4.3.6}$$

with the addition of the variable B indicating the specific barrier number variable set implemented.

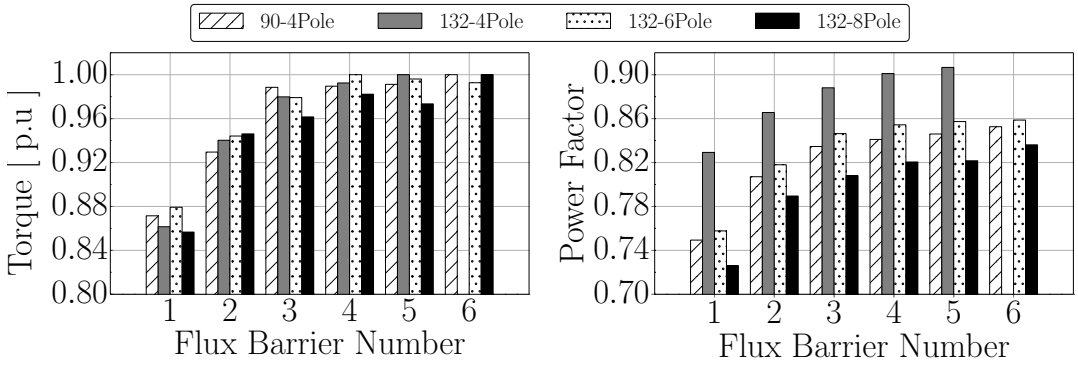

Figure 4.8: Maximised T_A and P_F for the initial step of the weighted optimisation flow diagram in Figure 4.7 [104, 105].

The weighted pareto front optimisation is then completed by shifting the respective weight from the one objective to the other in nineteen iteration steps. The study was repeated for rotor topologies implementing a varying number of flux barriers, with machine pole number four, six and eight implemented as indicated in Table 5.15.

Optimisation time for the various machines studied varied between 3.6 to 22 hour for the 90 and 132 frame size machines respectively. The combined total optimisation time, that includes 19 machines per pareto front, combined to a total optimisation time of 296 days.

The initial objective maximisation results of Equations 4.3.5 and 4.3.6 are presented in the bar charts in Figure 4.8. An observation with respect to barrier number can be made from this figure, with the maximised T_A and P_F converging at around the four flux barrier mark. It illustrates that four flux barriers are the optimum number when taking into consideration the large increase of optimisation variables compared to the small increase in objective function performance obtained. This observation seems to be consistent through the pole number range investigated.

The results of the weighted optimisation study are illustrated in Figure 4.9. In these figures, the pareto front for each flux barrier number, pole number combination, along with the objective function results, are shown. Interestingly, clearly noted form the objective function curve, it appears that the weighted objective results are flux barrier number independent. This observation is evident, with a clear contour curve representing the results for the weighted-optimisation objective for a fixed pole number and flux barrier number variation.

This flux-barrier-number independent objective curve led to an investigation to determine a possible optimum weighted factor ratio between T_A and P_F that can be selected by a designer if an optimum relationship is desired. In order to determine this possible relationship, the results of each machine topology and flux barrier number combination is normalised by implementing equations

$$T_A(X_{9-B})^R = \frac{T_A^N(X_{9-B}) - (T_A(X_{9-B}))_{min}}{(T_A(X_{9-B}))_{max} - (T_A(X_{9-B}))_{min}} \tag{4.3.7}$$

and

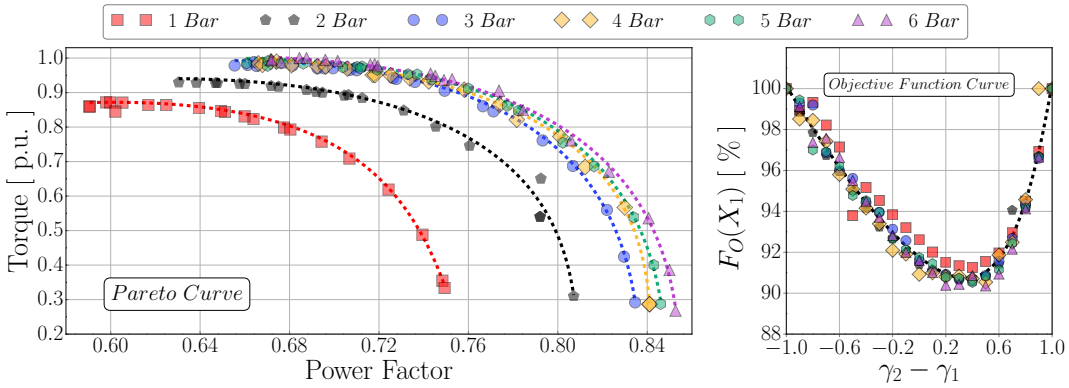

(a): 90 Frame, four pole machine.

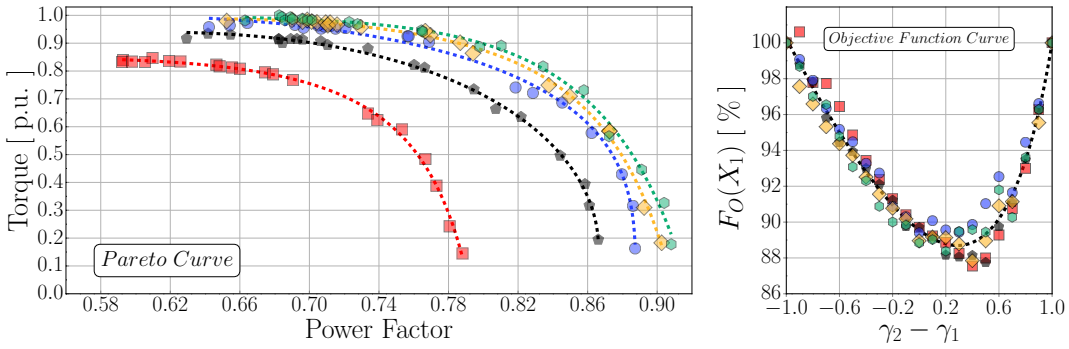

(b): 132 Frame, four pole machine.

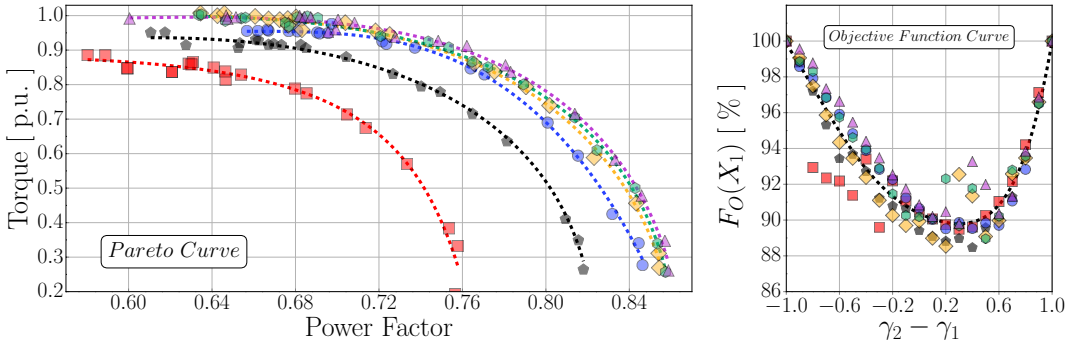

(c): 132 Frame, six-pole machine.

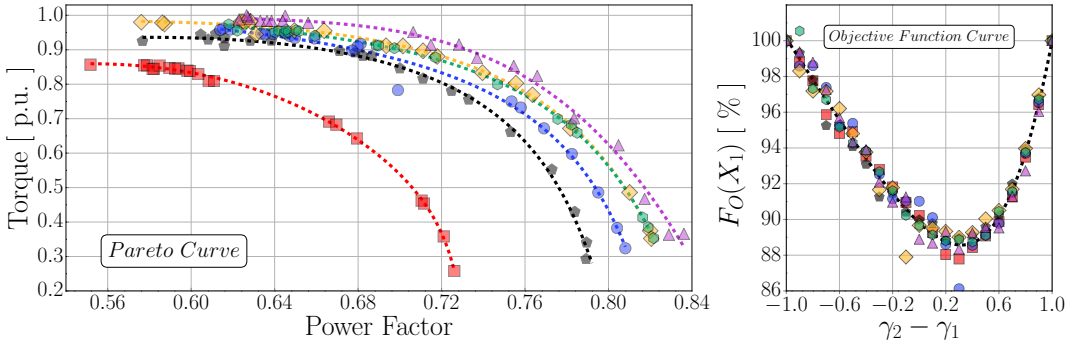

(d): 132 Frame, eight-pole machine.

Figure 4.9: Multi-objective, weighted factor pareto curve and objective function curve optimisation results [104, 105].

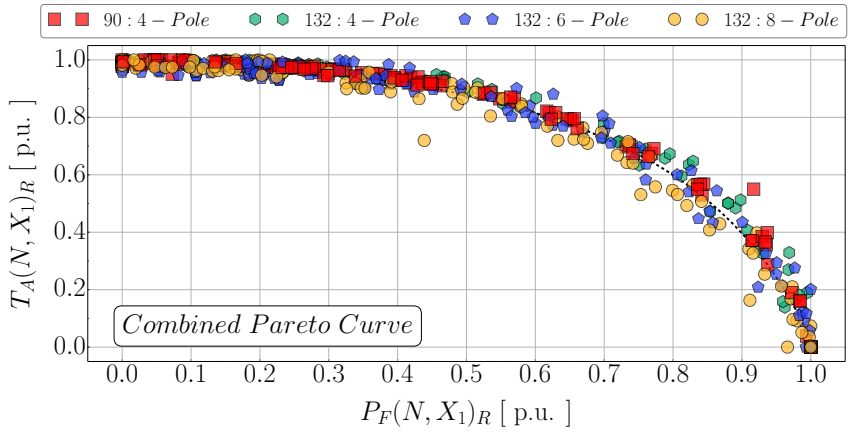

Figure 4.10: Scaled weighted factor optimisation results, illustrating the results of the RSMs implemented in Table 4.4 [104, 105].

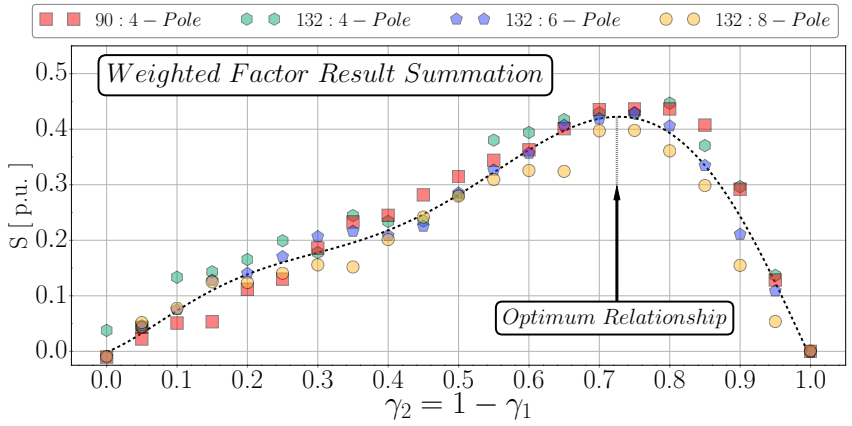

Figure 4.11: Summation results illustrating the P_F and T_A relationship [104, 105].

$$P_F(X_{9-B})^R = \frac{P_F^N(X_{9-B}) - (P_F(X_{9-B}))_{min}}{(P_F(X_{9-B}))_{max} - (P_F(X_{9-B}))_{min}} \tag{4.3.8}$$

with N the weighted factor step point represented in Figure 4.7 and R the calculated 'ratio' for each step N. The values $(T_A(X_{9-B}))_{min}$ and $(P_F(X_{9-B}))_{min}$ is read from the respective opposing objectives maximised results i.e, $(T_A(X_{9-B}))_{min}$ is equal to the T_A value at the maximised P_F point and likewise, $(P_F(X_{9-B}))_{min}$ is equal to the P_F value at the maximised T_A point. The results of these calculations are shown in Figure 4.10, with the normalised relationship pareto front for all the respective machines topologies and respective barrier numbers combinations plotted.

In order to determine a possible optimum relationship between the two objectives, equation

$$S(X_W) = \frac{\sum_1^B T_A(N, X_{9-B})^R}{B_n} + \frac{\sum_1^B P_F(N, X_{9-B})^R}{B_n} - 1 \tag{4.3.9}$$

is implemented, with B_n the number of barrier number combinations optimised per machine setup and with the '-1.0' value implemented to zero the relationship

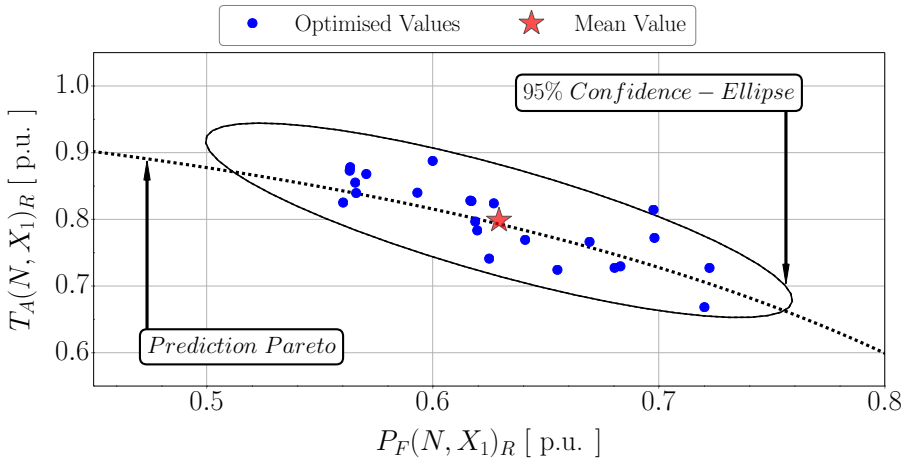

Figure 4.12: Scaled weighted factor optimisation results, illustrating the results of the RSMs implemented in Table 5.15.

at the $T_A(X_{9-B})_{max}$ or $P_F(X_{9-B})_{max}$ point. Observing the plotted curve in Figure 4.11, it is clear that there is an optimum relationship between P_F and T_A, with the respective weights at this point $\lambda_1 = \pm 25 \Rightarrow 30\%$ and $\lambda_2 = \pm 75 \Rightarrow 70\%$. This weighted factor optimum point illustrates that an optimum relationship, independent of flux barrier number, pole number and power range exists between P_F and T_A [103].

Additionally, an important observation can be made from the normalised pareto front curve plotted: from the curve it is evident that a flux barrier, pole number and power level independent relationship exists that describes the relationship between P_F and T_A. This relationship is described by the fitted curve equation

$$y = \frac{a}{\sqrt{b^2 - x^2}} + c \tag{4.3.10}$$

with $a = -1.26087$; $b = 1.17596$; $c = 2.06220$.

This relationship forms an important part in the weighted factor optimisation because it allows the designer to predict optimisation results prior to machine optimisation pareto front mapping. This thus reduces design time by allowing the designer to select a weighted factor point applicable to a specific application.

In order to increase the accuracy of the prediction curve Equation 4.3.10, confidence levels and mean estimate values for each weighted factor is determined from the plotted results (ellipse calculation in Appendix B.3). The mean estimate values, x_{mean} and y_{mean}, and the x-axis level confidence x_{low} and x_{high} is determined by implementing the confidence ellipse as presented in Figure 4.12, with the example implementing the objective weights $\gamma_1 = 0.3$ and $\gamma_1 = 0.7$. The complete set of calculated mean estimate points along with the confidence intervals can be found in Table 4.5.

Table 4.5: Weighted factor mean estimate and 95% confidence interval for objective functions $T_A(X_1)$ and $P_F(X_1)$ [104, 105].

Objective Weights		**Mean Estimate**♠		95% **Confidence**♠	
P_F	T_A	P_F	T_A	P_F	P_F
γ_2	γ_1	x_{mean}	y_{mean}	x_{low}	x_{high}
0.0	1.00	0.00000	1.00000	0.00000	0.00000
0.05	0.95	0.04034	1.00306	0.00000	0.11015
0.10	0.90	0.08796	0.99430	0.00000	0.22598
0.15	0.85	0.11712	0.99202	0.00000	0.32116
0.20	0.80	0.14110	0.99191	0.00000	0.28819
0.25	0.75	0.16569	0.98993	0.00000	0.30960
0.30	0.70	0.18946	0.99193	0.00000	0.28700
0.35	0.65	0.22863	0.98015	0.06402	0.40772
0.40	0.60	0.24385	0.97708	0.05051	0.35162
0.45	0.55	0.28125	0.96744	0.09683	0.38539
0.50	0.50	0.33501	0.95714	0.14551	0.88607
0.55	0.45	0.40894	0.93277	0.26461	0.48832
0.60	0.40	0.44828	0.91253	0.26024	0.58189
0.65	0.35	0.52184	0.86932	0.34583	0.66851
0.70	0.30	0.62934	0.79853	0.51163	0.75531
0.75	0.25	0.69336	0.73750	0.58843	0.80128
0.80	0.20	0.77700	0.64090	0.70459	0.83891
0.85	0.15	0.86359	0.49053	0.79137	0.91992
0.90	0.10	0.93959	0.29720	0.88075	0.98673
0.95	0.05	0.98208	0.12585	0.93615	1.00000
1.00	0.00	1.00000	0.00000	1.00000	1.00000

♠ - Equation 4.3.10 mean estimate variables and confidence ; $\boldsymbol{P_F}$ - Power factor ; $\boldsymbol{T_A}$ - Average torque ; $\boldsymbol{x_{mean}}$ - x axis mean estimate $\boldsymbol{y_{mean}}$ - y axis mean estimate ; $\boldsymbol{\gamma_1}$ - average torque weight ; $\boldsymbol{\gamma_2}$ - power factor weight

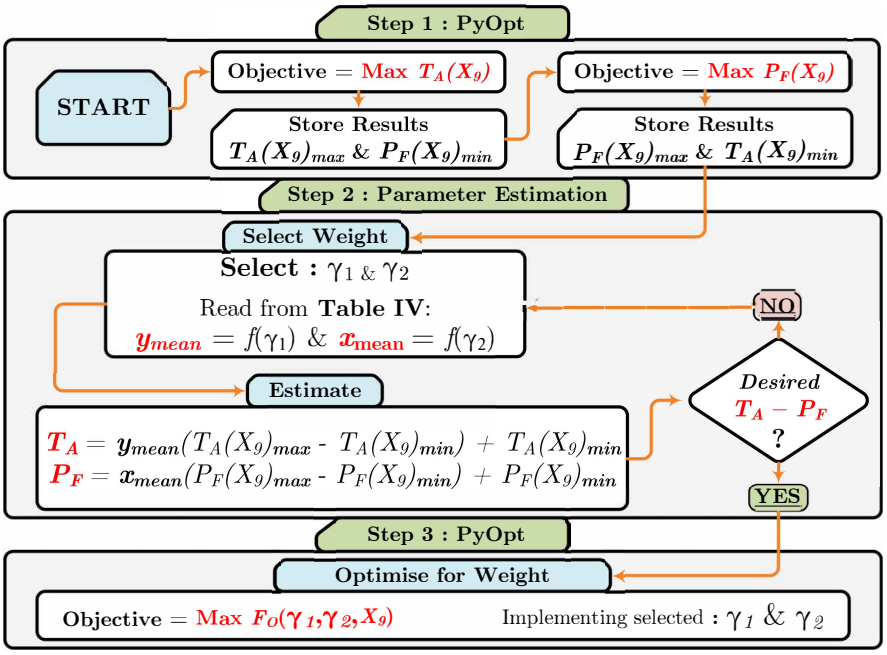

Figure 4.13: Weighted factor T_A and P_F estimation step flow diagram [104, 105].

4.3.2 Pareto Curve Prediction

In order to investigate the accuracy of the prediction pareto, machines are estimated and optimised for verification. The estimation process for predicting machine performance is presented in the flow diagram of Figure 4.13. The estimation process consists of 3 main steps:

1. The initial independent maximisation to determine $T_A(X_{9-B_r})_{max}$ and $P_F(X_{9-B_r})_{max}$ by implementing objective functions Equations 4.3.5 and 4.3.6. $T_A(X_{9-B_r})_{min}$ and $P_F(X_{9-B_r})_{min}$ is read from the opposing maximised variable results, i.e. $T_A(X_{9-B_r})_{min}$ equals the T_A value from the results of $P_F(X_{9-B_r})_{max}$ and $P_F(X_{9-B_r})_{min}$ equals the P_F results from $T_A(X_{9-B_r})_{max}$.

2. The iterative numeric estimation of T_A and P_F by rewriting Equations 4.3.7 and 4.3.8 to

$$T_A = y_{mean}(T_A(X_{9-B_r})_{max} - T_A(X_{9-B_r})_{min}) + T_A(X_{9-B_r})_{min} \tag{4.3.11}$$

and

$$P_F = x_{mean}(P_F(X_{9-B_r})_{max} - P_F(X_{9-B_r})_{min}) + P_F(X_{9-B_r})_{min} \tag{4.3.12}$$

with

$$x_{mean} = f(\gamma_2) \tag{4.3.13}$$

$$y_{mean} = f_(\gamma_1) \tag{4.3.14}$$

read from Table 4.5.

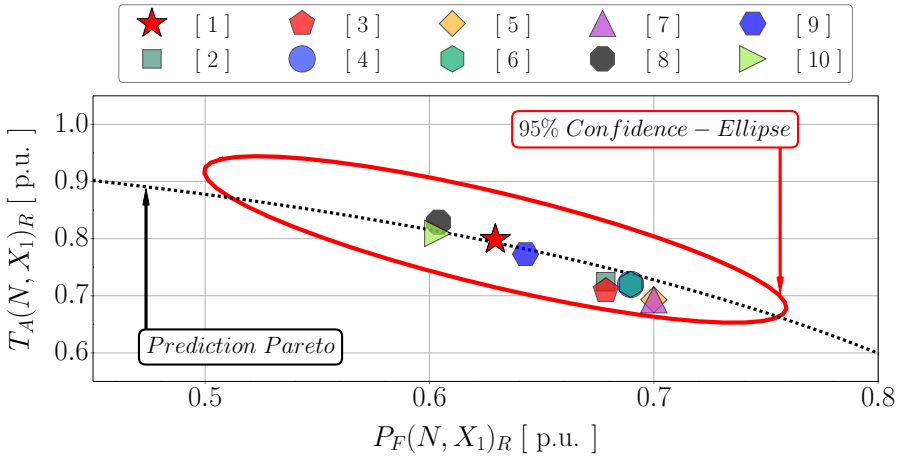

Figure 4.14: Optimised machine comparison to estimated weighted factor result, with 95% confidence ellipse (Machine specifications [1-10] shown in Table 4.6) [104, 105].

3. If the desired T_A and/or P_F value is reached, the correlating weighted factors are used in the objective function Equation 4.3.4 to optimise the design of the machine.

This optimisation prediction is subject to the following optimisation machine model constraints:

1. $RO_O \leqslant \frac{3}{4} ST_O$
2. $\theta_{P_3} \leqslant \theta_{P_1}$
3. RO_I is fixed
4. No centre flux barrier web support,

with RO_O, ST_O, and RO_I illustrated in Fig. 3.10 and 4.15, and with θ_{P_1} and θ_{P_3} presented in Fig. 4.2 and Table 4.1.

In order to verify whether this method can also apply to models implementing symmetric rotors, induction machine stator retrofit rotors and in high power level machines, the optimisation method is applied to the listed model cases in Table 4.6. These cases consist of :

1. a stator and rotor designed eight-pole, four asymmetric flux barriers RSM in the 5Mw power range, with 3 winding layouts and with dimensions determined as in Appendix A.1.
2. a stator and rotor designed ten-pole, four asymmetric flux barriers RSM in the 5Mw power range, with 3 winding layouts and with dimensions determined as in Appendix A.1.
3. a stator and rotor designed four-pole, six symmetric flux barrier RSM implementing the 90 frame size machine dimensions in Table 5.15

Table 4.6: Optimised machines, implementing weighted factor $30\%T_A$ - $70\%P_F$ results: estimated and optimised [104, 105].

				Estimated		Optimised			
N	P	B_r	M_W	T_A	P_F	T_A		P_F	
				[Nm]	[ ]	[Nm]	[p.u]	[ ]	[p.u]
[1]♠	Theoretical True Estimated $\boldsymbol{\lambda_1 = 30\%}$ and $\boldsymbol{\lambda_2 = 70\%}$								
Asymmetric Rotor ($h = 2.5\ mm$; $J = 4.0\ A/mm^2$)									
[2]♠	8	4	9-9	116.1k	0.726	108.7k	0.936	0.743	1.023
[3]♠	8	4	8-9	117.5k	0.723	110.0k	0.936	0.742	1.026
[4]♠	8	4	7-9	117.5k	0.723	105.2k	0.895	0.747	1.033
[5]♠	10	4	9-9	117.6k	0.726	108.9k	0.926	0.739	1.018
[6]♠	10	4	8-9	118.1k	0.729	107.1k	0.907	0.745	1.022
[7]♠	10	4	7-9	117.6k	0.729	105.1k	0.894	0.745	1.022
Symmetric Rotor ($h = 0.3\ mm$; $J = 6.4\ A/mm^2$)									
[8]♠	4	6	6-6	17.65	0.781	18.29	1.036	0.776	0.994
[9]♠	6	5	6-6	18.61	0.726	18.31	0.984	0.729	1.004
IM Retrofit ($h = 0.3\ mm$; $J = 6.4\ A/mm^2$)									
[10]♠	4	4	6-6	10.17	0.785	10.23	1.006	0.783	0.998

♠ - Plotted estimate versus optimised results in Fig. 4.14 ; $\boldsymbol{N}$ - Machine Number in Fig. 4.14 ; $\boldsymbol{B_r}$ - Flux Barrier Number ; $\boldsymbol{P}$ - Number of Poles ; $\boldsymbol{h}$ - Air gap length ; $\boldsymbol{J}$ - Current Density ; $\boldsymbol{M_W}$ - Machine Winding

4. a stator and rotor designed six-pole, five symmetric flux barrier RSM implementing the 90 frame size machine dimensions in Table 5.15

5. a retro-fit rotor four-pole, four asymmetric flux barrier RSM implementing a 90 frame size induction machine stator with dimensions in Table 5.15

The results of this optimisation study are presented in Table 4.6 and Figure 4.14. As seen in the figure and table, the results for the small machines fall well within the confidence ellipse with the largest deviation in P_F prediction equal to 0.6% and the largest deviation in T_A prediction equal to 3.6% compare to the actual optimised values. There is however a large deviation in the high power, 5Mw machines estimated and optimised. This deviation still however falls within the 95% confidence range, with the larger deviation attributed to the increase of the air-gap height to a more realistic 2.5mm, compared to the 0.3 mm for the small machines, and an increase in the flux barrier web width from 0.5mm to 2.5mm.

These results illustrate that the weighted factor optimisation technique can be implemented, not only for the full machine optimisation implementing asymmetric rotors but also:

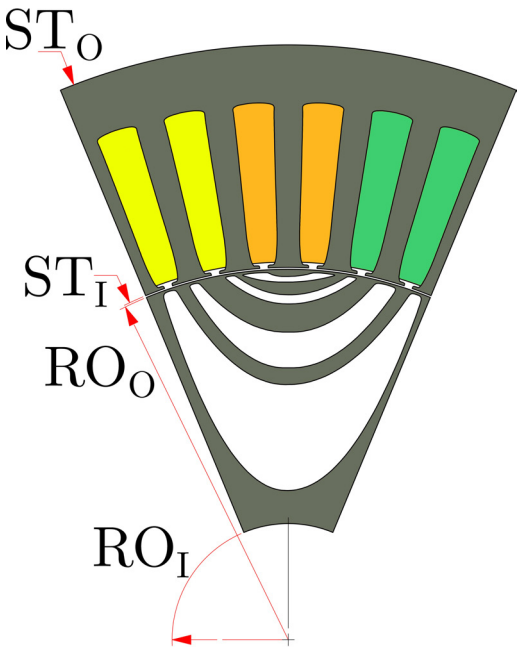

Figure 4.15: Pareto curve selected eight-pole, 48 Slot RSM with RO_O=20.5 mm, RO_I=65.39 mm, RT_O=105 mm, and stack length 0.11 m, with air-gap length 0.35 mm.

- for RSM optimisation implementing symmetric rotors
- for RSM optimisation in the very high 5Mw power range and
- for RSM optimisation implementing an induction machine stator with RSM retrofit rotor.

In order to validate the optimisation results, a machine is selected in the next section for manufacture and testing.

4.4 Motor Design Selection & Manufacture

In order to validate the multi-objective optimisation and investigate the implementation of a RSM in the medium speed range, an eight-pole, four flux barrier RSM is selected from the optimised pareto front.

The selection of this specific topology is motivated by:

1. The investigation into the medium speed range, with the eight-pole machine running at 33.3Hz for rated operating speed of 500rpm.
2. A cost saving with respect to lamination manufacture, with the increase to five flux barriers having no significant effect, clear from Figure 4.9d, and the increase to six flux barrier proving to cost intensive for the limited gain in performance.

Table 4.7: Symmetric–asymmetric optimisation comparison strategy results of the 24 stator slot machines.

45% T_A : 55% P_F Optimisation Results									
Objective	**$T_R(X_9)$**			**$T_R(X_{10})$: 62°**			**$T_R(X_{10})$: 70°**		
Function	$T_A^{\blacktriangle}$	$T_R^{\blacktriangledown}$	$P_F^{\blacktriangle}$	$T_A^{\blacktriangle}$	$T_R^{\blacktriangledown}$	$P_F^{\blacktriangle}$	$T_A^{\blacktriangle}$	$T_R^{\blacktriangledown}$	$P_F^{\blacktriangle}$
θ	**62°**	**68°**	**70°**	**62°**	**63°**	**70°**	**64°**	**70°**	**71°**
T_A [Nm]	82.5	80.0	77.4	81.8	81.6	76.0	82.4	79.8	78.5
T_A [p.u]	**1.0**	0.97	0.94	0.99	0.99	0.92	1.0	0.97	0.95
T_R [%]	12.3	10.5	10.6	5.8	5.1	9.2	8.0	5.1	5.2
T_R [p.u]	1.17	**1.0**	1.01	0.55	0.49	0.88	0.76	0.49	0.50
P_F [ ]	0.69	0.72	0.72	0.68	0.69	0.71	0.69	0.72	0.72
P_F [p.u]	0.96	1.0	**1.0**	0.94	0.96	0.99	0.96	1.0	1.0

▲ - Maximum Point; ▼ - Minimum Point ; T_A - Average Torque ; T_R - Torque Ripple ; P_F - Power Factor

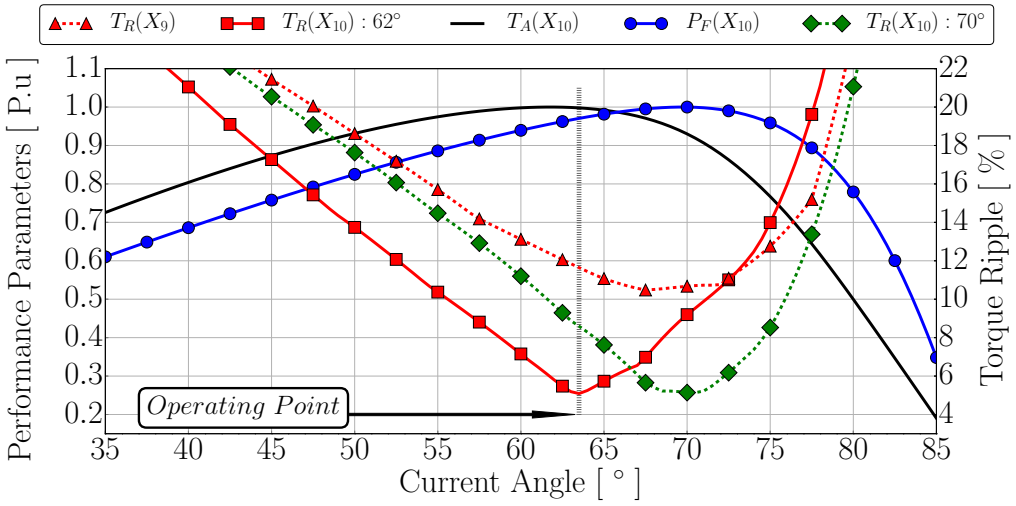

Figure 4.16: Selected machine performance parameters average torque, torque ripple, and power factor versus current angle map.

The weighted ratio selected for the manufactured machine is slightly more shifted towards the T_A objective, with the weighted factors $\lambda_1 = 45\%$ and $\lambda_2 = 55\%$ selected. This selection is motivated by a desire for a higher T_A value at rated conditions. The specific machine selection is simplified by the additional advantage of the studies multiple optimised machines library.

The eight-pole, four flux barrier RSM selected for the simulation data validation is presented in Figure 4.15. In order to reduce the T_R of the selected machine to acceptable levels, the second step of the asymmetric optimisation technique in the study conducted in Chapter 3 is implemented, with the simplified steps illustrated in Figure 4.5 (Step O_2). This step includes the minimisation of the T_R by only implementing the asymmetric flux barrier tip angles. The initial machine and T_R

Table 4.8: Stress and deformation analysis and comparison between structural analysis done in JMag and Algor Multiphysics on the selected eight-pole RSM machine optimized

Stress & Deformation Analysis								
			JMag			***Algor***		
Speed	**Temp♣**	**E-M♠**	**Mises ℜ**	**SF**	**Def ***	**Mises ℜ**	**SF**	**Def ***
[*P.u*]	[C°]		$[MPa]$		$[\mu m]$	$[MPa]$		$[\mu m]$
6	20	NA	93.9	3.19	8.56	102.9	2.92	8.82
6	20	√	135.0	2.22	13.9	NA	NA	NA
6	150	NA	93.9	3.19	108.9	102.9	2.92	109.2
6	150	√	135.0	2.22	114.6	NA	NA	NA

♣ - Lamination Temperature ; ♠ - Electromagnetic Forces ; ℜ - Von Mises Peak Stress ; * - Maximum Point Deformation

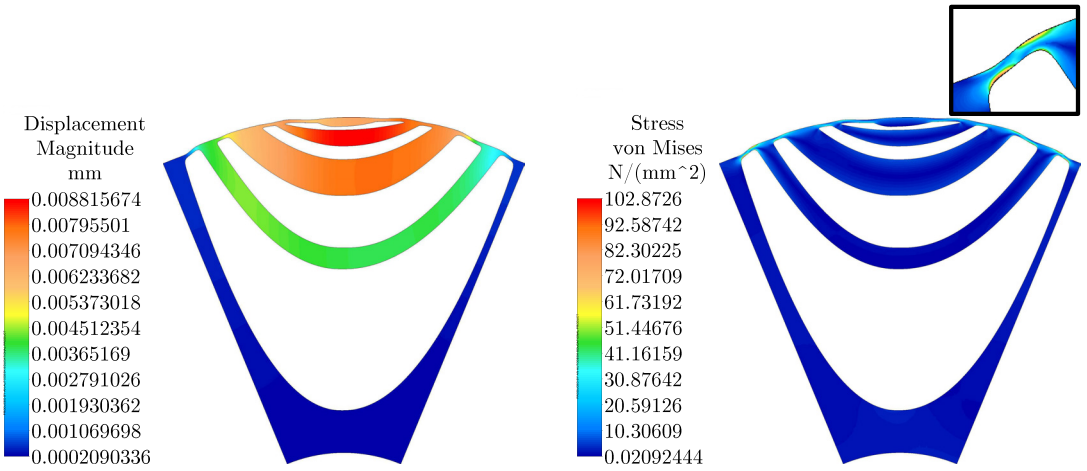

Figure 4.17: Stress and deformation analysis and comparison between structural analysis done in JMag and Algor Multiphysics on the selected 8 pole RSM rotor and IM stator [104, 105]

optimised machine parameters are shown in Table 4.7 and Figure 4.16, with the initial machine variables represented by X_9 and the T_R optimised machine by X_{10}.

As seen in the table, T_R was significantly reduced to in the order of 5%, more than a 50% reduction, with only a slight reduction in remaining parameters like T_A and P_F. The T_R current angle point was selected at the peak T_A point, but an alternative peak power factor current angle point could also be selected if peak power factor rated operating conditions are desired. This alternative is illustrated in Figure 4.16 and shows the versatility of the asymmetric rotor pole with respect to T_R reduction.

In order to ensure the structural rigidity of the rotor at rated conditions, two independent structural finite element packages were implemented for the structural analysis. This analysis of the lamination includes a 3D analysis in Algor and a 2D analysis in JMag. The lamination was simulated at six times the rated speed, 3000rpm, with laminations temperatures at a minimum of 20C° and a maximum of

(a)

(b)

(c)

(d)

Figure 4.18: Eight-pole rotor and stator manufacture [104, 105].

(a): Test bench station that includes two rapid prototyping machines sending switching frequencies to the back to back connected inverters that feed the IM and RSM.

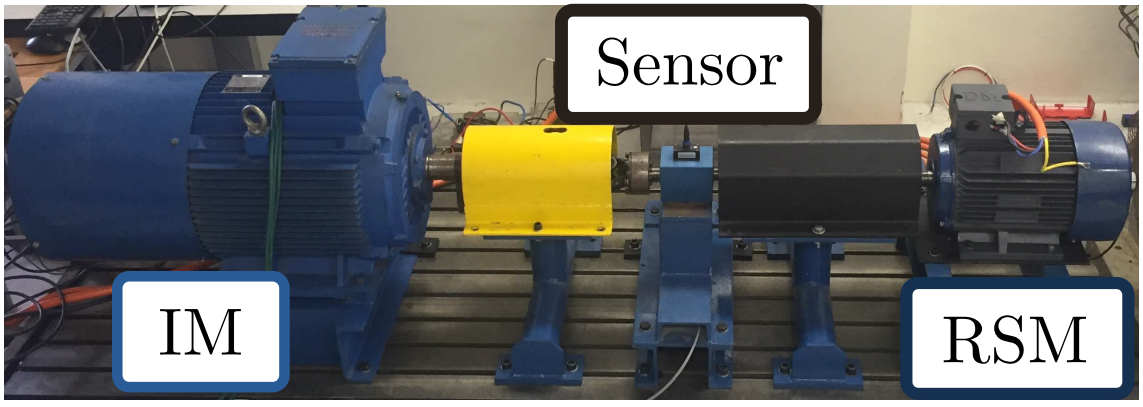

(b): Test bench setup that includes a back to back connected IM and RSM, separated by a torque sensor.

Figure 4.19: Testing station and bench of the 8 pole RSM design.

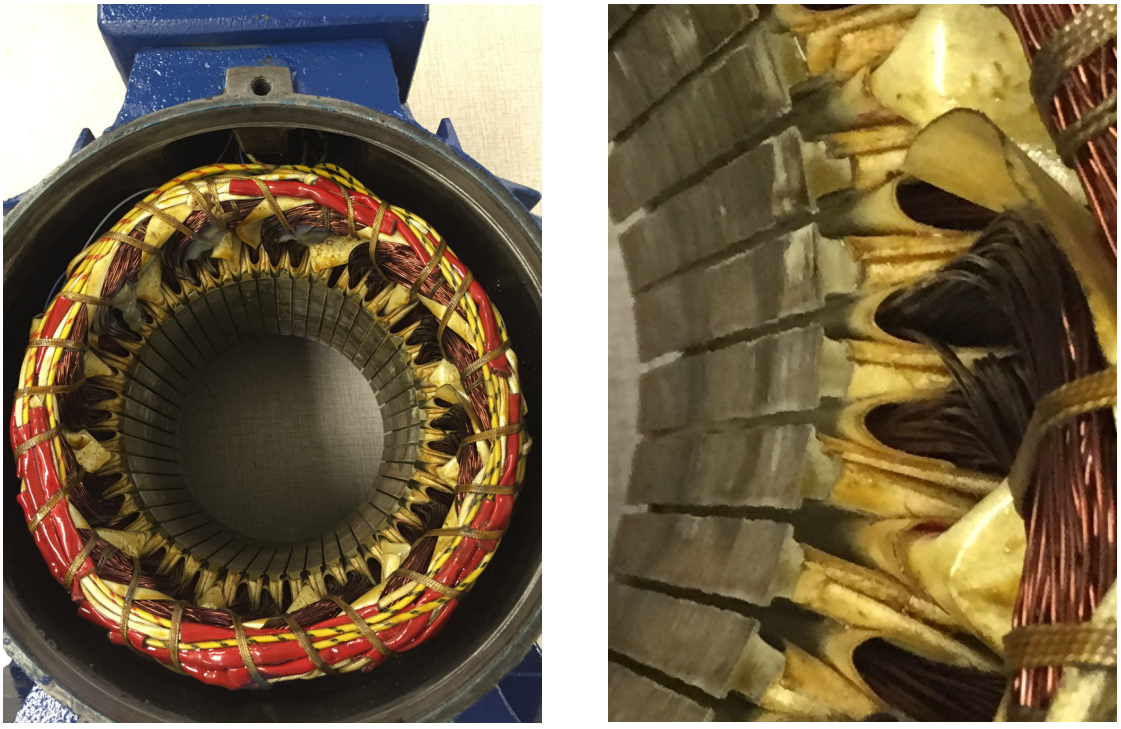

(a): Machine winding illustration. **(b):** Illustration of poor slot fill factor.

Figure 4.20: RSM designed stator winding and fill factor.

150C°.

Due to the inability of Algor to implement electromechanical forces in the simulation, the initial results validation was conducted in both packages with only centrifugal forces present. The results of these two simulations are illustrated in Table 4.8 and Figure 4.17.

Once the simulation results were validated, the simulation was repeated in JMag to included the electromechanical forces, with the results in the table clearly indicating that the centrifugal force is the main contributing factor to stresses and deformation. Additionally, at these extreme condtions, the laminations proved to be structurally sound and within the structural limitations of the lamination material, with $SF > 2$, with

$$SF = \frac{peak(\sigma_{Mises})}{\sigma_{yield}}. \tag{4.4.1}$$

Once the mechanical integrity of the rotor lamination at rated conditions were proven to be within material limits, the laminations where manufactured. The rotor laminations, rotor assembly and the completed machine assembly are shown in Figure 4.18.

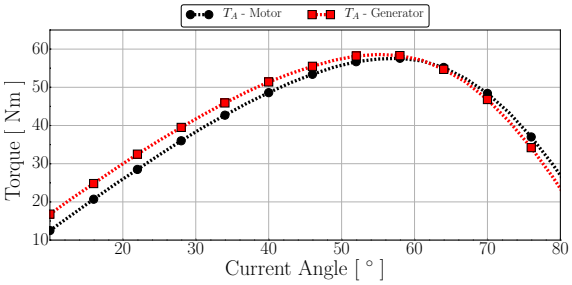

(a): Measured average torque for motor and generator modes.

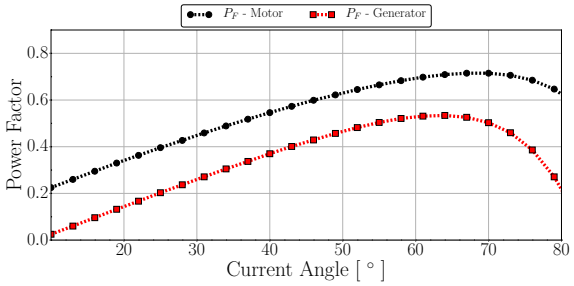

(b): Measured power factor for motor and generator modes.

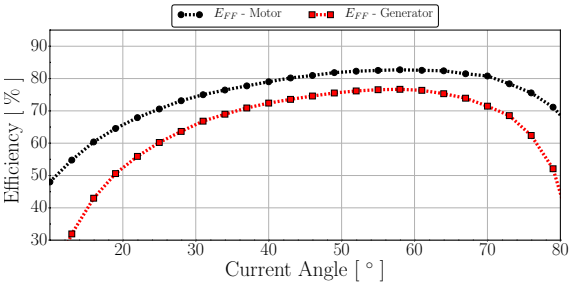

(c): Measured efficiency for motor and generator modes.

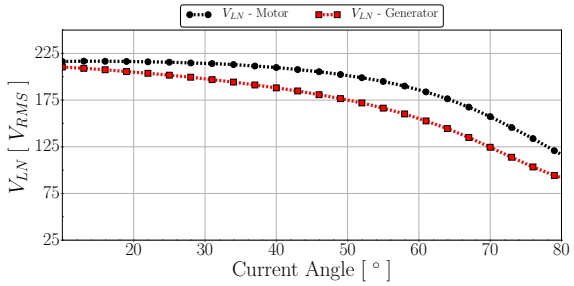

(d): Measured phase voltage for motor and generator modes.

Figure 4.21: Measured versus simulated parameters versus current angle change of the machine in motoring and generating mode.

4.5 Machine Testing

This section will consist of two sections, the first section will discuss the machine testing under motor mode in order to validate the weighted factor optimisation technique discussed in the previous section. The second section will consist of the motor versus generator performance evaluation in order to refine the reluctance synchronous generator model.

The test bench setup is presented in Figure 4.19. It consists of a back to back connected induction machine and the designed reluctance machine. Both machines are inverter fed and controlled by two previously developed rapid prototyping machines.

After an inspection of the manufactured machine, one important deviation was found with the simulated machine. During the winding process, the manufacturers had great difficulty in achieving the 0.45 fill factor implemented in the optimisation. A figure of the stator and slot is illustrated in Figure 4.20. As a result, the most realistic fill factor that could be achieved was 0.3. In order to keep the current density constant, the phase current had to be reduced. The winding diagram of the stator can be found in Appendix B.4. The model was updated with the new fill factor and all comparisons made between the simulated and testing results were done with the updated model.

Machine testing results for motor versus generator mode is presented in Figure 4.21 and in Table 4.9. The thermal imaging of the machine running at steady state

Table 4.9: Peak performance parameter comparison between motor and generator modes.

RSM Testing Results						
Performance Parameter		Motor Mode		Generator Mode		Mode Deviation♠
			$\theta^{\bigstar}$		$\theta^{\bigstar}$	p.u
$\boldsymbol{T_A^{\blacktriangle}}$	[Nm]	57.6	58	58.6	55	1.017
$\boldsymbol{P_F^{\blacktriangle}}$	[ ]	0.71	70	0.53	64	0.747
$\boldsymbol{E_{FF}^{\blacktriangle}}$	[%]	82.7	58	76.7	58	0.928
$\boldsymbol{V_{LN}^{\blacklozenge}}$	[V_{rms}]	190	58	166	55	0.874

★ - Peak value current angle ; ▲ - Peak value ; ♦ - Value at peak $\boldsymbol{T_A}$; ♠ - Motor parameters as base ; $\boldsymbol{T_A}$ - Average Torque ; $\boldsymbol{T_R}$ - Torque Ripple ; $\boldsymbol{E_{FF}}$ - Efficiency ; $\boldsymbol{V_{LN}}$ - RMS Phase Voltage ; $\boldsymbol{\theta}$ - Current Angle

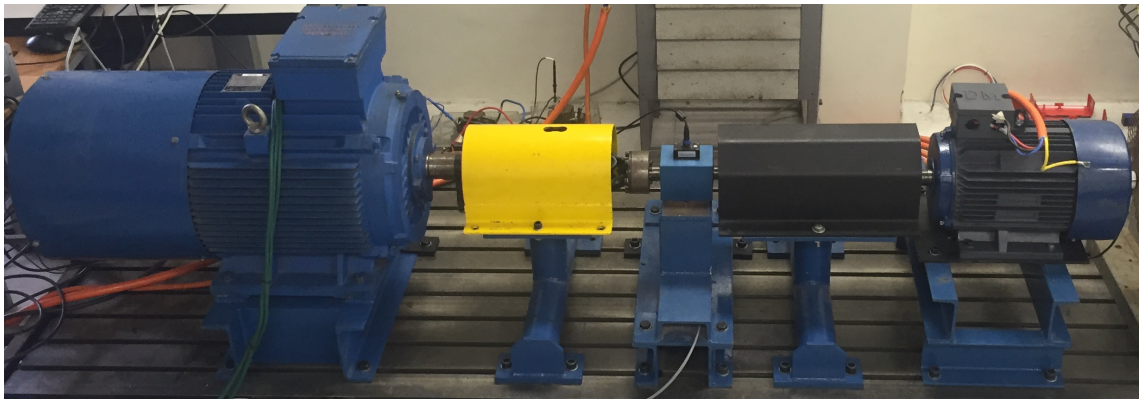

(a): Testing setup of machine under test.

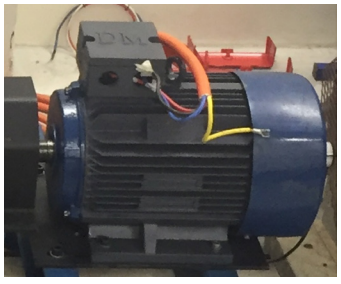

(b): Machine under test.

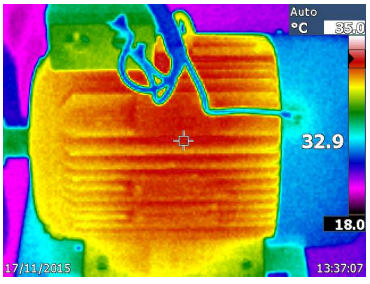

(c): Initial Temperature

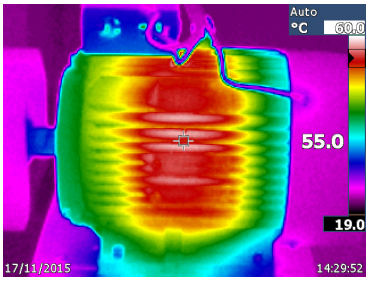

(d): Steady Temperature.

Figure 4.22: Thermal measurements before and after steady state temperature is reached during full load testing at the peak average torque current angle point (13:37 to 14:29 on 17/11/2015).

under full load at the peak torque current angle point is presented in Figure 4.22.

4.5.1 Motoring Mode Versus Simulation

The testing results under motor operation versus simulation results are presented in Table 4.10 and Figure 4.23. The P_F is compared to the simulated values by

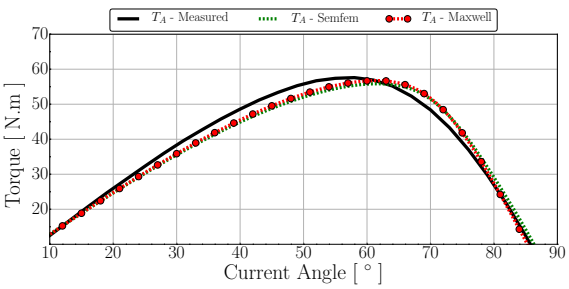

(a): Simulated versus measured average torque, current angle map.

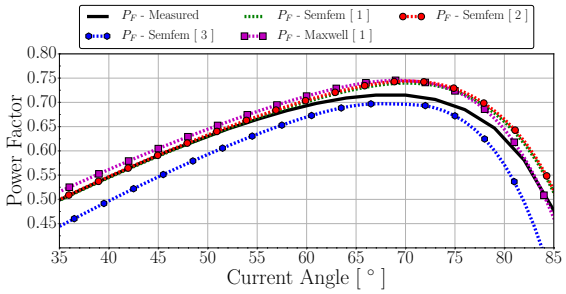

(b): Simulated versus measured power factor, current angle map.

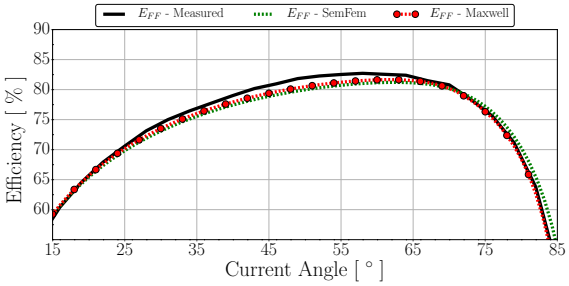

(c): Simulated versus measured efficiency, current angle map.

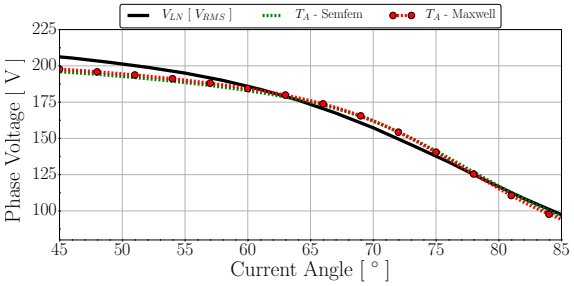

(d): Simulated versus measured phase voltage, current angle map.

Figure 4.23: Measured versus simulated parameters of the fully designed machine model in motoring mode.

implementing three methods of calculation,

1. by implementing the power triangle Equation

$$cos(\theta) = \frac{P_{in}}{S} = \frac{\omega_M T_A + P_C + P_R + P_M}{3V_{LN}I} \tag{4.5.1}$$

   , that includes copper, core and mechanical losses.

2. by implementing the phasor diagram angle in Figure 2.9a, that includes copper and core losses but excludes mechanical losses

3. by implementing Equation 2.5.14 (as was implemented in the optimisation study), that excludes copper, core and mechanical losses

From Table 4.10, It is clear that all three calculated P_F values correlate closely to the tested values. The implemented equation during optimisation (method (3)) indicates the closest correlation, with a deviation of just 2.5%. Subsequent deviations consist of 3.5% by implementing method (1) and 4% by implementing method (2).

Generally there is good correlation between the testing results and simulated values from both Semfem, that was implemented during the design, and Maxwell implemented for validation. There is however a current angle offset between the simulated and measure current angle at peak average torque. The author argues that this deviation is due to a difference in material properties between the simulated and

Table 4.10: Motor test results versus simulation.

Test Results Vs Semfem Vs Maxwell Models												
Performance Parameter		Test Results		Semfem T_R=20°C			Semfem T_R=65°C			Maxwel T_R=65°C		
			$\theta^{\bigstar}$		$\theta^{\bigstar}$	p.u$^{\spadesuit}$		$\theta^{\bigstar}$	p.u$^{\spadesuit}$		$\theta^{\bigstar}$	p.u$^{\spadesuit}$
$\boldsymbol{T_A^{\blacktriangle}}$	[Nm]	57.60	58	55.85	62	0.907	55.85	62	0.970	56.74	61	0.985
$\boldsymbol{P_{F-(1)}^{\blacktriangle}}$	[ ]	0.715	70	0.731	70	1.023	0.740	70	1.035	0.759	69	1.062
$\boldsymbol{P_{F-(2)}^{\blacktriangle}}$	[ ]	0.715	70	0.735	70	1.028	0.744	70	1.040	0.786	69	0.987
$\boldsymbol{P_{F-(3)}^{\blacktriangle}}$	[ ]	0.715	70	0.696	70	0.974	0.697	70	0.975	0.698	69	0.976
$\boldsymbol{E_{FF}^{\blacktriangle}}$	[%]	82.71	58	83.23	63	1.0006	81.21	63	0.982	81.66	62	0.987
$\boldsymbol{V_{LN}^{\blacklozenge}}$	[V_{rms}]	190	58	183.3	58	0.965	185.5	58	0.976	186.9	58	0.984
$\boldsymbol{R_A^{\blacksquare}}$	[Ω]	1.96	-	1.95	-	-	2.57	-	-	2.57	-	-

★ - Peak value current angle ; ▲ - Peak value ; ♦ - Value at peak measured $\boldsymbol{T_A}$; ♠ - Test parameters as base ; ■ - DC terminal resistance at 20°$\boldsymbol{C}$; [**1**] - From power angle equation ; [**2**] - From phasor angle ; [**3**] - From speed voltage equation ; $\boldsymbol{T_A}$ - Average Torque ; $\boldsymbol{P_F}$ - Power Factor ; $\boldsymbol{T_R}$ - Torque Ripple ; $\boldsymbol{E_{FF}}$ - Efficiency ; $\boldsymbol{V_{LN}}$ - RMS Phase Voltage ; $\boldsymbol{\theta}$ - Current Angle ; $\boldsymbol{R_A}$ - Phase Resistance

NOTE: A important factor to mention is after the submission of the journal, the machine winding was changed to try and achieve a better fill factor. This is the reason for test result deviation between the journal results and measurements in the table [104, 105].

tested machine. The main motivation for this is that due to the largely unavailable precise material properties from the supplier, material properties for the simulation of the machine were read from the closest material properties the author could find.

Ibrahim in [107] studied the effect of varying material properties on RSM performance. The study found that certain material may affect the location of the peak T_A point with respect to current angle. The T_A versus current angle change results obtained are presented in Figure 4.24, where an average 5° current angle offset between materials were found, similar to the measured offset found in Figure 4.23a.

4.5.2 Generator Mode Versus Simulation

The measured versus simulation results for the machine under generator mode are illustrated in Figure 4.25 and in Table 4.11. Once again, P_F was calculated implementing three methods,

1. by implementing the power triangle Equation

$$cos(\theta) = \frac{P_{out}}{S} = \frac{\omega_M T_A - P_C - P_R - P_M}{3V_{LN}I}. \tag{4.5.2}$$

   , that includes copper, core and mechanical losses.

2. by implementing the phasor diagram angle in Figure 2.9a, that includes copper and core losses but excludes mechanical losses

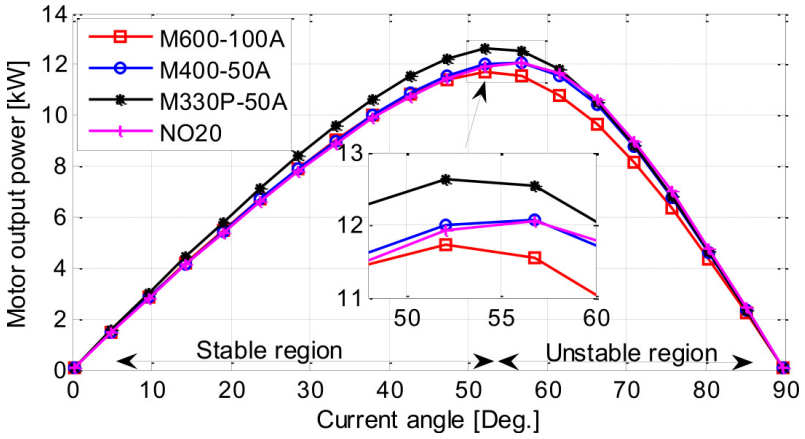

Figure 4.24: Direct result of the study by Ibrahim, illustrating what effect material variation has on the peak average torque current angle position, presented here as Motor output power ($\omega_m T_A$) versus current angle change. [107].

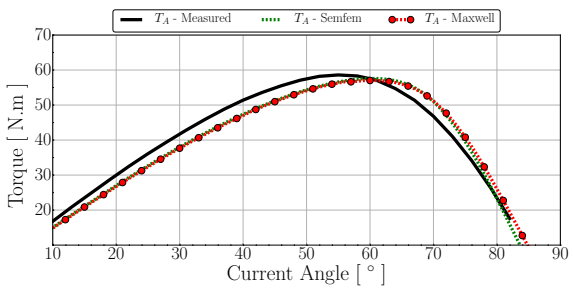

(a): Simulated versus measured average torque, current angle map.

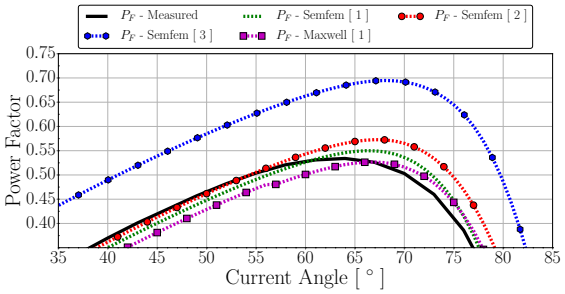

(b): Simulated versus measured power factor, current angle map.

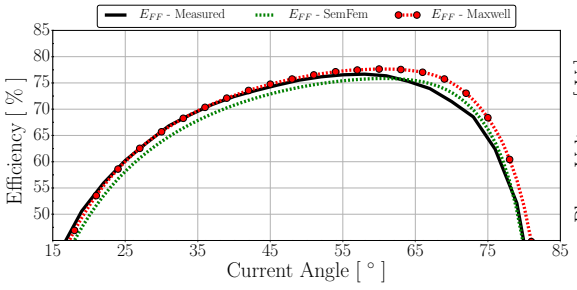

(c): Simulated versus measured efficiency, current angle map.

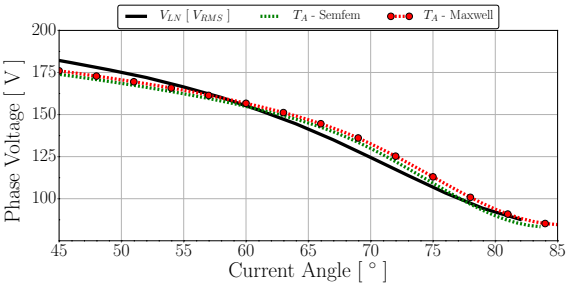

(d): Simulated versus measured phase voltage, current angle map.

Figure 4.25: Measured versus simulated parameters of the fully designed machine model in generating mode.

Table 4.11: Generator test results versus simulation.

Test Results Vs Semfem Vs Maxwell Models												
Performance Parameter		**Test Results**		**Semfem** T_R=20°C			**Semfem** T_R=65°C			**Maxwell** T_R=65°C		
			$\theta^{\bigstar}$		$\theta^{\bigstar}$	p.u$^{\spadesuit}$		$\theta^{\bigstar}$	p.u$^{\spadesuit}$		$\theta^{\bigstar}$	p.u$^{\spadesuit}$
$\boldsymbol{T_A^{\blacktriangle}}$	[Nm]	58.60	55	57.59	60	0.983	57.59	60	0.983	57.02	60	0.973
$\boldsymbol{P_{F-[1]}^{\blacktriangle}}$	[ ]	0.534	64	0.566	66	1.060	0.550	66	1.030	0.527	67	0.986
$\boldsymbol{P_{F-[2]}^{\blacktriangle}}$	[ ]	0.534	64	0.574	67	1.075	0.559	66	1.046	0.566	69	1.060
$\boldsymbol{P_{F-[3]}^{\blacktriangle}}$	[ ]	0.534	64	0.695	68	1.301	0.695	68	1.301	0.679	69	1.272
$\boldsymbol{E_{FF}^{\blacktriangle}}$	[%]	76.67	58	78.90	61	1.029	75.84	61	0.989	77.64	60	1.013
$\boldsymbol{V_{LN}^{\blacklozenge}}$	[V_{rms}]	166.4	55	163.9	55	0.985	162.2	55	0.975	164.45	55	0.988
$\boldsymbol{R_A^{\blacksquare}}$	[Ω]	1.96	-	1.95	-	-	2.57	-	-	2.57	-	-

★ - Peak value current angle ; ▲ - Peak value ; ♦ - Value at peak measured $\boldsymbol{T_A}$; ♠ - Test parameters as base ; ■ - DC terminal resistance at 20°$\boldsymbol{C}$; **[1]** - From power angle equation ; **[2]** - From phasor angle ; **[3]** - From speed voltage equation ; $\boldsymbol{T_A}$ - Average Torque ; $\boldsymbol{P_F}$ - Power Factor ; $\boldsymbol{T_R}$ - Torque Ripple ; $\boldsymbol{E_{FF}}$ - Efficiency ; $\boldsymbol{V_{LN}}$ - RMS Phase Voltage ; $\boldsymbol{\theta}$ - Current Angle ; $\boldsymbol{R_A}$ - Phase Resistance

3. by implementing Equation 2.5.14 (as was implemented in the optimisation study), that excludes copper, core and mechanical losses .

When analysing the simulation versus test results it is clear that although the implementation of method [3], that was implemented in the optimisation, holds for the machine under motoring mode, a 30% deviation between the calculated and measured P_F exists for the machine under generator mode, shown in Figure 4.25b. Considering the alternative methods implemented, method [1] is the most accurate, with a 3% deviation, compared to the 4.6% deviation calculated by method [2]. This critically illustrates the major effect that, not only copper and core losses have on a RSM in generator mode, but also the mechanical losses.

Generally, excluding the initial P_F estimation with method [3], the test results and measured values agree well. Additionally, as the case during motor mode, there is a 5° offset of the current angle at the peak T_A points. The main reason for the deviation in the motoring mode is, as described earlier, attributed to the different material properties

In order to compare the performance of the two operating modes across the speed range, a speed range map for both modes is presented in Figures 4.26 and 4.27. This map clearly shows the large decrease in comparable P_F between the operating modes across the entire speed range. The only advantage the machine under generator mode holds above the motoring mode is its lower phase voltage value across the current angle range. The machine under generator mode thus has a wider power speed range compared to the motoring mode as seen in the speed map figures.

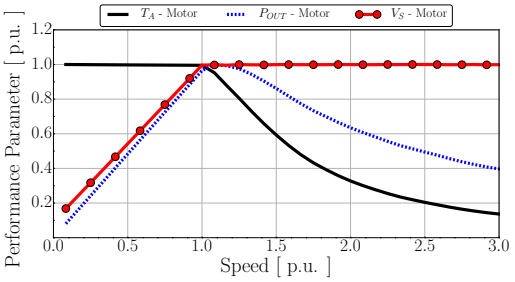

(a): Motor power speed range.

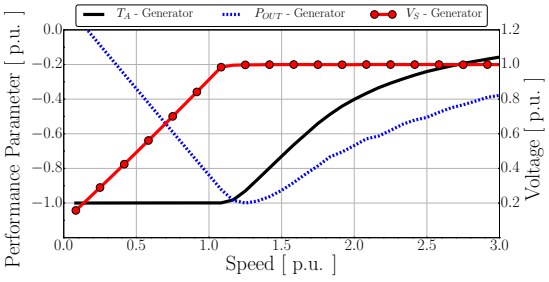

(b): Generator power speed range.

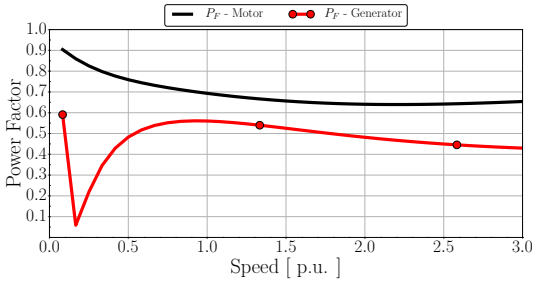

(c): Motor generator mode power factor in the power speed range.

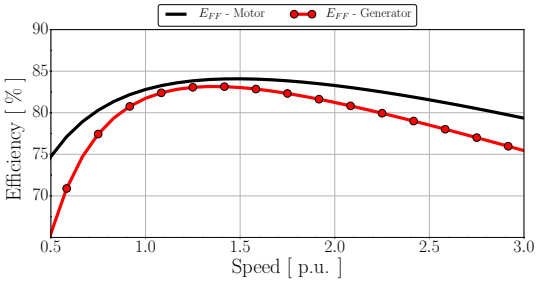

(d): Motor generator mode efficiency in the power speed range.

Figure 4.26: Machine speed range performance in motoring and generator mode implementing the Maxwell model under maximum torque per ampere control.

4.6 Conclusion

In this chapter, a weighted factor optimisation technique was used to study the relatively poor power factor of RSM's compared to its relatively competitive torque density. This optimisation study showed that there is a relationship between the average torque and power factor that can be implemented in the prediction of optimisation results. Additionally, it was shown that this prediction method can be used to design machines by selecting desired performance parameters and designing for the specific machine.

Furthermore, it was shown that this relationship is flux barrier number, pole number and power level independent, with the relationship also holding for machines optimised with retrofit stators. This relationship was proven with example estimation machines falling within the 95% confidence zone. Testing the machine validated optimised average torque and power factor values, with efficiency and phase voltage also agreeing well.

An additional study was conducted with the machine operating in generator mode. It was found that in order to accurately estimate power factor for RSM's operating in generator mode, the entire phasor angle model needs to be implemented. In the next chapter, this verified model will be implemented in the design study of RSM's in the megawatt power range.

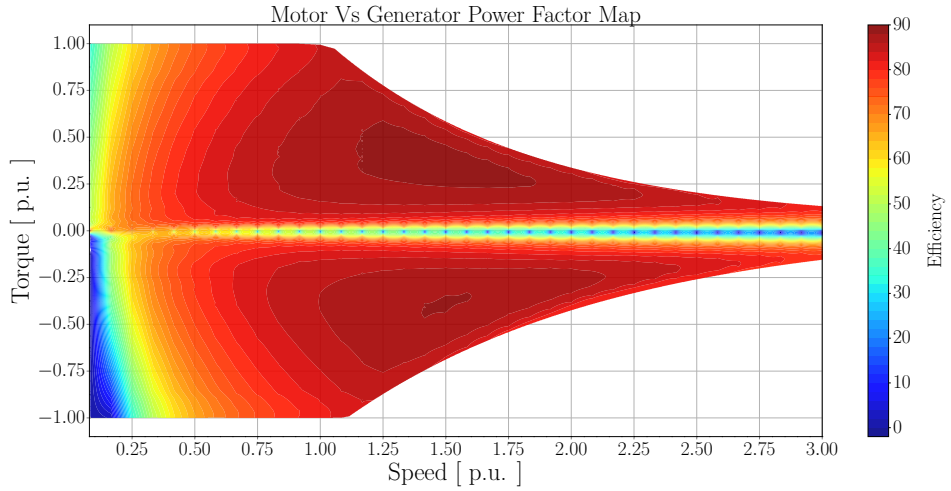

(a): Efficiency map in the torque speed region.

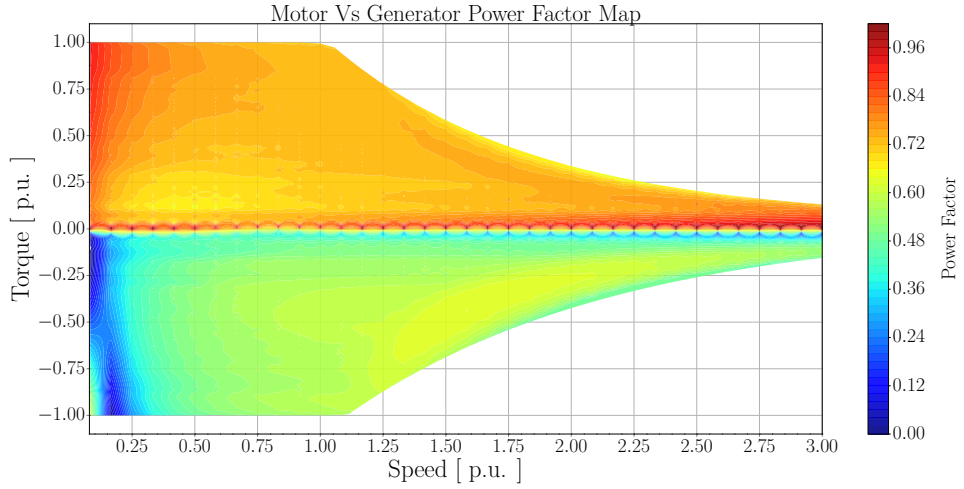

(b): Power factor map in the torque speed region.

Figure 4.27: Efficiency and power factor map of machine in motor and generator mode in the torque speed region.

Chapter 5

Megawatt RSG Optimisation Study

In this chapter, the fifth and sixth objectives of the study are discussed. The first topic of this chapter includes the study into implementing a reluctance synchronous machine in the 5 MW power range for wind energy applications as RSG. The subsequent study includes the development of an assisted reluctance synchronous generator (ARSG) model to further improve the performance of the reluctance generator in order to be more competitive with the currently implemented permanent magnet synchronous generators (PMSG).

Extremely sparse literature in this specific field exists, with available RSG studies all implementing an existing IG or PMSG stator with rotor retrofit design, with no literature available for the design optimisation of an ARSM. Due to this fact, the aim of the study is to determine the feasibility of implementing the proposed generators by assuming near perfect generator conditions. These conditions include

- a generator operation with no mechanical constraints i.e. no mechanical deformation of the rotor under full load and rated speed, and
- a generator design assuming manufacturability.

5.1 Reluctance Synchronous Generator Design

5.1.1 Model

In order to implement the developed RSM model in Chapter 4, the model had to be adapted to more realistically represent generators in the high power range. Importantly it must be noted that although the model was adapted to reflect a more realistic generator in this power range, the generator model will be designed for ideal conditions.

The model updates to the design include :

1. the increase of the machine air-gap length from 0.3 mm to 2.5 mm

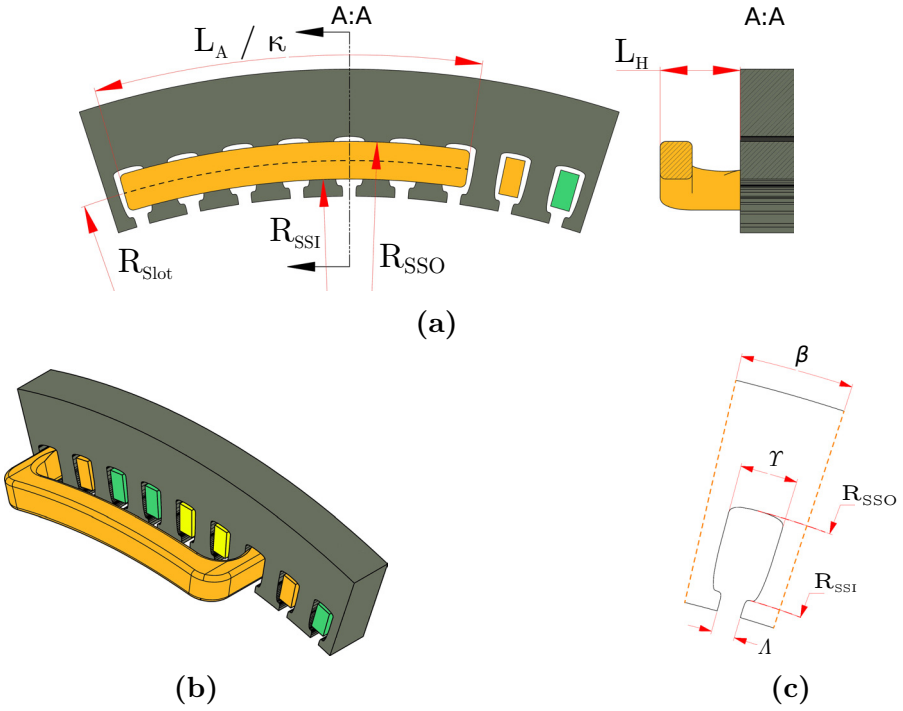

Figure 5.1: Megawatt end winding length estimation.

2. the increase of the flux barrier web width from 0.5 mm to 2.5 mm

3. an update to the end winding length estimation, with the detailed model presented in Figure 5.1. The length of one end winding can be estimated by:

$$L_{end} = L_A + 2L_H \tag{5.1.1}$$

with

$$L_A = R_{Slot}\kappa \tag{5.1.2}$$ and $$L_H = R_{SSO} - R_{SSI} \tag{5.1.3}$$

seen in Figure 5.1a

4. an update to the stater slot entrance, with

$$\Lambda = 0.5\Upsilon \tag{5.1.4}$$

seen in Figure 5.1c.

In order to investigate the proposed generator, a flux barrier number per pole had to be selected. For this selection, the results obtained in Chapter 4, with additional results obtained by Palmieri and by Moghaddam in their respective studies [21, 46] are selected for analysis. The results of Chapter 4, of the study of Palmieri and Moghaddam are presented in Figure 5.2 and summarized in Table 5.1. These results consist of machines optimised by maximising T_A, with air-gap lengths varying between 0.25 to 0.55 mm, with the power level varying between 2 and 25 KW and

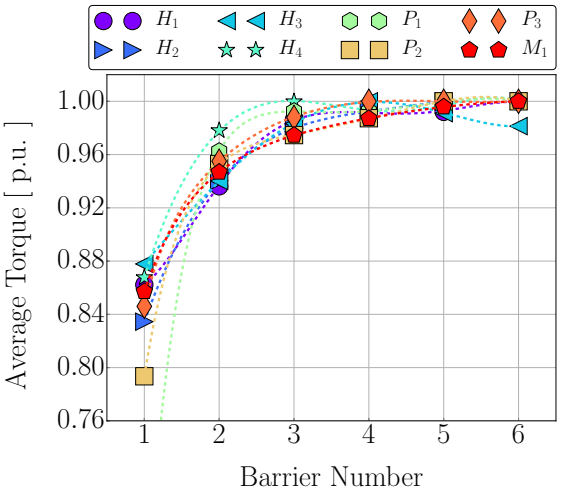

Figure 5.2: Maximized T_A results for flux barrier numbers per pole ranging from 1 to 6 from Figure 4.8 and results obtained by Palmieri and Moghaddam in [21, 46](Legend refer to Table 5.1).

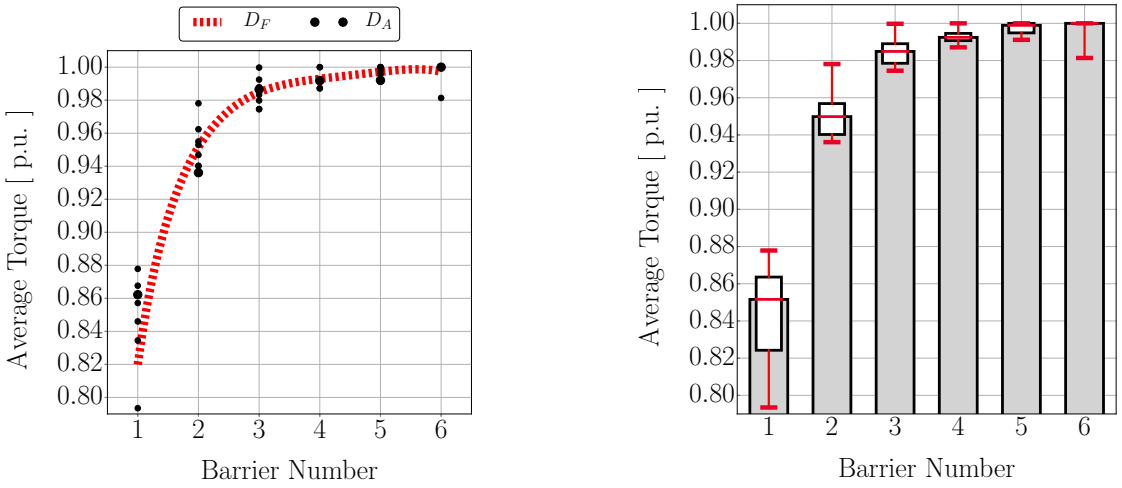

(a): Contour fit

(b): Bar Plot

Figure 5.3: Contour fit and bar plot with 95% confidence box plot for the results obtained in Figure 5.2 and Table 5.1, with D_A the results and D_F the least square error curve fit to D_A

with the number of stator slots per pole S_P varying between 3 and 12. In each of these optimisations, T_A was maximised for flux barrier numbers between one and six.

Analysing the combined per-unit results of each of these studies in Figure 5.2, it is clear that the maximum average torque achievable for the specific topology optimised converges around the four flux barrier per pole mark. The combined results of Figure 5.2 and Table 5.1 is shown in Figure 5.3, where a curve fit and bar plot with 95% confidence interval is applied to each of the flux barrier combination studies.

Table 5.1: Summarize results of the maximization of T_A versus flux barrier number for results obtained in Chapter 4 and by Moghaddam and Palmieri in [21, 46].

Researcher	P	S_p	B_r	h [mm]	n [rpm]	P_{max} [kW]
H_1	4	6	$1 \Rightarrow 6$	0.3	1500	3.3
H_2	4	9	$1 \Rightarrow 5$	0.35	1500	13.3
H_3	6	6	$1 \Rightarrow 6$	0.35	1000	9.4
H_4	8	6	$1 \Rightarrow 6$	0.35	450	4.1
P_1	4	3	$1 \Rightarrow 6$	0.5	5000	2
P_2	4	6	$1 \Rightarrow 6$	0.5	5000	2
P_3	4	12	$1 \Rightarrow 6$	0.5	5000	2
M_1	4	9	$1 \Rightarrow 6$	0.55	1500	25

$\boldsymbol{P}$ - Number of poles ; $\boldsymbol{S_P}$ - Stator slots per pole ; $\boldsymbol{B_r}$ - Number of flux barriers ; $\boldsymbol{h}$ - Air gap length ; $\boldsymbol{P_{max}}$ - Maximum power for specific model ; $\boldsymbol{H_{1-3}}$ - Results from Figure 4.8 ; $\boldsymbol{P_{1-3}}$ - Results from **Palmieri** in [46]; $\boldsymbol{M_1}$ - Results from **Moghaddam** in [21].

Table 5.2: Air gap study machine.

Study	P_{max} [kW]	P	S_p	B	ST_O [mm]	L_S [mm]	h [mm]	n [rpm]
A_S	26	10	9	$1 \Rightarrow 6$	200	200	2.5	500

$\boldsymbol{P}$ - Number of poles ; $\boldsymbol{S_P}$ - Stator slots per pole ; $\boldsymbol{B}$ - Number of flux barriers ; $\boldsymbol{h}$ - Air gap length ; $\boldsymbol{P_{max}}$ - Maximum power for specific model

Furthermore, with this data set ranging over a large power range (2 to 25 kW), stator rotor profile combinations and air-gap length variations, it can be assumed that any machine optimised within these ranges will conform to the confidence range and curve in Figure 5.3a. Therefore it can be assumed that for each machine analysis in this range, four flux barriers per pole would provide the best T_A result without unnecessarily increasing the optimisation variables by increasing the flux barrier number, this with minimal gains in T_A.

Comparing the intended generator model with the optimised results in Table 5.1, one question arises: will the optimisation results conform to the curve in Figure 5.3a if the air gap height is drastically increased. In order to determine this, a 26 kW machine is selected and optimised with flux barrier numbers ranging between one and six, with the increased air gap length similar to the intended generator air gap in the megawatt study. The machine specifications are presented in Table 5.2.

The study consisted of the maximisation of T_A, with no other machine specification like torque ripple, efficiency or power factor taken into consideration, with the optimisation strategy implemented in Figure 4.4 once again implemented for the maximization. The results of this study are shown in Figure 5.4. As can be clearly seen in this figure, not only do the converging average torque apply to the sub 0.5 mm air gap length machines, it also applies to machines with air gap lengths up to

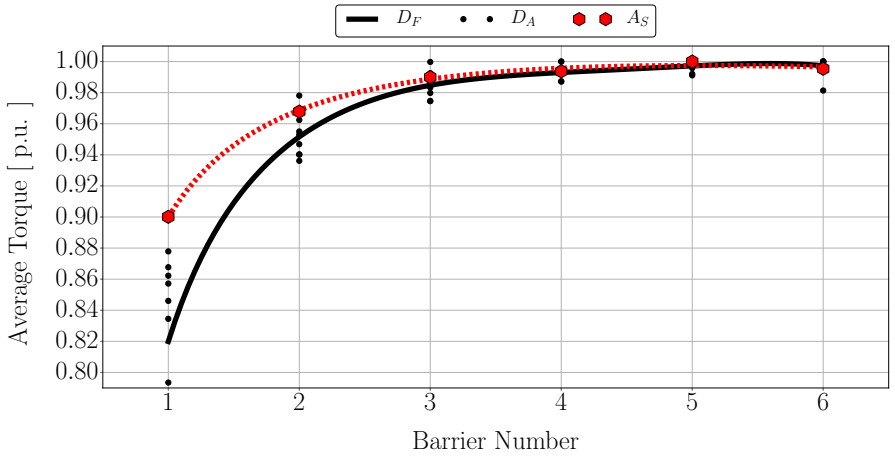

Figure 5.4: Maximized T_A results A_S for flux barrier numbers ranging from one to six, with results for the machines in Table 5.2 as D_A and D_F the curve fit to D_A.

2.5 mm.

For the selected stator model in Figure 5.1, the total number of variables for the stator slot consists of five. This is a reduction from the required eight variables in Chapter 4. The reduction in variable count is as a result of the consistent maximized values obtained in the results of Chapter 4, with all the excluded variables repeatedly converging on the same value. These excluded variables consist of

$$X = \begin{bmatrix} R_{SSI} & R_{\%23} & \theta_{\%22} \end{bmatrix}^T \tag{5.1.5}$$

with R_{SSI} the stator slot inner radius, $R_{\%23}$ the approach angle point for the spline fitting of point P_3 and $\theta_{\%22}$ the departure angle of the spline fitting of point P_2. These variables are presented in Figures 4.3a and 4.3b and in Table 4.1.

In addition to the reduction in variables for the stator slot, symmetric flux barriers are selected for the optimisation study. The motivation for this is twofold. Firstly, due to the high number of simulation steps required for accurate torque harmonic simulation, torque ripple will not be included in this study, hence the large reduction in torque harmonics found in Chapter 4 by implementing an asymmetric flux barrier will not be relevant. Secondly, implementing symmetric flux barriers greatly reduce the total number of variables, thus helping to keep the optimisation time to a minimum. The selection of symmetric flux barriers reduces the required variables per flux barrier from eight to five, with a total reduction in variables just for the flux barriers from 32 to 20.

With the addition of the generator volume dimensions (L_S - stack length, ST_O - stator outside radius and RO_I - rotor inside radius), the current angle and the five variables per flux barrier, each generator optimization consisted of 29 variables represented by

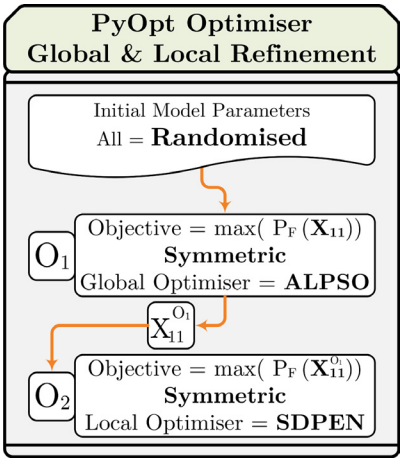

Figure 5.5: Two stage global and local refinement optimisation strategy flow diagram.

$$X_{11} = \begin{bmatrix} \alpha \\ \beta \\ R \\ P_{1sp} \\ P_{3sp} \\ \theta \\ L_S \\ ST_O \\ RO_I \\ R_{GAP} \\ R_{SSO} \\ R_{P_3} \\ \alpha_{34} \\ R_{P_4} \end{bmatrix} = \begin{bmatrix} \alpha_{(1)} & . & . & \alpha_{(4)} \\ \beta_{(1)} & . & . & \beta_{(4)} \\ R_{(1)} & . & . & R_{(4)} \\ P_{1sp(1)} & . & . & P_{1sp(4)} \\ P_{3sp(1)} & . & . & P_{3sp(4)} \\ \theta & & & \\ L_S & & & \\ ST_O & & & \\ RO_I & & & \\ R_{GAP} & & & \\ R_{SSO} & & & \\ R_{P_3} & & & \\ \alpha_{34} & & & \\ R_{P_4} & & & \end{bmatrix}. \tag{5.1.6}$$

5.1.2 Optimisation Study

The optimisation suite selected for the optimisation study is once again PyOpt, with the optimisation flow diagram in Chapter 4, Figure 4.4, once again implemented in conjunction with SEMFEM. In addition, a new two stage optimisaition strategy is implemented, presented in Figure 5.5. The strategy consists of an initial global optimisation by implementing a particle swarm optimiser available in PyOpt, the Augemented Lagragian Particle Swarm Optimizer (ALPSO). The second step in the optimisation strategy is a refinement of the results obtained by ALPSO, with the optimiser implemented SDPEN, the same optimiser extensively and successfully used in Chapter 4.

The motivation for implementing this two stage strategy lies in the large model range the optimiser must work in, with stator diameters and stack lengths largely unconstrained. This presented global minima convergence problems when only implementing SDPEN as the optimiser, with the optimiser constantly converging in

Table 5.3: Megawatt medium speed generators studied at 500 rpm.

Machine Poles		4	6	8	10	12	14
S_P	[ ]	12	12	9	9	9	9
W_L	[ ]	10:12	10:12	7:9	7:9	7:9	7:9
f_e	[Hz]	16.7	25.0	33.3	41.7	50.0	58.3
J_S	[A/mm^2]	4.5	4.5	4.5	4.5	4.5	4.5
S_{FF}	[ ]	0.35	0.35	0.35	0.35	0.35	0.35
h	[mm]	2.5	2.5	2.5	2.5	2.5	2.5

S_P - Stator Slots per Pole ; J_S -Stator Current Density ; W_L - Winding Layout ; F_E - Electrical Frequency ; S_{FF} - Sator Fill Factor; h - Air gap length

local minima points. Additionally, in order to fall within the competitive range of currently implemented generators in the medium speed range, constraints had to be included in the optimisation study, which even further increased the complexity of the problem.

In order to investigate the feasibility of implementing RSM's in this high power range, P_{OUT} and E_{FF} were constrained, with P_F the objective being maximised. To keep the generator within the intended power level and E_{FF}, a penalty constraint method is implemented, as illustrated to be effective in particle swarm optimisers in [108]. The optimisation objective function equation and penalty constraints consist of the minimisation of Equation 5.1.7:

$$P_O = W_1 P_P^H + W_2 P_P^L + W_3 P_\eta^L - P_F(X_{11}) \tag{5.1.7}$$

$$\text{Subject to :} \quad \begin{cases} 0 \leqslant G_j(X_{11}) \leqslant 1 \quad ; \quad j = 1, 2, ..., n \\ 5.0MW \leqslant P_{OUT}(X_{11}) \leqslant 5.05MW \\ E_{FF}(X_{11}) \geqslant 98.0\% \end{cases} \tag{5.1.8}$$

with the penalty function for power level exceeding the constrained value

$$P_P^H = \begin{cases} (P_{OUT} - P_H)/P_H \quad ; \quad P_{OUT}(X_{11}) > 5.05MW \quad : \quad P_H = 5.05MW \\ 0.0 \quad ; \quad P_{OUT}(X_{11}) < 5.05MW \end{cases} \tag{5.1.9}$$

and with the penalty function with power level lower than the constraint value

$$P_P^L = \begin{cases} (P_L - P_{OUT})/P_{OUT} \quad ; \quad P_{OUT}(X_{11}) < 5.00MW \quad ; \quad P_L = 5.0MW. \\ 0.0 \quad ; \quad P_{OUT}(X_{11}) > 5.00MW \end{cases} \tag{5.1.10}$$

The E_{FF} penalty function is defined by:

Table 5.4: 5 MW RSG optimisation result summary

Poles		4	6	8	10	12	14
T_A	[kNm]	-97.4	-98.4	-98.4	-98.4	-98.4	-98.4
P_{OUT}	[MW]	**5.0**	**5.05**	**5.04**	**5.05**	**5.05**	**5.05**
P_F	[ ]	**0.870**	**0.877**	**0.852**	**0.853**	**0.829**	**0.802**
θ	[°]	75.1	74.8	74.2	73.4	72.3	70.7
E_{FF}	[%]	**98.0**	**98.0**	**97.9**	**98.0**	**98.0**	**98.0**
M_A	[t]	33.8	26.6	18.0	14.8	12.4	11.6
L_S	[m]	6.00	4.31	3.34	1.88	1.51	1.64
ST_O	[m]	1.25	1.45	1.51	1.89	2.00	1.94

T_A - Average Torque ; P_{OUT} - Terminal Power Out; P_F - Power Factor ; θ - Current Angle ; E_{FF} - Efficiency ; M_A - Active Mass ; L_S - Stack Length ; ST_O - Stator Outside Diameter

$$P_{\eta}^{L} = \begin{cases} (E_L - E_{FF})/E_{FF} \quad ; \quad E_{FF}(X_{11}) < 98.0\% \quad ; \quad E_L = 98\%. \\ 0.0 \quad ; \quad E_{FF}(X_{11}) > 98.0\% \end{cases} \tag{5.1.11}$$

with the penalty weights for each of the respective penalties defined by:

$$W_1 = 5 \quad ; \quad W_2 = 5 \quad ; \quad W_3 = 20 \tag{5.1.12}$$

Each of these respective weights were determined by gradually increasing the weight until the constraint held after the optimiser converged.

In order to study a varying range of generators in the defined medium speed range, fixed at 500 rpm, generators ranging from four to fourteen poles are selected for the optimization. The respective generators are presented in Table 5.3. Implementing the two stage optimisation strategy in Figure 5.5 and the optimisation flow diagram in Figure 4.4, each of the generators presented in Table 5.3 is optimised.

5.1.3 Result Analysis

The results of this optimisation study applied to all the machines in Table 5.3 are shown in Figures 5.6 to 5.17 and in Tables 5.5 to 5.10. The summarised results are compared in Table 5.4. From these results it is clear that the penalty constraints method was effective in keeping the optimiser within the defined limits. Furthermore, very competitive P_F values where achieved, with the highest value for the four-pole generator equal to 0.87, with this tapering down gradually to 0.8 for the 14 pole generator.

Additional comparison of the results can be found in Figure 5.18, where the optimised generators' active mass, aspect ratio, P_F and volume dimensions are presented against the generator pole number. When analyzing Figure 5.18a, it is clear that a drastic reduction in active mass is achieved with the increase in pole numbers, as the P_F also decreases. Additionally, as the generator poles increase, so the aspect ratio decreases as seen in Figure 5.18a.

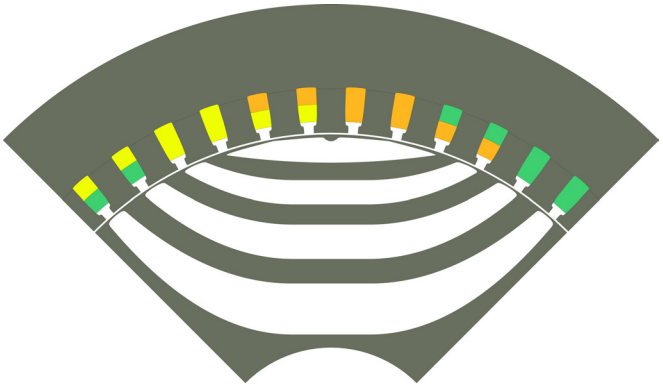

Figure 5.6: 4 Pole 5MW generator

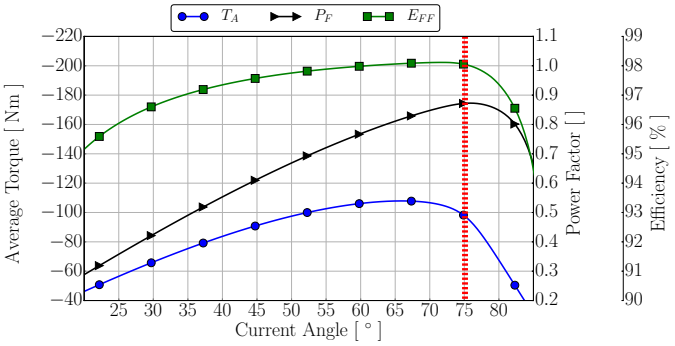

Figure 5.7: 4 Pole 5MW current angle map

Table 5.5: 4 Pole 5MW generator performance

Performance Results	
Average Torque [kNm]	-97.4
Power Out [MW]	**5.0**
Power Factor [ ]	**0.870**
Current Angle [°]	75.1
Efficiency [%]	**98.0**
Active Mass [tn]	33.8
Stack Length [m]	6.00
Stator Diameter [m]	1.25
Aspect Ratio [ ]	4.8

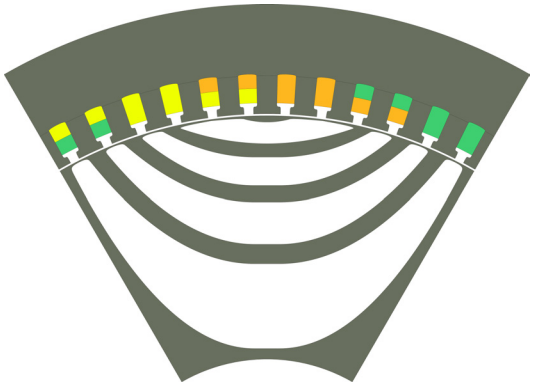

Figure 5.8: 6 Pole 5MW generator

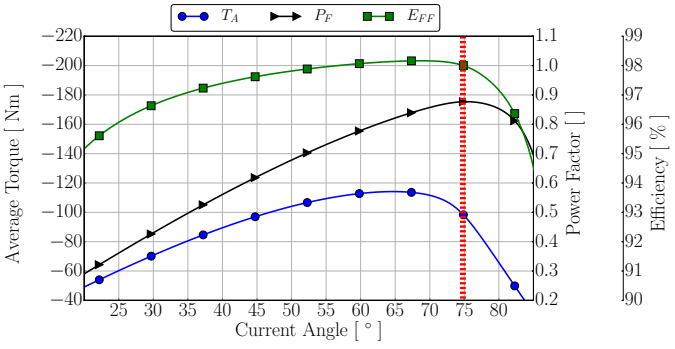

Figure 5.9: 6 Pole 5MW current angle map

Table 5.6: 6 Pole 5MW generator performance

Performance Results	
Average Torque [kNm]	-98.4
Power Out [MW]	**5.05**
Power Factor [ ]	**0.877**
Current Angle [°]	74.8
Efficiency [%]	**98.0**
Active Mass [tn]	26.6
Stack Length [m]	4.31
Stator Diameter [m]	1.45
Aspect Ratio [ ]	2.97

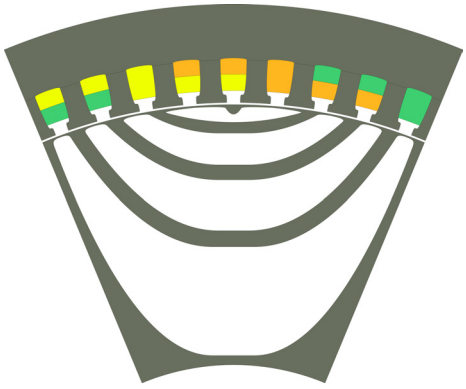

Figure 5.10: 8 Pole 5MW generator

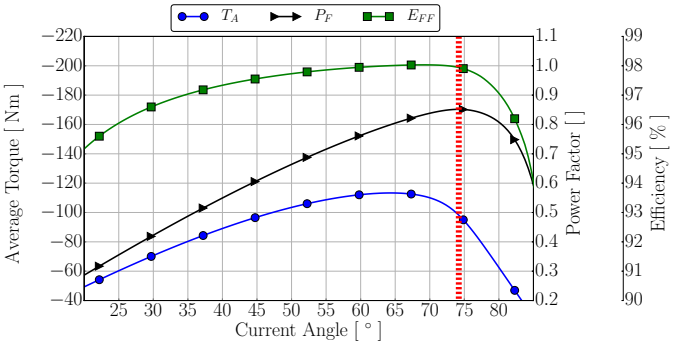

Figure 5.11: 8 Pole 5MW current angle map

Table 5.7: 8 Pole 5MW generator performance

Performance Results	
Average Torque [kNm]	-98.4
Power Out [MW]	**5.04**
Power Factor [ ]	**0.852**
Current Angle [°]	74.2
Efficiency [%]	**97.9**
Active Mass [tn]	18.0
Stack Length [m]	3.34
Stator Diameter [m]	1.51
Aspect Ratio [ ]	2.21

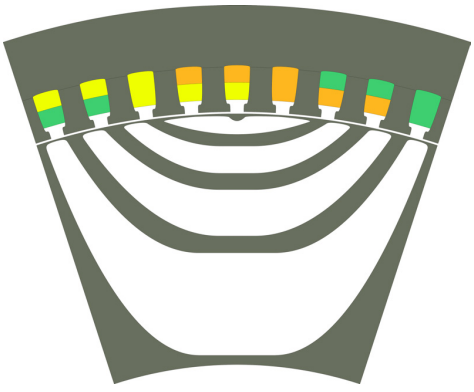

Figure 5.12: 10 Pole 5MW generator

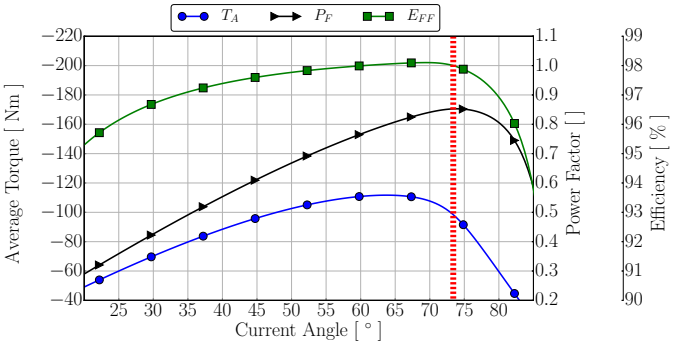

Figure 5.13: 10 Pole 5MW current angle map

Table 5.8: 10 Pole 5MW generator performance

Performance Results	
Average Torque [kNm]	-98.4
Power Out [MW]	**5.05**
Power Factor [ ]	**0.853**
Current Angle [°]	73.4
Efficiency [%]	**98.0**
Active Mass [tn]	14.8
Stack Length [m]	1.88
Stator Diameter [m]	1.89
Aspect Ratio [ ]	1.0

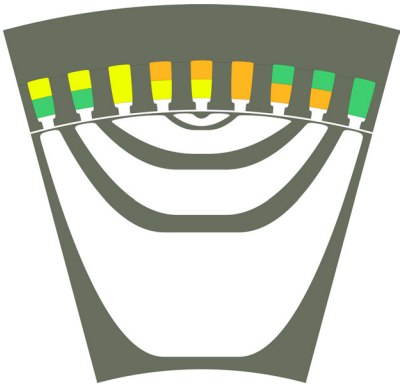

Figure 5.14: 12 Pole 5MW generator

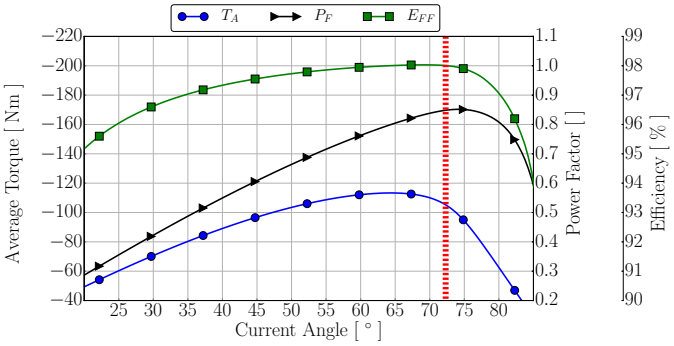

Figure 5.15: 12 Pole 5MW current angle map

Table 5.9: 12 Pole 5MW generator performance

Performance Results	
Average Torque [kNm]	-98.4
Power Out [MW]	**5.05**
Power Factor [ ]	**0.829**
Current Angle [°]	72.3
Efficiency [%]	**98.0**
Active Mass [tn]	12.4
Stack Length [m]	1.51
Stator Diameter [m]	2.00
Aspect Ratio [ ]	0.76

Figure 5.16: 14 Pole 5MW generator

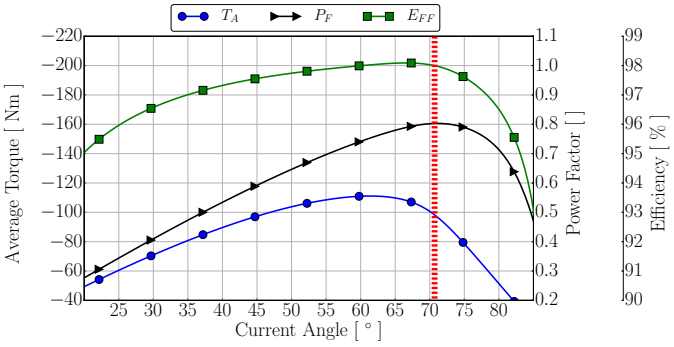

Figure 5.17: 14 Pole 5MW current angle map

Table 5.10: 14 Pole 5MW generator performance

Performance Results	
Average Torque [kNm]	-98.4
Power Out [MW]	**5.05**
Power Factor [ ]	**0.802**
Current Angle [°]	70.7
Efficiency [%]	**98.0**
Active Mass [tn]	11.6
Stack Length [m]	1.64
Stator Diameter [m]	1.94
Aspect Ratio [ ]	0.85

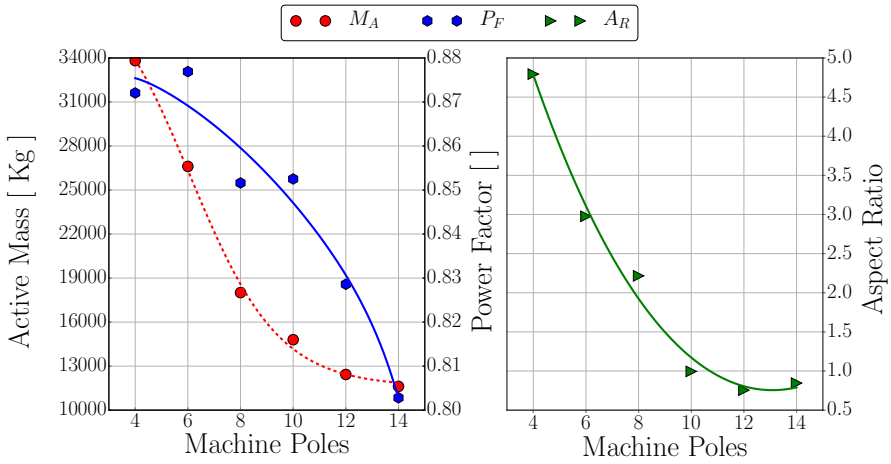

(a): Active mass, P_F and aspect ratio versus generator pole number.

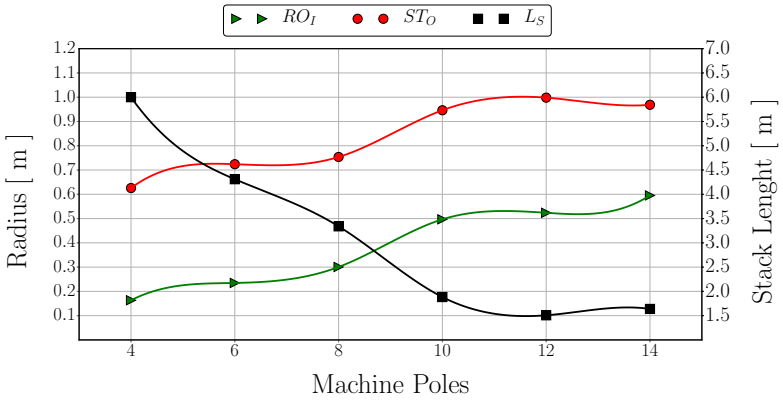

(b): Stack length, inside rotor and outside stator radius versus pole number.

Figure 5.18: 5 MW design optimisaition results.

In order to select an optimum generator for the specific power range, the active mass and P_F results in Table 5.4 are scaled by implementing equations

$$M_A^S(n) = \frac{M_A^M(n) - (M_A)_{min}}{(M_A^M)_{max} - (M_A^M)_{min}} \quad ; \quad n = 1, 2, .., 6 \tag{5.1.13}$$

and

$$P_F^S(n) = \frac{P_F^M(n) - (P_F^M)_{min}}{(P_F^M)_{max} - (P_F^M)_{min}} \quad ; \quad n = 1, 2, .., 6 \tag{5.1.14}$$

with

$$M_A^M = \begin{bmatrix} 33.8 & 26.6 & 18.0 & 14.8 & 12.4 & 11.6 \end{bmatrix} \tag{5.1.15}$$

and

$$P_F^M = \begin{bmatrix} 0.870 & 0.877 & 0.852 & 0.853 & 0.829 & 0.802 \end{bmatrix}. \tag{5.1.16}$$

The scaled results by implementing Equations 5.1.13 and 5.1.14 are presented in Figure 5.19. In this figure, the per unit deviation of the generator active mass and

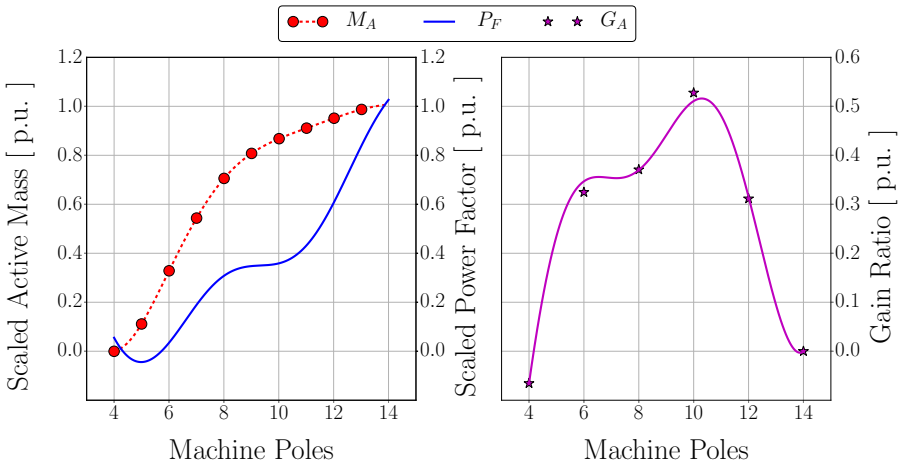

Figure 5.19: Scaled active mass, P_F and gain ratio plotted against generator pole number.

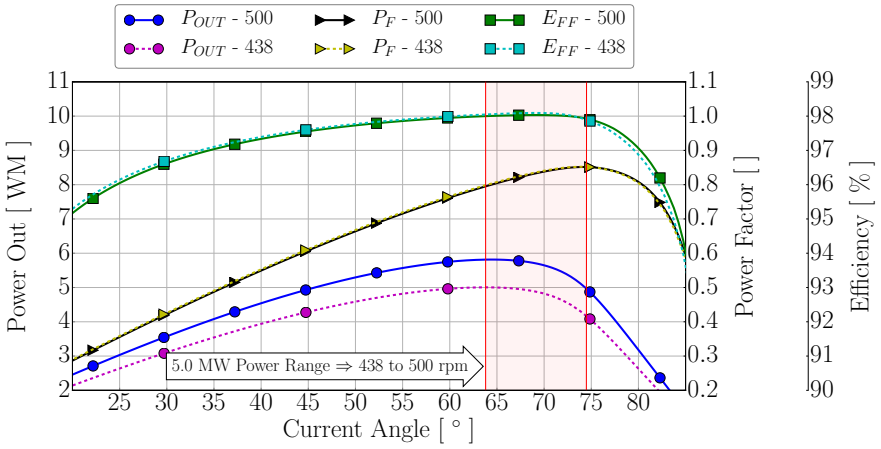

Figure 5.20: E_{FF}, P_F and P_{OUT} versus current angle change of the 10 pole megawatt generator at 438 and 500 rpm.

P_F is plotted against pole number change. The aim of this per unit transformation is to determine what generator pole number will be most suitable for operation in the 500 rpm, medium speed range. In order to determine this, the Gain ratios of the generators are calculated by,

$$G_A(n) = (1 - M_A^S(n)) - (1 - P_F^S(n)) \quad ; \quad n = 1, 2, ..., 6 \tag{5.1.17}$$

with $M_A^S(n)$ and $P_F^S(n)$ the scaled active mass and power factor results from Equations 5.1.13 and 5.1.14. The result of gain ratio calculation is shown in Figure 5.19. The gain ratio effectively describes the difference in reduction of M_A versus the reduction in P_F, with a large reduction in M_A and a low reduction in P_F yielding a high gain ratio. From Figure 5.19, it is clearly shown that the most gain is achieved by the ten-pole generator. This generator is thus selected for further analysis.

Presented in Figure 5.20 is the performance parameter plot against current angle change of the selected machine. Shown in Table 5.11 is the peak capability for each

Table 5.11: 10 Pole, megawatt optimisation results with 5 MW operating range between 438 and 500 rpm

Performance	T_A [kNm]	P_{OUT} [MW]	E_{FF} [%]	P_F [ ]	θ [°]
438 rpm ⇒ 500 rpm @ I_A = 1 p.u.					
$(T_A)_{MAX}$ |	-111.7 ⇒ -111.7	**5.00** ⇒ 5.73	98.0 ⇒ 98.0	0.799 ⇒ 0.799	63.8 ⇒ 63.8
$(E_{FF})_{MAX}$ |	-108.8 ⇒ -108.7	4.90 ⇒ 5.58	98.1 ⇒ 98.1	0.834 ⇒ 0.837	68.8 ⇒ 69.3
$(P_F)_{MAX}$ |	-95.8 ⇒ -95.5	4.31 ⇒ **5.00**	98.0 ⇒ 98.0	0.852 ⇒ 0.853	73.9 ⇒ 73.5

T_A - Average Torque ; P_{OUT} - Terminal Power Out ; P_F - Power Factor ; θ - Current Angle ; E_{FF} - Efficiency

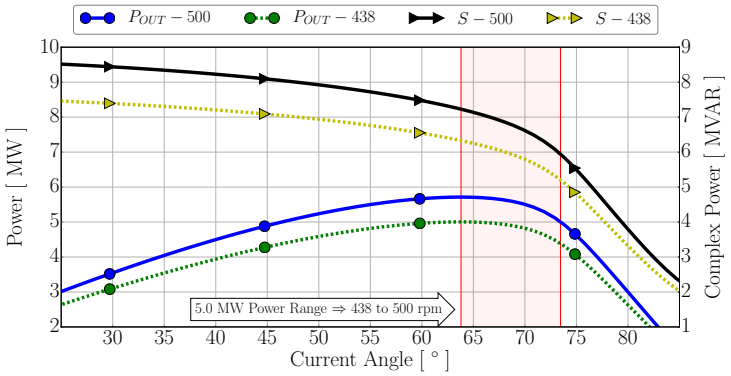

Figure 5.21: P_{OUT} and S versus current angle change of the 10 pole megawatt generator at 438 and 500 rpm.

of the performance parameters. Seen in the results, the generator performance envelope fixed at 5 WM is between 438 and 500 rpm, with E_{FF} above 98% and P_F between 0.8 and 0.85, with the current angle values between 63 and 74 °.

A further analysis of the machine's complex power (S) versus current angle change is shown in Figure 5.21 and in Table 5.12 for the two speed ranges, 438 and 500 rpm. As can be seen in this figure and table, the minimum required drive rating to achieve 5 MW at 500 rpm is 5.8 MVAR. If, however, the drive rating is increased by 8% to 6 MVAR, the generators constant power speed range can be improved, with the generator able to operate at a conspicuous 5 MW between 438 and 500 rpm.

5.1.4 Core Loss

In order to validate the core loss estimation technique implemented in the optimisation study, presented in Chapter 2.4, an additional core loss calculation is done on the selected 10 pole machine. For this estimation, the well known Steinmetz equation [109] is implemented to calculate both the core losses on the stator and rotor.

The motivation for implementing the initial, simplified core loss estimation tech-

Table 5.12: 10 Pole, megawatt optimisation results with 5 MW operating range between 438 and 500 rpm

Shaft Sped	P_{OUT} [MW]	S [MVAR]	E_{FF} [%]	P_F [ ]	θ [°]
438 rpm ⇒ 500 rpm @ I_A = 1 p.u.					
438 rpm	5.0	6.3 [**1.00 p.u.**]	98.0	0.799	63.8
500 rpm	5.0	5.8 [**0.92 p.u.**]	98.0	0.852	73.5

T_A - Average Torque ; P_{OUT} - Terminal Power Out ; P_F - Power Factor ; θ - Current Angle ; E_{FF} - Efficiency

Table 5.13: 10 Pole, megawatt machine core loss comparison.

Model Area	P_C **- Kamper** [W]	P_C **- Steinmetz** [W]	**Deviation** ★ [p.u.]
Rotor	0	2100	0.0
Stator Tooth	8363	7851	1.065
Stator Yoke	21570	19020	1.134
Total	29900	28900	1.035

★ - Steinmetz results used as p.u. value i.e. P_C - Kamper / P_C - Steinmetz

nique is twofold, firstly, the estimation only implements the material properties of the stator and its model dimensions. Considering the large variability of the rotor profile, this simplified the post processing of each simulation step and reduced the possibility of incorrect calculation for rotor core losses. Secondly, and more importantly, this technique only requires a few static step solutions in order to estimate the core losses, versus the complete hysteresis loop required by the Steinmetz equation. Considering the small static steps required during simulation to accurately model torque harmonics, the simulation time required to model both one complete hysteresis loop and an accurate torque harmonic wave would be infeasible during the optimisation on the large model.

The Steinmitz core loss estimation implements equation

$$P_C = C_m F^{\alpha} B^{\beta} \tag{5.1.18}$$

as presented in [109]. This loss calculation is a built in function of the finite element simulation package that calculates the losses per mesh element for the simulation model over an electrical period. The calculated losses for the rotor, stator tooth and stator yoke is shown in Table 5.13. Clearly seen from the table is the conservative estimation of the implemented technique, with a combined core loss deviation between the two techniques of only 3.5 %.

Shown in Figure 5.22 is the core losses estimated for each mesh element by implementing the Steinmetz equation. Clearly seen from this figure and Table 5.13,

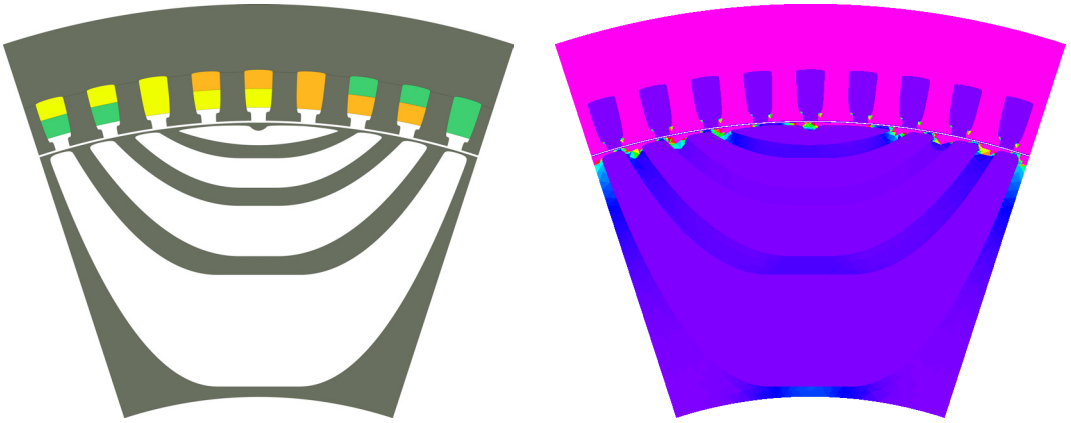

(a): Generator model **(b):** Steinmetz core losses

Figure 5.22: 10 Pole, RSG 5MW Steinmetz core loss.

the majority of the core losses can be found in the stator, with minimal losses on the rotor mostly concentrated on the rotor surface as expected.

Considering the current optimisation time of between 188 and 887 hours for each of the models, the implementation of the Steinmetz equation during optimisation would simply not be feasible. Especially considering the negligible effect it has on the combined machine losses, and the machine efficiency as a result.

5.2 Assisted Reluctance Synchronous Generator Design

In this section, the design and optimisation of a wound field, assisted reluctance synchronous generator (ARSG) is discussed. Additionally, the generator design includes the implementation of the DC-link current as field current. The implementation of the DC-link current as field current was first proposed by Kamper in [49], with the study focusing on the design of a compensated and assisted wound field motor in the 1.5 KW power range.

In order to study the effects of implementing a DC-linked field winding in the megawatt power range, the ten-pole generator stator found to be most competitive in the medium speed range is implemented. The study consists of a retrofit rotor design optimisation study, with the ten-pole RSG directly compared to the retrofit rotor ARSG.

5.2.1 Model

The proposed model implementing the DC-link current as field current is presented in Figure 5.23a, with a representation of the rotor in Figure 5.23b. With the addition of this assisting field winding, the contributing d-axis flux linkage needs to be incorporated in the generator model, with the updated equivalent DQ-circuit and phasor diagram seen in Figure 5.24. With the addition of the field winding, the respective flux linkages are now calculated by

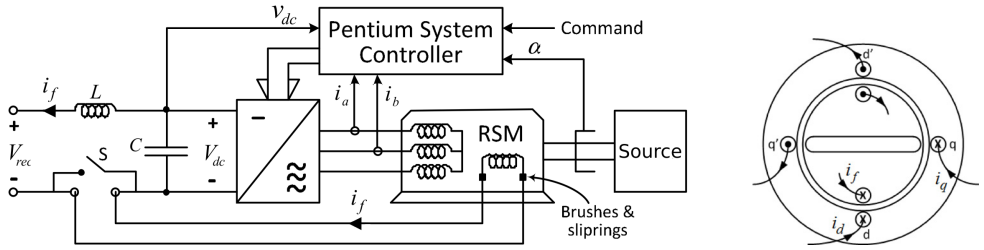

(a): DC-link rotor current ARSG drive system. **(b):** ARSG

Figure 5.23: Assisted reluctance synchronous generator drive system [49].

$$\lambda_d = \lambda_{ds} + \lambda_{df} = L_d I_d + L_{df} i_f \tag{5.2.1}$$

$$\lambda_q = \lambda_{ds} = L_q I_q \tag{5.2.2}$$

$$\lambda_f = \lambda_{ff} + \lambda_{df} = L_f I_f + L_{df} i_d \tag{5.2.3}$$

with the rest of the equivalent circuit parameters estimated as set out in Section 2.4.

In order to accurately simulate the proposed drive system, the equation

$$P_F = I_{DC} V_{DC} / N_{INV} = 3 V_S I_S cos\theta = P_S \tag{5.2.4}$$

must hold, with the equation effectively describing the power balance between the generator and the DC-link, with N_{INV} the inverter efficiency. In order to effectively estimate and balance Equation 5.2.4, I_{DC} and V_{DC} must be estimated. Furthermore, because of the additional assisting flux of the field winding, generator performance parameters like P_F and V_S are also affected, thus forcing an iterative approach to solving and balancing Equation 5.2.4.

The iterative estimation consists of the following steps :

1) The simulation of the RSG with field current equal to zero, i.e switch S closed in Figure 5.23. From this initial simulation V_S and P_F are estimated and the initial terminal power P^1_{OUT} is recorded.

2) V_{DC} is then in turn calculated by

$$V_{DC} = \sqrt{2}\sqrt{3} V_S \tag{5.2.5}$$

with the equation assuming a loss less inverter and space vector modulation at a unity modulation index. I_{DC} is then estimated by rewriting the power balance equation to

$$I_F = \frac{3 V_S I_S N_{INV} cos\theta}{V_{DC}}. \tag{5.2.6}$$

with N_{INV} set conservatively to 96%. The number of winding turns can then be calculated by

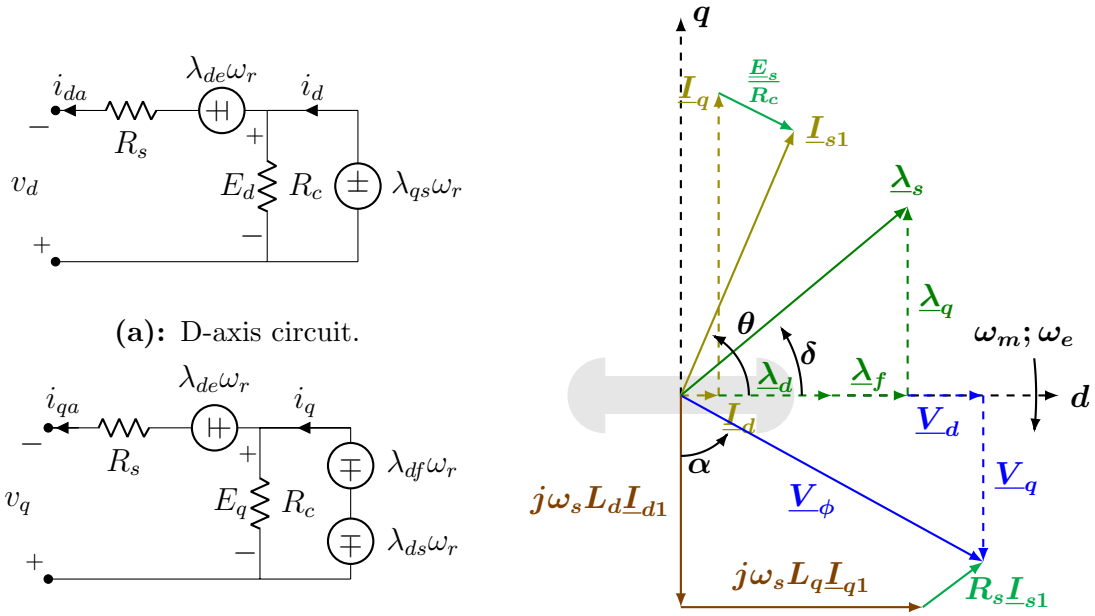

(a): D-axis circuit.

(b): Q-axis circuit.

(c): Generator phasor diagram.

Figure 5.24: Equivalent OCC, SCC diagrams implemented in testing.

$$Z_F = round[\frac{J_F F_{FF} F_A}{I_F}] \tag{5.2.7}$$

with J_F the field current density, F_{FF} the field winding fill factor, F_A the available rotor slot area for the field winding and with I_F the field current equal to the DC-link current previously calculated. Because the winding number Z_F must be an integer to realistically represent the field winding, the answer from Equation 5.2.7 is rounded off to the nearest integer. The field winding parameters are

$$J_F = 4.5A/mm^2 \qquad F_{FF} = 0.35 \tag{5.2.8}$$

with F_A determined directly from the FE simulation package.

The coil wire length for one winding turn is calculated by

$$L = 0.5(L_S + 2L_{arc})P \tag{5.2.9}$$

with L_S the stack length and with L_{ARC} the end winding arc length calculated by implementing Figure 2.11 and Equations 2.4.12 to 2.4.17 in Chapter 2. The winding resistance is then in turn estimated by

$$\Omega_F = \frac{0.5\rho Z_F L}{F_{FF} F_A}. \tag{5.2.10}$$

with the field resistance implemented to estimate the correct V_{DC} by implementing

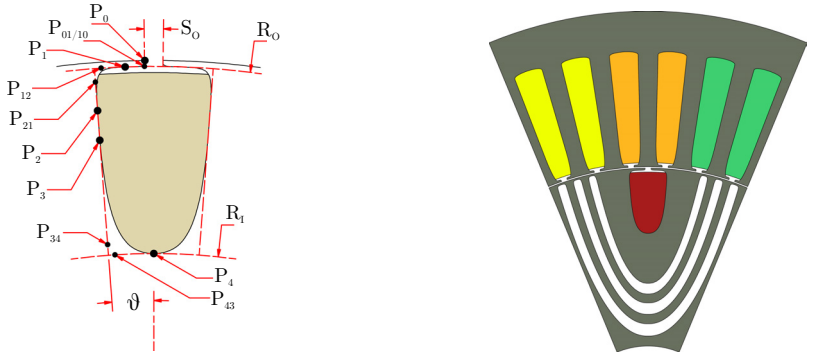

(a): Proposed rotor slot **(b):** Proposed Rotor

Figure 5.25: Proposed ARSM rotor slot design.

Table 5.14: Variables of the proposed rotor slot.

Rotor Slot Main Point		
Polar	R	θ
P_0	ROO	$0.5\pi + 0.5S_O$
P_1	$R_O = ROO - 5mm$	$0.5(\theta_{P_2} - \theta_{P_0}) + \theta_{P_0}$
P_2	R_{P_2}	θ_{P_2}
P_3	R_{P_3}	θ_{P_2}
P_4	R_{P_4}	θ_{P_4}
Spline Angle Points		
$P_{01} = P_{10}$	R_{P_1}	$0.5(\theta_{P_1} - \theta_{P_0}) + \theta_{P_1}$
$P_{12} = P_{21}$	R_{P_1}	$0.5(\theta_{P_2} - \theta_{P_1}) + \theta_{P_2}$
P_{34}	$R_{P_{34}}$	θ_2
P_{43}	R_{P_4}	θ_{43}

$$V_{DC} = V_{rec} + I_F \Omega_F. \tag{5.2.11}$$

With V_{DC} re-estimated, Equations 5.2.6 and 5.2.7 is re-calculated for a more accurate result. Finally, taking into consideration the V_S and P_F change, the I_S for the stator is updated with

$$I_S = \frac{P^1_{OUT}}{3V_S cos\theta} \tag{5.2.12}$$

with P^1_{OUT} equal to the initial power calculated from the RSG simulation step one where $I_F = 0$. The problem is then solved by iteratively repeating step two until the power balance Equation 5.2.4 holds.

3) Finally the efficiency of the machine is updated with the addition of the field winding resistance losses, with

$$P^R_R = I^2_F R_R \tag{5.2.13}$$

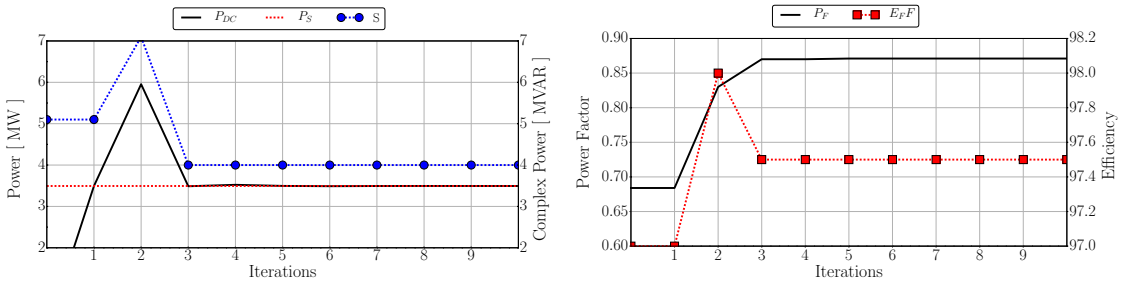

(a): Power balance **(b):** P_F and E_{FF}.

Figure 5.26: ARSG iterative power balance estimation.

with the total losses estimated with Equation 2.5.10 adapter to include the rotor losses

$$P_T = P_B + P_{W\&V} + P_R + P_C + P_R^R. \tag{5.2.14}$$

Effectively, during the estimation of the field current, the stator current density is reduced in order to compensate for the P_F and V_S increase as a result of the added field winding. The main motivation for implementing this current density reduction technique lies in the retrofit machine design being proposed. Because of the limitations of implementing an existing stator, the power level of the machine needs to be kept within the desired constraints. Considering the initial results, a much more competitive machine would be possible if the entire machine, which includes the rotor and stator, is implemented in the machine's design optimisation. This complex design study however falls beyond the scope of this study.

To study the effectiveness of the proposed, iterative solver, a rotor slot model is developed, seen in Figure 5.25. The rotor slot consists of four main points connected by the same bezier spline implement in Chapter 3 and described in Appendix B.2. The implementation of the spline gives the optimiser the ability to shape the rotor slot to form part of the flux barrier profile. The rotor slot variables are set out in Table 5.14, with the total number of variables for the slot equal to seven. Finally, in order to have a realistic rotor slot opening, the slot opening angle is defined by

$$S_O = 0.6\theta_{P_2} \tag{5.2.15}$$

which defines the rotor slot opening fixed at 60% of the rotor slot width. The motivation for this is:

1. to allow a large opening to effectively wind the rotor and
2. to generate a more realistic rotor profile, with a large overhanging slot bridge not feasible.

In order to determine the number of iterations required before the power equation is balanced, an initial study is done on an un-optimised rotor. The results of this initial study is shown in Figure 5.26 and in Table 5.15. As seen from the figure,

Table 5.15: Simulation Loop Results.

Sim	P_{Field} [MW]	P_S [MW]	S [MVAR]	I_s [p.u.]	P_F [ ]	V_S [p.u.]	V_{DC} [p.u.]	I_F [p.u.]	Z_F [ ]	E_{FF} [%]
0	**0.0**	**3.49**	**5.1 [1.0 p.u.]**	**1.0**	**0.684**	**1.00**	**1.0**	**0.0**	**1**	**97.0**
1	3.49	3.49	5.1 [1.0 p.u.]	1.00	0.684	1.00	1.0	1.35	13	97.0
2	5.95	3.49	7.1 [1.39 p.u.]	0.587	0.830	1.41	1.40	1.63	10	97.0
3	3.48	3.49	4.0 [0.78 p.u.]	0.588	0.870	1.34	1.34	1.00	17	98.0
4	3.52	3.49	4.0 [0.78 p.u.]	0.583	0.870	1.35	1.35	1.00	17	97.5
5	**3.49**	**3.49**	**4.0 [0.78 p.u.]**	**0.583**	**0.871**	**1.35**	**1.35**	**1.00**	**17**	**97.5**

P_{Field} - Field winding power ; P_S Stator power ; I_S - Stator current ; P_F - power factor ; V_S - Stator phase voltage ; V_{DC} - Bus voltage ; I_F - Field current ; Z_F - Field turn number ; E_{FF} -Efficiency ; S - Complex Power

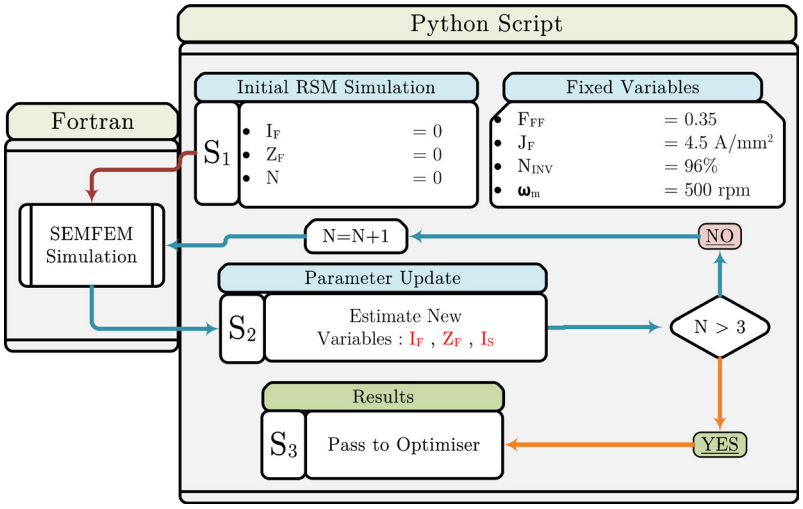

Figure 5.27: Estimation flow diagram.

the power equation is balanced within three iterations. Furthermore, looking at the results in the table, a drastic increase in P_F is achieved, from 0.684 to 0.871, with the E_{FF} and generator P_{OUT} kept constant. Additionally, it can be noted that the reduction in stator current density during the estimation proved to be effective, with the power level kept constant after a 41.7% reduction in current magnitude. Most importantly, it is noted that the required inverter rating for the machine is drastically reduced from 5.1 MVAR to 4.0 MVAR, a more than 20% reduction.

Considering the results, it is shown that the power balance can be achieved within three iterations and that the field winding model is highly effective in increasing the machine power factor and hence reducing the required inverter rating. Taking this into consideration, the simulation strategy that is implemented for each optimisation function call is developed and presented in Figure 5.27. In this diagram, the initial step for the RSG simulation is represented by S_1, with the field winding estimation conducted in step S_2. This step is then iteratively repeated until the simulation steps exceed 3, with the initial RSG simulation counted as iteration zero.

Due to the iterative nature of the solution process, extensive optimisation time

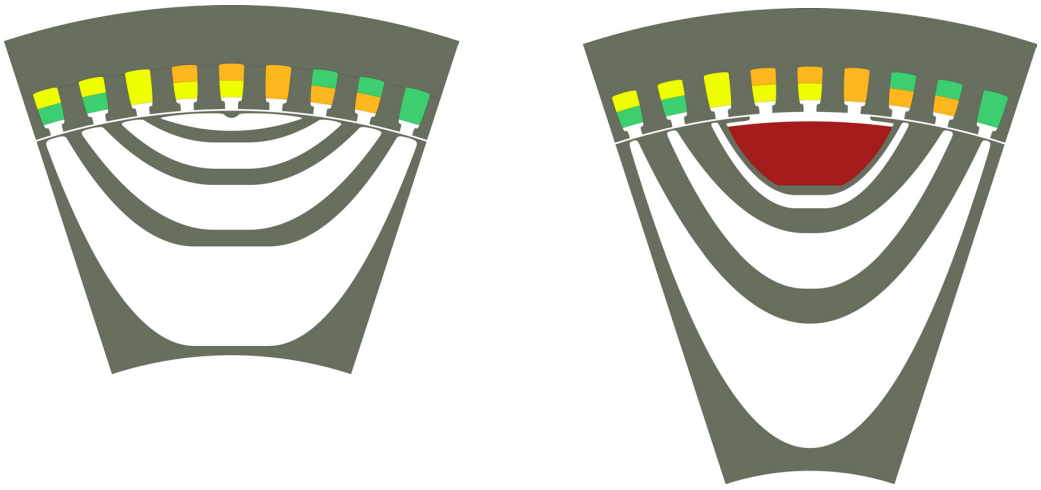

(a): 10 Pole 5 MW RSG **(b):** 10 Pole 5 MW ARSG

Figure 5.28: RSG and ARSG optimised rotor profiles.

is expected. This is among the main reasons why an existing stator, with retrofit rotor, is implemented for the optimisation study. Furthermore, as with the RSG study, symmetric flux barriers are implemented, with a large reduction in variables compared to the asymmetric flux barriers. Finally, for this study, the rotor slot is seen as a flux barrier, thus for the model, only three flux barriers are implemented, with the rotor slot forming the fourth in order to directly compete with the designed ten-pole RSG. The total number of variables are 24, which includes the rotor inner radius, the seven rotor slot variables, the five variables per flux barrier and the current angle. The variables are represented by

$$X_{12} = \begin{bmatrix} \alpha & \beta & R & P_{1sp} & P_{3sp} & \theta & RO_I & R_{P_2} & R_{P_3} & R_{P_4} & R_{P_{34}} & \theta_{P_2} & \theta_{P_4} & \theta_{P_{43}} \end{bmatrix}^T \tag{5.2.16}$$

5.2.2 Optimisation Study

For the optimisation study, the same optimisation strategy and optimisation suite PyOpt is implemented as for the RSG study, with the optimisation flow diagram once again implemented as in Chapter 4, Figure 4.4. The only addition to the strategy is instead of directly calling the SEMFEM package per function call, the iterative solver in Figure 5.27 is called per function call. In order to draw a direct comparison between the RSG and ARSG, the exact same optimisation method is also implemented, with the penalty function, along with the respective weights one again implemented. The optimization consists of the minimisation of the objective function equation

$$P_O = W_1 P_P^H + W_2 P_P^L + W_3 P_\eta^L - P_F(X_{12}) \tag{5.2.17}$$

$$\text{Subject to :} \quad \begin{cases} 0 \leqslant G_j(X_{12}) \leqslant 1 \quad ; \quad j = 1, 2, ..., n \\ 5.0MW \leqslant P_{OUT}(X_{12}) \leqslant 5.05MW \\ E_{FF}(X_{12}) \geqslant 98.0\% \end{cases} \tag{5.2.18}$$

with the penalty function for power level exceeding the constrained value

$$P_P^H = \begin{cases} (P_{OUT} - P_H)/P_H \quad ; \quad P_{OUT}(X_{12}) > 5.05MW \quad : \quad P_H = 5.05MW \\ 0.0 \quad ; \quad P_{OUT}(X_{12}) < 5.05MW \end{cases} \tag{5.2.19}$$

The penalty function with power level below the constraint value is

$$P_P^L = \begin{cases} (P_L - P_{OUT})/P_{OUT} \quad ; \quad P_{OUT}(X_{12}) < 5.00MW \quad ; \quad P_L = 5.0MW. \\ 0.0 \quad ; \quad P_{OUT}(X_{12}) > 5.00MW \end{cases} \tag{5.2.20}$$

and the E_{FF} penalty function is defined by

$$P_\eta^L = \begin{cases} (E_L - E_{FF})/E_{FF} \quad ; \quad E_{FF}(X_{12}) < 98.0\% \quad ; \quad E_L = 98\%. \\ 0.0 \quad ; \quad E_{FF}(X_{12}) > 98.0\% \end{cases} \tag{5.2.21}$$

with the penalty weights for each of the respective penalties defined by

$$W_1 = 5 \quad ; \quad W_2 = 5 \quad ; \quad W_3 = 20 \tag{5.2.22}$$

As with the RSG study, the optimisation was conducted at a fixed shaft speed of 500 rpm, with the stator parameters identical to the RSG model parameters.

5.2.3 Result Analysis

The optimised ARSG rotor is shown in Figure 5.28, with the converged generator parameters shown in Table 5.16. The initial clear observation that can be made is the large reduction in internal rotor radius, this to accommodate the new rotor slot winding. Furthermore, when analysing the results in Table 5.16, a large reduction in the stator current density is seen, from 4.5 to 2.5 A/mm^2, this to be expected from the design model.

The parameter map across the current angle range for the ARSG is shown in Figure 5.29. As seen in this map, the optimised machine is capable of operating not only as the first row results indicate in Table 5.16, but up to unity P_F at just over 90 degrees current angle. The reason why the optimiser converged on this point is twofold, firstly because the field winding number must be a integer, the optimiser converged to the closest possible solution considering the constraints and objective.

Table 5.16: 10 Pole ARSG optimisation results

Optimisation Results										
I_S [p.u.]	T_A [kNm]	P_{OUT} [MW]	S [MAR]	P_F [ ]	θ [°]	E_{FF} [%]	M_A [tn]	Z_F [ ]	J_F [A/mm^2]	J_S [A/mm^2]
1.00	-97.5	**5.0**	5.36	**0.94**	74.5	**98.0**	18.6	15	4.50	2.50
0.955	-97.5	**5.0**	5.05	**1.00**	94.0	**98.0**	18.6	15	4.67	2.39

T_A - Average Torque ; P_{OUT} - Terminal Power Out ; S - Complex Power ; P_F - Power Factor ; θ - Current Angle ; E_{FF} - Efficiency ; M_A - Active Mass ; J_F - Field winding current density ; Z_F - Field winding turns ; J_S - Stator winding current density

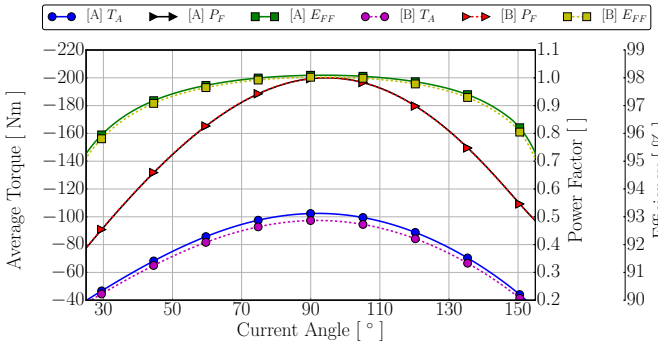

Figure 5.29: ARSG current angle map results of : [A] $I_S = 1.0$ p.u ; [B] $I_S = 0.955$ p.u.

Secondly, the rotor field current density was restricted to 4.5 A/mm^2, with the optimiser limiting the operating point to this value as seen in Table 5.16. In order to operate at the unity P_F point at a higher current angle, the current magnitude is reduced by 4.5 % in order to operate on the 5 MW power level, with this current angle map also shown in Figures 5.29 and 5.30, with the results in row two in Table 5.16.

A comparison between the maximum operating performance parameters of the RSG and the retrofitted ARSG is shown in Table 5.17. In this table, the maximum performance parameters T_A, P_F and E_{FF} of the RSG and the ARSG is compared, with the ARSG operating with the switch S in Figure 5.23a open and closed, i.e with and without the field winding supplied with current. Further comparisons between the RSG and ARSG are shown in Figures 5.31, with P_F, T_A and E_{FF} compared for the two respective states of the ARSG, when $I_F = 0$ and 1 p.u.

When analysing the results in Table 5.17, considering the RSG and ARSG with $I_F = 0$ p.u., it is shown that even though the ARSG reluctance only performance is slightly reduced when compared with the RSG, P_{OUT} at the maximum E_{FF} and P_F point still exceeds the desired 5 MW constraint. Furthermore, E_{FF} of the two machines are identical, with a reduction of $\pm 5\%$ in P_F from 0.853 to 0.817 at the maximum P_F operating point.

However, when considering the ARSG with field current, it completely outperforms the RSG when considering P_F, with the ARSG also able to operate at unity P_F at close to its maximum P_{OUT} and E_{FF} operating points. Furthermore, when considering the T_A versus current angle plots in Figures 5.31b, 5.31d and 5.31f, it

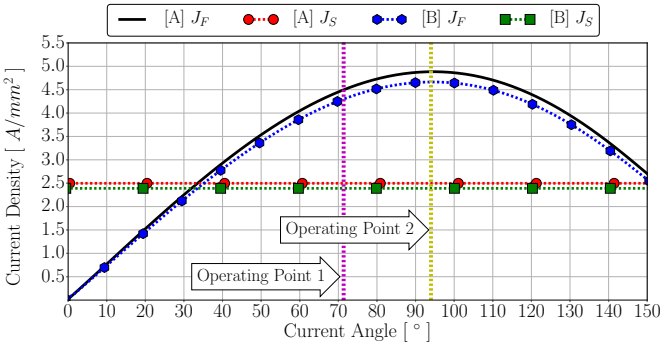

Figure 5.30: ARSG current angle map results of the rotor and field current density for: [A] $I_S = 1.0$ p.u for Operating Point 1; [B] $I_S = 0.955$ p.u. for Operating Point 2

Table 5.17: 10 Pole RSG and ARSG maximum performance parameters.

Performance Parameter / **Generators**	T_A [kNm]	P_{OUT} [MW]	P_F []	θ [°]	E_{FF} [%]
Performance Results		(T_A)$_{MAX}$			
RSG	-111.7	5.85	0.80	63.8	98.1
ARSG : $I_F = 0$ p.u. ; $I_S = 1$ p.u.	-116.0	6.08	0.763	62.8	98.0
ARSG : $I_F = 1$ p.u. ; $I_S = 1$ p.u.	-102.4	5.36	1.0	92.0	98.1
Performance Results		(P_F)$_{MAX}$			
RSG	-96.4	5.05	0.853	73.9	98.0
ARSG : $I_F = 0$ p.u. ; $I_S = 1$ p.u.	-99.6	5.22	0.817	73.8	97.8
ARSG : $I_F = 1$ p.u. ; $I_S = 1$ p.u.	-102.2	5.36	1.0	95.0	98.1
Performance Results		(E_{FF})$_{MAX}$			
RSG	-108.7	5.69	0.837	69.3	98.1
ARSG : $I_F = 0$ p.u. ; $I_S = 1$ p.u.	-115.5	6.05	0.785	65.8	98.0
ARSG : $I_F = 1$ p.u. ; $I_S = 1$ p.u.	-102.4	5.36	1.0	93.0	98.1

T_A - Average Torque ; P_{OUT} - Terminal Power Out ; P_F - Power Factor ; θ - Current Angle ; E_{FF} - Efficiency ; I_F - Rotor field current

is clear that with the addition of the field current, the ARSG performs very similar to traditional, wound field salient pole synchronous machines, as expected. These results show that, for operation on and below unity operating speeds, ARSG's are capable of extremely competitive performance, with E_{FF} and power levels comparable with RSG's, but with the additional capability of operating at unity P_F.

An additional comparison of required drive rating between the RSG and ARSG is shown in Figure 5.32 and Table 5.18. In this figure and table, the complex power is compared for both machines operating at 500 rpm and 5 MW rated power, the initial design objectives for the generator, with the ARSG operating at a reduced current magnitude in order to operate at unity P_F.

As clearly seen in these results, a large reduction in required inverter rating is

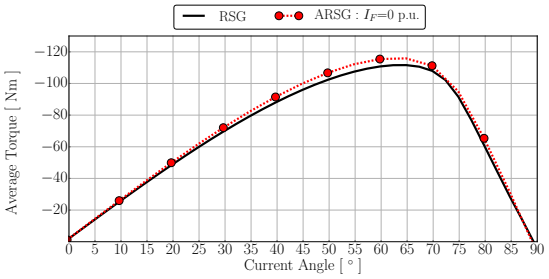

(a): T_A against current angle change for the **RSG** versus **ARSG** with I_F= 0 p.u.

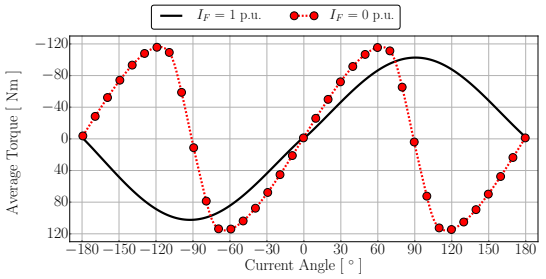

(b): **ARSG** T_A against current angle change with I_F= 0 & 1 p.u.

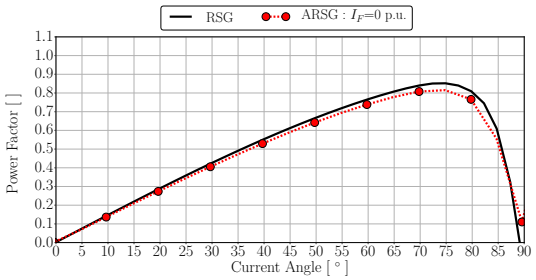

(c): P_F against current angle change for the **RSG** versus **ARSG** with I_F= 0 p.u.

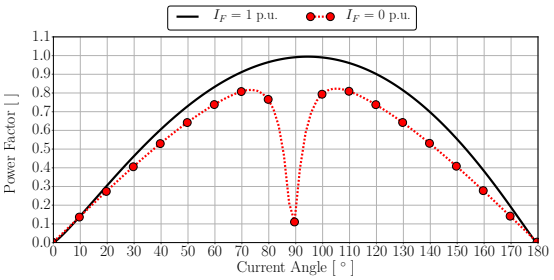

(d): **ARSG** P_F against current angle change with I_F= 0 & 1 p.u.

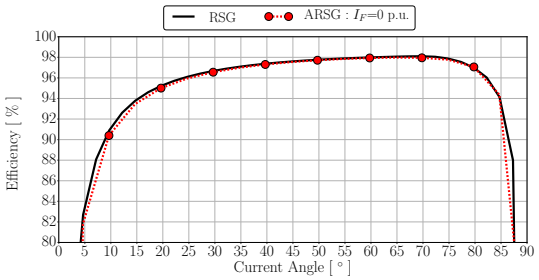

(e): E_{FF} against current angle change for the **RSG** versus **ARSG** with I_F= 0 p.u.

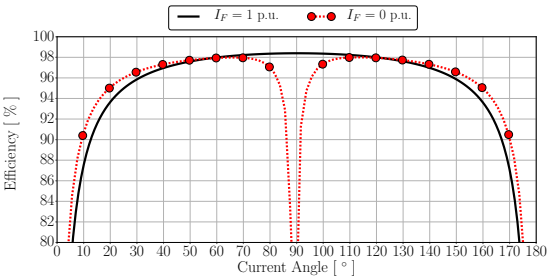

(f): ARSG E_{FF} against current angle change with I_F= 0 & 1 p.u.

Figure 5.31: Optimised generator performance comparison between the RSG and ARSG versus current angle change, with the ARSG operating with and without field current.

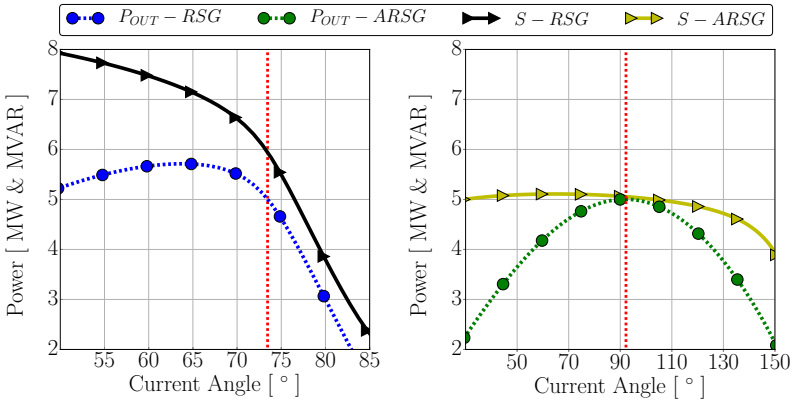

Figure 5.32: Operating point inverter rating requirement for the RSG versus ARSG.

Table 5.18: 10 Pole, megawatt optimisation results at 5 MW operating point with shaft speed 500 rpm

Machine	P_{OUT} [MW]	S [MVAR]	E_{FF} [%]	P_F [ ]	θ [°]	J_S [A/mm^2]	J_F [A/mm^2]
RSG	5.0	5.8 [**1.00 p.u.**]	98.0	**0.852**	73.5	4.5	0.0
ARSG	5.0	5.05 [**0.871 p.u.**]	98.0	**1.00**	94.0	2.39	4.67

T_A - Average Torque ; P_{OUT} - Terminal Power Out ; P_F - Power Factor ; θ - Current Angle ; E_{FF} - Efficiency ; S - Complex Power ; J_S - Stator Current Density ; J_F - Rotor Current Density

achieved with the ARSG retrofit rotor, with the required level reduced by around 13%. This critically shows that by implementing the assisted winding on the rotor, the ARSG is highly competitive in the current 5 MW power market that is dominated by permanent magnet generators.

In an analysis of the optimised rotor profile, it is noted that the rotor slot and 3^{rd} flux barrier are in close proximity. This profile result is most likely because of the limited space the optimiser had to work within, with the stator dimensions fixed for the retrofit rotor study. Once again this also illustrates that, in order to achieve a more optimum machine package, a complete machine must be optimised, that includes the rotor and stator profiles. This statement is further motivated by the fact that the current machine stator operates at only 2.39 A/mm^2 in order to fall within the required power range. By optimising the complete machine package, the stator diameter will most likely be reduced, with an increase in current density as a result. However, as previously stated, this complete machine investigation falls outside the scope of the present study.

5.3 Core Loss

As with the RSG study, in order to validate the core loss estimation implemented in the optimisation an additional core loss calculation is done on the ARSG machine.

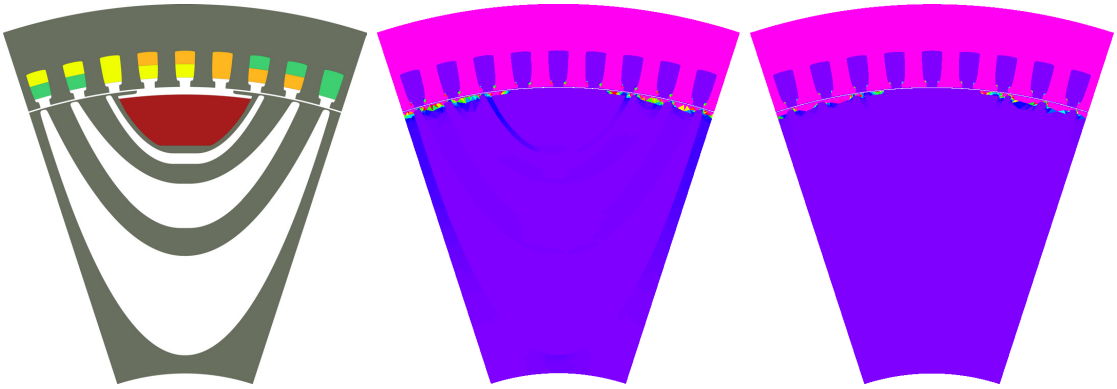

(a): Generator model **(b):** $I_F = 0$ p.u. $\theta = 64°$ **(c):** $I_F = 1$ p.u. $\theta = 94°$

Figure 5.33: 10 Pole, 5MW Steinmetz core loss.

Table 5.19: 10 Pole, ARSG megawatt machine core loss comparison.

Model Area	P_C **- Kamper** [W]	P_C **- Steinmetz** [W]	**Deviation** [p.u.]
$\boldsymbol{I_S = 1}$ **p.u.** ; $\boldsymbol{I_F = 0}$ **p.u.** ; $\boldsymbol{P_{OUT} = 2.4}$ **MW** ; $\boldsymbol{J_S}$ = 2.39 $\boldsymbol{A/mm^2}$			
Rotor	0	930	0.0
Stator Tooth	5902	7004	0.843
Stator Yoke	22619	16515	1.370
Total	28521	24450	1.167
$\boldsymbol{I_S = 1}$ **p.u.** ; $\boldsymbol{I_F = 1}$ **p.u.** ; $\boldsymbol{P_{OUT} = 5}$ **MW** ; $\boldsymbol{J_S}$ = 2.39 $\boldsymbol{A/mm^2}$			
Rotor	0	1334	0.0
Stator Tooth	13606	17224	0.790
Stator Yoke	42235	47172	0.895
Total	55800	65730	0.849

Once again, the additional investigation consisted of the implementation of the built in Steinmetz equation [109] to estimate core losses in the entire machine.

The results of the estimation was applied to the ARSG with $I_F = 0$ and 1 p.u. in order to compare the estimation for both rotor models. The results of the comparison is shown in Table 5.19 and in Figures 5.33.

As can be seen in the results for $I_F = 0$ p.u., the implemented model during optimisation once again shows conservative results, with the model's estimated losses 16 % higher than that of the Steinmetz equation, with this result similar to the finding for the 10 pole RSG machine. However, for the ARSG, the opposite was found, with the implemented model underestimating the core losses by 15 % compared to the Steinmetz equation.

Table 5.20: 10 Pole, megawatt optimisation core lost comparison.

Machine	Core Loss Model	P_{OUT} [MW]	P_C [kW]	E_{FF} [%]
RSG	Kamper	5.0	29.9	98.0
RSG	Steinmetz	5.0	28.9	98.0
ARSG : $I_F = 0$ p.u.	Kamper	2.39	28.5	97.0
ARSG : $I_F = 0$ p.u.	Steinmetz	2.39	24.5	97.2
ARSG : $I_F = 1$ p.u.	Kamper	5.0	55.8	98.0
ARSG : $I_F = 1$ p.u.	Steinmetz	5.0	65.7	97.8

P_{OUT} - Terminal Power Out ; E_{FF} - Efficiency ; P_C - Core Losses

When considering the effect these variations between the models have on the total efficiency, the variation is considered almost negligible, with the results of the estimation shown in Table 5.20. For the RSG study, there is no effect on the machine efficiency, with both models producing an overall efficiency of 98 %. For the ARSG study, the deviation of the models only had a 0.2 % effect for both where $I_F = 0$ and 1.0 p.u., with the total machine efficiency reducing from 98.0 to 97.8 % for $I_F = 1$ p.u. and a 2% increase for the model where $I_F = 0$ p.u.

Considering the unrealistic increase in simulation time the Steinmetz equation requires, and the multiple simulations required for one function call to balance the energy balance, the implementation of the Steinmetz equation in optimisation would be simply infeasible with the current equipment available during the study. This especially considering the current optimisation time for the ARSG, with the optimiser taking a combined 293 hours to converge.

5.4 Conclusion

In this chapter, reluctance synchronous generators (RSGs), operating at 5 MW in the medium speed range with a shaft speed fixed at 500 rpm were studied. The study consisted of two main sections, the first an optimisation study to investigate non assisted RSGs in the power range. The second study consisted of the design optimisation of an assisted reluctance synchronous generator (ARSG), with the study implementing an optimised generator stator that was designed in initial study for a retrofit rotor design. Importantly it must be noted that both studies were conducted by assuming complete mechanical feasibility, that includes no deformation under peak load and manufacturability.

In the initial RSG study, it was found that a ten-pole generator outperforms all the generators studied between four and fourteen poles when considering active mass and power factor. Furthermore, it was found that optimised RSGs can realistically operate with power factors in excess of 0.8. This result warrants further investigation into the field that includes a more holistic design optimization that

Table 5.21: 5 MW ARSG versus ABB PMSG generator [110].

Machine	P_{OUT} [MW]	S [MVAR]	E_{FF} [%]	M_A [tn]	P_F [ ]
ABB - PMSG	5.0	5.26★	98.0	18.2	0.95+★
ARSG	5.0	5.05	97.8♦ - 98.0■	18.5 ♣	1.0^X - 0.99^I

P_{OUT} - Terminal Power Out ; P_F - Power Factor ; E_{FF} - Efficiency ; S - Complex Power ; ♣ - Active mass only ; ★ - Typical operating with a power factor of 0.95 or more. Actual values not available ; X - Excluding mechanical losses ; I - Including mechanical losses ; ■ - Kamper core losses ; ♦ - Steinmetz core losses

includes mechanical constraints and mechanical design.

The subsequent study consisted of a retrofit rotor, ARSG optimisation study that implemented the ten-pole stator selected in the previous study. In this study it was shown that by implementing the ARSG rotor, a unity power factor can be achieved, with a significant reduction in required inverter rating as a result. Furthermore it showed the feasibility of implementing this type of generator in this high power range. This result thus warrants further investigation, with this study only focusing on the retrofit optimization. By implementing a complete model, a much more competitive machine can be designed, with less active mass in a smaller package. With ARSG design in a more holistic manner, the generator topology has the capability to achieve very competitive performance compared to permanent magnet synchronous generators when considering the large reduction in manufacturing costs.

Finally, Table 5.21 compares the designed ARSG with the currently implemented PMSG from ABB. As compared in this table, it can be seen that the ARSG has very competitive performance characteristics, with efficiency and power factor within the current implemented machine range. It should be however noted that machine mass was not included in the optimization study. However, the ARSG's mass compares favorably with the PMSG, with similar weights around at 18 tons. This mass can however be drastically reduced by implementing a complete machine model in the optimisation, this motivated by the current very low 2.4 A/mm^2 current density the stator is operating at.

Chapter 6

Conclusion & Future Work

In this thesis, reluctance synchronous machines (RSM), and variations thereof, were studied and designed by implementing finite element analysis and numeric optimization. The study focused and investigated the inherent comparative weaknesses in the performance characteristics of this specific type of machine, with possible mitigation techniques and performance predictions processes developed in order to partially and fully mitigate these weaknesses. Furthermore, the study investigated the implementation of this type of machine in the high power ranges, with the additional development of a assisted RSM.

In conclusion of the objectives, studies and results obtained by the respective chapters, general conclusions are listed along with future work recommendations in the field.

6.1 General Conclusion and Contributions

Reluctance synchronous machines have enjoyed a large increase in interest and study in recent years. The main motivation for this increase in interest is motivated by the desire to achieve more efficiency, cost effective drives, with international standards, like the IEC, increasingly applying pressure on industry to manufacture and implement more efficient drives systems. To this end, RSMs have been identified as possible alternatives to currently implemented induction machines. RSMs however have inherent comparative weaknesses. In this study, these inherent weaknesses are studied, with possible mitigation techniques proposed. Additional work consists of the implementation of the machine in the 5 MW power range as wind generator, with an additional assisted reluctance synchronous model developer in order to propose a more feasible implementation of this type of machine in the power range.

In concluding, the studies findings, that are considered as the contributions of this study, are summarised below:

- The first inherent weakness identified in literature for RSMs is its relatively high torque ripple. This is due to the inherent design of the rotor, with rotor and stator slot harmonics forming the main contribution to this high torque ripple commonly found. It is shown in Chapter 3 that by implementing an asymmetric rotor pole structure, torque ripple can be drastically reduced

to well below 5%. Furthermore, it is shown that by implementing the proposed asymmetric profile, a combined maximized average torque and minimized torque ripple current angle point is possible, with successful prototype manufacture and testing conducted to validate the design process. This asymmetric rotor profile proves that RSM torque ripple can be reduced to within acceptable levels without rotor skew, which is currently implemented with negative effects on subsequent performance parameters of the machine like power factor and average torque.

- The second inherent weakness identified in literature for RSMs is its low power factor. This is due to the lack of field excitation on the rotor, with only the reluctance force implemented in the torque production. It is shown in the study that there is an inherent relationship between average torque and power factor, with the two parameters forming contradicting objectives during optimization.

  Furthermore, it is shown that by implementing the determined relationship pareto curve, optimisation relationships can be predicted with a 95% confidence interval, with only the maximised average torque and power factor values required. This relationship gives the designer the ability to select specific machine parameters required for a specific application, before optimisation, and subsequently optimising for the selected parameters to develop the machine lamination profile. By implementing this design procedure, a machine is designed and manufactured, with performance parameters successfully validated.

  In a further analysis of RSMs operating in motor and generator mode, it was found that the inherent weakness of power factor is even more renounced in generator mode. Results show a decrease of 25% for power factor when operating in generator mode, this compared to motor mode for the specific machine tested. This result illustrates that when designing RSMs for operation in generator mode, copper and mechanical losses (as far as possible) must be included in the power factor estimation. This versus only implementing the D and Q-axis inductances in motoring mode, which is commonly implemented with relatively high accuracy.

- In the final study, reluctance synchronous generators(RSG) for wind energy application in the 5 MW, medium speed is investigated. The initial investigation consists of an optimisation study, on a largely unconstrained machine model, to determine what pole number will perform optimally in the medium speed range, with machines optimised consisting of four to fourteen poles. The main objective of the study is to determine, when assuming mechanical feasibility, what the maximum achievable power factor can be per pole number, with power output and efficiency constrained in order to be competitive. The results indicate that the maximum achievable power factor for the machine in this power range varies between 0.8 and 0.87. Furthermore, when analysing the feasibility of the aspect ratio, active mass and power factor, it was found that the 10 pole machine outperforms the other machines analysed and was therefore selected for further analysis.

In a subsequent study, the ten-pole machine stator identified in the previous study was implemented in a retrofit, assisted reluctance synchronous generator(ARSG) study. This study implemented the DC-link inverter current as field current in order to improve power factor and thus reduce the inverter power rating. The result of the study found that by implementing the ARSG rotor, the machine is capable of operating at unity power factor.

6.2 Future Work

Items recommended that future work in the specific areas discussed must include the following:

- **The asymmetric rotor profile structure**: It became clear during the study that the more available rotor outer radius surface the optimiser is given, the lower the torque ripple values became during optimisation. It also became clear that the limiting factors during the optimisation is twofold:

  1. As the pole number increases, so the available outer rotor pole surface area decreased, with a less effective torque ripple reduction as a result. To this end, the inverse also showed to be true, with the highest torque ripple reduction achieved with the four-pole machine. Considering this fact, future work implementing this asymmetric rotor profile should take into consideration the outer stator radius during optimisation, because the larger the outside stator radius is, the larger the variation in outer rotor radius becomes, giving the optimiser more freedom.

     Additionally, it is highly recommended when considering the design optimisation of a two-pole RSM to implement the asymmetric flux barrier profile. Two-pole machines inherently have the widest outer rotor surface variability per volume, and the author is confident that a very competitive torque ripple value is achievable. Additionally, when considering the required rotor stability and balance at higher speeds, the asymmetric rotor would contribute greatly towards the reduction of torque harmonics.

     Finally, in recent literature, attempts have been made to design inside out reluctance synchronous machines, either with concentrated or overlap winding. Considering the large increase in outside rotor surface area, which is now the inside rotor surface, the optimiser will have a much larger variable area to work in, with very competitive torque ripple results expected.

     Additionally, from a mechanical structural integrity point of view, the fact that displacement due to compression forces are much simpler to minimise or mitigate compared to displacement due to tension forces, this inside out rotor design might be more feasible for RSM design for certain applications. This design will allow for much simpler flux guide supports, or possible exclusion thereof, which will increase the saliency ratio and thus reduce the inverter rating. This is especially applicable

to high power RSM's in the high kW to MW power range. It is highly recommended that in future studies, inside out rotors be investigated with the addition of the asymmetric flux barrier designed.

2. Line start reluctance synchronous machines have lately come into the spotlight as possible replacement for currently implemented induction motors and permanent magnet line start synchronous machines for line start applications. Due to the possibility of achieving a very low torque ripple and its highly variable profile, it is highly recommended that in future studies, the asymmetric rotor profile be implemented for the design. This may also have a positive effect on the synchronisation capabilities, with this fact however requiring proof through in depth study.

- **The assisted reluctance synchronous machine:** During the retrofit rotor, assisted reluctance synchronous generator(ARSG) study, the ARSG was found to operate with very competitive performance, with performance comparable to the currently implemented permanent magnet synchronous generators. During the study however, a stator current density reduction technique was implemented in order to keep the investigated machine within the power level of the study objective. The reason for this is due to the implementation of a stator for the retrofit rotor design, and the aim to compare the RSG and ARSG performance for the same stator.

  By implementing this technique, the current density for the ARSG was reduced by 47%, when compared to the original RSG stator current density with identical power levels. It is therefore recommended for future studies that the entire machine, including the rotor and stator, be optimised to achieve a more competitive machine. This holistic machine design has the potential to produce a more compact machine that implements less active material, with possible performance parameters comparable to permanent magnet synchronous machines. This statement however requires proof through in depth study and analysis.

Appendices

Appendix A

Optimisation Overview

A.1 Weighted Factor Megawatt Dimension Determination

In this section, the design optimisation of a medium speed RSM in the 5 MW power range will be investigated. Because of the varying speeds possible in the medium speed range, a fixed 500 rpm is selected for the medium speed RSM investigation. Taking this fix speed into consideration, two machine layouts will be investigated that consist of an eight and ten pole RSM, with an electrical frequency of $33.3Hz$ and $41.7Hz$ respectively.

The study implements the previous work conducted, with the optimisation techniques and machine models developed implemented in the optimisation. The study consists of two independent investigations, the first of which is a parameter optimisation to determine the optimum machine dimensions. The second, the machine optimisation implementing the optimum weighted factor determined in Section 4.3.1.

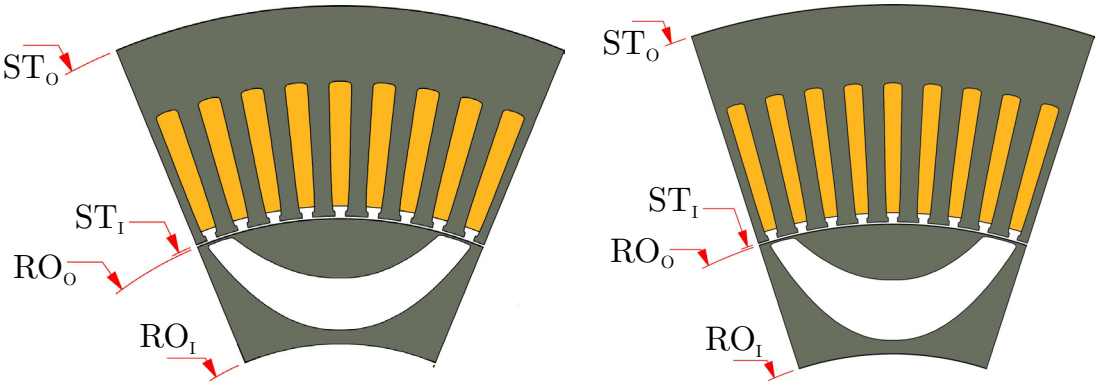

(a): Eight pole RSM. **(b):** Ten pole RSM.

Figure A.1: Machine dimension study results implementing one flux barrier.

A.1.1 Machine Dimension Optimisation

The machine dimension study consists of an investigation to determine the optimum machine dimensions for the selected eight and ten pole RSM in the 5 MW power range. The process of investigation is the minimisation of machine active mass (M_A), which includes active copper, rotor and stator lamination mass, subject to the machine power larger (P_{ower}) than 6 MW, with

$$P_{ower}(X_1) \geqslant 6MW \tag{A.1.1}$$

and with the model variables including an inequality constraint of

$$0 \leqslant G(X_1) \leqslant 1. \tag{A.1.2}$$

This 6Mw limit is selected in order to give the designer some freedom in the selection of the weighted power factor torque relationships described in Section 4.3.1. A final machine stack length will ultimately be adjusted in order to achieve an exact 5MW to compare optimised machine topologies.

In order to simplify the machine model by reducing the model variables, only one flux barrier is selected for the machine mass minimisation, with the optimisation variables consisting of

$$X_1 = \begin{bmatrix} \alpha & \beta & R & P_{1sp} & P_{3sp} & P_{5sp} & \theta & R_{GAP} & R_{P_3} & R_{P_4} & R_{SSO} & \alpha_{34} & ST_O & RO_I & L_S \end{bmatrix}^T. \tag{A.1.3}$$

The results of this investigation for the two machines are illustrated in Figure A.1, with the determined optimisation dimensions in Table A.1.

Table A.1: Machine dimension study results.

Poles	$\boldsymbol{P_{ower}}$ [Mw]	$\boldsymbol{ST_O}$ [m]	$\boldsymbol{RO_O}$ [m]	$\boldsymbol{RO_I}$ [m]	$\boldsymbol{L_S}$ [m]	$\boldsymbol{h}$ [mm]	$\boldsymbol{J}$ [A/mm^2]
8	6.0	0.565	0.360	0.240	2.43	2.5	4.0
10	6.0	0.715	0.475	0.332	1.23	2.5	4.0

$\boldsymbol{ST_O}$ - Stator Outer Radius ; $\boldsymbol{RO_O}$ - Rotor Outer Radius ; $\boldsymbol{RI_I}$ - Rotor Inner Radius ; $\boldsymbol{L_S}$ - Stack Length ; $\boldsymbol{h}$ - Air Gap Hight ; $\boldsymbol{J}$ - Current Density

A.1.2 Weighted Machine Optimisation

In this section, the main stator dimensions determined will be implemented for the design study in the megawatt power range. Additionally, the gained knowledge from the weighted optimisation study in Section 4.3.1 will be implemented, with the optimum weighted ratio between power factor and T_A of 70% and 30% receptively implemented.

The study will consist of multiple combinations of flux barriers and winding layouts. Initially it will only cover the results of the eight and ten pole machines implementing four flux barriers and three stator winding layouts respectively. The future intended work will include

Table A.2: $5M_W$, $500rpm$ eight and ten pole $30-70$ weighted factor optimisation results .

Poles	Objective Function	θ [°]	P_{ower} [MW]	T_R [%]	P_F [ ]	Steinmidz E_{FF} [%]	M_A [tn]	L_S [m]	RO_O [m]
9 by **9** - Corded Machine Optimisation Results									
8	$T_O(X_2)$	70.9	5.00	42.6	0.74	98.6	10.3	2.14	0.413
10	$T_O(X_2)$	75.9	5.00	35.4	0.74	98.2	7.81	1.08	0.538
8 by **9** - Corded Machine Optimisation Results									
8	$T_O(X_2)$	69.8	5.00	77.1	0.74	98.6	10.3	2.12	0.409
10	$T_O(X_2)$	68.6	5.00	74.9	0.75	98.2	8.05	1.10	0.541
7 by **9** - Corded Machine Optimisation Results									
8	$T_O(X_2)$	65.3	5.00	38.6	0.75	98.6	10.8	2.21	0.409
10	$T_O(X_2)$	65.8	5.00	27.0	0.75	98.2	8.21	1.12	0.537

θ - Current Angle ; P_{OWER} - Power ; T_A - Torque Ripple ; P_F - Power Factor ; E_{FF} - Efficiency ; M_A - Active Machine Mass ; L_S - Stack Length ; RO_O - Rotor Outer Radius

1. an increase from four to six flux barriers, as was shown in Section 4.3.1 that five flux barriers have no significant improvements to the power factor, T_A ratio

2. implementation of the T_R reduction technique implemented in the initial study in Section 3.3 to reduce T_R.

3. mechanical analysis on the rotor structure, with mechanical modifications and possible mitigation techniques to structural deformation.

The optimisation technique presented in Figure 4.7 is once again implemented, with the exception of the weighted shift iteration steps replaced with the fixed optimum weighted factor. The optimisation objective consists of

$$F_O(X_1) = (0.3)(\frac{T_A(X_1)}{T_A(X_1)_{max}}) + (0.7)(\frac{P_F(X_1)}{P_F(X_1)_{max}}) \tag{A.1.4}$$

with the respective maximisations of $T_A(X_1)_{max}$ and $P_F(X_1)_{max}$ once again conducted implementing Equations 4.3.5 and 4.3.6 respectively.

The initial results of the optimisation study conducted on the eight and ten pole machine layouts with three winding combinations is illustrated in Table A.2. It must be noted that no attention was given to T_R during the optimisation, hence the high values presented in the results. The efficiency result is calculated by implementing the Steinmidz equation, with similar results obtained in a study by [29].

The final optimised results of the weighted factors for the two pole with three winding layouts is illustrated in Figure A.2.

(a): 8-Pole 9-by-9 : $30\% - T_A$: $70\% - P_F$

(b): 10-Pole 9-by-9 : $30\% - T_A$: $70\% - P_F$

(c): 8-Pole 8-by-9 : $30\% - T_A$: $70\% - P_F$

(d): 10-Pole 8-by-9 : $30\% - T_A$: $70\% - P_F$

(e): 8-Pole 7-by-9 : $30\% - T_A$: $70\% - P_F$

(f): 10-Pole 7-by-9 : $30\% - T_A$: $70\% - P_F$

Figure A.2: Optimised ten pole machines with a 8 by 9 corded winding layout.

Appendix B

Numeric First Principles

B.1 Least Square Polynomial Fit

In this section, the method implemented in the polynomial fitting is presented. The fitting consists of a least square polynomial fit, with the equation :

$$p(x) = p[0] * x^{degree} + ... + p[degree] \tag{B.1.1}$$

fitted to the selected points with a polynomial equation of a certain "degree". For the specific flux barrier construction, a second order polynomial is selected. The solution of the fitting minimizes the square error

$$E = \sum_{j=0}^{k} |p(x_j) - y_j|^2 \tag{B.1.2}$$

in the equations :

$$x[0]^n * p[n] + ... + x[0] * p[1] + p[0] = y[0] \tag{B.1.3}$$

$$x[1]^n * p[n] + ... + x[1] * p[1] + p[0] = y[1] \tag{B.1.4}$$

$$x[k]^n * p[n] + ... + x[k] * p[1] + p[0] = y[k] \tag{B.1.5}$$

The coefficient matrix of the coefficients p is a Vandermonde matrix.

B.2 Bezier Cubic Splines

In this section, a first principle description of the spline fitting implemented is illustrated in Figure B.1. In this figure, spline function $f(x, y)$ is described by equations B.2.3 and B.2.10 as described in [111].

$$x = At^3 + Bt^2 + Ct + D \tag{B.2.1}$$

$$y = Et^3 + Ft^2 + Gt + H \tag{B.2.2}$$

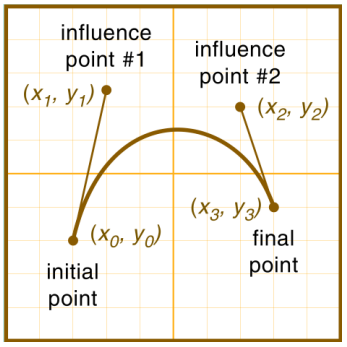

Figure B.1: Bezier Cubic Spline first principles illustration [111].

$$A = x_3 - 3x_2 + 3x_1 - x_0 \quad \text{(B.2.3)} \qquad E = y_3 - 3y_2 + 3y_1 - y_0 \quad \text{(B.2.4)}$$

$$B = 3x_2 - 6x_1 + 3x_0 \quad \text{(B.2.5)} \qquad F = 3y_2 - 6y_1 + 3y_0 \quad \text{(B.2.6)}$$

$$C = 3x_1 - 3x_0 \quad \text{(B.2.7)} \qquad G = 3y_1 - 3y_0 \quad \text{(B.2.8)}$$

$$D = x_0 \quad \text{(B.2.9)} \qquad H = y_0 \quad \text{(B.2.10)}$$

B.3 Covariance Error Ellipse

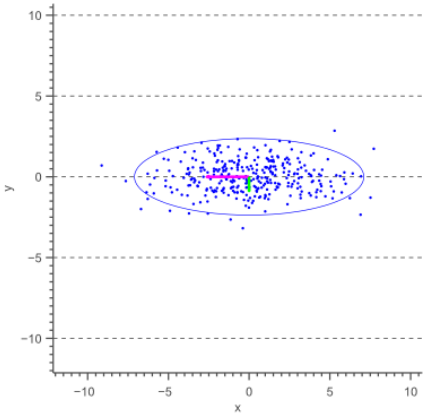

Figure B.2: Ellipse on the origin [112].

The general equation of an axis aligned ellipse, that is centred at the origin, with major axis 2a and minor axis length 2b is represented by [113]:

$$(\frac{x}{a})^2 + (\frac{y}{b})^2 = 1 \quad \text{(B.3.1)}$$

In the case of a data analysis fit, as shown in Figure B.2, the ellipse axes consists of the standard deviations σ_x and σ_y. With this deviation, the equation becomes

$$(\frac{x}{\sigma_x})^2 + (\frac{y}{\sigma_y})^2 = s \tag{B.3.2}$$

where s defines the scale of the ellipse. The values for s depend on the desired confidence level and is equal to : 4.605 for 90%, 5.991 for 95% and 9.210 for 99%. In the case where covariance exists, the ellipse will not be aligned with axis. In this case, a secondary axis needs to be created as in Figure B.3.

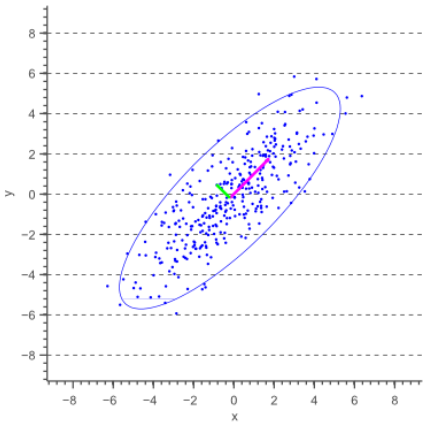

Figure B.3: Ellipse on the origin with secondary axis [112].

In this situation, the standard deviation needs to be calculated according to the new axis. This direction is the direction in which the data varies the most and is defined by the covariance matrix. The vectors shown in Figure B.3 represent the eigenvectors and the eigenvalues of the covariance matrix. Relighting the equation for the standard deviation, the new major and minor axis is defined by $2\sqrt{s\lambda_1}$ and $2\sqrt{s\lambda_2}$, with λ_1 and λ_2 representing the eigenvalues. In order to obtain the orientation of the secondary axis, the largest eigenvector is implemented with equation

$$\alpha = arctan\frac{v_1(y)}{v_2(x)} \tag{B.3.3}$$

with v the eigenvector with the largest eigenvalue. Implementing these new axes coordinates, the new ellipse is presented in Figure B.4. Finally, the central axis position is determined from the mean offsets in the x and y axis.

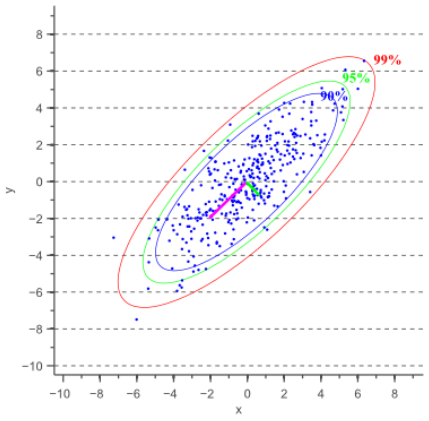

Figure B.4: Ellipse on the origin with secondary axis and confidence levels [112].

B.4 Eight Pole Winding Diagram

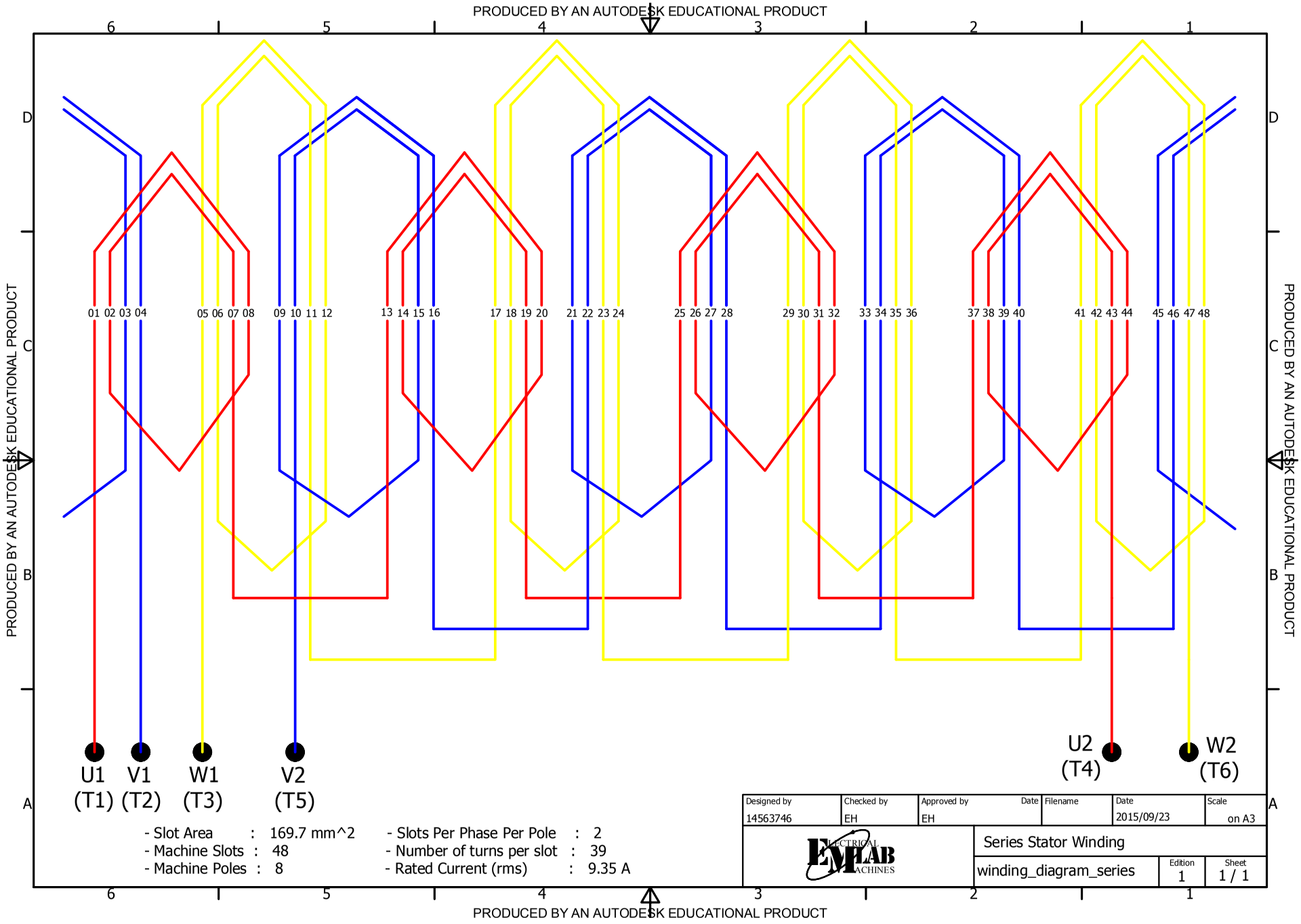

- Slot Area : 169.7 mm^2
- Machine Slots : 48
- Machine Poles : 8
- Slots Per Phase Per Pole : 2
- Number of turns per slot : 39
- Rated Current (rms) : 9.35 A

Designed by	Checked by	Approved by	Date	Filename	Date	Scale
14563746	EH	EH			2015/09/23	on A3

ELECTRICAL EMLAB MACHINES

Series Stator Winding

winding_diagram_series | Edition 1 | Sheet 1 / 1

PRODUCED BY AN AUTODESK EDUCATIONAL PRODUCT

Bibliography

[1] ABB, *Technical note IEC 60034-30-1 standard on efficiency classes for low voltage AC motors*. ABB Online Standards, 2015. [Available Online - http://www.abb.com/motors&generators],Nov.

[2] A. T. de Almeida, F. J. T. E. Ferreira, and G. Baoming, "Beyond induction motors 2014 ; technology trends to move up efficiency," *IEEE Transactions on Industry Applications*, vol. 50, pp. 2103–2114, May 2014.

[3] IEC, *Rotating Electrical Machines - Part 30 : Efficiency Classes of Single-Speed,Three-Phase, Cage-Induction Motors (IE-Code)*. Ed. 1, 2008. 60034-30, Nov.

[4] A. de Almeida, *Improving the Penetration of Energy-Efficient Motors and Drives*. University of Coimbra, 2000. prepared for the SAVE Programme, European Commission.

[5] A. De Almeida, F. Ferreira, J. Fong, and P. Fonseca, *EuP Lot 11 Motors, Ecodesign Assessment of Energy Using Products*. University of Coimbra, 2008. ISR-Univ. Coimbra, Brussels, Belgium, Final Report for the European Commission, Feb.

[6] A. Almeida, F. Ferreira, J. Fong, and B. Conrad, *Electric motor ecodesign and global market transformation,*. IEEE Ind, 2008. Commercial Power Syst. Conf., Clearwater Beach, FL, USA, May 4-8, pp. 1-9.

[7] WEG, *W22 Super Premium Three-Phase Unduction Motor*. WEG Motor Catalogue, 2016.

[8] A. T. De Almeida, F. J. T. E. Ferreira, and A. Q. Duarte, "Technical and economical considerations on super high-efficiency three-phase motors," *IEEE Transactions on Industry Applications*, vol. 50, pp. 1274–1285, March 2014.

[9] R. R. Moghaddam, *Synchronous Reluctance Machine (SynRM) in Variable Speed Drives (VSD) Applications*. PhD thesis, Royal Institute of Technology, [Available Online - http://www.diva-portal.org/smash/record.jsf?pid=diva22011.

[10] H. Kiriyama, S. Kawano, Y. Honda, T. Higaki, S. Morimoto, and Y. Takeda, "High performance synchronous reluctance motor with multi-flux barrier for

the appliance industry," in *Industry Applications Conference, 1998. Thirty-Third IAS Annual Meeting. The 1998 IEEE*, vol. 1, pp. 111–117 vol.1, Oct 1998.

[11] M. J. Kamper, F. Van der Merwe, and S. Williamson, "Direct finite element design optimisation of the cageless reluctance synchronous machine," *Energy Conversion, IEEE Transactions on*, vol. 11, pp. 547–555, Sep 1996.

[12] A. Vagati, "The synchronous reluctance solution: a new alternative in ac drives," in *Industrial Electronics, Control and Instrumentation, 1994. IECON '94., 20th International Conference on*, vol. 1, pp. 1–13 vol.1, Sep 1994.

[13] T. A. Lipo, "Synchronous reluctance machines-a viable alternative for ac drives?," *Electric Machines & Power Systems*, vol. 19, no. 6, pp. 659–671, 1991.

[14] E. Warner, *GLOBAL WIND REPORT ANNUAL MARKET UPDATE*. Market Forecast for 2015, 2015. [Available Online - http://www.gwec.net],Nov.

[15] EIA, *U.S. Energy Informaion Administration: Annual Energy Outlook 2015, With Projections to 2040*. U.S. Energy Information Administration,Office of Integrated and International Energy Analysis, U.S. Department of Energy, Washington, DC 20585, 2015. [Available Online - http://www.eia.gov/forecasts/aeo],Nov.

[16] A. Smith, T. Stehly, and W. Musial, *National Renewable Energy Laboratory (NREL) : 2014-2015 Offshore WindTechnologies Market Report*. NREL Publications, 2015. [Available Online - http://www.nrel.gov/research/publications.html],Nov.

[17] B. Hamilton, M. Bielecki, C. Bloch, T. Decker, L. Frantzis, K. Midura, J. Paidipati, and F. Zhao, "Offshore wind market and economic analysis 2014 annual market assessment.," *Prepared for the U.S. Department of Energy by Navigant Consulting, Inc., Burlington, Massachusetts.*, May 2014.

[18] DoE, *Advanced Magnet Lab and NREL*. Next-Generation Drivetrains, 2013. [Available Online - http://apps1.eere.energy.gov/wind/],Nov.

[19] J. Kostko, "Polyphase reaction synchronous motors," *American Institute of Electrical Engineers, Journal of the*, vol. 42, pp. 1162–1168, Nov 1923.

[20] R. R. Moghaddam, F. Magnussen, C. Sadarangani, and H. Lendenmann, "New theoretical approach to the synchronous reluctance machine behavior and performance," in *Electrical Machines, 2008. ICEM 2008. 18th International Conference on*, pp. 1–6, Sept 2008.

[21] R. R. Moghaddam, "Synchronous reluctance mahine (synrm) design," Master's thesis, Royal Institute of Technology (KTM), Sweden, Power Electrical Engineering, 2007.

[22] R. R. Moghaddam, *Synchronous Reluctance Machine (SynRM) in Variable Speed Drives (VSD) Applications*. PhD thesis, Royal Institute of Technology (KTM), Sweden, Power Electrical Engineering, 2001.

[23] A. Vagati, A. Canova, M. Chiampi, M. Pastorelli, and M. Repetto, "Improvement of synchronous reluctance motor design through finite-element analysis," in *Industry Applications Conference, 1999. Thirty-Fourth IAS Annual Meeting. Conference Record of the 1999 IEEE*, vol. 2, pp. 862–871 vol.2, 1999.

[24] A. Vagati, M. Pastorelli, G. Francheschini, and S. Petrache, "Design of low-torque-ripple synchronous reluctance motors," *Industry Applications, IEEE Transactions on*, vol. 34, pp. 758–765, Jul 1998.

[25] A. Vagati, A. Canova, M. Chiampi, M. Pastorelli, and M. Repetto, "Design refinement of synchronous reluctance motors through finite-element analysis," *Industry Applications, IEEE Transactions on*, vol. 36, pp. 1094–1102, Jul 2000.

[26] A. Vagati, G. Franceschini, I. Marongiu, and G. Troglia, "Design criteria of high performance synchronous reluctance motors," in *Industry Applications Society Annual Meeting, 1992., Conference Record of the 1992 IEEE*, pp. 66–73 vol.1, Oct 1992.

[27] V. R. Maldonado, *Synchronous reluctance motor and drive package: The energy efficiency alternative*. ABB, 2013. [Available Online - http://www.abb.com].

[28] M. J. Karnper and A. F. Volschenk, "Effect of rotor dimentions and cross magnitisation on Ld and Lq inductance of reluctance synchronous machines," *IEE Proceedings - Electric Power Applications*, vol. 141, pp. 213–220, 1994.

[29] P. Roshanfekr, S. Lundmark, T. Thiringer, and M. Alatalo, "A synchronous reluctance generator for a wind application-compared with an interior mounted permanent magnet synchronous generator," in *Power Electronics, Machines and Drives (PEMD 2014), 7th IET International Conference on*, pp. 1–5, April 2014.

[30] T. Lange, B. Kerdsup, C. Weiss, and R. De Doncker, "Torque ripple reduction in reluctance synchronous machines using an asymmetric rotor structure," in *Power Electronics, Machines and Drives (PEMD 2014), 7th IET International Conference on*, pp. 1–5, April 2014.

[31] N. Bianchi, D. Durello, and E. Fornasiero, "Multi-objective optimization of a pm assisted synchronous reluctance machine, including torque and sensorless detection capability," in *Power Electronics, Machines and Drives (PEMD 2012), 6th IET International Conference on*, pp. 1–6, March 2012.

[32] E. Lovelace, T. Jahns, and J. H. Lang, "A saturating lumped-parameter model for an interior pm synchronous machine," *Industry Applications, IEEE Transactions on*, vol. 38, pp. 645–650, May 2002.

[33] G. Pellegrino, F. Cupertino, and C. Gerada, "Automatic design of synchronous reluctance motors focusing on barrier shape optimization," *Industry Applications, IEEE Transactions on*, vol. PP, no. 99, pp. 1–1, 2014.

[34] F. Parasiliti and M. Villani, "Magnetic analysis of flux barriers synchronous reluctance motors," in *18th International Conference on Electrical Machines, 2008. ICEM 2008.*, pp. 1–6, Sept 2008.

[35] G. Pellegrino and F. Cupertino, "Fea-based multi-objective optimization of ipm motor design including rotor losses," in *Energy Conversion Congress and Exposition (ECCE), 2010 IEEE*, pp. 3659–3666, Sept 2010.

[36] F. Cupertino, G. Pellegrino, and C. Gerada, "Design of synchronous reluctance machines with multi-objective optimization algorithms," *Industry Applications, IEEE Transactions on*, vol. PP, no. 99, pp. 1–1, 2014.

[37] T. Matsuo and T. Lipo, "Rotor design optimization of synchronous reluctance machine," *Energy Conversion, IEEE Transactions on*, vol. 9, pp. 359–365, Jun 1994.

[38] M. Obata, S. Morimoto, M. Sanada, and Y. Inoue, "Performance of pma-synrm with ferrite magnets for ev/hev applications considering productivity," *Industry Applications, IEEE Transactions on*, vol. 50, pp. 2427–2435, July 2014.

[39] W. Villet, M. Prins, C. Vorster, and M. Kamper, "Saliency performance investigation of synchronous machines for position sensorless controlled ev drives," in *Sensorless Control for Electrical Drives and Predictive Control of Electrical Drives and Power Electronics (SLED/PRECEDE), 2013 IEEE International Symposium on*, pp. 1–8, Oct 2013.

[40] P. Lazari, J. Wang, L. Chen, and X. Chen, "Design optimisation and performance evaluation of a rare-earth-free permanent magnet assisted synchronous reluctance machine for electric vehicle traction," in *Power Electronics, Machines and Drives (PEMD 2014), 7th IET International Conference on*, pp. 1–6, April 2014.

[41] L. Chen, J. Wang, P. Lombard, P. Lazari, and V. Leconte, "Design optimisation of permanent magnet assisted synchronous reluctance machines for electric vehicle applications," in *Electrical Machines (ICEM), 2012 XXth International Conference on*, pp. 2647–2653, Sept 2012.

[42] C. Spargo, B. Mecrow, and J. Widmer, "Higher pole number synchronous reluctance machines with fractional slot concentrated windings," in *Power Electronics, Machines and Drives (PEMD 2014), 7th IET International Conference on*, pp. 1–6, April 2014.

[43] S. E. Sibande, M. Kamper, R. Wang, and E. Rakgati, "Optimal design of a pm-assisted rotor of a 110 kw reluctance synchronous machine," in *AFRICON,*

2004. 7th AFRICON Conference in Africa, vol. 2, pp. 793–797 Vol.2, Sept 2004.

[44] A. Kallaste, T. Vaimann, and A. Belahcen, "Design of permanent magnet assisted synchronous reluctance machine," in *Electric Power Engineering (EPE), Proccedings of the 2014 15th International Scientific Conference on*, pp. 579–582, May 2014.

[45] A. Vagati, B. Boazzo, P. Guglielmi, and G. Pellegrino, "Design of ferrite-assisted synchronous reluctance machines robust toward demagnetization," *Industry Applications, IEEE Transactions on*, vol. 50, pp. 1768–1779, May 2014.

[46] M. Palmieri, M. Perta, F. Cupertino, and G. Pellegrino, "Effect of the numbers of slots and barriers on the optimal design of synchronous reluctance machines," in *Optimization of Electrical and Electronic Equipment (OPTIM), 2014 International Conference on*, pp. 260–267, May 2014.

[47] N. Bianchi, M. Degano, and E. Fornasiero, "Sensitivity analysis of torque ripple reduction of synchronous reluctance and interior pm motors," in *Energy Conversion Congress and Exposition (ECCE), 2013 IEEE*, pp. 1842–1849, Sept 2013.

[48] M. Ferrari, N. Bianchi, and E. Fornasiero, "Rotor saturation impact in synchronous reluctance and pm assisted reluctance motors," in *Energy Conversion Congress and Exposition (ECCE), 2013 IEEE*, pp. 1235–1242, Sept 2013.

[49] M. Kamper and W. Villet, "Design and performance of compensated reluctance synchronous machine drive with extended constant power speed range," in *Energy Conversion Congress and Exposition (ECCE), 2012 IEEE*, pp. 4330–4337, Sept 2012.

[50] F. Zhang, G. Jia, Y. Zhao, Z. Yang, W. Cao, and J. Kirtley, "Simulation and experimental analysis of a brushless electrically-excited synchronous machine with a hybrid rotor," *Magnetics, IEEE Transactions on*, vol. PP, no. 99, pp. 1–1, 2015.

[51] N. Limsuwan, Y. Shibukawa, D. D. Reigosa, and R. D. Lorenz, "Novel design of flux-intensifying interior permanent magnet synchronous machine suitable for self-sensing control at very low speed and power conversion," *IEEE Transactions on Industry Applications*, vol. 47, pp. 2004–2012, Sept 2011.

[52] E. Carraro, M. Degano, and N. Bianchi, "Permanent magnet volume minimization in permanent magnet assisted synchronous reluctance motors," in *Ecological Vehicles and Renewable Energies (EVER), 2013 8th International Conference and Exhibition on*, pp. 1–4, March 2013.

[53] N. Limsuwan, T. Kato, K. Akatsu, and R. Lorenz, "Design and evaluation of a variable-flux flux-intensifying interior permanent magnet machine," in *Energy*

Conversion Congress and Exposition (ECCE), 2012 IEEE, pp. 3670–3677, Sept 2012.

[54] I. Boldea, L. Tutelea, and F. Blaabjerg, "Bega - a biaxial excitation generator for automobiles: comprehensive characterization and test results," in *Industry Applications Conference, 2004. 39th IAS Annual Meeting. Conference Record of the 2004 IEEE*, vol. 3, pp. 1682–1690 vol.3, Oct 2004.

[55] N. Bianchi and S. Bolognani, "Performance analysis of an ipm motor with segmented rotor for flux-weakening applications," in *Electrical Machines and Drives, 1999. Ninth International Conference on (Conf. Publ. No. 468)*, pp. 49–53, 1999.

[56] N. Limsuwan, Y. Shibukawa, D. Reigosa, and R. D. Lorenz, "Novel design of flux-intensifying interior permanent magnet synchronous machine suitable for power conversion and self-sensing control at very low speed," in *2010 IEEE Energy Conversion Congress and Exposition*, pp. 555–562, Sept 2010.

[57] Y. Wang, D. M. Ionel, M. Jiang, and S. J. Stretz, "Establishing the relative merits of synchronous reluctance and pm assisted technology through systematic design optimization," *IEEE Transactions on Industry Applications*, vol. PP, no. 99, pp. 1–1, 2016.

[58] N. Bianchi, E. Fornasiero, M. Ferrari, and M. Castiello, "Experimental comparison of pm-assisted synchronous reluctance motors," *IEEE Transactions on Industry Applications*, vol. 52, pp. 163–171, Jan 2016.

[59] N. Bianchi and H. Mahmoud, "An analytical approach to design the pm in pmarel motors robust toward the demagnetization," *IEEE Transactions on Energy Conversion*, vol. PP, no. 99, pp. 1–10, 2016.

[60] S. S. R. Bonthu and S. Choi, "Design procedure for multi-phase external rotor permanent magnet assisted synchronous reluctance machines," in *2016 IEEE Applied Power Electronics Conference and Exposition (APEC)*, pp. 1131–1137, March 2016.

[61] J. X. Shen, S. Cai, H. Shao, and H. Hao, "Evaluation of low-cost high-performance synchronous motors for ventilation application," in *2015 International Conference on Sustainable Mobility Applications, Renewables and Technology (SMART)*, pp. 1–6, Nov 2015.

[62] A. Sun, J. Li, R. Qu, B. Zhao, D. Li, H. Fang, and Y. Sun, "Magnetization and performance analysis of a variable-flux flux-intensifying interior permanent magnet machine," in *2015 IEEE International Electric Machines Drives Conference (IEMDC)*, pp. 369–375, May 2015.

[63] A. Sun, J. Li, R. Qu, J. Chen, and H. Lu, "Rotor design considerations for a variable-flux flux-intensifying interior permanent magnet machine with improved torque quality and reduced magnetization current," in *2015 IEEE Energy Conversion Congress and Exposition (ECCE)*, pp. 784–790, Sept 2015.

[64] B. Yan, X. Zhu, and L. Chen, "Design and evaluation of a new flux-intensifying permanent magnet brushless motor," in *Electrical Machines and Systems (ICEMS), 2014 17th International Conference on*, pp. 673–677, Oct 2014.

[65] T. Fukushige, N. Limsuwan, T. Kato, K. Akatsu, and R. D. Lorenz, "Efficiency contours and loss minimization over a driving cycle of a variable-flux flux-intensifying interior permanent magnet machine," in *2013 IEEE Energy Conversion Congress and Exposition*, pp. 591–597, Sept 2013.

[66] N. Limsuwan, T. Fukushige, K. Akatsu, and R. D. Lorenz, "Design methodology for variable-flux, flux-intensifying interior permanent magnet machines for an electric-vehicle-class inverter rating," in *2013 IEEE Energy Conversion Congress and Exposition*, pp. 1547–1554, Sept 2013.

[67] X. Zhu, S. Yang, Y. Du, Z. Xiang, and L. Xu, "Electromagnetic performances analysis and verification of a new flux intensifying permanent magnet brushless motor with two-layer segmented permanent magnets," *IEEE Transactions on Magnetics*, vol. PP, no. 99, pp. 1–1, 2016.

[68] I. Boldea, V. Coroban-Schramel, G. D. Andreescu, F. Blaabjerg, and S. Scridon, "Bega starter/alternator 2014 ; vector control implementation and performance for wide speed range at unity power factor operation," *IEEE Transactions on Industry Applications*, vol. 46, pp. 150–158, Jan 2010.

[69] I. Boldea, V. Coroban-Schramel, G. D. Andreescu, S. Scridon, and F. Blaabjerg, "Bega starter/alternator - vector control implementation and performance for wide speed range at unity power factor operation," in *Industry Applications Society Annual Meeting, 2008. IAS '08. IEEE*, pp. 1–8, Oct 2008.

[70] V. Coroban-Schramel, I. Boldea, G. D. Andreescu, and F. Blaabjerg, "Active-flux based motion sensorless vector control of biaxial excitation generator/motor for automobiles (bega)," in *2009 IEEE Energy Conversion Congress and Exposition*, pp. 2131–2138, Sept 2009.

[71] H. Shaogang, W. Dong, and S. Xufang, "Analysis of biaxial excitation generator/motor for automobiles using tooth flux method," in *Electrical Machines and Systems (ICEMS), 2011 International Conference on*, pp. 1–4, Aug 2011.

[72] M. J. Kamper, *Design Optimisation of Cageless Flux Barrier Rotor Reluctance Synchronous Machine*. PhD thesis, Stellenbosch University, 1996.

[73] S. Gerber, "A finite element based optimisation tool for electrical machines.," Master's thesis, University of Stellenbosch, Available Online - http://hdl.handle.net/10019.1/6635, 2011.

[74] B. Silwal, P. Rasilo, L. Perkkio, A. Hannukainen, T. Eirola, and A. Arkkio, "Evaluation and comparison of different numerical computation methods for the electromagnetic torque in electrical machines," in *Electrical Machines and Systems (ICEMS), 2013 International Conference on*, pp. 837–842, Oct 2013.

[75] J. Pyrhönen, T. Jokinen, and V. Hrabovcová, *Design of Rotating Electrical Machines*. Wiley, J and Sons, 2014, ISBN : 978-1-118-58157-5.

[76] C. Voster, "Design of a reluctance synchronous machine for an electric vehicle with a multi speed gearbox," Master's thesis, Stellenbosch University, [Available Online - http://hdl.handle.net/10019.1/86242], 2014.

[77] E. Howard, M. J. Kamper, and S. Gerber, "Flux barrier and skew design optimisation of reluctance synchronous machines," in *Electrical Machines (ICEM), 2014 International Conference on*, pp. 1186–1192, Sept 2014.

[78] E. Howard, M. J. Kamper, and S. Gerber, "Asymmetric flux barrier and skew design optimization of reluctance synchronous machines," *IEEE Transactions on Industry Applications*, vol. 51, pp. 3751–3760, Sept 2015.

[79] T. Hubert, M. Reinlein, A. Kremser, and H. G. Herzog, "Torque ripple minimization of reluctance synchronous machines by continuous and discrete rotor skewing," in *Electric Drives Production Conference (EDPC), 2015 5th International*, pp. 1–7, Sept 2015.

[80] J. Tsuchiya, K. Mishima, and G. Kimura, "A study on torque ripple reduction of synchronous reluctance motor," in *Power Electronics and Drive Systems, 2001. Proceedings., 2001 4th IEEE International Conference on*, vol. 2, pp. 452–455 vol.2, Oct 2001.

[81] R. R. Moghaddam, F. Magnussen, and C. Sadarangani, "Novel rotor design optimization of synchronous reluctance machine for low torque ripple," in *Electrical Machines (ICEM), 2012 XXth International Conference on*, pp. 720–724, Sept 2012.

[82] S. Taghavi and P. Pillay, "New title: A novel grain oriented lamination rotor core assembly for a synchronous reluctance traction motor with a reduced torque ripple algorithm," *IEEE Transactions on Industry Applications*, vol. PP, no. 99, pp. 1–1, 2016.

[83] M. Sanada, K. Hiramoto, S. Morimoto, and Y. Takeda, "Torque ripple improvement for synchronous reluctance motor using asymmetric flux barrier arrangement," in *Industry Applications Conference, 2003. 38th IAS Annual Meeting. Conference Record of the*, vol. 1, pp. 250–255 vol.1, Oct 2003.

[84] N. Bianchi, S. Bolognani, D. Bon, and M. Pre, "Rotor flux-barrier design for torque ripple reduction in synchronous reluctance and pm-assisted synchronous reluctance motors," *Industry Applications, IEEE Transactions on*, vol. 45, pp. 921–928, May 2009.

[85] J. Baek, S. S. R. Bonthu, S. Kwak, and S. Choi, "Optimal design of five-phase permanent magnet assisted synchronous reluctance motor for low output torque ripple," in *2014 IEEE Energy Conversion Congress and Exposition (ECCE)*, pp. 2418–2424, Sept 2014.

[86] A. Fratta, G. P. Troglia, A. Vagati, and F. Villata, "Evaluation of torque ripple in high performance synchronous reluctance machines," in *Industry Applications Society Annual Meeting, 1993., Conference Record of the 1993 IEEE*, pp. 163–170 vol.1, Oct 1993.

[87] D. Miljavec, "Torque ripple in synchronous reluctance motor," in *Electrotechnical Conference, 1998. MELECON 98., 9th Mediterranean*, vol. 2, pp. 1233–1236 vol.2, May 1998.

[88] O. Birte, L. Szabo, H. V. der Auweraer, C. Faria, A. Popp, and C. Martis, "Study of torque ripple and noise for different rotor topologies of a synchronous reluctance machine," in *2015 9th International Symposium on Advanced Topics in Electrical Engineering (ATEE)*, pp. 933–938, May 2015.

[89] Y. C. Choi, M. H. Park, M. M. Lee, J. H. Lee, and J. S. Chun, "Rotor optimum design on torque ripple reduction for a synchronous reluctance motor with concentrated winding using rsm," in *2007 IEEE International Electric Machines Drives Conference*, vol. 2, pp. 1721–1725, May 2007.

[90] M. Ferrari, N. Bianchi, A. Doria, and E. Fornasiero, "Design of synchronous reluctance motor for hybrid electric vehicles," in *Electric Machines Drives Conference (IEMDC), 2013 IEEE International*, pp. 1058–1065, May 2013.

[91] P. Alotto, M. Barcaro, N. Bianchi, and M. Guarnieri, "Optimization of ipm motors with machaon rotor flux barriers," in *Electromagnetic Field Computation (CEFC), 2010 14th Biennial IEEE Conference on*, pp. 1–1, May 2010.

[92] X. Bomela and M. Kamper, "Effect of stator chording and rotor skewing on performance of reluctance synchronous machine," *Industry Applications, IEEE Transactions on*, vol. 38, pp. 91–100, Jan 2002.

[93] M. Nashiki, A. Satake, Y. Kawai, T. Yokochi, and S. Okuma, "A new flux-barrier-type reluctance motor with a slit rotor," *Industrial Electronics, IEEE Transactions on*, vol. 46, pp. 1199–1206, Dec 1999.

[94] J.-M. Park, S.-I. Kim, J.-P. Hong, and J.-H. Lee, "Rotor design on torque ripple reduction for a synchronous reluctance motor with concentrated winding using response surface methodology," *Magnetics, IEEE Transactions on*, vol. 42, pp. 3479–3481, Oct 2006.

[95] R. Moghaddam, F. Magnussen, and C. Sadarangani, "Novel rotor design optimization of synchronous reluctance machine for high torque density," in *Power Electronics, Machines and Drives (PEMD 2012), 6th IET International Conference on*, pp. 1–4, March 2012.

[96] G. Pellegrino, F. Cupertino, and C. Gerada, "Barriers shapes and minimum set of rotor parameters in the automated design of synchronous reluctance machines," in *Electric Machines Drives Conference (IEMDC), 2013 IEEE International*, pp. 1204–1210, May 2013.

[97] G. N. Vanderplaats, *Multidiscipline Design Optimisation*. Springer, 2007.

[98] J. H. J. Potgieter, *Optimal topology and critical evaluation of slip synchronous permanent magnet wind generator*. PhD thesis, Stellenbosch University, [Available Online - http://www.tinaja.com/glib/ellipse4.pdf], 2014.

[99] M. H. A. Prins, "Design of a field-intensified interior permanent magnet synchronous machine for electric vehicle application," Master's thesis, Stellenbosch University, [Available Online - http://hdl.handle.net/10019.1/86242], 2014.

[100] K. Schittkowski and C. Zillober, "Nonlinear programming," in *Encyclopedia of Life Support Systems (EOLSS), UNESCO, Topic: Optimization and Operations Research*, pp. 157–177, 2003.

[101] R. Ynag and C. Chuang, "Optimal topology design using linear programming," in *Computers & Structures, 1994 ELSEVIER*, pp. 265–275, July 1994.

[102] J. A. Snyman, *PRACTICAL MATHEMATICAL OPTIMIZATION "An Introduction to Basic Optimization Theory and Classical and New Gradient-Based Algorithms"*. Springer, 97 ed., 2005. Chapter 1.3.8 - Scaling of Design Variables.

[103] R. T. Marler and J. S. Arora, "The weighted sum method for multi objective optimization: New insights," *Structural and Multidisciplinary Optimization ; Springer-Verlag*, Dec 2010.

[104] E. Howard and M. J. Kamper, "Weighted factor multi-objective design optimisation of a reluctance synchronous machine," in *2015 IEEE International Electric Machines Drives Conference (IEMDC)*, pp. 1781–1789, May 2015.

[105] E. Howard and M. Kamper, "Weighted factor multi-objective design optimisation of a reluctance synchronous machine," *IEEE Transactions on Industry Applications*, vol. PP, no. 99, pp. 1–1, 2016.

[106] R. E. Perez, P. W. Jansen, and J. R. R. A. Martins, "pyOpt: A Python-based object-oriented framework for nonlinear constrained optimization," *Structures and Multidisciplinary Optimization*, vol. 45, no. 1, pp. 101–118, 2012.

[107] M. N. Ibrahim, P. Sergeant, and E. M. Rashad, "Synchronous reluctance motor performance based on different electrical steel grades," *IEEE Transactions on Magnetics*, vol. 51, pp. 1–4, Nov 2015.

[108] K. Parsopoulos and M. Vrahatis, "Particle swarm optimization method for constrained optimization problems," *Frontiers in Artificial Intelligence and Applications series : Intelligent Technologies - Theory and Applications: New Trends in Intelligent Technologies*, vol. 76, pp. 214–220, 2002.

[109] C. P. Steinmetz, "On the law of hysteresis," *Proceedings of the IEEE*, vol. 72, pp. 197–221, Feb 1984.

[110] ABB, *Wind Generators: Medium Speed Permanent Magnet Generators (MS PMG).* ABB Online Standards, 2012. [Available Online - http://www.abb.com/motors&generators],Nov.

[111] D. Lancaster, *Approximating a Circle or an Ellipse Using Four Bezier Cubic Splines.* The Guru's Lair. [Available Online - http://http://www.tinaja.com],Nov. 2013.

[112] V. Spruyt, *How to draw a covariance error ellipse?* 2013. Computer Vision for Dummies. [Available Online - http://www.visiondummy.com/2014/04/draw-error-ellipse-representing-covariance-matrix/],Nov. 2013.

[113] J. Unpingco, *Python for Probability, Statistics, and Machine Learning.* Springer, 2016, ISBN : 978 331 930 7176.